UniversidadeVigo

Departamento de Química Física

PhD Thesis

GOLD NANOSTARS: SYNTHESIS, STABILIZATION AND APPLICATIONS AS SURFACE-ENHANCED RAMAN SCATTERING TAGS

Director: Professor Luis Manuel Liz Marzán

Candidate: Ana Belén Serrano Montes

CIC biomaGUNE
Biomaterialetako Ikerkuntza Kooperatiboko Zentroa
Centro de Investigación Cooperativa en Biomateriales

Vigo, Diciembre de 2015

D. Luis Manuel Liz Marzán, Catedrático del Departamento de Química Física de la Universidad de Vigo informa que:

Ana Belén Serrano Montes, licenciada en Química, ha realizado en el Centro de Investigaciones Cooperativas en Biomateriales (CICbiomaGUNE) de San Sebastián bajo su dirección el trabajo descrito en la presente memoria, que lleva por título "Gold Nanostars: Synthesis, Stabilization and Applications as Surface-enhanced Raman Scattering Tags", y que presenta para optar al grado de Doctor por la Universidad de Vigo con Mención Internacional.

Vigo, 14 de Diciembre de 2015

Fdo. Luis Manuel Liz Marzán

A mi madre

Contents

Thesis Scope

This PhD thesis focuses on the preparation and stabilization of star-shaped gold nanoparticles (nanostars), and their use in various applications based on surface-enhanced Raman scattering (SERS) spectroscopy.

A general introduction is presented in **Chapter 1** where basic concepts about the synthesis of gold nanoparticles, surface functionalization and optical properties of metal nanoparticles, as well as the SERS phenomenon are introduced.

Chapter 2 describes the stabilization of gold nanostars using a combination of an aromatic dithiol and a surfactant. Further gold nanostar-seeded growth leads to a series of exotic nanostructures containing an internal gap in which the aromatic thiol is trapped. Due to the presence of hot-spots at these gaps, the new structures are excellent SERS-encoded probes for sensing and imaging applications.

Gold nanostars can be also stabilized using a mixture of a thiolated polyethylene glycol (PEG-SH) and smaller thiol molecules such as dodecanethiol (DDT) or SERS-active thiols. Functionalization with PEG and DDT is achieved through a solvent-exchange method, not only for gold nanostars but also for other nanoparticles including silver and gold spheres and gold nanorods. In **Chapter 3,** this general phase-transfer method for obtaining hydrophobic plasmonic nanoparticles with high stability is detailed. The self-assembly of these nanoparticles leads to SERS-active substrates, that can be compared according to their SERS efficiency. **Chapter 4** describes the preparation of SERS-encoded gold nanostars using the same strategy, yet employing Raman-active thiols in this case to induce the phase-transfer. These SERS-active nanostars are applied as SERS-tags for cell differentiation.

Chapter 5 deals with the optical response from PEG-stabilized gold nanostars assembled onto colloidal substrates. More specifically, polystyrene beads were loaded with gold nanostars and SERS-labelling was also applied for *in vivo* cell imaging.

In summary, this PhD thesis is expected to contribute to the design of different plasmonic nanomaterials with tailored surface functionality, high colloidal stability, biocompatibility and a huge potential for SERS applications. Star-shaped gold nanoparticles are the most prominent candidates in this direction. In particular, SERS-nanoprobes show great promise for biomedical applications and the results presented here could have enormous implications towards the engineering of new SERS-based multifunctional nanoplatforms.

CHAPTER 1

General Introduction

Light-driven technologies have contributed for centuries to improve our quality of life by means of numerous advances in medicine, communications, culture and energy. During the past few decades, a large effort has been made to advance such light based technologies through a precise control over the employed materials. In this context, a new research field called "Plasmonics" has emerged. Plasmons are coherent oscillations of charges in free-electron materials such as metals, in response to incoming light.[1] When such oscillations are restricted to a metal-dielectric interface,[2] and light interacts with particles that are much smaller than its wavelength, a local charge oscillation around the particle is produced, which is known as localized surface plasmon resonance (LSPR).[3] This ability of confining light at nanoscale dimensions provides plasmonic nanoparticles with numerous unique properties, including large electromagnetic field enhancements, high photothermal conversion efficiencies and rich spectral responses. These properties are extremely useful for applications across many different fields, such as biomedicine and biotechnology,[4] biosensing,[5] solar energy technology,[6] nanocatalysis[7] or computacional sciences,[8] among others.

Despite the wide range of existing plasmonic materials (copper,[9] aluminum[10], heavily doped semiconductors and metal oxides,[11] chalcogenides[12] and graphene[13] have been recently used), the most commonly utilized materials are still the noble metals gold and silver. Although LSPRs are more efficient in silver, gold nanoparticles (AuNPs) have received special attention due to their superior chemical inertness and synthetic accessibility.[14,15] The use of nanosized gold can be traced back to illustrious ancient examples such as the Lycurgus cup[16] and Faraday's pioneering colloids.[17] Although the preparation of monodisperse gold spherical particles is well known since the mid 20th century,[18] a tremendous progress has been achieved during the last decade in the synthesis of AuNPs with anisotropic morphologies.[19–21]

Anisotropic AuNPs are of special interest due to their structural, optical and catalytic properties, which are different and most often superior to those of spherical AuNPs.[20] For example, the high electric field enhancements that anisotropic nanoparticles (rods, cubes, prisms or stars, among others) present at sharp edges and tips, render them extremely attractive as plasmonic enhancers for surface enhanced Raman scattering (see Section **1.4**). Among many existing anisotropic gold nanostructures star-shaped nanoparticles (*gold nanostars*) have achieved a huge interest. These novel nanoplatforms have numerous applications in various fields, mainly due to their plasmon tunability into the near infrared (NIR) region and the multiple hot-spots generated at their branches (see Section **1.3**).[22] In this context, this thesis focuses on gold nanostars as functional plasmonic nanoparticles.

The following sections of this introduction introduce basic aspects on the preparation of gold nanoparticles, highlighting the synthesis of anisotropic gold nanostructures. General aspects of surface functionalization are also considered. An overview of the different materials and strategies for obtaining nanostructures with the desired surface properties is provided. The optical properties of plasmonic nanoparticles and the surface enhanced Raman scattering effect will be also briefly introduced. Finally, a general outlook on some relevant applications of plasmonic nanoparticles is provided. Special attention is devoted to bioapplications including sensing, imaging and therapy.

1.1 Synthesis of Gold Nanoparticles

In 1857 Michael Faraday described the first scientific method for the production of colloidal gold nanoparticles. Fine particles were formed by the aqueous reduction of a gold salt by white phosphorous and stabilization with carbon disulfide. Some years later, Zsimondy noticed the existence of anisotropic nanoparticles and he received the Nobel Prize in 1925 "for his demonstration of the heterogeneous nature of colloidal solutions and for the methods he used". He invented the ultramicroscope, which allowed him to visualize the shape of the AuNPs.[23] In 1951, Turkevich *et al.* studied the growth and nucleation processes to generate gold spheres by citrate reduction.[18] In this now widespread method, a gold salt and sodium citrate are stirred in water and the temperature, the ratio of gold to citrate, and the order of addition of the reagents control the size distribution of the obtained particles. Some fifty years later, seed-mediated growth methods were developed for the synthesis of large spherical as well as non-spherical AuNPs,[24] which allow control over the nucleation and growth processes, thereby obtaining improved monodispersity. Seed-mediated growth usually comprises two steps. First, small spherical nanoparticles (seeds) are prepared and then added to a "growth" solution that contains Au^{3+} ions, surfactants and a chemical reducing agent to induce anisotropic growth. While the seeds are synthesized using a strong reducing agent, such as sodium borohydride, the growth solution contains a milder reducing agent (often ascorbic acid, AA). The metal salt is reduced to an intermediate state so that only catalyzed reduction on the nanoparticle surface is allowed, avoiding the nucleation of new particles in the solution. Size, shape and surface properties are controlled by the amount and nature of reducing agent and stabilizer, as well as by their ratio to the Au precursor.

Murphy et al.[25] and Nikoobakht and El-Sayed[26] were pioneers in developing modern concepts of seed-mediated synthesis of rod-shaped nanoparticles. $HAuCl_4$ is first converted to $HAuBr_4$ and subsequently reduced to $HAuBr_2$ by AA in the presence of cetyltrimethylammonium bromide (CTAB) and silver nitrate ($AgNO_3$). AuNRs are formed after adding small citrate AuNPs to the growth solution, catalyzing the reduction of Au^+ to Au^0.[25] The yield can be increased up to 99% and monodispersity improved when the seeds are formed upon reduction of $HAuCl_4$ with $NaBH_4$ at 0 °C in the presence of CTAB, followed by the addition of $AgNO_3$.[26] Numerous reports describe the effect on the shape, yield and dispersity of the obtained AuNRs of the following parameters: seed concentration, size and structure, ascorbic acid concentration, temperature, pH or gold precursor and surfactant concentrations.[24,27–31] The AuNR growth mechanism was explained in the first studies assuming that the cationic surfactant micelles could act as a "soft template", directing nanoparticle growth.[25] However, the concentrations of AuNP seeds and silver ions (Ag^+) have been proved to also play a critical role in AuNR synthesis.[21] While single-crystalline CTAB-capped seeds lead to single-crystalline AuNRs with {520} faces on the side and a mixture of {111} and {100} faces on the ends,[32,33] multiply twinned crystalline citrate-capped seeds grow into multiply twinned rod structures with {100} faces on the sides and {111} facets at the tips.[34] When seeded growth is carried out on single crystal seeds but in the absence of Ag^+ nanospheres are obtained, suggesting that silver ions are adsorbed at the gold nanoparticle surface in the form of AgBr, then restricting the growth and stabilizing the surface of the nanorod.[25] The role of Ag^+ is not only crucial for the formation of AuNRs, but also for other nanoparticle shapes, such as concave cubic Au nanocrystals, {730}-faceted bypiramids[35,36] or high-index AuNRs.[28,37,38]

Gold nanostructures with star-like shapes are particularly exotic. Gold nanostars (AuNSs) consisting of a central core from which multiple sharp arms protrude have been successfully prepared following a wide variety of wet-based synthetic routes.[39] One of first the methods developed for the synthesis of branched gold nanoparticles was inspired by the seeded-growth process described above (**Figure 1.1a**).[26] Different capping agents have been studied, including surfactants and polymers. The preferential adsorption of the capping molecules on certain crystalline facets of the metal seed surface has been suggested to trigger the anisotropic growth process, by modifying the growth rates along specific crystallographic directions. The influence of additives such as $AgNO_3$ has been also reported to affect the growth of AuNSs, so that a higher degree of control on the nanoparticle star-shape can be achieved by the addition of silver ions at different stages of the growth process.[40–43]

The reducing agent also plays a significant role on the resulting shape of the nanoparticles. For instance, hydroxylamine has been used to grow three-dimensional thorny nanoparticles from 14 nm citrate seeds in the present of silver ions but without the need of templates and surfactants (**Figure 1.1c**).[44] A different but particularly efficient reduction protocol was developed on the basis of previous work on the synthesis of particles with smooth surfaces and well defined shapes, including spheres, wires, decahedrons, octahedrons, among others[45,46] High yield production of monodisperse branched nanoparticles from 15 nm PVP-coated Au seeds was obtained when $HAuCl_4$ was reduced using N,N-dimethylformamide (DMF) in combination with poly(vinylpyrrolidone) (PVP) as stabilizer. The reduction kinetics of $AuCl_4^-$ on the Au seed surface can be controlled using the combined reducing ability of DMF and PVP, which also plays a role in the anisotropic growth. When intermediate concentrations of PVP were used, much more uniform nanoparticles were obtained compared to those nanoparticles obtained with a high concentration of PVP. Therefore, a rapid, kinetically controlled and preferential growth along various crystal faces that enables the formation of nanparticles with stable star/flower-like shapes (**Figure 1.1d**) was proposed. This synthetic procedure also allows tuning both the size and the optical properties of the obtained nanostars. With decreasing [$HAuCl_4$]/[Au seed] ratio the obtained nanoparticles get smaller with shorter and lower number of spikes. The smaller nanoparticles display a significant blue-shift of the main plasmon band, with a higher intensity of the band-to-shoulder ratio corresponding to the core (see **Figure 1.3c** in **Section 1.3**).[47] The same method has also been employed to grow tips on other nanostructures such as AuNWs[48] or AuNRs,[49] as templates.

The formation of multiple branches is promoted by blocking certain crystal facets of the Au seeds by the surfactants and the silver ions. However, the use of these chemicals hinders the application of the obtained nanostars due to: (i) the toxicity of CTAB, (ii) aggregation after required washing steps, and (iii) the difficulty of replacing the surfactant with biorelevant molecules. Therefore, surfactant-free gold nanostars are of particular interest for the development of further applications. Vo-Dinh *et al.* demonstrated a simple and surfactant-free wet chemistry method for the production of monodisperse gold nanostars in high yield (**Figure 1.1b**).[50] This synthesis is fast and employs similar reagents to those of the well-known silver-assisted seed-mediated syntheses of AuNRs and AuNSs.[26,39,43,51] $HAuCl_4$ is reduced using AA in the presence of $AgNO_3$ and Au seeds under acidic conditions. Ag^+ has been reported to be necessary for the formation of Au nanostars, enhancing the anisotropic growth of the certain crystal facets on multi-twinned seeds, but not on single crystalline CTAB-seeds.[52] However, in absence of Ag^+, polydisperse spheres and rods are obtained. Hydrochloric acid (HCl) is also necessary for the formation of Au nanostars, meaning that chloride ions might play a similar role to other halides influencing the anisotropic growth.[53] Replacing HCl with HNO_3 leads to absence of branches. Moreover, size control can also be achieved by varying seed concentration. The same strategy has been demonstrated to yield unusual geometries using various hybrid nanostructures as seeds. Thus, gold spikes were grown onto Au-silica Janus particles, leading to Janus nanostars,[54] whereas gold nanoparticles of different shapes protected by radial mesoporous silica shells were used as templates for the growth multiple gold tips.[55]

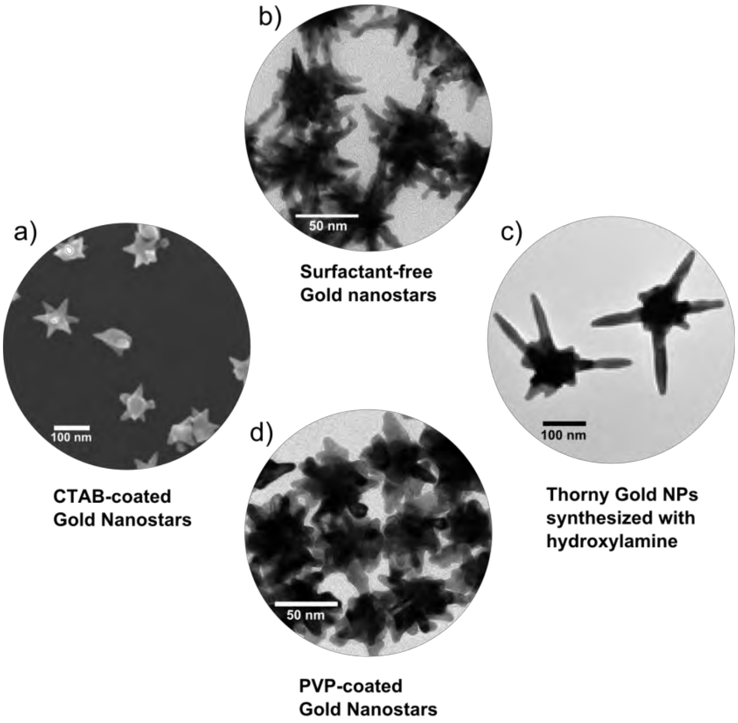

Figure 1. 1 Examples of AuNSs produced using synthetic procedures. (**a**) SEM image of AuNSs synthesized using CTAB as template). (**b**-**d**) TEM images of AuNSs synthesized with no surfactants (**b**), using hydroxylamine as reducing agent (**c**) and following the PVP-DMF assisted-method (**d**). Reproduced with permissions from ref **42** Copyright © 2006 American Chemical Society and ref **44** Copyright © 2007 American Chemical Society.

Beyond AuNRs and AuNSs, other remarkable morphologies including nanoparticles with the structure of one of the Platonic solids (tetrahedron, hexahedron, octahedron, dodecahedron and icosahedron),[56,57] flat platelets (usually with triangular or hexagonal shapes),[58,59] nanowires (synthesized by the tip-selective growth of AuNRs),[60] nanodumbbells (formed when tiny amounts of iodide influence AuNR growth)[53] or nanocages,[61] among others, have been achieved.

1.2 Surface Functionality of Metal Nanoparticles

Surface modification and functionalization of the as-synthesized nanoparticles constitutes an essential requisite in order to provide them not only with superior stability, but also with biocompatibility and specificity.[15,62,63] Ligand molecules are required to bind the metal surface by either chemisorption, electrostatic attraction or hydrophobic interactions. Gold surfaces may form strong and stable bonds (Au-S,~ 50 Kcal mol^{-1}) to molecules with thiols (-SH) or disulfide groups (S-S), which are common anchoring groups utilized for the attachment of other molecules.[64] Other functional ligands such as amines (*i.e.* dodecylamine or oleyamine) also interact with gold surfaces; however the binding forces are comparatively weak. Particle solubility is provided by the interactions of the ligand molecules with the solvent. Thus, charged or polar ligands provide solubility in polar or aqueous media, while particles coated with hydrophobic ligands are also soluble in non-polar organic solvents, such as hexane, chloroform or toluene. Certain amphiphilic ligand molecules, *e.g.* poly(ethylene) glycol (PEG), provide nanoparticles with solubility in a number of solvents, with intermediate polarity.[63]

A common strategy for improving the colloidal stability of the nanoparticles after synthesis is the so-called “ligand exchange”. A representative example is the functionalization of citrate-capped AuNPs with thiolated ligands (*i.e.* mercaptoundecanoic acid, MUA; mercaptopropionic acid, MPA) where the negatively charged citrate ions adsorbed on the particle surface are readily replaced by thiolated ligands, with stronger binding to the Au surface.[65] On the other hand, CTAB cationic surfactant, which is highly relevant for the shape control of Au nanoparticles, appears to be toxic to the cells at micromolar concentrations on its own. Therefore, replacement or overcoating of the surfactant bilayer adsorbed on the nanoparticles surface is required to get biocompatible nanoparticles.[66]

Ligand exchange is also a popular strategy for phase transfer from organic solvents into aqueous solutions (or vice versa).[67] In this case, the molecules stabilizing the nanoparticles in the starting phase are replaced by other ligands with stronger binding features, inducing the transfer to the second phase with high colloidal stability. While transfer between organic solvents can spontaneously occur (ligands such as mercaptocarboxylic acid are soluble in both organic and aqueous media), transfer from water to organic solvent is hindered by the poor solubility of the hydrophobic ligands in aqueous solutions. Additionally, different agents can be used to facilitate the phase transfer process. For instance, acetone decreases the surface tension at the interface, while strong acids or bases protonate negatively charged groups (or deprotonate positively charged amino groups), leading to particles with lower surface charge and thus less stable in aqueous media.

Coating with polymers is another highly versatile tool to solubilize hydrophobic nanoparticles in physiological media and including surface functionality.[68] The use of amphiphilic polymers containing reactive groups such as maleimide is a typical example of nanoparticle functionalization *via* hydrophobic interactions. The hydrophobic side chains of the polymer intercalate the hydrophobic ligand molecules of the nanoparticles, while the hydrophobic backbone is exposed to the outer aqueous environment. Besides the weak interactions between particle and polymer (van der Waals forces between the aliphatic chains), the number of contact points leads to a very stable coating.[69]

Furthermore, the physico-chemical characteristics of nanoparticles (*e.g.* hydrophobicity, surface charge, drug-release properties, and biological behavior) can also be modulated by coating with synthetic polymers such as polylactic acid (PLA), polyethylene glycol (PEG), polyvinyl alcohol (PVA), polylactic-co-glycolic acid (PLGA), poly-3-caprolactone (PCL), polyvinylpyrrolidone (PVP), polymethyl methacrylate (PMMA), and polyalkylcyanoacrylates (PACA). For example, surface-modified sulfonic groups help to improve blood compatibility and positively charged polyelectrolytes such as poly(ethyleneimine) (PEI) facilitate non-viral gene delivery applications. Currently, the most common functionalization coatings include the use of PEG, PEI, polyacrylic acid (PAA) and amphiphilic block co-polymers with or without PEG.[70] The linear synthetic polyether PEG is one of the most used ligands for *in situ* coating and grafting of nanoparticles. It is highly soluble in a number of organic polar and apolar solvents, as well as in water. PEG coated nanoparticles are more stable in solvents with high ionic strength and in biological environments, and they present less non-specific binding to protein and cells.[63]

Alternatively, nanoparticles can also be modified with coating shells such as silica, which can be considered as an inorganic polymer. Different methods have been developed for the preparation of nanoparticles with core@silica geometry. Generally, gold nanoparticles are coated with a silica shell by means of the well-known Stöber process, using tetraethylorthosilicate (TEOS) as a silica source.[71] Besides, the porous silica shell can be coated by hydrolysis and subsequent condensation of TEOS and octadecyltrimethoxysilane (C_{18}TMS), as a pore generator.[72] In general, silica coating can be considered an excellent tool leading to hybrid functional materials with enhanced stability and biocompatibility.[73]

Among all the strategies for particle solubilization and stabilization, ligand exchange methods usually lead to NPs with limited colloidal stability, while polymer encapsulation appears to be a versatile method and does not depend on the chemical nature of the underlying NP core.[68] The important role of the modification of the nanoparticle surface in many biological applications is highlighted, e.g. by the strong effect that surface charge has on both cellular uptake and biodistribution of nanoparticles. Positively charged nanostructures have enhanced affinity to negatively charged cell surfaces, thereby being the most likely candidates to cross cellular membranes and enter the cytoplasm of cells, an important aspect to consider in drug delivery applications.[74] Furthermore, nanostructures with active targeting capability binding to specific cancer cells can be synthesized, thus increasing the local concentration at the desired region in a living organism. The binding of the target moiety (*e.g.* antibody, peptide, folate) can occur either directly to the NP surface or to the terminal end of an attached polymer chain, such as carboxylic acid-modified PEG.[75]

In conclusion, surface functionalization of nanoparticles is a key requisite to provide stability in physiological enviorements, biocompatibility, impart functionality, amplify sensitivity and create cellular targeting effects, while maintaining the original properties of nanomaterials.[70]

1.3 Optical Properties of Plasmonic Nanoparticles

When light interacts with metal nanoparticles much smaller than its wavelength, a coherent oscillation of the surface conduction electrons around the particle, known as localized surface plasmon resonance (LSPR), is generated (**Figure 1. 2**).[76,77] As a result, metal NPs exhibit strong absorption and scattering in the UV-Visible (UV-Vis) range, which confer them with bright colours that have intrigued scientists for centuries.

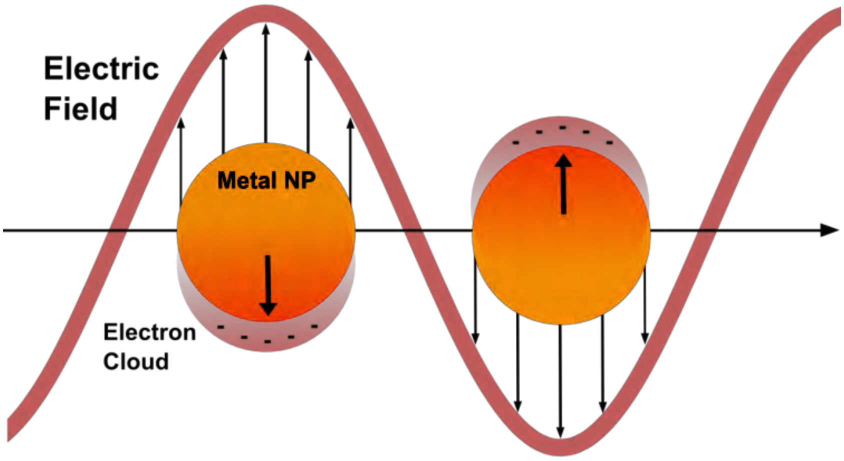

Figure 1. 2 Illustration of the localized surface plasmon resonance effect.

Michael Faraday recognized in 1857 that the intense red colour of gold solutions was actually due to its *state of tenuity and division*.[17] Later in 1905, Gustave Mie presented a general solution to Maxwell's equations that describes the extinction of spherical particles of arbitrary size.[78,79] Gans was able to extend this theory to ellipsoidal geometries.[80]

In the case of particle sizes much smaller than the wavelength of light, the following equation applies:[81]

$$E(\lambda) = \frac{24\pi^2 N_A a^3 \varepsilon_m^{3/2}}{\lambda\, ln(10)} \left[\frac{\varepsilon_i}{(\varepsilon_r + \chi\varepsilon_m)^2 + \varepsilon_i^2}\right] \qquad \textit{Equation 1.1}$$

where $E(\lambda)$ is the extinction (sum of absorption and scattering), N_A is the density of nanoparticles, a is the radius of the sphere, ε_m is the dielectric constant of the medium surrounding the sphere, λ is the wavelength of the incident radiation, ε_i and ε_r are the imaginary and real components of the nanoparticle's dielectric function, respectively, and χ is the term that describes the aspect ratio of the nanoparticle (equal to 2 for a sphere). The LSPR spectrum of an isolated metallic nanosphere in an external dielectric medium thus depends on the nanoparticle radius a, the nanoparticle material (ε_i and ε_r) and the dielectric constant of the nanoenvironment ε_m. Thus, 20 nm gold and silver nanoparticles are primarily absorbers whereas 80 nm nanospheres are also very good at scattering the incident electromagnetic radiation in all directions,[82] see the calculated spectra shown in **Figure 1. 3**.

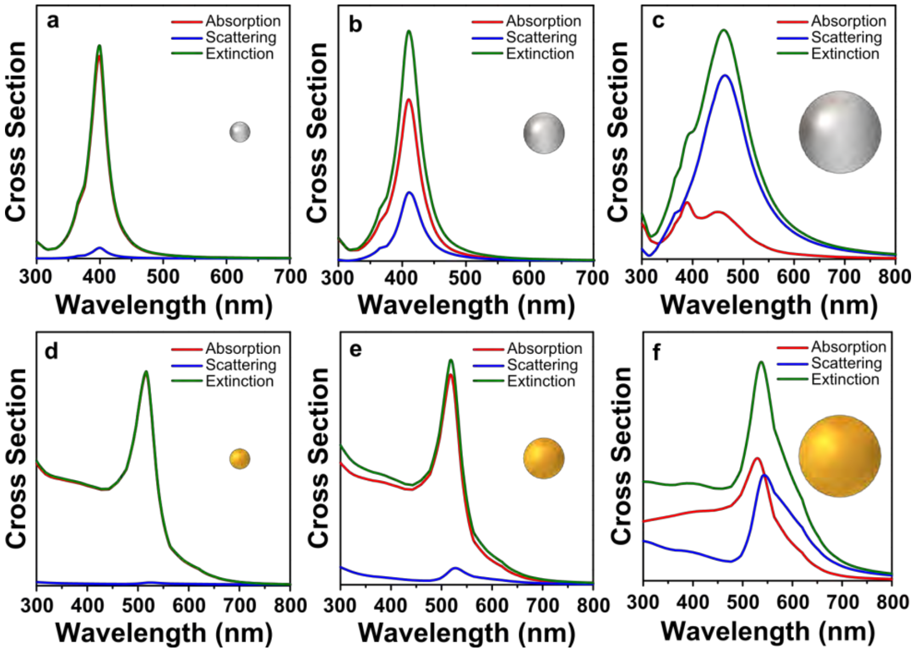

Figure 1. 3 Calculated extinction (green), absorption (red) and scattering (blue) spectra of: 20 (**a**), 40 (**b**) and 80 nm (**c**), silver nanoparticles and 20 (**d**), 40 (**e**) and 80 nm (**f**), gold nanoparticles. Calculations were carried out by means of the boundary element method (BEM).[83]

During the last decades, tremendous progress in the understanding of the optical features of anisotropic nanoparticles has been made. This development has enforced the development of computational tools such as the discrete dipole approximation (DDA),[84] the boundary element method (BEM)[85] or, more recently, the finite difference time domain method (FDTD).[86] In addition, novel and sophisticated synthetic procedures have allowed the preparation of nanoparticles with controllable sizes and shapes.[20,21,87] **Figure 1.4** shows experimental Vis-NIR spectra of gold nanoparticles of different shapes: gold nanospheres (AuNPs), nanorods (AuNRs) and nanostars (AuNSs). For AuNRs two plasmon bands are observed, corresponding to longitudinal and transverse plasmon resonance modes and related to light absorption and scattering along the long axis and the short axis of the particles, respectively.[88] It should be noted that the wavelength of the plasmon band varies with the refraction index of the surrounding media.[89] For AuNSs, the spiky shape gives rise to a main LSPR band and a less intense shoulder that correspond to the tip and core plasmon modes, respectively. As the nanostar diameter decreases, the main plasmon band blue shifts and gets narrower, while the band/shoulder corresponding to the core becomes more intense.[47] The possibility of tuning the plasmon band of anisotropic nanoparticles to be in resonance with common Vis-NIR light sources is an essential feature, affording excellent opportunities toward biological applications.[15,90]

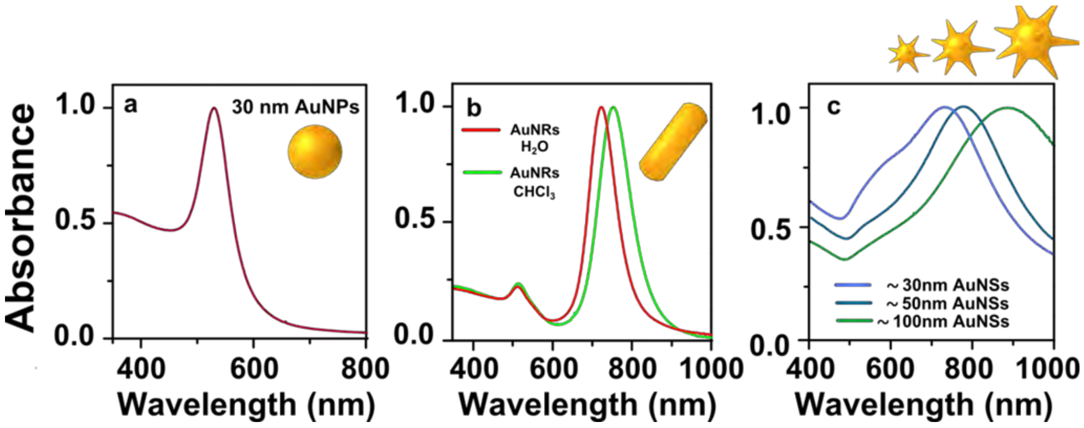

Figure 1. 4 Vis-NIR spectra of 30 nm AuNPs (**a**), AuNRs in H_2O (red) and in $CHCl_3$ (green) (**b**), and AuNSs of different sizes (**c**).

1.4 Surface enhanced Raman Scattering

Surface enhaced Raman Scattering (SERS) is an ultrasensitive vibrational spectroscopic technique that allows the detection of molecules on or nearby the surface of plasmonic nanostructures.[91] The signal levels observed in SERS are many orders of magnitude higher than those in conventional Raman scattering. Enhancements up to 10^{14} have been reported under special conditions where single molecules are being studied.[92,93] Since its discovery in 1977,[94] there has been discussion regarding the principal mechanism contributing to the SERS phenomenon. Nowadays, it is commonly accepted that there are two main contributions resulting from electromagnetic and chemical interactions between the adsorbate and the particle. It is well known that the most drastic signal increase is mainly due to the electromagnetic enhancement (EM) mechanism (~10^6),[91,92] while the chemical mechanism (CE) provides a minor enhancement (~10^2).[95,96]

The excitation of an LSPR is therefore a necessary condition for the observation of SERS since it leads to an increased local electric field relative to the incident electric field in the vicinity of the metal nanoparticle, which then acts as a nanoantenna. Therefore, a molecule near a nanostructured metal surface will experience a significantly enhanced incident intensity that excites its Raman scattering modes and the scattered Raman signal will thus be greatly magnified. When both the incident light and the scattered signal of molecules are in resonance the plasmon frequency, the SERS signal is maximized, leading to the $|E|^4$ enhancement.[92] Such high electric near fields are responsible for the significantly increased signal observed in SERS relative to standard Raman scattering. This is a brief description of the EM enhancement, which is the same for any type of molecule, but has a strong analyte distance-dependency: only molecules on or very close to the metal surface can experience the enhanced field.[97]

While the EM enhacement depends on the inherent properties of the metal surface (material, size, shape...), the CE enhacement is achieved via changes in the scattering cross section of the analyte, mainly due to charge transfer processes between the metal surface and the adsorbate. Generally, enhancement due to both mechanisms is reported as an enhacement factor(EF), a fundamental metric that is calculated as a ratio between the SERS intensity and the normal Raman intensity of the analyte and can be expressed as:

$$EF = \frac{I_{SERS}/N_{SERS}}{I_{NRS}/N_{NRS}} \qquad \textit{Equation 2.1}$$

where I_{SERS} and I_{NRS} are the SERS and normal Raman scattering intensities, respectively, and N_{SERS} and N_{NRS} are the number of molecules contributing to the scattering intensity.

During the last decades, researchers have attempted to develop new plasmonic nanostructures for SERS (usually known as SERS substrates). Gold, silver or copper are the most widely used materials since they have their LSPRs covering most of the visible and NIR wavelength range.[98] In particular, gold nanoparticles are extensively used as SERS substrates due to their easy synthesis, long-term stability and high biocompatibility.[99] The ideal SERS substrate needs to be prepared in a reproducible way, be chemically stable and exhibit high and spatially uniform EF. Higher SERS efficiency is obtained when metal nanospheres are partially aggregated, since junctions between nanoparticles function as SERS hot spots where larger EM fields occur.[100] Such aggregation can be easily promoted by changing the solvent, increasing the ionic strength of the suspension or decreasing the pH of the solution, or just spontaneously induced by the adsorption of the analyte. Notwithstanding, aggregation processes are hard to control and the production of controlled and reproducible SERS substrates still remains a challenge. Alternatively, anisotropic nanoparticles have been used to generate hot spots. Gold nanorods, nanowires, nanotriangles or nanostars, can sustain high EM fields at their "sharp tips" upon excitation with light of appropriated energy,[101–103] rendering them ideal substrates for SERS applications.[48,104] Among these nanostructures, AuNSs are of especial interest. The spikes can act as efficient nanoantennas so that EM field is expected to be very high at the edge of each tip, giving rise to multiple intrinsic SERS hot spots within a single nanoparticle. Advances in electron microscopy techniques such as electron energy loss spectroscopy (EELS) in scanning transmission electron microscopy (STEM), have allowed mapping the spatial distribution of the low energy plasmon mode in gold nanostars, showing its high localization at the tips (**Figure 1.5b,c**).[103] Even more, SERS EFs can be calculated using BEM and the results for a gold nanoparticle with one or two tips (mimicking a nanostar) show that the EF at the tip resonance wavelength can be even higher (10^8) than those for a sphere dimer (**Figure 1.5e**). Consequently, large Raman signal amplification can occur with no need for the formation of hot spots within nanoparticle aggregates in solution, which ultimately makes this system extremely appealing for SERS, especially for Raman imaging applications.[86,105–107]

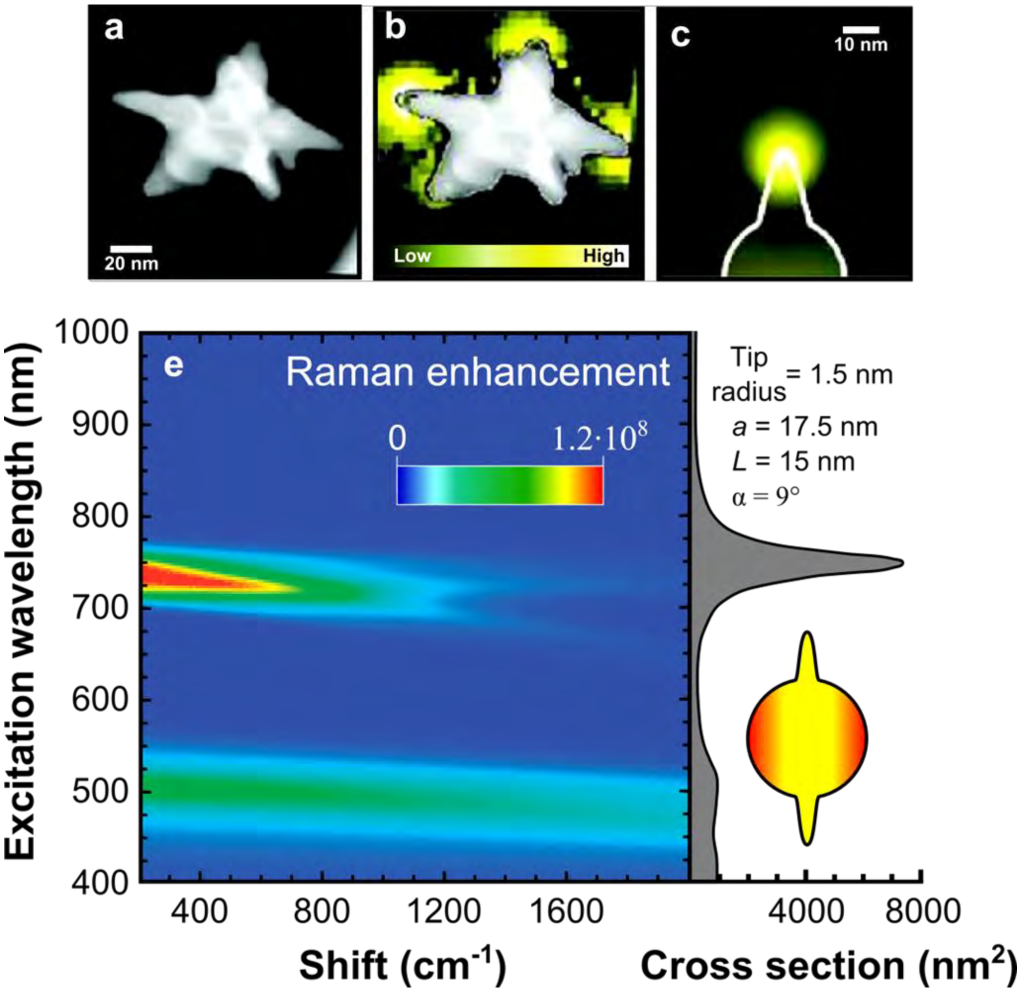

Figure 1. 5 (**a**) High resolution STEM dark-field image of a single Au nanostar. (**b**) EELS intensity mapping over the same particle. (**c**) Calculated EELS intensity map of the plasmon resonance in a particle tip, showing high localization near the tip apex, in agreement with the observed EELS image. (**e**) Left: calculated Raman enhancement in a two-tip gold particle in air. The excitations involved in the Raman process are assumed to be localized 2 nm away from the gold surface. Right: scattering cross section of the same particle. The particle shape and geometrical parameters are shown in the insets, where $\boldsymbol{L}$ is the tip length, $\boldsymbol{a}$ is the core sphere radius, and $\boldsymbol{\alpha}$ is the semi-angle of aperture of the tip. Reproduced with permissions from ref [103] Copyright © 2009, American Chemical Society and ref [46] Copyright © 2008, IOP Publishing.

1.5 Applications of Plasmonic Nanoparticles

As discussed above, plasmonic nanostructures display unique and fascinating optical properties that are related to their plasmon resonances and can be used for many applications, including sensing, imaging or even therapeutic purposes. The intense local electric field can enhance not only the scattering of molecules nearby the surface,[91] but also their photoluminescence properties.[108] The sensitivity of the LSPR to the medium dielectric constant and the inter-nanoparticle interactions has also been exploited for the optical detection of chemical and biological species.[109] In addition, LSPR also enhances the photothermal transduction process, which can be exploited for biomedical therapeutics such as photothermal therapy (PTT) or light-controlled drug delivery, among others.[4,110,111]

1.5.1 LSPR Sensing

The strong plasmon absorption and sensitivity to the local environment make metal nanoparticles appealing candidates as colorimetric sensors. Depending on the origin of the LSPR changes, two types of sensors can be distinguished: *aggregation* sensors and *refractive index* sensors.[109]

The read-out signal of *aggregation* sensors is based on the drastic color change produced by NP aggregation triggered by a target analyte. For example, metal ions can be detected using AuNPs that incorporate chelating agents onto their surface. Thus, AuNPs functionalized with phenanthroline can be used to effectively detect Li^+. Upon Li^+ binding, NP aggregation is induced, giving a linear response of color shift with the ion concentration.[112] Heavy metal ions, such as Pb^{2+}, Cd^{2+} and Hg^{2+}, can be also detected using 13 nm AuNPs that are functionalized with 11-mercaptoundecanoic acid (MUA). The surface carboxylate groups act as metal ion receptors. Mirkin and co-workers also employed DNA-functionalized AuNPs for the selective and sensitive detection of Hg^{2+} based on the thymidine-Hg^{2+}-thymidine coordination chemistry.[113] Following the same principle, the detection of other interesting chemical species, including avariety of anions (F^-, Cl^-, Br^-, I^-, NO_3^-, among others) or small organic molecules (glucose, adrenaline, glutathione), has also been reported.[114]

AuNP based colorimetric tests are a highly competitive technology for the detection of oligonucleotides.[115,116] In this approach, two different ssDNA-modified AuNP probes that present complementary bases to both ends of the target oligonucleotide are employed. AuNP aggregation is triggered by the presence of the target as a result of the hybridization of the DNA strands. Anisotropic NPs have been employed in DNA biosensing experiments as well. In particular, because thiolated oligonucleotides tend to bind to the tips of gold nanorods, end-to-end nanorod assembly takes place through hybridization of complementary ssDNA.[117] Apart from DNA, protein recognition has also been achieved using nanoparticle aggregation. For example, carbohydrate binding proteins, such as concanavalin A (Con-A) have been detected with carbohydrate (mannose) functionalized AuNPs.[118]

Refractive index sensors are based on the shift of the LSPR band. Local refractive index changes, such as those induced by biomolecular interactions at the surface of the nanostructures, can be monitored by LSPR peak shift. To sense chemical/biological species, the nanoparticles are also conjugated with recognition molecules specifically binding the target analyte and causing a plasmon band shift. The sensitivity is largely influenced by the particle size and shape. In this respect, AuNRs appear to be very suitable for plasmon sensing,[119] or biosensing as demonstrated for model biomolecules like streptavidin/biotin.[120] Other nanostructures, such as silver nanoprisms, also present high sensitivity and they have been used to sense important biomarkers, e.g. from Alzheimer's disease.[121]

1.5.2 SERS Sensing and Imaging

Raman spectroscopy is a powerful technique capable to provide rich molecular structure information. However, the direct application of this technique in sensitive detection and identification of analyte molecules is restricted by the low efficiency of inelastic photon scattering by molecules, which leads to a weak signal. As mentioned above, in the presence of plasmonic nanostructures such as AuNPs, the Raman scattering intensity from a molecule can be enhanced up to 10^{14} orders of magnitude.[92] Thereby, SERS can be applied to detect molecules at extremely low concentration, becoming of great interest not only in analytical chemistry but also in diagnostics.[97,98]

Two main strategies have been used for SERS detection using metal nanoparticles, using either label-free or Raman-reporter coated nanoparticles. Using label-free nanoparticles, the analyte molecules are directly adsorbed onto the nanoparticles and recognized by their enhanced Raman signal, so that no external label needs to be attached to the analyte of interest. For instance, by this approach TNT recognition in 2 pico molar (pM) level has been demonstrated using cysteine modified AuNPs. Due to the complex between cysteine and TNT, AuNP undergo aggregation leading to hot spots that enhance the Raman signal of the TNT molecules.[122] Zeptomolar detection of different chemisorbing and non-chemisorbing analytes (biomakers), can be achieved by sandwiching a drop-cast thin film of the analyte solution between a gold film and a subsequently drop-cast film of gold nanostars.[103] Molecular information about target cells can also be obtained using this label-free method. For example, head and neck cancer cells can be differentiated from normal cells by the assembly of immunogold nanorods on the surface of cancer cells.[123]

In the approach based on Raman-reporter coated nanoparticles, molecules with large Raman cross sections are adsorbed or covalently attached to the nanoparticles. These Raman reporters offer an intense and specific SERS spectrum, which is necessary for the indirect identification of the target molecule. SERS labeling represents a novel and attractive tool that shows extraordinary features for bioanalysis and presents many advantages over other optical probes (*e.g.* quantum dots (QDs) and organic fluorescent dyes). These advantages are mainly related to the high sensitivity, the narrow line widths of the vibrational spectral bands (offering multiplexing capability) and the high photostability of the SERS labels (also referred to as SERS-tags).[99] Ideal Raman labels exhibit the following properties: (i) high Raman scattering cross sections for high signal levels, (ii) a small number of atoms and high symmetry, leading to a minimal number of Raman bands for spectral multiplexing, (iii) low or no photobleaching for signal stability, and (iv) groups with high affinity for metallic surfaces, prone to chemisorption.[124] Common dyes reporters include Indocyanine Green, Crystal Violet, Methylene Blue, or Rhodamine 6G. “Colorless” molecules have also been used as Raman reporters, often thiolated molecules such as benzenethiol, mercaptopyridine, aminothiophenol or 4-mercaptobenzoic acid, among others.

SERS labels can be divided into two large groups. In the first group, the SERS-label (metal nanoparticle plus reporter) is covered by a protective layer that confers them with physical robustness, stable signals and immunity to their biological and chemical environment. The second group comprises SERS-tags, also known as SERS-probes, in which no protective layer is used and therefore has drawbacks related to the possibility of leaching of the Raman-molecule as well as the adsorption of interfering molecules.[99]

Using this last approach, Mirkin and co-workers demonstrated the multiplexed detection of oligonucleotide targets with gold nanoparticles labeled with oligonucleotides and commercially available dyes (Cy3, Cy3.5, Cy5, Rhodamine 6G, tetramethyl rhodamine and Texas red) in conjunction with subsequent silver staining (**Figure 1.6**).[125]

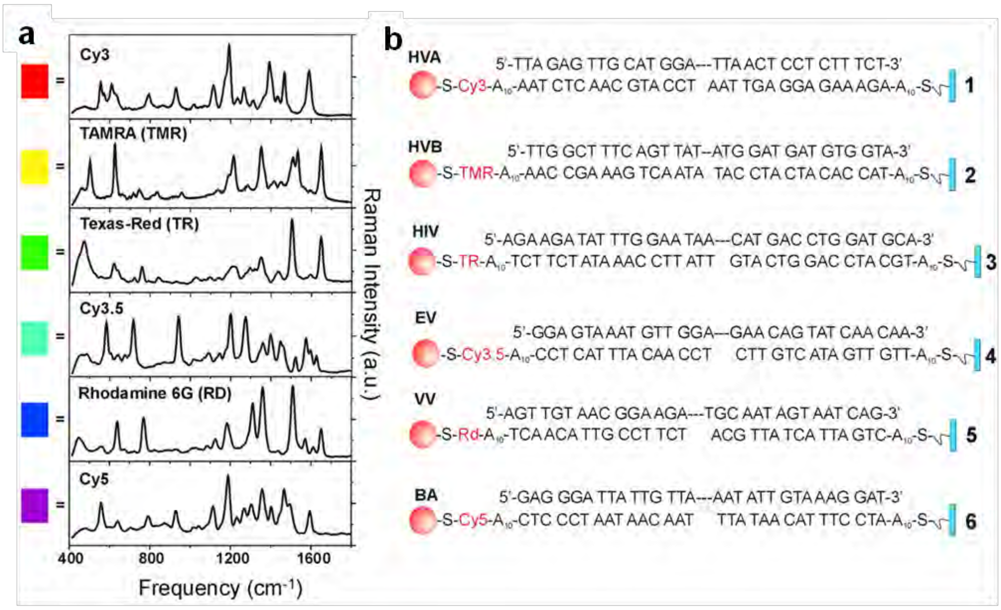

Figure 1. 6 (**a**) Raman spectra of six dye-labeled nanoparticle probes after Ag enhancing on a chip. (**b**) Six DNA sandwich assays with corresponding target analysis systems. Reproduced with permission from ref [125] Copyright © 2002, American Association for the Advancement of Science.

Notwithstanding, for other practical applications encapsulation of the SERS-probes is required. The protective shell usually improves colloidal stability, water solubility and biocompatibility, and provides the functional groups for further bioconjugation. Different encapsulation strategies include the use of proteins, organic polymers or silica. For instance, Nie and co-workers used polyethylene glycol (PEG) to protect 60 nm AuNPs labeled with crystal violated and they showed the first use of SERS tags for *in vivo* tumor targeting. When the particles were conjugated to tumor-targeting ligands and by 785 illumination, they obtained the highest SERS signal at the tumor site.[126] Chen and co-workers also reported a facile preparation of SERS-tags using an amphiphilic diblock copolymer, polystyrene block-poly(acrylic acid). The NP surface was coated via thermodynamically controlled self-assembly.[127] Poly(N-isopropylacrylamide) was used to prepare dye-encoded gold octahedrons, which were then employed as SERS tags for the detection and imaging of tumor biomarkers.[128] Bovine serum albumin (BSA) is also commonly used for surface coating. BSA can absorb on the surface of the metal nanoparticles via weak interaction and produce a protective shell. Vo-Dinh *et al.* used BSA-protected NIR SERRS (surface enhanced resonance Raman scattering) probes made of gold nanostars for quantitative multiplexing *in vivo* and *in vitro*.[129] Another attractive encapsulation method is the silica coating, which provides high mechanical stability and the option for long-term storage. Natan and co-workers introduced the concept of silica encapsulation for analyte-tagged nanoparticles.[130] Later on, Schlücker's group designed an alternative method to prepared silica-encapsulated SERS probes that comprised a self-assembled monolayer (SAM) of Raman labels, demonstrating that SAM leads to higher sensitivity compared to sub-monolayer Raman reporter covering.[131] Encoded gold nanostars were also encapsulated with silica, showing notably higher SERS efficiency, as compared to encoded spherical particles.[132]

In general, SERS-labels have been widely used for the detection of biomarkers in cancer cells[133] and other diseases,[134] as well as viral and bacterial microorganisms,[135] and also for *in vivo* imaging of cells, tissues and organs.[99] In this respect, Raman imaging has emerged as a novel and powerful tool for optical *in vivo* imaging analysis that offers several advantages over other imaging methods.[136] The proof of principle for SERS imaging using SERS-labeled primary antibody for target localization in tissue was first demonstrated by Schlücker *et al.* in 2006.[137] They targeted prostate-specific antigen (PSA) and after incubation of the prostate tissue sections with antibody-modified Au/Ag SERS-labeled nanoshells, the characteristic Raman spectra of the SERS tags only for the PSA (+) epithelium were obtained. Multiplexed *in vivo* SERS imaging was also demonstrated in mice using labeled silica-coated AuNPs.[138] The authors demonstrated the ability of Raman spectroscopy to separate the spectral fingerprints of up to ten different subcutaneously injected tags (**Figure 1.7**). In addition, SERS nanotags with novel NIR Raman reporters were used for *in vivo* multiplex targeted imaging. The authors also performed SERS mapping at tumor and liver areas, proving the selective targeting of positive nanotags in tumor site.[139]

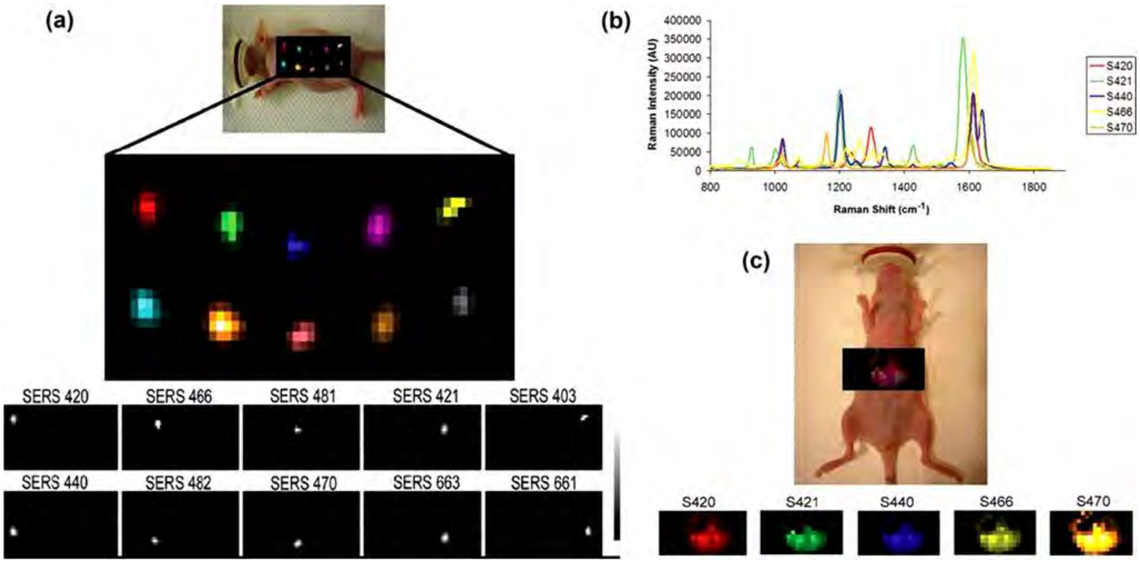

Figure 1. 7 (**a**) Evaluation of multiplexing 10 different SERS NPs *in vivo*. Raman map of 10 different SERS particles injected subcutaneously in a nude mouse. Arbitrary colors have been assigned to each unique SERS NP batch injected. *Panels below* depict separate channels associated with each of the injected SERS NPs. Grayscale bar to the right depicts the Raman intensity, where white represents the maximum intensity and black represents no intensity. (**b** and **c**) Demonstration of deep-tissue multiplexed imaging 24 h after intravenous injection of five unique SERS NP batches simultaneously. (**b**) Graph depicting five unique Raman spectra, each associated with its own SERS batch. (**c**) Raman image of liver overlaid on digital photo of mouse, showing accumulation of all five SERS batches accumulating in the liver after 24 h post injection. *Panels below* depict separate channels associated with each of the injected SERS NP batches (ref [138]).

1.5.3 Two-Photon Photoluminescence Imaging

An outstanding property of plasmonic nanoparticles, especially for non-spherical morphologies (e.g. nanorods, nanocages, nanoshells, nanostars), is the efficient plasmon-enhanced two-photon photoluminescence (TPL). TPL has also become as a powerful technique for cellular imaging. The resonant coupling of the plasmon band with the incident laser greatly amplifies the nanoparticles TPL as result of the recombination of electron-hole pairs. Furthermore, non-spherical nanoparticles display plasmon bands that can be tuned to NIR wavelengths, where biological tissues exhibit relatively small extinction coefficients, what is preferable for *in vivo* imaging.[140] The effective use of AuNRs as high contrast agent for TPL imaging was demonstrated by labeling cancer cells with anti-EGFR nanorod conjugates, allowing the noninvasive three-dimensional imaging of a variety of molecular signatures.[141] The TPL contrast of nanostars functionalized with wheat-germ agglutinin has also been used to image the nanoparticle uptake in breast cancer cells as well as nanostars circulating in the vasculature of *in vivo* models.[50] Besides, other plasmonic structures such as Au nanocages[142] or Au nanoshells,[143] have also been exploited as strong TLP contrast agents. However, TPL imaging is currently limited by its broad photoluminescence band. Unlike SERS, which has distinct spectral information capable of multiplex detection, TLP has only one broad band, which hinders its use for multiplex detection. Still, this new powerful TLP imaging using multi-photon microscopy, results in high resolution cellular imaging of plasmonic nanoparticles.

1.5.4 Plasmonic Nanoparticles as Therapeutic Agents

The use of plasmonic nanoparticles as therapeutic actuators has given rise to new opportunities for alternative treatments. The current trends go beyond the mere use of plasmonic nanoparticles as diagnostic agents and therapeutic actuators, in the direction of *theranostics*,[144] *i.e.* the combination of therapy and diagnostics functionalities in a single nanostructure. Nanoparticles exhibit passive accumulation at tumor sites, through a process known as enhanced permeability and retention (EPR),[145] which provides the possibility to release a drug once the target is reached[146] or to photothermally destroy cancer cells. Nanoparticles can additionally protect drugs from degradation inside the body before they actually reach their target, thereby leading to a better control over the therapeutic timing by means of a slower release.[147] In addition, particle surfaces can be functionalized with multiple molecules, acting as useful multifunctional elements,[68,148] with the potential of active targeting.

Photothermal Therapy (PTT)

The use of plasmonic nanoparticles as photoabsorbing agents can enhance the efficiency of visible and NIR light absorption by several orders of magnitude as compared to conventional phototherapy agents, with the additional advantage of a high photostability.[110]

Gold nanoparticles are excellent candidates as nanoheaters. The wide variety of available dimensions and morphologies allow us to optimize the photothermal response, as the spectral location of the LSPR wavelength depends on the particle dimensions and shape.[89,149] Additionally, conjugation chemistry has been largely developed to functionalize AuNPs with specific biorecognition elements for different kinds of cancer cells. Whereas the availability of nanomaterials with LSPR in the second NIR region (1000-1350 nm) is still limited, LSPR tunability from the UV up to the first transparency window (650-950 nm) has been readily achieved. Therefore, nanoparticle morphologies with the optimum LSPR wavelength matching the 808 nm optimum value for biological applications can be easily selected. Optimal transmission of light in the first transparency window through the tissue is achieved because of a combination of low scattering and low energy absorption, providing a maximum penetration of the radiation and minimizing the autofluorescence.[150,151]

With this in mind, gold nanoshells comprising a silica core and a thin Au shell, were reported as the first viable plasmonic phototherapy.[152] Their photothermal response,[153,154] surface modification for specific targeting[153] and potential as theranostic agents,[155] have been extensively investigated. Currently, these particles are under FDA-trials as AuroLase® Therapy for "Refractory Head and Neck Cancer" and "Primary and/or Metastatic Lung Tumors".[156] Other shapes, including gold nanocages, have been designed for different biomedical applications including PTT, with positive results for the treatment.[61,157] AuNRs have also been demonstrated as effective nanoheaters for PTT, e.g. anti-EGFR-conjugated NRs are highly efficient toward cancer cell diagnosis and selective PTT.[158] Also TAT-functionalized AuNSs were recently reported to display efficient photothermolysis using 0.2 W/cm^2 irradiance, which proved to be an ultra-effective PTT for prostate cancer treatment.[159]

Even if all the different particle geometries have been demonstrated to be effective as photoactivated nanoheaters, it is still challenging to identify the most efficient particle size and morphology for selective local heating. Recent studies have allowed comparing the heating efficiency for particles of different shapes.[160] For example, using quantum dot (QD) based double-beam fluorescence thermometry, the heating efficiency of five different geometries (AuNRs, AuNSs with long and short tips, AuNCs and Au nanoshells) was analyzed, resulting the most efficient heaters the long-tip AuNSs.[161] Thus, from the point of view of cancer therapeutics, plasmonic nanostructures presenting strong absorptions can ensure the effective laser therapy, rendering a minimal invasive treatment and emerging as a new generation of photothermal agents.[110]

Drug Delivery

The use of plasmonic nanoparticles for delivering chemotherapeutic drugs, both *in vitro* and *in vivo*, has recently gained much attention. Again, gold nanomaterials can be considered as ideal nanocarriers, since they can be easily functionalized with targeting ligands and cytotoxic drugs and deliver the therapeutic cargo to cancer cells, reducing to the minimum the toxicity of the healthy cells.[4] The release of the drug from the gold nanoparticle can be regulated through two different approaches: i) via internal stimuli, where the physicochemical characteristics of the cellular microenvironment (such as pH, ions) biologically enables the controlled release, and ii) via external stimuli, which employs the support of an exogenous process such as increasing the temperature or light irradiation. Particularly, photo-active drug release using plasmonic nanoparticles has been widely studied. This case is similar to PTT, yet requiring lower laser power and shorter irradiation time, but the light-induced plasmonic heating can be exploited to release the chemical payload.[162]

Different strategies have been studied, aiming at efficient binding or encapsulation followed by selective release with high spatial and temporal resolution. One of them comprises the functionalization of the NP surface with a molecule that can bind the drug of interest, so that upon temperature change, a conformational change enables release of the drug. For example, 4′,6-diamidino-2-phenylindole (DAPI) reversibly binds to double stranded DNA, thereby allowing its release from DNA modified Au nanoshells upon irradiation at the LSPR wavelength and DNA dehybridization (**Figure 1.6a**).[163] Another alternative is the use of thermo-responsive polymers, such as poly(N-iso-propylacrylamide) (pNIPAM) or poly(lactic-*co*–glycolic acid) (PLGA),[164] where the application of light can cause rapid shrinkage of the hydrogels and released the drug (**Figure 1.6b**). For example, Xia and co-workers used AuNCs coated with pNIPAM to modulate drug release at temperatures slightly above the lower critical solution temperature (LCST) of the polymer (32 °C).[165] Other approaches include the use of polyelectrolyte multilayers, which are loaded with a drug in the inner cavity and contain plasmonic nanoparticles at the multilayer wall (**Figure 1. 6c**),[166] as well as the use of liposomes that contain hydrophobic particles embedded at the lipid bilayer (**Figure 1. 6d**) or hydrophilic particles encapsulated inside the cavity.[167] In all cases, the release of the drug can be induced upon irradiation under NIR light.

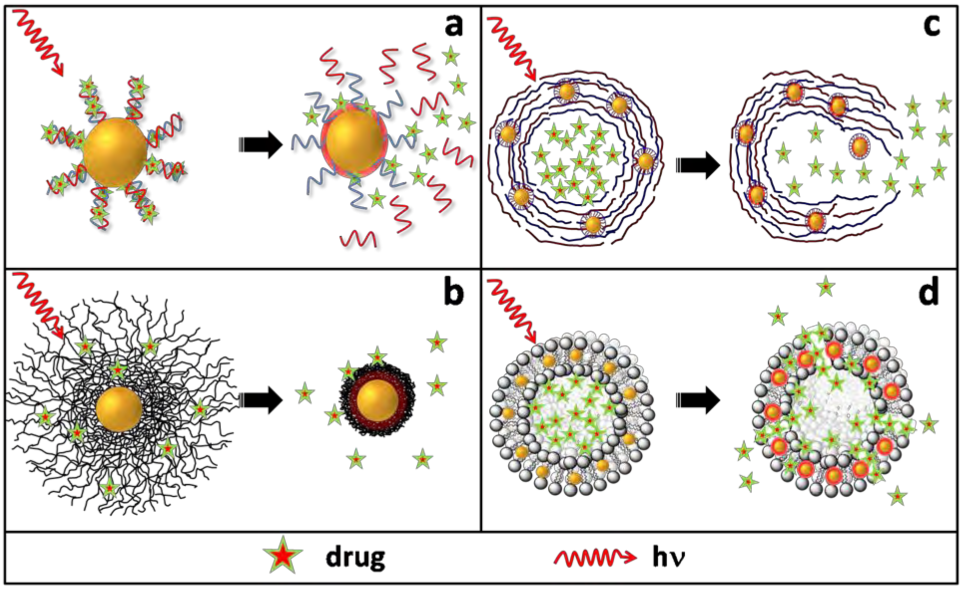

Figure 1. 8 Examples of different nanocarriers and drug release mechanisms: (**a**) a plasmonic nanoparticle is functionalized with double stranded DNA chains that can bind a drug. Upon irradiation, the temperature increases, DNA dehybridizes and the drug is released. (**b**) A plasmonic nanoparticle is modified with a smart polymer that shrinks upon a temperature increase, inducing the release of the drug. (**c**) Polyelectrolyte multilayer capsules loaded with a drug in the inner cavity and plasmonic nanoparticles at the wall, which induce the release of the drug once they are irradiated under NIR light. (**d**) Liposomes with Au NPs embedded in the bilayer with encapsulated drug, so that optical energy converts into localized heat, inducing a phase transition of the liposome and drug release.

In general, the load of gold nanoparticles with drugs, or other cargos such as genes, prevents the degradation of the drug prior to reaching the target, thereby minimizing premature releasing in the circulating system and enhancing the efficiency of the drug. Although this field is still in its early days, these new nanovehicles have the potential to produce ultimate and useful therapeutic benefits.[162]

CHAPTER 2

Stabilization and Encapsulation of Gold Nanostars Mediated by Dithiols

ABSTRACT

Surface chemistry plays a pivotal role in regulating the morphology of nanoparticles, maintaining colloidal stability and mediating the interaction with target analytes towards practical applications such as surface enhanced Raman scattering (SERS)-based sensing and imaging. We report the use of a binary ligand mixture composed of 1,4-benzenedithiol (BDT) and hexadecyltrimethylammonium chloride (CTAC), to provide gold nanostars with long-term stability. This is despite of BDT being a bifunctional ligand, which usually leads to bridging and loss of colloidal stability. We found however that neither BDT nor CTAC alone are able to provide sufficient colloidal and chemical stability. BDT-coated Au nanostars were additionally used as seeds to direct the encapsulation with a gold outer shell, leading to the formation of unusual gold nanostructures. Furthermore, BDT was exploited as a probe to reveal the enhanced local electric fields in the different nanostructures, showing that semishell configurations provide significantly high SERS signals as compared to other core-shell configurations obtained during seeded growth.

2.1 Introduction

Among a variety of possible nanoparticle morphologies, colloidal gold nanostars have been pinpointed as highly efficient SERS substrates due to their mentioned tunable LSPR and nanoantenna effects by controlling core size, along with tip length and sharpness.[46,86,104,168,169] Among the reported syntheses of AuNSs, surfactant-free AuNSs are of high interest. The bare surfaces are more suitable for surface functionalization and effective analyte chemisorption (usually hindered when using PVP or CTAB capped AuNSs[170]) and therefore higher SERS signal can be ensured. Additionally, toxicity issues derived from the surfactant are also avoided.[171,172] However, these AuNSs typically display poor stability, resulting in changes of the morphology of the nanoparticles (reshaping) and corresponding LSPR blueshifts, which has also been reported for other nanostructures with sharp tips.[173,174] In the absence of capping molecules, colloidal stability is also compromised, as van der Waals attractions become dominant, eventually leading to particle aggregation. These observations clearly indicate that the surface properties of AuNSs play a critical role on the colloidal and chemical stability, which is crucial for SERS-relevant applications.[175]

Various strategies have been developed to functionalize the AuNS surface, mediating the interaction of the nanoparticles with target analytes towards practical SERS applications. For instance, the introduction of capping molecules like polymer stabilizers,[46] thiolated PEG,[50] surfactants,[129,176] and proteins such as bovine serum albumin,[129] as well as protective inorganic shells,[132,177] were used to improve colloidal stability prior to eventual application. A conceptually different strategy concerns the use of reduced-graphene oxide (rGO) as support, with no need for additional polymer stabilizer or surfactant during AuNS synthesis.[178] Alternatively, an additional metal layer directly coated on the AuNS surface has been recently employed to develop stable SERS probes. Additional NS-templated silver overgrowth produces hybrid particles and enables stronger SERS signal upon adsorption of Raman tags on the outer surface.[176] However, few attempts have been directed toward incorporating the Raman tag between metal layers within the same particle, so as to generate plasmonic hotspots for the development of highly efficient SERS probes.[179,180]

We herein propose the use of 1,4-benzenedithiol (BDT) together with hexadecyltrimethylammonium chloride (CTAC), with the aim of stabilizing AuNSs by avoiding both reshaping and aggregation, as well as directing the seeded growth of a gold shell around BDT-primed AuNS seeds, which may incorporate intrinsic hot spots. Electron tomography, SERS and UV-Vis spectroscopy show that various exotic nanostructures were obtained, all of them containing embedded BDT Raman tags. Interestingly, we find that semishell-coated nanostars display significantly enhanced SERS, as compared to other coated nanostructures and to nanostars with no coating shell.

2.2 Experimental Section

Materials

Hydrogen tetrachloroaurate (III) trihydrate ($HAuCl_4 \cdot 3H_2O$, ≥ 99.9%), silver nitrate ($AgNO_3$, ≥ 99.0%), L-ascorbic acid (AA, ≥ 99%), sodium citrate tribasic dihydrate (≥98%), 1,4-benzenedithiol (BDT), hexadecyltrimethylammonium chloride (CTAC), O-[2-(3-Mercaptopropionylamino)ethyl]-O′-methylpolyethylene glycol (PEG-SH, 5000 Mw), 4-mercaptobenzoic acid (MBA), 4-aminothiophenol (ATP) and bis(p-sulfonatophenyl) phenylphosphine dihydrate dipotassium salt (BSPP), were all purchased from Sigma-Aldrich. Hydrochloric acid solution (37 wt%) was purchased from Panreac. Milli-Q water (18.2 MΩ·cm) was used in all experiments

Synthesis of gold nanostars and incubation with different capping agents

AuNSs were prepared by a modified seed-mediated growth method.[50] Briefly, the seed solution was prepared by adding 5 mL of 1% citrate solution to 95 mL of boiling 0.5 mM $HAuCl_4$ solution under vigorous stirring. After 15 min of boiling, the solution was cooled down to room temperature and then kept at 4 °C for long-term storage. The as-synthesized Au nanoparticle seeds had an average size of 14.8±1.5 nm, with an LSPR maximum at 519 nm. For gold nanostar synthesis, different amounts of the citrate-stabilized seed solution (final [Au0] = 0.05 mM for small AuNSs with core/overall size ratio of 23nm/39nm, and 5 μM for larger AuNSs with core/overall size ratio of 55nm/98nm) were added to 10 mL of $HAuCl_4$ (0.25 mM) solution containing 10 μL of HCl (1.0 M) in a 20 mL glass vial at room temperature under moderate stirring.

Quickly, 100 µL of $AgNO_3$ (3 mM) and 50 µL of AA (100 mM) were added simultaneously to the above solution. The solution rapidly turns from light red to blue or greenish-black, depending on the final concentration of Au^0. Specifically, 1 mL and 100 µL of gold nanoparticle seeds were added to the growth solution to obtain the small and the large AuNSs, respectively. Immediately after synthesis, equal amounts of AuNSs solution were transferred to different capping molecule solutions: BDT (10 µM), CTAC (1 mM), mixture of BDT (10 µM) and CTAC (1 mM), ATP (10 µM), MBA (10 µM), PEG-SH (10 µM), and BSPP (10 mM), and incubated for 30 minutes. Afterwards, all sample solutions together with a control sample (AuNSs without capping molecule incubation) were centrifuged twice, washed to remove the supernatant and redispersed in CTAC solution (5 mM for BDT, CTAC, (BDT+CTAC), MBA, and ATP) and water (PEG-SH, BSPP and bare). Corresponding UV-Vis spectra were obtained after washing. Kinetic studies were performed by monitoring the UV-Vis spectra of freshly prepared AuNSs (~23 nm core size), incubated with different capping molecules for different times ranging from ~1 min to 24 h, immediately after synthesis and without washing.

Gold shell growth using AuNS-BDT as seeds

The as-prepared AuNS modified by the BDT+CTAC binary mixture were used as seeds for gold shell growth. Typically, a growth solution containing CTAC (310 µL, 0.1 M), $HAuCl_4$, and AA (20 µL, 1.0 M) was first prepared to obtain a transparent solution. Afterwards, Au NS-BDT seed solution ($[Au^0]$ = 0.48 mM) was added to the growth solution under vigorous mixing. The reaction solutions were left undisturbed overnight and then the product was washed twice by centrifugation and redispersion in CTAC solution (5 mM). The morphology of the nanostructures obtained by seeded growth was tuned by changing the R value ($R = [Au^{3+}] / [Au^0]$) during the synthesis.

Instrumentation and characterization

UV-Vis spectroscopy (Agilent UV-Visible, ChemStation) was used to collect extinction spectra of colloidal solutions in 1 mm quartz cuvettes or 10 mm plastic cuvettes (kinetic studies). Conventional transmission electron microscopy (TEM) images were obtained using a JEOL JEM-2010 operating at 120 kV. Tilt series for electron tomography were acquired using a FEI Tecnai G2 electron microscope operated at 200 kV, in combination with a Fischione 2020 single tilt holder. Projection images were collected over an angular range of ±74° with 3° tilt increments. The tilt series were aligned using the FEI INSPECT 3D software and subsequently reconstructed via the simultaneously iterative reconstruction technique (SIRT) implemented in the ASTRA tomography toolbox. High resolution high angle annular dark field scanning transmission electron microscopy (HAADF-STEM) micrographs were acquired using a double corrected Titan 50-80 microscope operated at 300 kV. A Raman-IR microscope (Renishaw in Via Raman spectrometer) was used for solution SERS studies under 785 nm laser excitation, using ethanol as the calibration sample. Glass vials (Thermo Scientific, National C4015-96, 1 mL clear sepcap vials, 8 × 40 mm) were used for all solution Raman measurements.

2.3 Results and Discussion

2.3.1 Morphological and Colloidal Stability of Gold Nanostars

Surfactant-free AuNSs were prepared following a seeded-growth protocol reported by Vo-Dinh and co-workers using citrate-coated spheres as seeds.[50] The stability of the as-synthesized colloidal system was studied by comparing the effect of different capping molecules on the optical and morphological features of the particles. **Figure 2.1** shows the UV-Vis spectra of AuNS (~23 nm core size) after incubation (30 min) with different capping molecules, including cetyltrimethylammonium chloride (CTAC), 1,4-benzenedithiol (BDT), and a CTAC/BDT mixture. The first observation from this graph is that uncapped AuNSs undergo rapid transformation as indicated by a strong blueshift of the LSPR band, which was confirmed by TEM analysis showing that aged particles feature rounded tips (**Figure 2.1b**). A similar effect (though not so pronounced) was found for AuNSs that were incubated with CTAC (LSPR maximum ~660 nm), whereas BDT leads to a broadened LSPR band centered around 830 nm, indicating aggregation that was confirmed by visual observation (see photograph in the inset of **Figure 2.1a**). In contrast, upon incubation with a BDT/CTAC mixture, the width of the LSPR band was preserved, which is in agreement with TEM observation of sharp nanostar spikes (**Figure 2. 1b**).

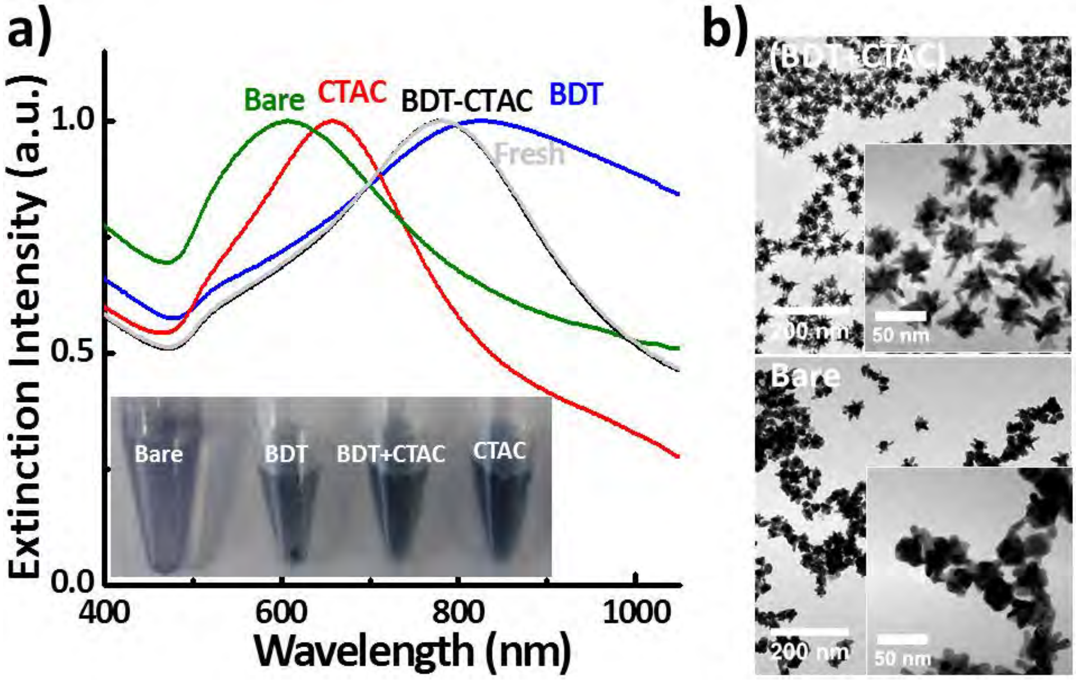

Figure 2. 1 (**a**) UV-Vis spectra of gold nanostars (~23 nm core size) after incubation with different capping molecules (CTAC, BDT, and BDT/CTAC mixture) and control samples (Bare: without capping but similar processing; Fresh: spectrum recorded ~40 seconds after the growth reaction without washing). Inset: Photographs taken 3 hours after vortex shaking and gentle sonication of the corresponding colloids. (**b**) TEM images of gold nanostars in the presence and in the absence of the BDT/CTAC mixture.

Comparison with other common capping ligands such as thiolated polyethylene glycol (PEG-SH, O-[2-(3-Mercaptopropionylamino)ethyl]-O′-methylpolyethylene glycol), 4-aminothiophenol (ATP), 4-mercaptobenzoic acid (MBA), and bis(p-sulfonatophenyl) phenylphosphine dihydrate dipotassium salt (BSPP) (**Figure 2.2**) resulted in significant blue shifts and reshaping for all of these ligands.

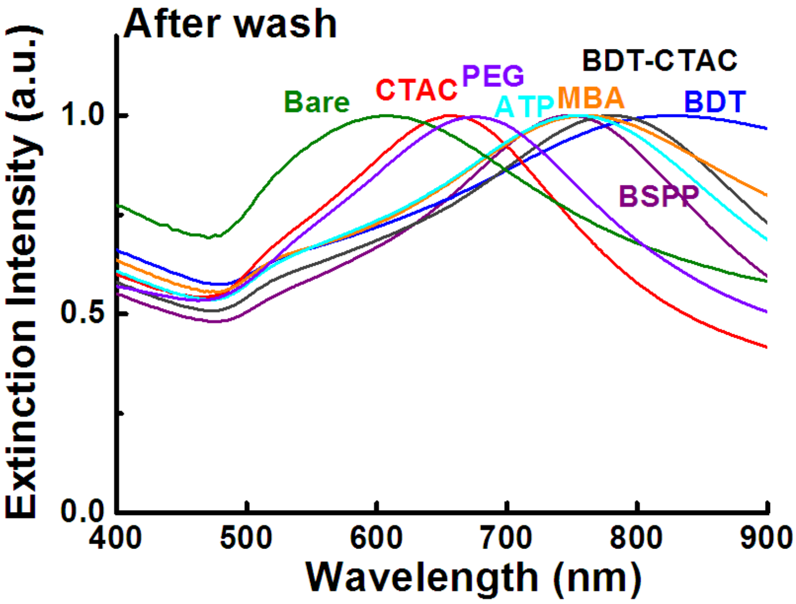

Figure 2. 2 UV-Vis spectra of freshly prepared Au nanostars (~23 nm core size) after incubation with different capping molecules followed by washing (bare, CTAC, PEG-SH, ATP, MBA, BSPP, a mixture of BDT and CTAC, BDT only).

The evolution of the different samples was monitored by UV-Vis spectroscopy (**Figure 2.3**), which confirms that, whereas the LSPR band of the colloid comprising bare gold nanostars rapidly blueshifts, along with a decrease in extinction intensity and a dramatic change after 24 hours, introduction of CTAC slows down the blue shift rate. When a mixture of BDT and CTAC was added, the blue shift of the LSPR band was immediately quenched and the LSPR peak intensity was maintained. Such a significant improvement of AuNSs stability upon addition of a thiolated molecule is likely due to the formation of Au–S bonds that limit the mobility of Au surface atoms, as recently reported for mercaptopropionic acid.[62] Note that, as compared with monothiolated molecules (e.g. ATP and MBA, **Figure 2.2**), the dithiolated BDT was found to provide the longest LSPR stability, possibly because of the higher probability of Au-thiol interaction. We postulate that the role of CTAC is the effective stabilization of the colloidal system, since AuNSs capped with CTAC only display a narrow LSPR band (no aggregation) but significantly blue-shifted because of reshaping (**Figure 2.1**). This synergistic effect combining the higher stability provided by the thiolated ligand and the surfactant was observed not only for gold nanostars, but also for gold nanospheres,[181] arrowhead gold nanorods (polypeptide-SH and CTAB),[182] or standard nanorods (PEG-SH and CTAB).[183] The stability of BDT-modified AuNSs in CTAC is in fact surprising, given that usually disulfide ligands are likely to promote bridging of Au NPs into aggregates. In this case the presence of CTAC screens the potential binding of BDT with AuNSs, and ultimately endows significant colloidal stability to the system. We thus conclude that, the binary mixture comprising BDT and CTAC shows an excellent capability to stabilize the freshly prepared gold nanostars.

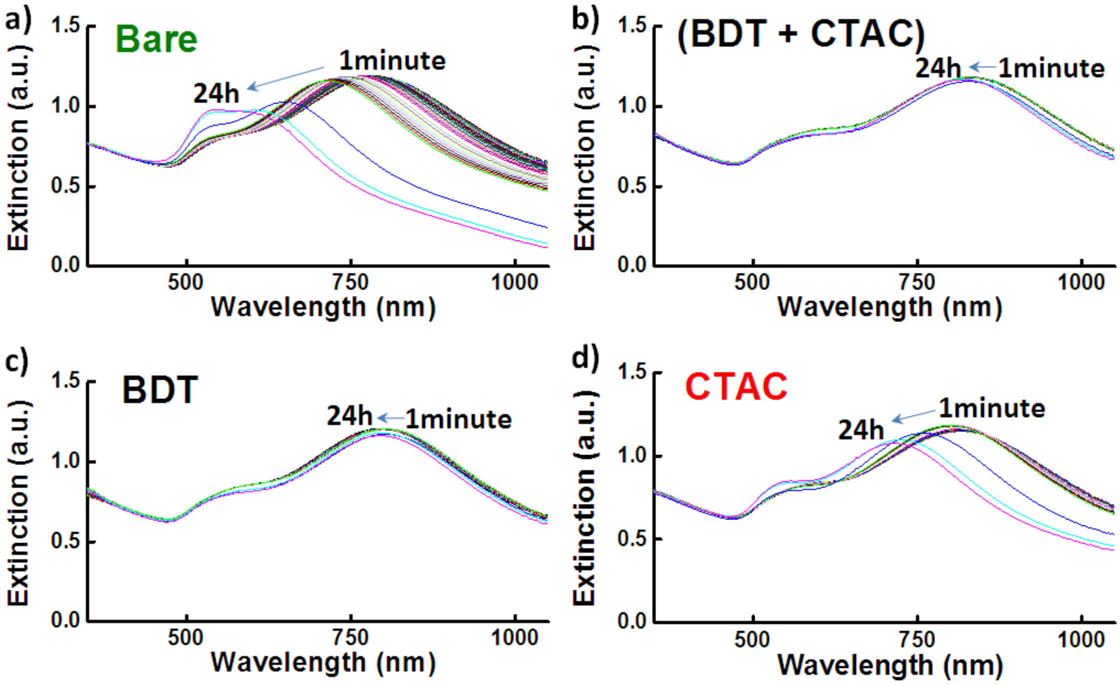

Figure 2. 3 Kinetic study of AuNS incubated with different capping molecules. UV-Vis spectra of freshly prepared AuNS (~23 nm core size) after introducing capping molecules from 1 min to 24 h: **a**) bare AuNS, **b**) AuNS with a BDT/CTAC mixture, **c**) AuNS with BDT only, **d**) AuNS with CTAC only.

2.3.2 Encapsulation via Seeded Growth

BDT-modified gold nanostars were used as seeds to direct further encapsulation within gold shells, considering that the strong binding between thiol groups and reduced gold atoms should affect the shell growth mode. Indeed, we found that standard seeded growth did not occur, but instead a series of exotic gold nanostructures were obtained with distinct LSPR features (**Figure 2.4**), by simply tuning the concentration ratio (R=[Au^{3+}]/[Au^0]). Chemical reduction by ascorbic acid (AA) of increasing amounts of $HAuCl_4$ on the capped AuNS led to a gradual decrease of the intensity of the band corresponding to the LSPR tip mode (~785 nm), while a higher energy band near the core mode emerged and progressively redshifted and increased in intensity. More specifically, for R values higher than 4.8, the tip band was completely damped, with a dominant band centered at 560 nm. The corresponding TEM images in **Figure 2.4b** indicate that for increasing R values the gold nanostars get gradually encapsulated within an external gold shell. For R = 4.8 a small number of spikes are exposed outside of the shell and when the R value increases up to 19.1, the gold nanostars seem to be fully covered by the shells (**Figure 2.4b**). The morphological evolution can thus explain the changes in the UV-Vis spectra, which were also observed when using larger AuNSs as seeds (core size ~55 nm) (**Figure 2.5**), both regarding morphological and optical changes. In this case however, at small R values satellite nanostructures (big nanostar decorated with multiple gold spheres) were dominant, in contrast to the core-shell geometry obtained using small nanostars as seeds. For large R values however, similar core-shell configurations were obtained for larger nanostars.

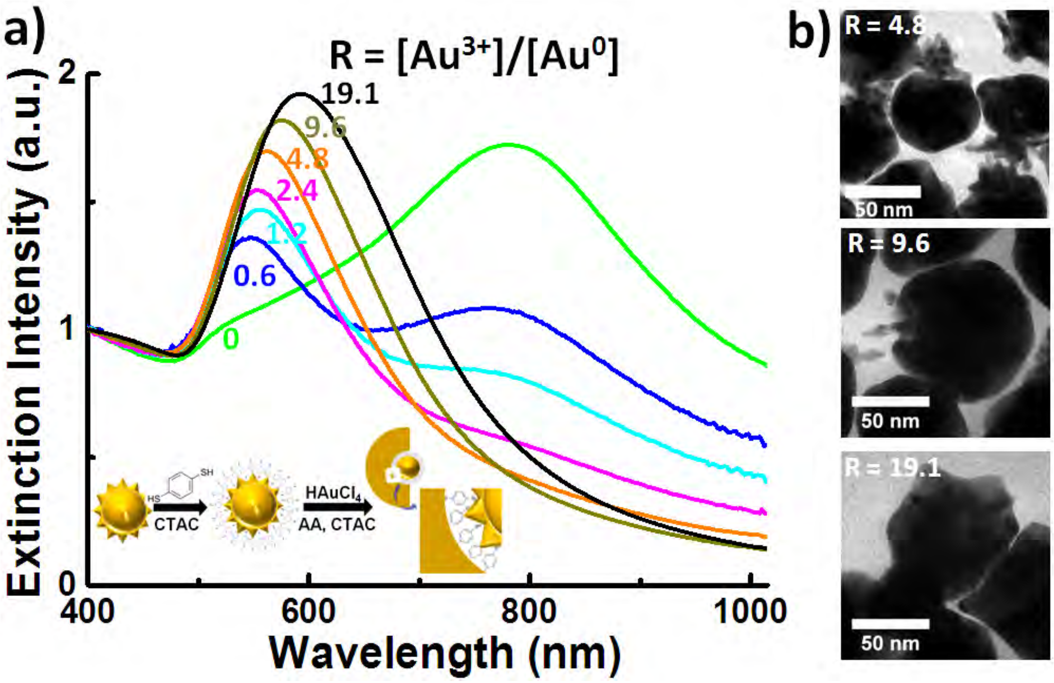

Figure 2. 4 (**a**) UV−Vis extinction spectra of Au nanostars (~23 nm core size) during BDT-mediated seeded growth at different R values (R = $[Au^{3+}]/[Au^0]$ = 0, 0.6, 1.2, 2.4, 4.8, 9.6, 19.1). The inset is a schematic illustration of the expected seeded growth, where CTAC and AA act as surfactant and reducing agent, respectively. (**b**) TEM images of representative Au nanostructures formed by reduction at different R values.

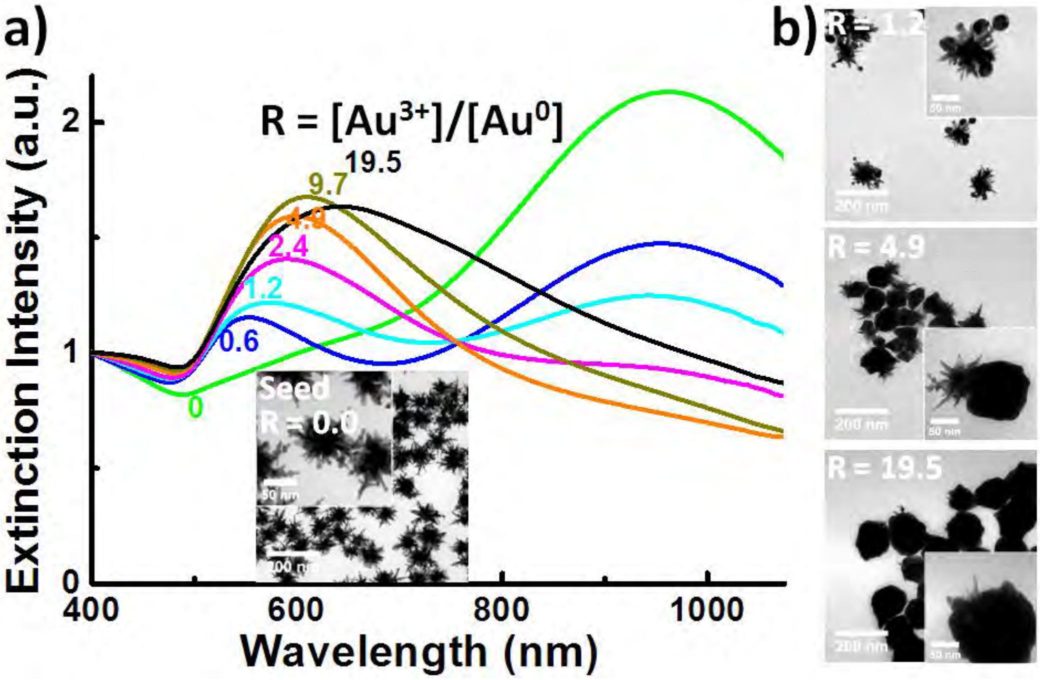

Figure 2. 5 (**a**) UV−Vis extinction spectra of Au nanostars (~55 nm core size) via BDT-mediated shell growth at different R values (R = 0, 0.6, 1.2, 2.4, 4.9, 9.7, and 19.5). The inset shows TEM images of AuNS-BDT seeds. (**b**) TEM images of coated AuNS at different R values.

HAADF-STEM tomography analysis was additionally carried out to reveal the three-dimensional morphology of the coated particles, aiming to discern potential internal gaps and connecting bridges between the nanostar seed and the shell. Note the intensity of HAADF-STEM images scales with the square of the atomic number of the elements present in the particle and with the sample thickness. Hence, the internal gaps within the particle decrease the intensity level in these regions of the HAADF-STEM images and therefore can be clearly recognized. For consistency, six different nanoparticles were investigated using HAADF-STEM tomography. A representative visualization of a 3D reconstruction and a 2D slice through it are depicted in **Figure 2.6**. The 3D visualization displays the internal gaps as bubble-like regions highlighted with an arrow (**Figure 2.6a**). The internal gaps can also be clearly observed in the 2D slice image, corresponding to dark regions between the seed and shell (**Figure 2.6b**), while the same image also shows the presence of linking bridges between the nanostar seed and the shell. An estimate of the internal gap distances from electron tomography images yielded an average value of 4.5 nm, though obviously narrower gaps are also present at some areas. Incidentally, electron tomography confirmed that the seed was not located at the center of the encapsulated shell but rather at the edge. This observation indicates that the shell growth started from one or more of the AuNS tips and then asymmetrically continued, gradually surrounding the seed. This model is consistent with the autocatalytic nature of seeded growth as well as with the electron tomography images obtained for NS-seeded nanostructures at different growth stages (R values), which include dimer, semishell and full shell morphologies (**Figure 2.7**).

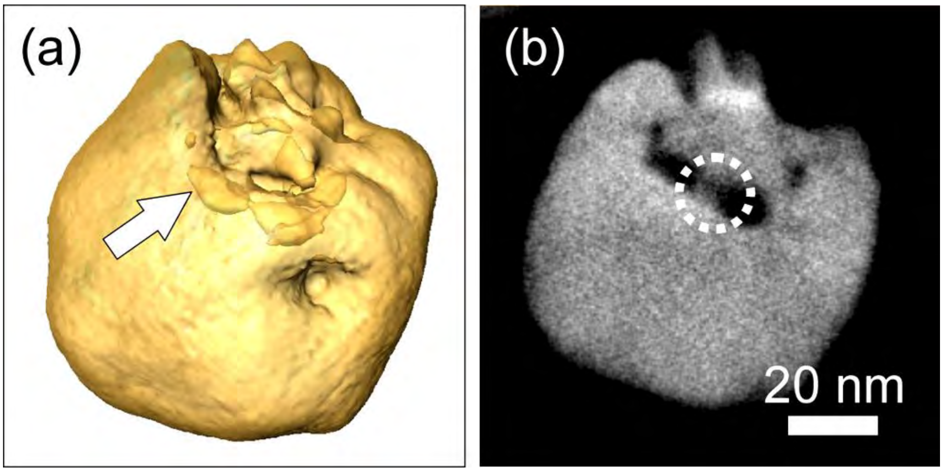

Figure 2. 6 (**a**) 3D rendering of an electron tomography reconstruction for a semishell covered Au nanostar (~23 nm core size, R = 9.6). The gaps between the nanostar seed and the semishell can be clearly identified (example indicated by an arrow). (**b**) A slice through the reconstruction reveals both the connections (highlighted with a dashed circle) and gaps between seed and shell.

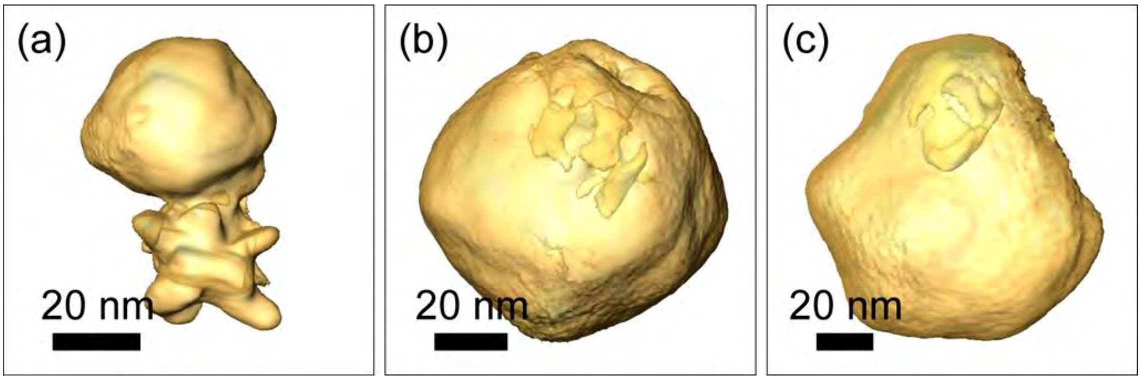

Figure 2. 7 3D rendering of electron tomography reconstructions of core-shell gold nanostars with increasing R values: (**a**) AuNS-sphere dimer (R = 4.8), (**b**) semishell-coated AuNS (R = 9.6), (**c**) encapsulated AuNS (R = 19.1).

Further information regarding the growth pathway of the shell on AuNS is provided by the crystalline structure, which was investigated for selected particles by means of high resolution HAADF-STEM imaging at atomic resolution. High resolution images and their corresponding fast Fourier transform (FFT) spot patterns obtained from 6 different positions on a semishell-coated Au nanostar (**Figure 2.8**) revealed that the crystalline orientations are not identical, meaning that the particle was tilted to a different zone axis for each of the high resolution images. This observation indicates that the growth of the shell may start from more than one spot on the original AuNS (likely several tips). It should however be noted that overlapping regions between parts of the seed and shell make it difficult to precisely determine where on the seed the shell growth started. Compared with previous work on core-shell particles with internal gaps mediated by ligands, such as DNA,[179,184,185]block copolymers[180] or other small molecules,[181,186] we show for the first time this type of seeded growth at atomic resolution and in 3D, which helps us to better understand this unusual growth mode.

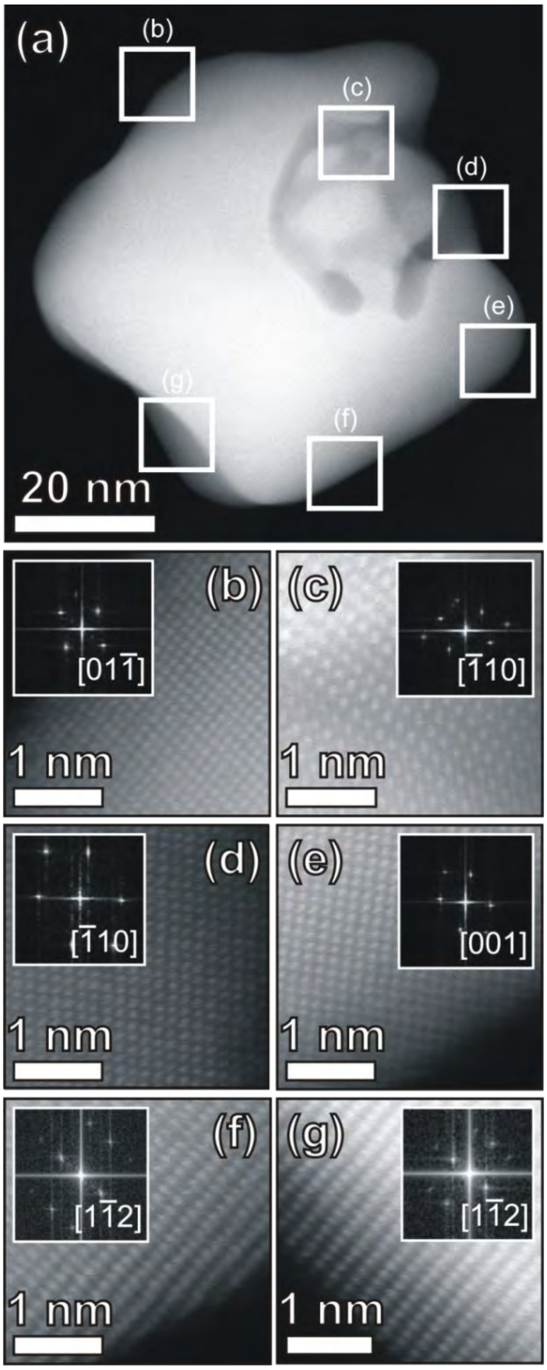

Figure 2. 8 (**a**) HAADF-STEM image providing an overview of a semishell-coated Au nanostar and (**b-g**) high-resolution HAADF-STEM images collected from several regions highlighted in (**a**). The corresponding FFT patterns of the high-resolution HAADF-STEM images are displayed in the insets.

2.3.3 Surface-enhanced Raman Scattering (SERS)

One of the attractive features of this intriguing morphology is the presence of internal gaps, which are likely to display enhanced electric fields, therefore acting as intrinsic hot spots for SERS.[168] Since BDT has a reasonably high Raman scattering cross section and it should be located precisely at the gaps between the AuNS core and the outer shell, it is suitable as an internal standard to test the efficiency of such intrinsic hot spots. SERS spectra from stable colloids (785 nm excitation wavelength) were collected at constant BDT-modified AuNS concentration (based on particle number). Comparison of the CH bending mode (1072 cm^{-1}) SERS intensity after background subtraction showed a gradual increase up to an R value of 9.6, which yields a four-fold higher intensity as compared to the bare gold nanostar seeds (R = 0), even though the LSPR band of the seeds is in resonance with the laser excitation (785nm) (**Figure 2.9**). A decrease in SERS intensity was however observed for R values above 9.6. Interestingly, the maximum SERS intensity does not correspond to fully coated AuNS, even though the largest number molecular nanogaps between the core and the shell should be available. This discrepancy may be due to damping of light transmission through the outer shell or to additional contributions to E-field enhancement in anisotropic morphologies such as partly coated AuNSs. It thus appears that the morphology yielding the highest SERS intensity is the semishell-coated nanostar, which was also found for larger coated AuNSs (~55 nm core size) (**Figure 2.10**). Nanostructures comprising sharp tips generate intense electric near field by concentrating light onto the tips ('nanoanntena effect'), leading to a significant SERS enhancement.[168,187,188] In the case of semishell-coated AuNS, the semishell may direct the light toward the exposed core tips, further contributing to the overall near field enhancement.

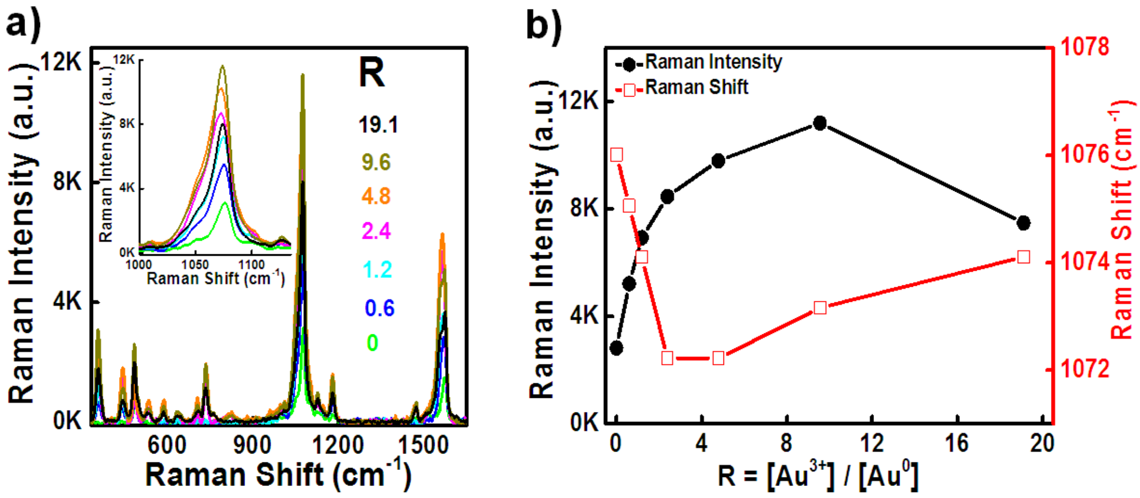

Figure 2. 9 (**a**) SERS spectra of BDT located within coated Au nanostars, synthesized at different R values (R = 0.0, 0.6, 1.2, 2.4, 4.8, 9.6, 19.1). All samples have the same concentration of BDT-modified AuNS seeds. (**b**) SERS intensity and position of BDT CH bending mode at different R values (background was subtracted).

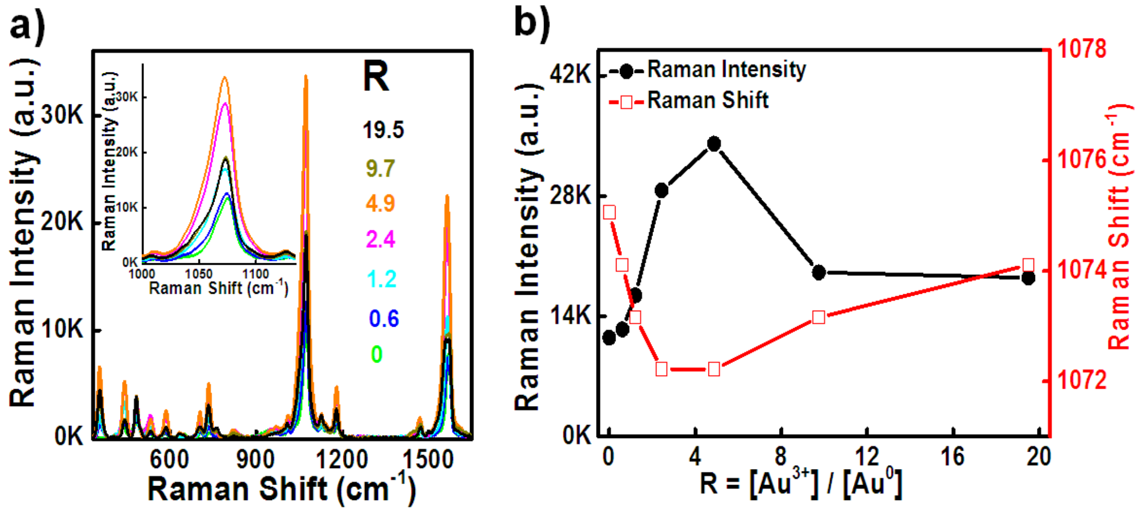

Figure 2. 10 (**a**) SERS spectra of BDT interfacing AuNS (~55 nm core size) synthesized at different R values (R = 0.0, 0.6, 1.2, 2.4, 4.9, 9.7, and 19.5). All samples have the same concentration of BDT-modified Au nanostars seeds. (**b**) Raman peak intensity and position of BDT (CH bending mode) at different R values at different stages of gold shell growth, after background subtraction.

Apart from intensity differences, the Raman shift of the CH bending mode peak (~1072 cm^{-1}) shows differences of ~4 cm^{-1} for growing shells up to R = 4.8, then shifting back to higher wavenumbers, as shown in **Figure 2.9b**. A similar behavior was observed for the phenyl ring stretching mode, where the peak at ~1572 cm^{-1} for AuNS seeds (R = 0) shifts to ~1563 cm^{-1} when the SERS intensity is close to the maximum value, then shifting back to 1573 cm^{-1} for fully encapsulated AuNS (R = 19.1) (**Figure 2.11a**). A similar trend was observed for the larger AuNS (~55 nm core size) (**Figure 2.11b**). The variation in Raman scattering frequency likely reflects the change of local environment around the BDT molecules interfacing different gold nanostructures. In a related report,[189] the orientation of 1,4-BDT relative to a gold surface was shown to affect the position of the phenyl ring stretching mode in the SERS spectrum, with lower wavenumbers for flat as compared to perpendicular orientation, due to different gold surface-ring π-orbital interactions. In our system, the growth of gold shells may generate a compression force that changes the BDT orientation from perpendicular to parallel relative to the gold seed surface, resulting in a shift of the Raman band (phenyl ring stretching mode) toward lower wavenumbers as the shell growth progresses. However, further growth of the gold shell would result in the uncovered BDT layer becoming more rigid and hard to bend or change the original orientation. Accordingly, BDT perpendicular orientation, even after full shell growth, plays a major effect on the Raman peak (phenyl ring stretching mode) and shifts back to higher wavenumbers. These data show that these particles comprising Raman tags interfacing gold nanostructures can probe the local E-field enhancement, as well as local environment changes.

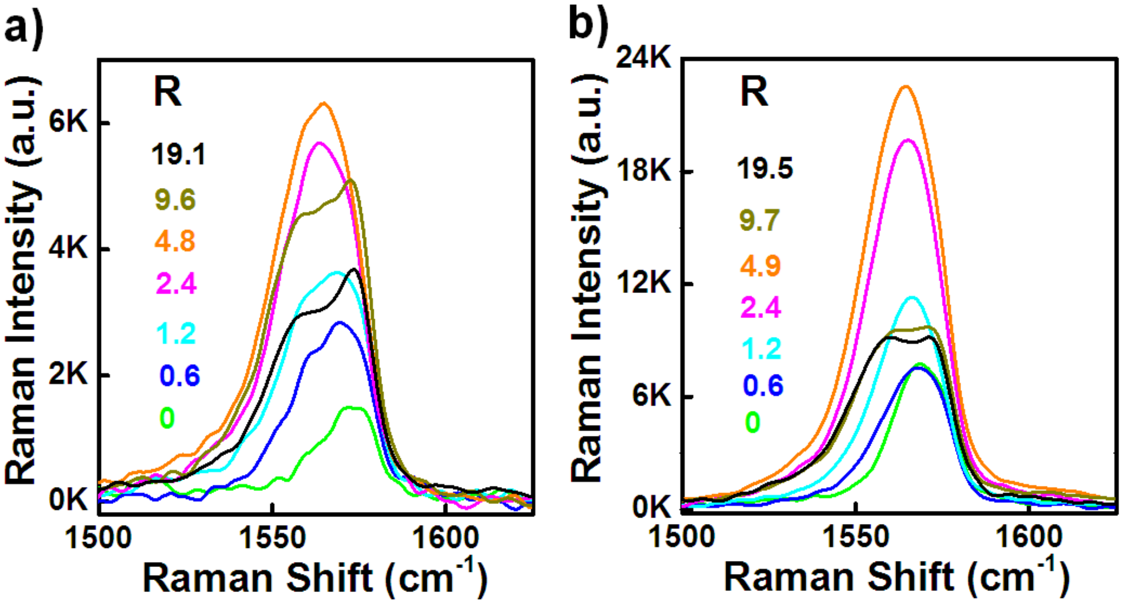

Figure 2. 11 SERS band of the phenyl ring stretching mode (~1570 cm^{-1}) at different stages of AuNS-BDT encapsulation: (**a**) encapsulation of AuNS (~23 nm core size) at different R values (R = 0, 0.6, 1.2, 2.4, 4.8, 9.6, and 19.1). (**b**) encapsulation of AuNS (~55 nm core size) at different R values (R = 0, 0.6, 1.2, 2.4, 4.9, 9.7, and 19.5). BGD means background signal. All samples have the same concentration of BDT-modified AuNS seeds.

2.4 Conclusions

In summary, we report a new strategy that combines an aromatic dithiol (BDT) and a surfactant (CTAC) to stabilize and encapsulate surfactant-free gold nanostars, even though the individual components cannot perform a comparable stabilizing effect. Seeded growth in the presence of BDT leads to a series of exotic nanostructures, in which internal gaps are consistently present, as confirmed by electron tomography. Optical characterization showed that semishell-coated nanostars show significant SERS intensity as compared to other geometries obtained along the seeded growth process. The roles of bifunctional ligand and surfactant in the gold nanostar-seeded growth are thus: 1) protecting the initial gold nanostars from reshaping and aggregation, 2) directing Au shell growth around the core, and 3) generating significantly enhanced SERS activity. Additionally, partially encapsulated nanostars display a Janus nature, with bare gold on one side and a thiol-modified surface on the other, which could be further modified with different functional groups/additional Raman active molecules, thus showing promise as functional SERS-coded probes for various applications such as sensing or imaging.

CHAPTER 3

Hydrophobic Plasmonic Nanoparticles: Stability and Self-Assembly into SERS-Active Monolayers

ABSTRACT

We present a general route for the transfer of Au and Ag nanoparticles of different shapes and sizes, from water into various organic solvents. Optimization of the experimental conditions for each type of nanoparticles is based on a combination of thiolated polyethylene glycol and a stabilizing agent for organic media such as dodecanethiol (DDT). The functionalized nanoparticles were effectively transferred into organic dispersions with long-term stability (months). Taking advantage of the excellent spreading of such organic dispersions on water, self-assembly of all nanoparticle types was achieved at the air/liquid interface, leading to extended nanoparticle arrays that could be in turn transferred onto solid substrates. The nanoparticle close packing achieved with this method provides extensive plasmon coupling, rendering these nanoparticle assemblies efficient substrates for surface-enhanced Raman scattering spectroscopy.

3.1 Introduction

Phase transfer of metallic nanoparticles represents a key aspect in the development of nanoscience and nanotechnology, since many specific applications require the transfer of the as-synthesized nanoparticles from polar to non-polar solvents, or vice versa.[67] A wide range of methods have been developed for the preparation of (mainly) water-based dispersions of noble metal nanoparticles (NPs) with well-defined morphologies and uniform sizes.[19,52] In particular, the synthesis of anisotropic nanoparticles is usually carried out in water, and their dispersion in organic solvents represents an important strategy to improve their processing into self-assembled nanostructures[190,191] or to successfully coat them with amphiphilic polymers.[192] Since previously reported phase-transfer methods are strongly limited to small particle dimensions (< 25 nm),[193–195] additional efforts are required for larger and/or anisotropic nanoparticles. Thus, akylamines were used to transfer Au and Ag nanoparticles with sizes up to 100 nm, octadecylamine being the most efficient one.[196] Tailor made ligands such as bidentated thiols[197] have also been designed to achieved this goal, as well as polymers such as thiolated polystyrene,[198] but the large amount of polymer required significantly hinders further application of the nanoparticles. PEGylation has also been employed to transfer large gold nanoparticles and nanorods, but either a common solvent[199] or mechanical forces[200] are needed for a successful transfer. Recently, a method that combines PEG-SH and dodecylamine has been reported[192] for the transfer of gold nanoparticles up to 60 nm, including CTAB-capped gold nanorods and silver nanoprims, which can be subsequently coated with an amphiphilic polymer, but this phase transfer process has been reported to be rather time consuming.

We propose a simple and rapid procedure based on a combination of commercially available PEG-SH and 1-dodecanethiol (DDT), as a general method to transfer gold nanostars of different sizes from aqueous dispersion into chloroform. In order to demonstrate the versatility of the method developed here, other nanoparticles such as gold and silver spheres as well as gold rods were studied. Due to the strong affinity of thiol groups to metal particle surfaces, complete transfer can be completed in a very short time and long-term stability is readily obtained. Although the combined use of PEG-SH and DDT readily leads to transfer of the nanoparticles, when DDT alone was used aggregation occurred, meaning that pre-stabilization with PEG-SH is a critical step to preserve the stability of large NPs, avoiding aggregation during phase transfer, which has been previously reported.[192,201] DDT was selected as an efficient stabilizer in non-polar solvents because the long aliphatic chain provides hydrophobic interactions between particles (steric repulsion). Notwithstanding, complete phase transfer from water can be achieved by means of other hydrophobic thiols that are soluble in chloroform, leading to dispersions that remain unaltered for several months, can be dried and redispersed in different solvents. Hydrophobic coatings are effective mediators for inducing the self-assembly of metal nanoparticles. Therefore, the phase transfer method presented here allows obtaining stable hydrophobic plasmonic NPs that can be redispersed in ethanol/hexane mixtures and effectively assembled at the liquid-air interface. Extended compact monolayers have been fabricated and easily transferred onto solid substrates that can be directly applied as plasmonic substrates for optical sensing applications. In particular, the obtained monolayers were used as SERS substrates with great potential toward ultra-sensitive (and selective) molecular detection.[93,103,202–206] These novel substrates offer advantages such as high reproducibility, robustness, and reliable signal generation. Because different particle sizes, shapes and materials can be used, a high flexibility is achieved in the design of substrates that can be tailored for specific applications.

3.2 Experimental Section

Materials

Milli-Q water (resistivity = 18.2 MΩ·cm) was used in all experiments. Hydrogen tetrachloroaurate trihydrate ($HAuCl_4·3H_2O$, ≥99.9%), sodium citrate tribasic dihydrate (≥98%), hexadecyltrimethylammonium bromide (CTAB, ≥99%), 5-bromosalicylic acid (90%), silver nitrate ($AgNO_3$, ≥99%), L-ascorbic acid (AA, ≥99%), tannic acid, 1-dodecanethiol (DDT, ≥98%), O-[2-(3-mercaptopropionylamino) ethyl]-O'-methylpolyethylene glycol (PEG-SH, MW 5,000 g/mol), 4-mercaptobenzoic acid (MBA, 90%), poly(isobutylene-alt-maleic anhydride), (average Mw ~6,000 g/mol), dodecylamine (98%) and chloroform ($CHCl_3$, ≥99.8%) were purchased from Sigma-

Aldrich. Hydrochloric acid solution (37%) was purchased from Panreac. All glassware was washed with aqua regia, rinsed 3-fold with Milli-Q water and dried before use.

Synthesis of Nanoparticles

Gold nanoparticle seed solution (Au seed) comprised an aqueous colloid (av. diameter 13±3 nm) that was prepared by adding 5 mL of 1wt% sodium citrate solution to 95 mL of boiling 0.5 mM $HAuCl_4$ under vigorous stirring. After 15 min of boiling, the solution was cooled down to room temperature and then stored at 4 °C for long-term storage. Spherical gold nanoparticles (AuNPs) with average diameters of 30±4 nm (Au 30), 50±5 nm (Au 50) and 100±10 nm (Au 100) were synthesized according to a previously reported seeded growth method.[207] As-synthesized AuNPs featured LSPR bands centered at 521, 530 and 555 nm, respectively, and they were used without further purification. AuNPs of 204±8 nm with LSPR peaks at 567 nm (dipole) and ~796 nm (quadrupole) were purchased from BBI solutions and washed using several centrifugation steps (870 g; 10 min) before use.

Gold nanostars (AuNSs) of different sizes were synthesized by a modified seed-mediated growth method.[50] Different amounts of citrate-stabilized gold nanoparticle seed solution were added to 10 mL of 0.25 mM $HAuCl_4$ containing 10 μL of 1.0 M HCl in a 20 mL glass vial at room temperature, under moderate stirring. Quickly, 100 μL of $AgNO_3$ (3 mM) and 50 μL of ascorbic acid (100 mM) were simultaneously added to the above solution, which rapidly turned from light red to blue or greenish-black, depending on the added amount of Au^0. Specifically, 1 mL, 500 μL and 100 μL of gold nanoparticle seeds were added to obtain small (*s*AuNS), middle (*m*AuNS) and big gold nanostars (*b*AuNS) with LSPR bands at 725, 770 and 884 nm and core/overall sizes of 23±2 / 34±4 nm, 35±3 / 63±7 nm and 56±4 / 98±7 nm, respectively. Immediately after growth, the solutions were stirred with PEG-SH (see PEG-SH concentrations in **Table 3.1**) for 15 min, washed by centrifugation at 1190 g, 25 min, 10 ºC and redispersed in water.

Single-crystalline gold nanorods (AuNRs) (61±5 nm length; 15±2 nm width) were synthesized through a seed-mediated method involving the prereduction of $HAuCl_4$ with salicylic acid.[31,208] Nanorods with an absorbance maximum at 735 nm were obtained within 4 h after seed addition. The AuNRs were then washed by centrifugation

(4760 g, 40 min, 29 ºC), and the pellet was redispersed in 0.05 M CTAB to remove excess reactants.

Silver nanoparticles (AgNPs) with average diameters of 28±6 nm (Ag 30), 51±8 nm (Ag 50) and 94±12 nm (Ag 100) were synthesized as reported.[209] The prepared AgNPs displayed LSPR bands centered at 420, 439 and 487 nm. The nanoparticle solutions were centrifuged after synthesis (7870 g, 20 ºC, 40 min for Ag 30 Ag 50; 20 min for Ag 100) to remove the excess of tannic acid used in the synthesis.

Phase Transfer

Gold and silver nanoparticles of different shapes and sizes were transferred from water to chloroform. The aqueous nanoparticle colloids were first stabilized with a suitable amount of PEG-SH, calculated to be between 0.6 and 1.4 molecules per nm^2 depending of each type of particle (**Table 1**). AuNPs and AuNSs were PEGylated directly without purification from the synthesis, whereas AuNRs and AgNPs were washed twice by centrifugation (4760 g, 40 min, 29 ºC) and redispersed in water to remove excess CTAB. Subsequently, a DDT solution (adjusted between 113 and 204 molecules per nm^2 to each NP) in $CHCl_3$ was added to the aqueous phase containing the NPs. Phase transfer occurred upon vigorous stirring for periods between 15 min and 1 hour for different nanoparticles. The transfer was assisted by addition of 20 - 40 µL HCl conc. to 5 mL of NPs solution (see **Table 1**) for AuNPs, AuNRs and AgNPs.[197] Upon transfer into $CHCl_3$, the organosols were purified by centrifugation and washing to remove excess of free DDT. Precipitation was facilitated by adding ethanol to the chloroform solution (1:5) and centrifugation conditions were optimized for each particle type (**Table 3.1**). For stability studies and further use, all samples were stored at 4 ºC.

Nanoparticle	**[NP] / M**	**PEG-SH molecules per nm^2**	**Molecules of DDT per nm^2**	**Centrifugation after phase transfer**
Au seeds	$4.8 \cdot 10^{-9}$	0.8	148	3900 g; 30 min; 20ºC
Au 30	$9.5 \cdot 10^{-10}$	0.6	150	2430 g; 15 min; 20ºC
Au 50	$2.0 \cdot 10^{-10}$	0.6	155	1550 g; 15 min; 20ºC
Au 100	$2.0 \cdot 10^{-11}$	0.6	165	600 g; 15 min; 20ºC
Au 200	$6.2 \cdot 10^{-13}$	1.4	125	470 g; 10 min; 20ºC
Ag 30	$7.8 \cdot 10^{-11}$	0.9	113	1550 g; 15 min; 20ºC
Ag 50	$2.5 \cdot 10^{-11}$	1.0	130	1190 g; 15 min; 20ºC
Ag 100	$3.9 \cdot 10^{-11}$	2.1	204	870 g; 15 min; 20ºC
AuNRs	$3.3 \cdot 10^{-10}$	1.4	133	2430 g; 15 min; 20ºC
*s*AuNSs*	$3.5 \cdot 10^{-10}$	1.4	155	1730 g; 25 min; 10ºC
*m*AuNSs*	$6.5 \cdot 10^{-11}$	1.4	155	1320 g; 25 min; 10ºC
*b*AuNSs*	$8 \cdot 10^{-12}$	1.4	155	970 g; 25 min; 10ºC

Table 3.1 Phase transfer conditions

* The diameter of small, middle and big AuNSs was estimated considering the diameter of a sphere of 30, 50 and 100 nm, respectively.

Self-assembly at the air/liquid interface and fabrication of plasmonic substrates

The dispersions of plasmonic nanoparticles in chloroform were dried under a gentle flow of dry nitrogen. The dry nanoparticles were then redispersed in an ethanol:hexane solvent mixture at 1:4 volume ratio to facilitate monolayer formation at the air/water interface. Ethanol was added first, immediately followed by addition of hexane. The resulting dispersions were immersed in an ultrasonic bath for 5s to ensure the absence of aggregates prior to spreading at the air/water interface. Plastic Petri dishes with a diameter of ca. 3 cm were used as water containers. For self-assembly of the nanoparticles at the air/water interface, the nanoparticle dispersions were gently spread drop-wise on top of the surface of pure water. Upon evaporation of the organic solvents, the water surface was covered by a monolayer of nanoparticles. In each case, the concentration of the dispersion was adjusted to obtain complete coverage of the water surface with a single monolayer of the nanoparticles. The monolayer was then transferred onto a substrate by gently touching the monolayer with the substrate parallel to the surface, which is known as "horizontal lifting", or "Langmuir-Schaeffer" technique. Transfer onto transmission electron microscopy (TEM) grids was performed to acquire TEM images; transfer onto glass substrates was performed for UV-Vis spectroscopy and SERS. Glass slides (24×24 mm^2 Menzel-Gläser, Thermo Scientific, Germany) were thoroughly cleaned by sonication in water with soap, ethanol, and acetone, 15 min for each solvent. After this cleaning procedure, the glass slides were thoroughly rinsed with Milli-Q ultrapure water and gently blow-dried with a stream of N_2 gas. Substrates were stored in sealed Petri dishes.

Sample Preparation for SERS

Prior to using self-assembled monolayers for SERS experiments the organic ligands were removed from the nanoparticle surface by UV/ozone cleaning (UV/ozone ProCleaner, Bioforce Nanoscience) for 1h. The substrates were cut into equal pieces with a surface area of ca. 5×2.5 mm^2 and immediately incubated in 300 mL of a 10 µM 4-MBA aqueous solution for 1 h, freshly prepared from a 1mM stock in ethanol. The samples were then extensively washed with Milli-Q water to remove unbound 4-MBA molecules, dried under moderate nitrogen flow and SERS spectra were collected, typically within 1-5 hours. In particular, AgNP assemblies were measured immediately after drying to avoid oxidation.

Polymer coating

For polymer coating and transfer back to water, 250 µL of *m*AuNS solution ([NP] $\sim1.5\text{x}10^{-10}$ M) in $CHCl_3$ were mixed with the prepared amphiphilic polymer (PMA) dissolved in $CHCl_3$ (V_P = 10 µL, c_P = 0.05 M, $R_{p/area}$ = 150 nm^{-2}) in a 25 mL round bottom flask. The mixture was stirred and the solvent was slowly evaporated. The resulting solid film containing the NPs was dissolved in 28 mM sodium borate buffer at pH = 12 (SBB 12). After polymer coating the particles were purified, concentrated and characterized by different techniques.

Characterization

TEM images were collected with a JEOL JEM-1400PLUS transmission electron microscope operating at 120 kV, using carbon coated 400 square mesh copper grids. Scanning electron microscopy (SEM) images were obtained using an ESEM Quanta250 FEG (FEI, The Netherlands). UV-Vis optical extinction spectra were recorded using an Agilent 8453 UV-Vis diode-array spectrophotometer and an Agilent Cary 5000 UV-Vis-NIR spectrophotometer. ^1H NMR spectra were acquired using a Bruker 500MHz spectrometer. SERS experiments were performed with a confocal Raman microscope (Renishaw InVia) equipped with a motorized scan stage, two Peltier-cooled CCD detectors and three excitation lasers of 532, 633 and 785 nm (maximum output powers of 41, 13 and 157 mW, respectively). The laser beam was focused onto the solid sample surface under ambient air conditions through a 100× objective with a numerical aperture of 0.85 and set to effective irradiation powers of 120 μW (@532nm), 100 μW (@633 nm) and 180 μW (@785 nm) as measured by a photodiode power sensor (PD300-3W, Ophir), or through an immersion 40× objective with NA 0.8 and set to effective powers of 250 μW (@532nm), 110 μW (@633 nm) and 1200 μW (@785 nm) when working in solution. The scattered light was collected with an integration time of 1 s. All SERS spectra presented here were averaged over 100 single spectra measured at different points on the substrate. Typically, a 20×20 μm^2 area was chosen and single spectra were collected with a point distance of 2 μm in x- and y-direction (= 10×10 spectra). The averaged spectra were baseline corrected using the Wire 3.4 software. Two-dimensional SERS maps were generated by plotting the baseline corrected intensity of the 4-MBA ring stretch mode at 1078 cm^{-1} as a function of the position on the defined grid.

3.3 Results and Discussion

Complete transfer of Au and Ag nanoparticles of different shapes and sizes was achieved using DDT as hydrophobic capping agent, with PEG-SH as pre-stabilizer (see **Experimental Section** for details). In order to confirm the presence of both ligands on the particle surface upon transfer into chloroform, NMR analysis was carried out (**Figure 3.1**). Comparison of the ^{1}H NMR spectra of the functionalized nanoparticles with those of solutions of both ligands confirms that the ligands are attached to the nanoparticles, as indicated by observed chemical shifts and broadening of signals,[210,211] and the perfect fit in the assignment of the number of protons for DDT. Moreover, the peaks for functional groups located near the metal are not observed, confirming the absence of free ligands.

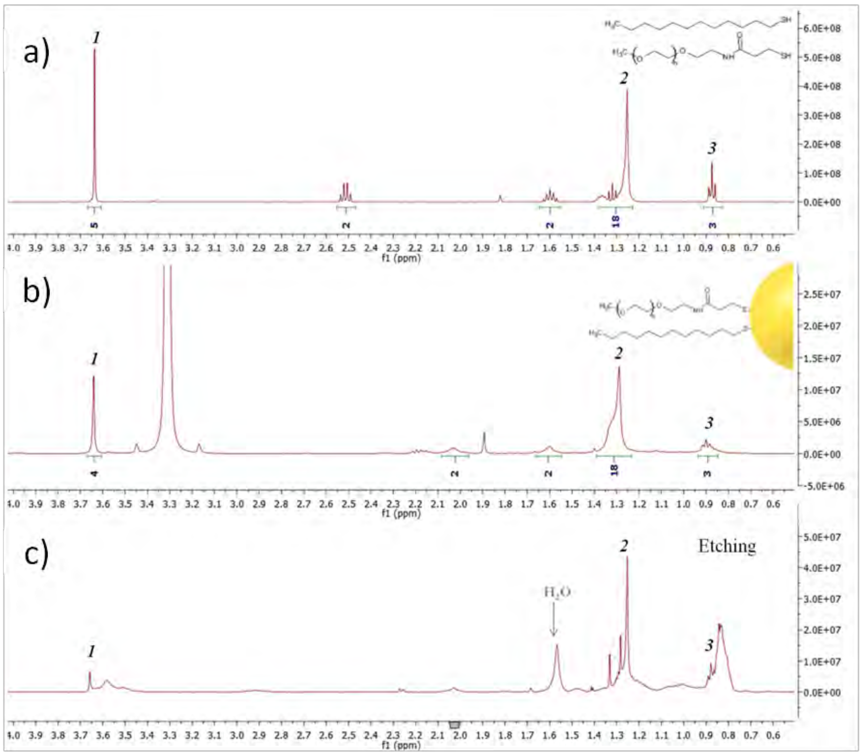

Figure 3.1. ^{1}H NMR spectra of: (**a**) PEG-DDT ^{1}H NMR (500 MHz, Chloroform-d) δ 3.64 (s, PEG-SH), 2.51 (q, 2H, CH_2SH), 1.64 – 1.55 (m, 2H, CH_2CH_2SH), 1.39 – 1.21 (m, 18H, $9CH_2$), 0.88 (t, 3H, CH_3). (**b**) 50nm AuNPs (PEG-DDT) in Methanol-d4, acquisition time 1h. The peaks of the ligands on the NP correspond to the ones observed in the spectra (**a**). (**c**) PEG-DDT ligands in Chloroform-d after the decomposition of 50nm AuNPs with cyanide, acquisition time 40 min.

Successful phase transfer was additionally indicated by the concomitant transfer of red, blue and yellow colors for AuNPs (and NRs), AuNSs and AgNPs respectively, from water to chloroform (**Figure 3.2**).

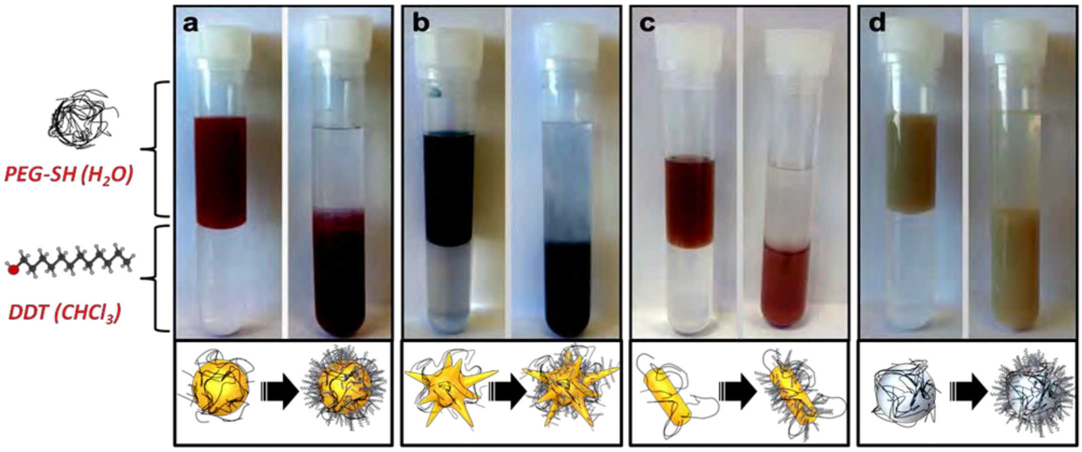

Figure 3.2. Phase transfer of pegylated Au 50 (**a**), *m*AuNSs (**b**), AuNRs (**c**) and Ag 100 (**d**) from water (upper phase) into DDT chloroform solution (lower phase). Left and right tubes correspond to nanoparticle solutions before and after phase transfer, respectively. Pictures were taken within an hour of each other.

On the other hand, both the redshift of the LSPR band without broadening and the well separated particles found in TEM images confirmed the absence of aggregation, as well as the preservation of particle size and shape upon phase transfer (**Figs. 3.3-3.6)**. The strong affinity between the thiol group and the metallic surfaces was essential to ensure rapid phase transfer, so that all the nanoparticles were transferred from water into chloroform within less than one hour, just 15 min in the case of AuNSs.

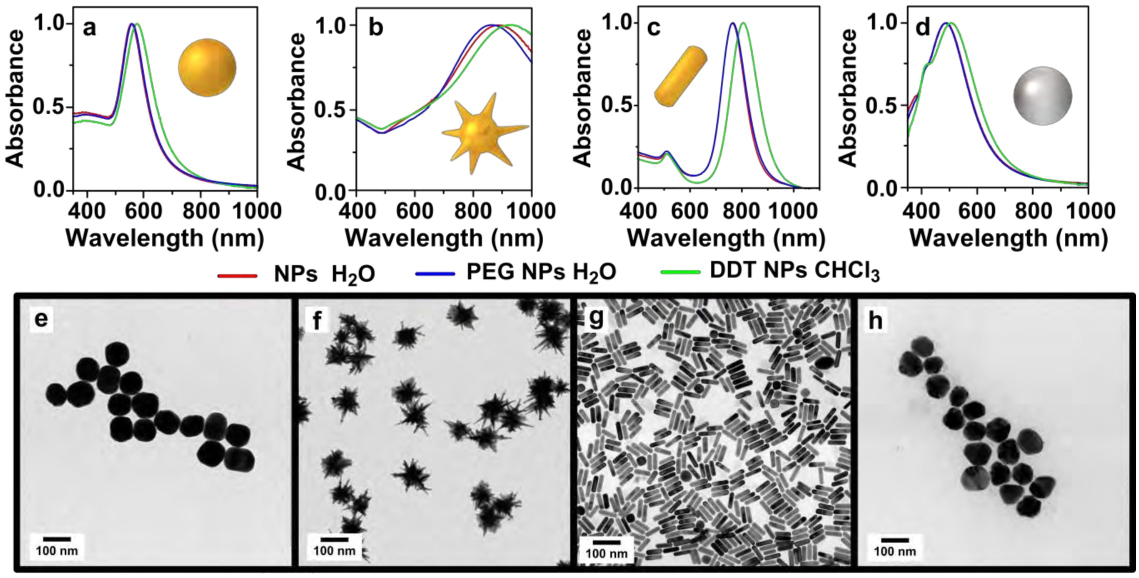

Figure 3.3. Vis-NIR spectra of NPs in water (red lines), after adding PEG-SH in water (blue lines) and after coating with PEG/DDT and transfer into $CHCl_3$ (green lines), and TEM images for Au 100 (**a**, **e**), *b*AuNSs (**b**, **f**), AuNRs (**c**, **g**) and Ag 100 (**d**, **h**).

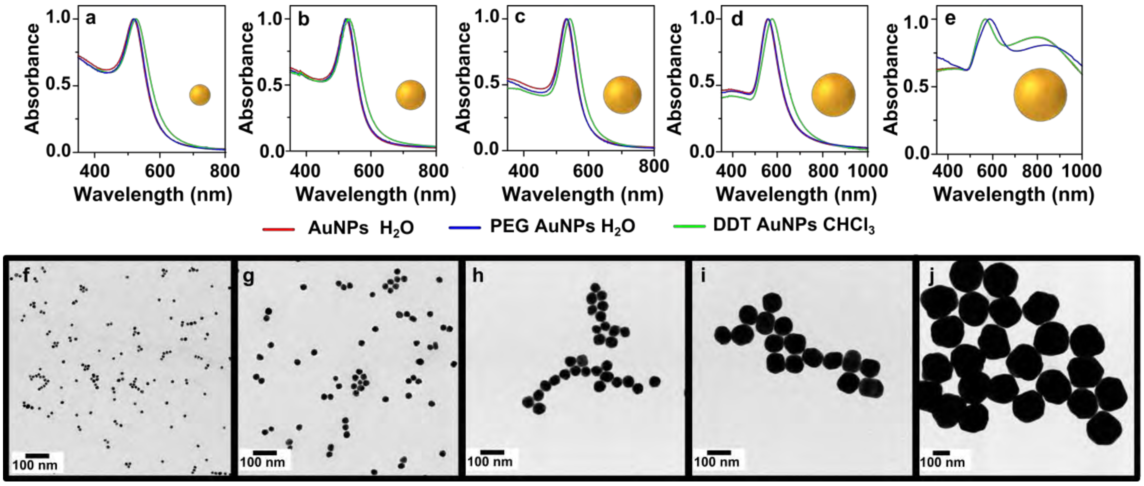

Figure 3.4. Vis-NIR spectra of AuNPs in water (red lines), after adding PEG-SH in water (blue lines) and after coating with PEG/DDT and transfer into $CHCl_3$ (green lines) (**a-e**). TEM images of the PEG/DDT coated nanoparticles (**f-j**) and size distribution histograms (**k-o**) of: AuNP seeds (**f**, **k**), Au 30 (**g**, **l**), Au 50 (**h**, **m**), Au 100 (**i**, **n**) and Au 200 (**j**, **o**), respectively.

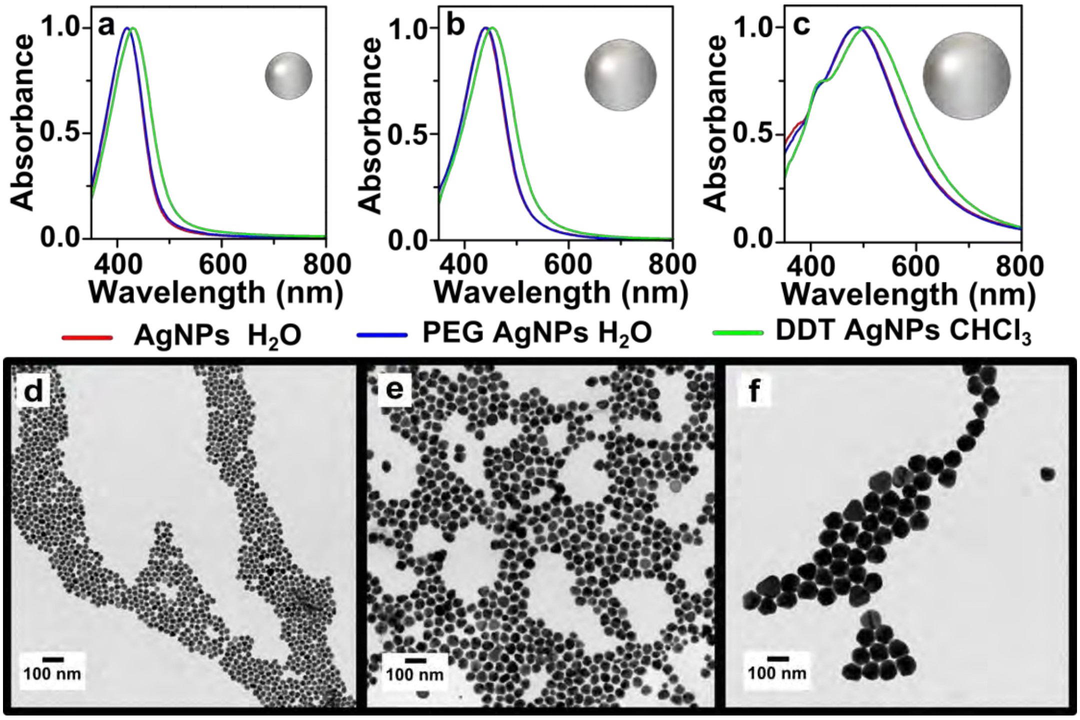

Figure 3.5. (**a-c**) Vis-NIR spectra of Ag 30 (**a**), Ag 50 (**b**) and Ag 100 (**c**) in water (red lines), after adding PEG-SH in water (blue lines) and after coating with PEG/DDT and transfer into $CHCl_3$ (green lines); (**d-f**) TEM images of the PEG/DDT coated Ag 30 (**d**), Ag 50 (**e**) and Ag 100 (**f**) nanoparticles in chloroform.

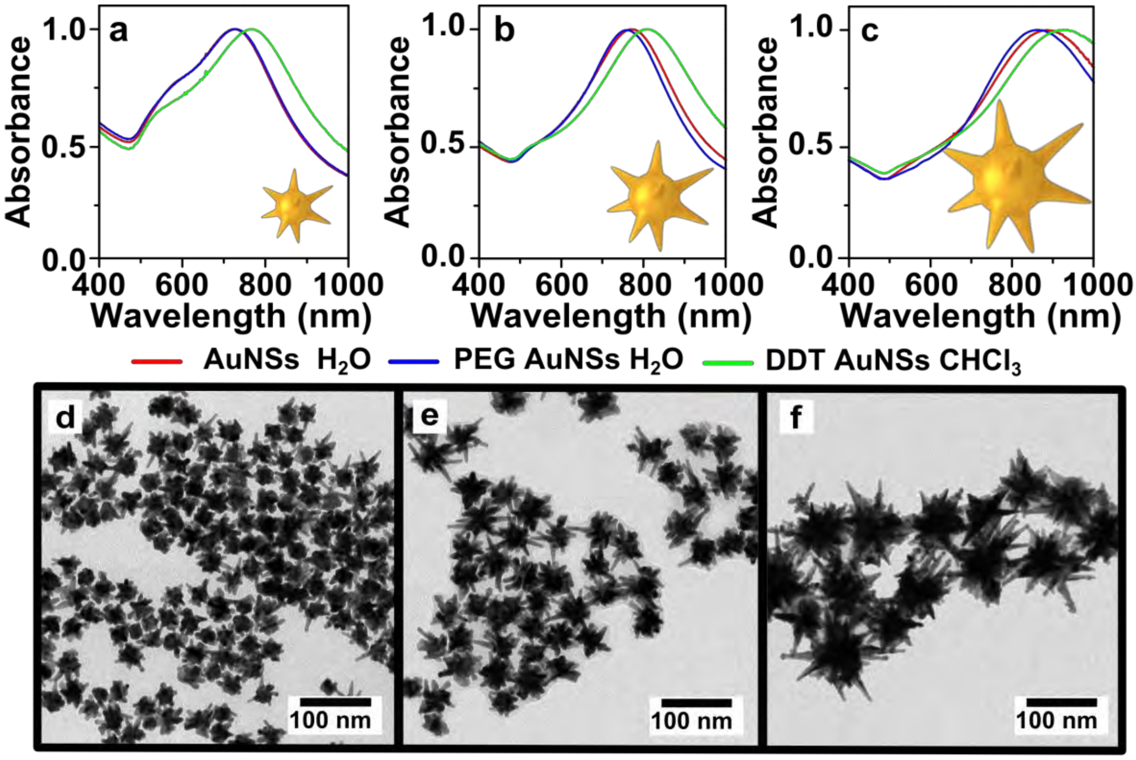

Figure 3.6. (**a-c**) Vis-NIR spectra of *s*AuNSs (**a**), *m*AuNSs (**b**) and *b*AuNSs (**c**) in water (red lines), after adding PEG-SH in water (blue lines) and after coating with PEG/DDT and transfer into $CHCl_3$ (green lines); (**d-f**) TEM images of the PEG/DDT coated *s*AuNSs (**d**), *m*AuNS (**e**) and *b*AuNSs (**f**) in $CHCl_3$.

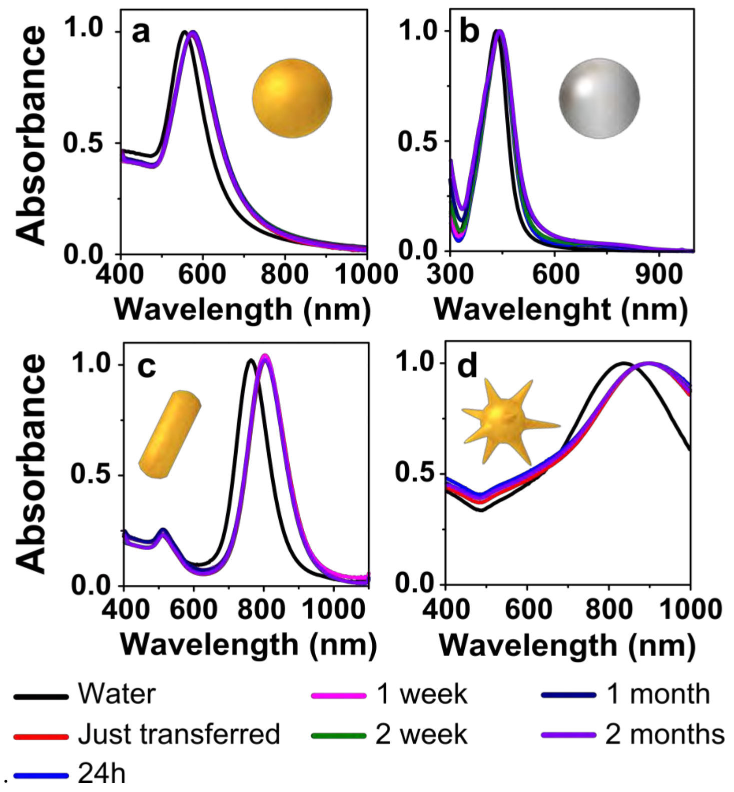

Figure 3.7. Normalized Vis-NIR spectra in water (black lines) and in chloroform (colored lines), after selected periods of time as labeled, for Au 100 (**a**), Ag 50 (**b**), AuNRs (**c**) and *b*AuNSs (**d**).

The pre-stabilization with PEG-SH was needed in all cases to avoid aggregation and facilitate the transfer of single (non-aggregated) particles. Addition of HCl further facilitated the process, in agreement with previous reports.[197,212] The obtained hydrophobic nanoparticles displayed a remarkable colloidal stability in chloroform, which was monitored by recording the corresponding Vis-NIR spectra during 2 months (**Figure 3.7**).

As shown in **Figs. 3.4-3.7** no trace of aggregation or sedimentation of the particles could be observed, either in the first step (pre-stabilization with PEG-SH) or in the second one (transfer into chloroform *via* DDT addition). Regarding the stability of AuNSs, upon storage in water the tips were observed to become more rounded as the LSPR band significantly blueshifted over time, in agreement with previous reports, but after PEG/DDT capping and phase transfer into chloroform, no LSPR shift was observed and the tips remained sharp, which is likely due to surface passivation through Au-S bonds[62] (**Figure 3.8**).

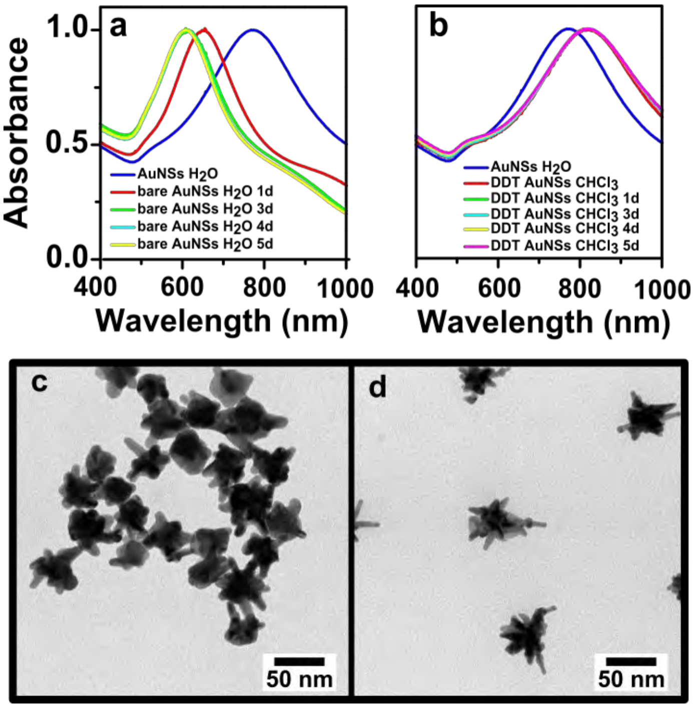

Figure 3.8. Vis-NIR spectral evolution (**a-b**) and TEM images (**c-d**) of bare (**a**, **c**) and PEG/DDT coated *m*AuNSs (**b**, **d**) after 5 days of nanoparticle synthesis. After synthesis and no particle coating the LSPR band significantly blueshifted (**a**) and the nanostars become more rounded over time (**c**). After PEG/DDT capping and phase transfer into chloroform, no LSPR shift was observed (b) and the tips remained sharp due to surface passivation through Au-S bonds (**d**).

Once the nanoparticles are transferred into chloroform they can be washed by centrifugation, dried and redispersed in different organic solvents. As an example, we show in **Figure 3.9** Vis-NIR spectra of AuNRs and *m*AuNSs dispersed in various solvents. The registered LSPR shifts are in agreement with the respective refractive indexes, except for hexane, where the particles present lower stability due to the lack of solubility of PEG-SH. PEG can be easily dissolved in organic solvents that display hydrogen bond donating capacity such as chloroform, but this does not apply to hexane.[199] Interestingly, when reducing the amount of PEG-SH and keeping a constant DDT concentration the colloidal stability in hexane or other non-polar solvents such as toluene can be notably improved, as confirmed by less broadened LSPR bands. A different strategy to improve NP solubility includes the selection of different thiolated hydrophobic molecules. For example, combining 11-mercaptoundecanol with DDT in a 1:1 ratio and adding a shorter PEG-SH molecule (750 Da) the solubility and stability of particles in slightly polar solvents such as ethyl acetate can be significant increased.

Other thiolated ligands soluble in chloroform were tested (not shown), confirming the wide versatility of the method presented here.

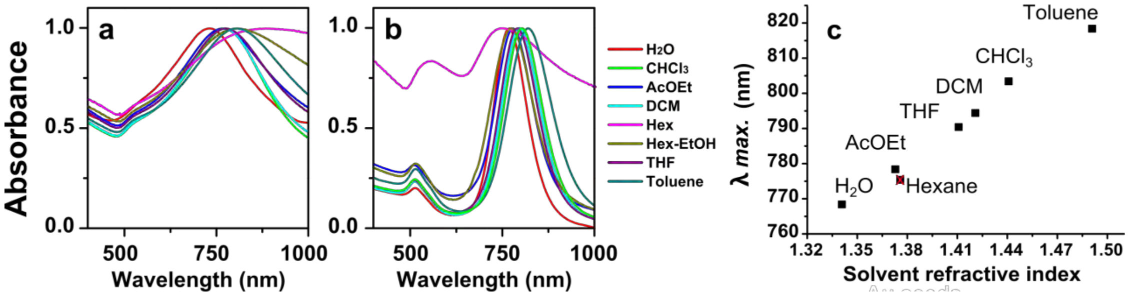

Figure 3.9. Vis-NIR spectra of *m*AuNSs (**a**) and AuNRs (**b**) dispersed in different organic solvents. (**c**) Maximum LSPR wavelength as a function of the refractive index of the solvents associated with the spectra in (**b**).

Ethanol:hexane mixtures (1:4) were used as spreading solvent. This mixture of solvents allowed us to obtain extensive nanoparticle monolayers, which were then transferred onto solid substrates (**Figure 3.10**).[59,213,214] Note that alternative solvents with larger spreading coefficient, i.e., mixtures of chloroform and isopropanol might be beneficial for the spreading of the nanoparticles. In all cases, long-range order was achieved, with dense packing of the plasmonic nanoparticles, which therefore leave very small interparticle gaps.

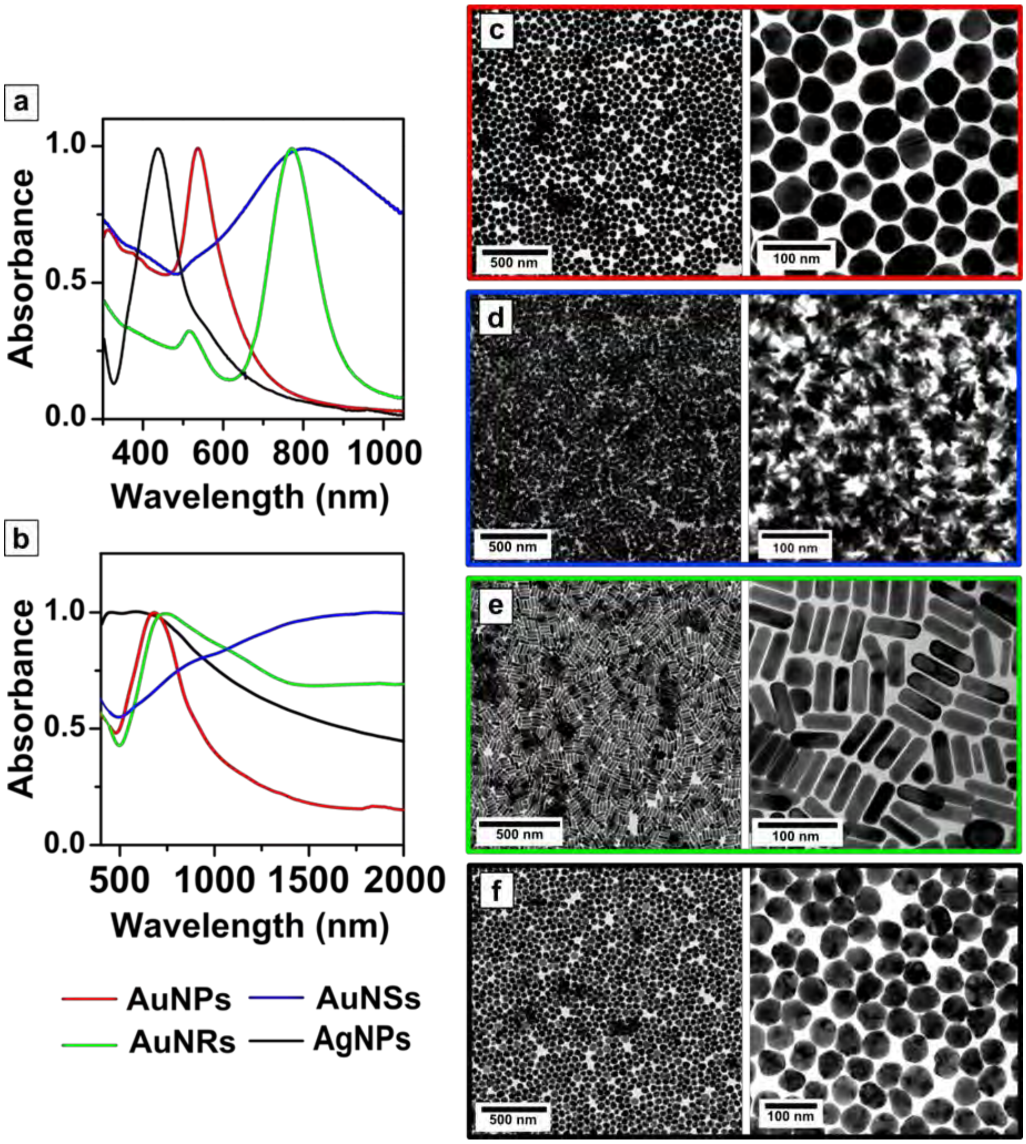

Figure 3. 10 (**a**) Vis-NIR spectra of different plasmonic nanoparticles dispersed in ethanol:hexane (1:4). (**b**) Vis-NIR spectra of plasmonic nanoparticle monolayers transferred onto transparent glass substrates. (**c-f**) TEM images of Au 50 (**c**), *m*AuNSs (**d**), AuNRs (**e**), and Ag 50 (**f**) monolayers upon transfer onto TEM grids.

High magnification TEM images from monolayers transferred onto carbon-coated copper grids show high packing density over large areas (**Figure 3.10 c-f**). As expected, such short interparticle distances lead to plasmon coupling, which is reflected in significant redshift and broadening of LSPR bands (**Figs. 3.10 b** and **3.11**). Plasmon coupling has been demonstrated to enhance the plasmonic features in 2D SERS-active platforms.[215]

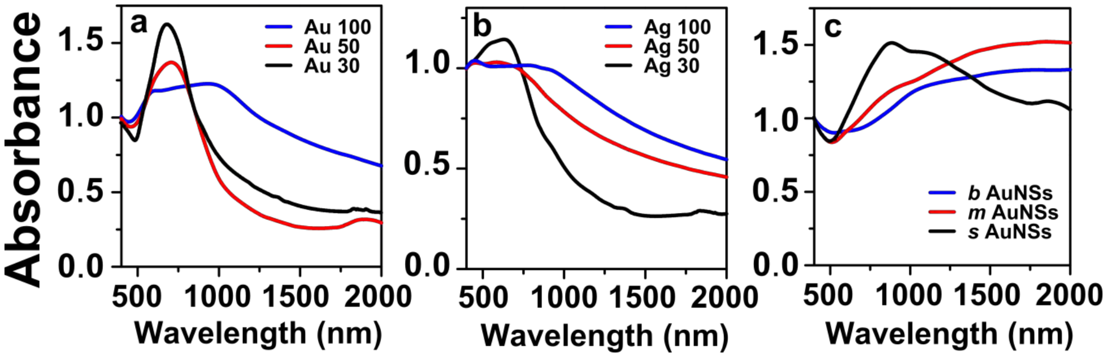

Figure 3. 11 Vis-NIR spectra of plasmonic substrates made of AuNPs (**a**), AgNPs (**b**) and AuNSs (**c**) of different sizes.

In the case of AuNSs, dense packing leads to a high degree of spike interdigitation, which is rarely achieved using chemical immobilization methods,[216] and leads to a particularly large extent of plasmon coupling as compared to nanospheres. Remarkably, these monolayers present several advantages for the fabrication of plasmonic substrates, such as readily achieved homogeneous large areas on the square centimeter range, whilst "coffee ring" or similar local effects are avoided. Formation of dense monolayers was therefore achieved through a simple experimental procedure for both phase transfer and assembly, which can be scaled up to arbitrarily large areas by simply selecting the appropriate amount of nanoparticles (**Figure 3. 12**).

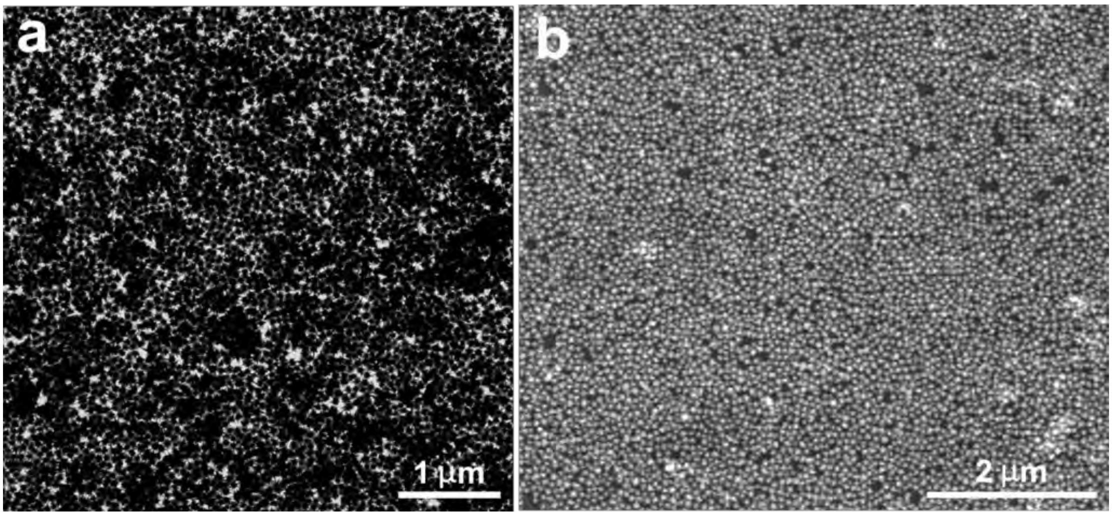

Figure 3.12. Large scale TEM (**a**) and SEM (**b**) images of *b*AuNS monolayers fabricated after the self-assembly of the PEG/DDT coated nanoparticles at the air-liquid interface.

Since phase transfer, self-assembly and cleaning processes are identical for all nanoparticles, regardless of size, shape, and composition, we can readily compare their relative performances as SERS substrates. We selected 4-mercaptobenzoic acid (4-MBA) as a covalently binding probe molecule, at a concentration of 10 µM, to probe the SERS activity using three different laser excitation wavelengths of 532, 633 and 785 nm. **Figs. 3.12**, **3.13** and **3.14** depict SERS spectra obtained with illumination at 785 nm, showing in all cases the characteristic vibrational fingerprint of (mainly deprotonated) 4-MBA, as assigned in previous works.[217–220]

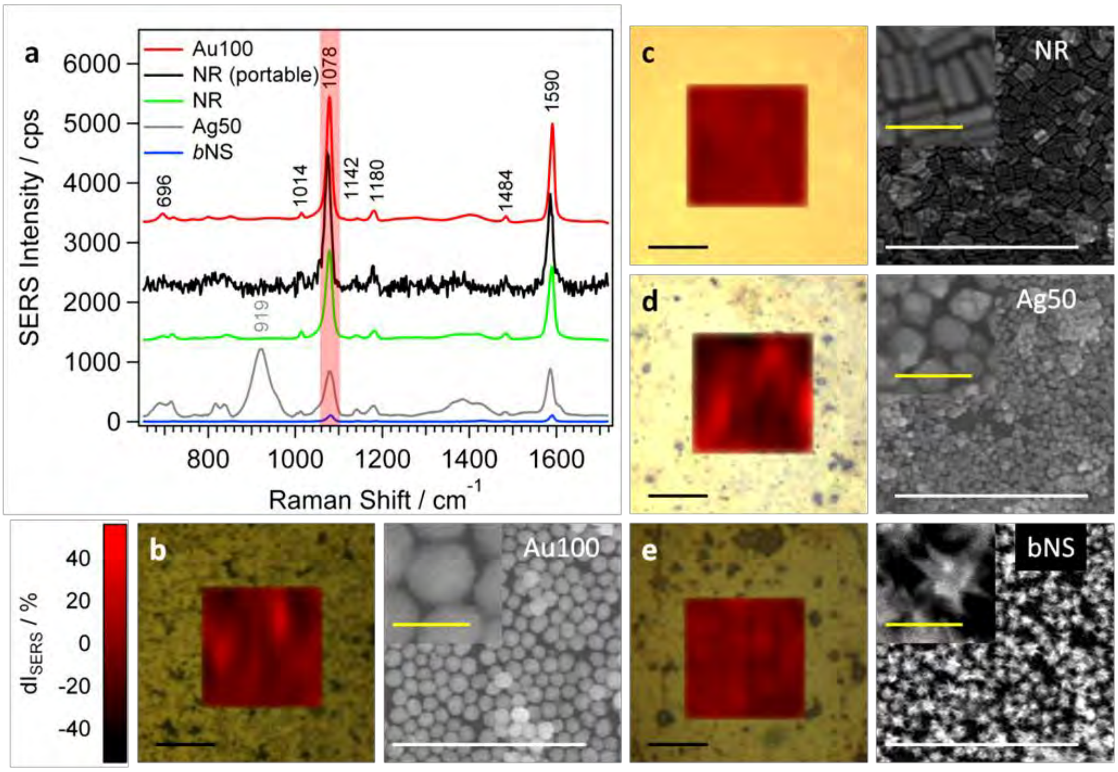

Figure 3.13. (**a**) Averaged SERS spectra of 4-MBA (10 µM) on Au 100 (**b**), AuNRs (**c**), Ag 50 (d) and *b*AuNSs (**e**). The corresponding SERS maps for the signal at 1078 cm^{-1} (red-shaded area in (**a**) as a function of the deviation from the average intensity dI (in %), together with representative SEM images of the assemblies before analyte incubation. The black SERS spectrum in (**a**) corresponds to the average of three 4-MBA spectra on the AuNR sample measured with a portable Raman spectrometer. Black, white and yellow scale bars: 10µm, 1µm and 100 nm, respectively.

The most prominent peaks at 1078 and 1587 cm^{-1} correspond to the excitation of ring breathing and axial ring deformation modes.[217,219] Several peaks with lower intensities were observed at 1484, 1180, 1142, 720 and 696 cm^{-1} and can be assigned as the 19a and 9b modes (based on the nomenclature for benzene),[221,222] in-plane CH bending,[219,222] out-of-plane ring hydrogen wagging and a mixture of OCO bending + in-plane ring compression + C-S stretching, respectively.[219] The broad bands around 1400 cm^{-1} and 845 cm^{-1} correspond to the COO$^-$ symmetric stretch mode and the bending mode, respectively.[217,219,223] An additional high signal around 920 cm^{-1}, which was exclusively registered from the Ag 50 sample, originates from organic residues formed during synthesis and plasma cleaning.

The highest SERS signal was observed from AuNR (**Figure 3.13c**) and AuNP films (**Figure 3.13b**), where the intensity was found to increase with increasing sphere diameter (**Figure 3.14**). The SERS performance of AgNP and in particular AuNS monolayers (**Figure 3.13d**,**e**) was significantly lower, with intensities one order of magnitude smaller than those from AuNP and AuNR films. This behavior can be explained taking into account that the highest enhancement is obtained on substrates with LSPR bands located between excitation the scattered frequencies.[224] At an excitation wavelength of 785 nm, this condition complies best with the AuNP and AuNR samples (**Figs. 3. 10b** and **3. 11**).

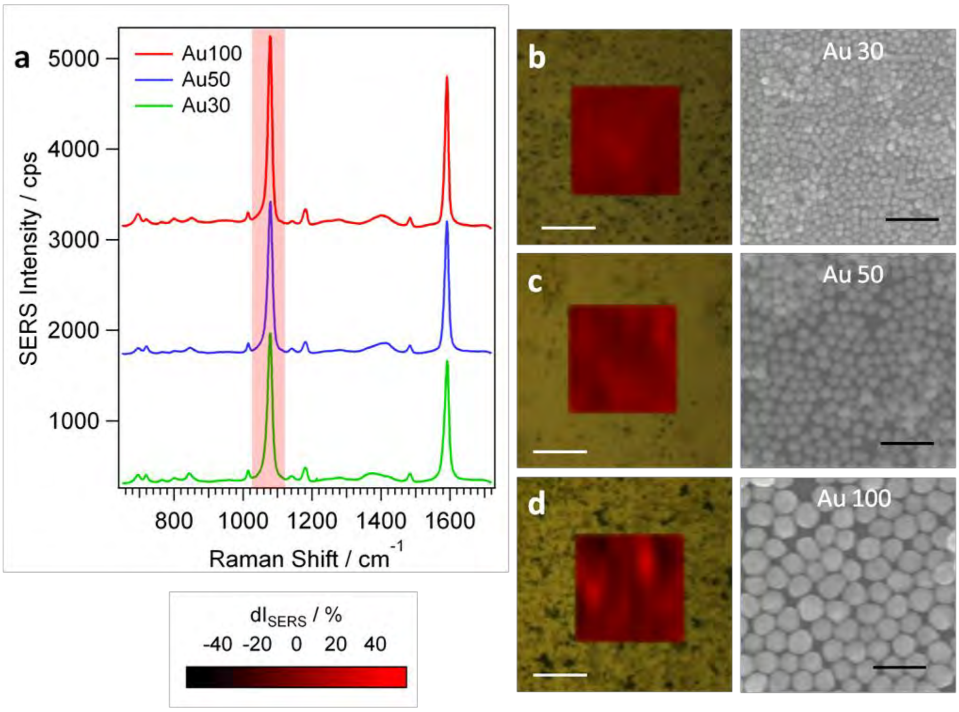

Figure 3.14. (**a**) Characteristic SERS spectra of 4-MBA (10 µM) on self-assembled AuNPs with different diameters, as labeled. Individual SERS spectra were measured with excitation at 785 nm, power of 200 mW and 1s collection time. SERS spectra were generated by averaging 100 single spectra from a 20×20 µm^2 grid within a point distance of 2 µm in x- and y- direction. (**b-d**) Optical and SEM images of self-assembled AuNP monolayers, as labeled. The white bar in the optical images corresponds to 10 µm, the black bar in the SEM images to 200 nm. SERS mappings show the spatial homogeneity by plotting the 4-MBA vibration at 1078 cm^{-1} for each sample (red-shaded peaks in **a**), presented as function of the deviation dI (in %) from the average signal.

The SERS signal intensity also depends on several additional surface specific factors, *e.g.* analyte binding affinity, presence of surfactants[170,175,225] or contaminants and surface defects.[226] Additionally, potential applications require reliability of the measured signal as a key factor. Due to the relatively large laser spot size (>1 µm^2), defects on the atomic scale do not play a significant role but shape imperfections, a small degree of disorder within the assembly and remaining organic residues may cause significant point-to-point intensity fluctuations. To avoid large errors and to statistically improve the signal, we averaged SERS spectra over 100 points located on a 20×20 µm^2 grid. To probe the local homogeneity we analyzed intensity fluctuations of single-point spectra presented as SERS maps in **Figs. 3.13**, **3.14** and **3.15.** The lowest signal variation from the averaged value (dI in %) was observed for the AuNR sample with 12% (**Figure 3.13c**).

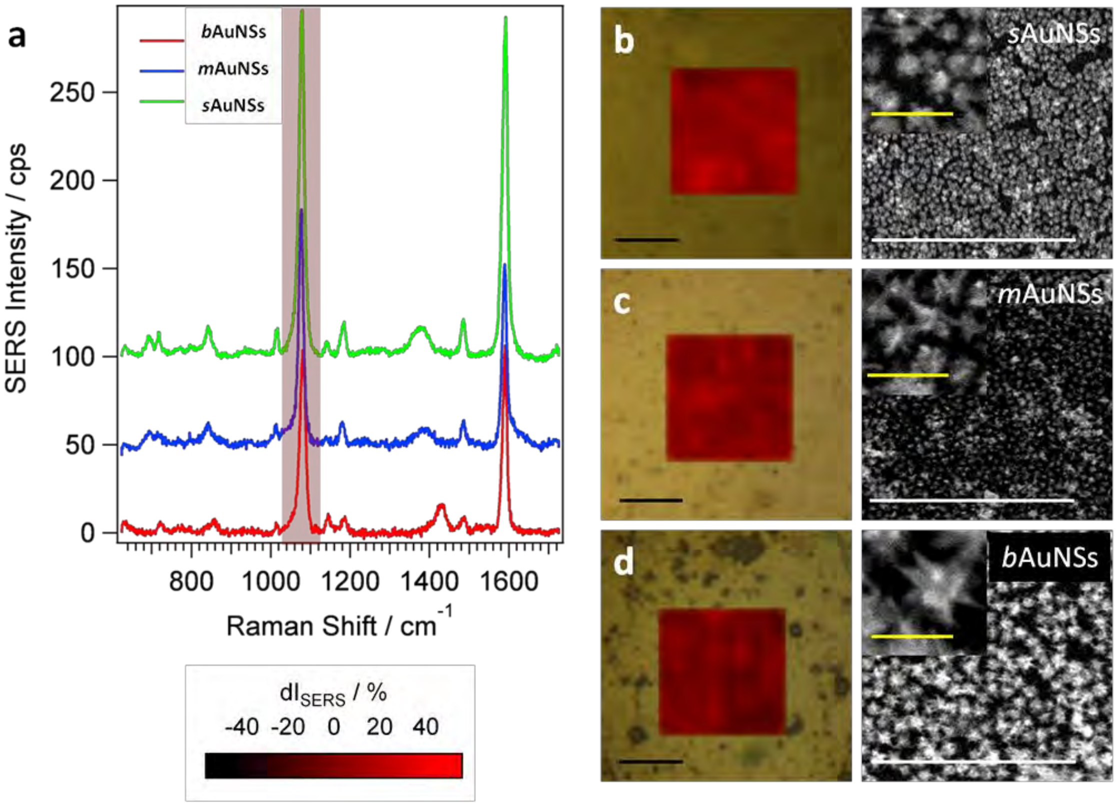

Figure 3.15. (**a**) Averaged SERS spectra of 4-MBA (10 µM) on assemblies of AuNSs with different diameters, as labeled. The corresponding SERS mappings for the signal at 1078 cm^{-1} (red-shaded peaks in (**a**) as a function of the deviation from the average signal dI (in %) of *s*AuNSs (**b**), *m*AuNSs (**c**) and *b*AuNSs (**d**), and representative SEM images of the assemblies before analyte incubation. Black, white and yellow scale bars: 10µm, 1µm and 100 nm, respectively.

The AuNP samples showed fluctuations ranging from 15% to 34% for increasing particle diameters (**Figs. 3.13b** and **3.14**), whereas the SERS signal from small, middle and big AuNSs was found to scatter within *ca.* 30% (**Figs. 3.13e** and **3.15**). The weakest homogeneity was found for Ag 50 (**Figure 3.13d**), with signal deviations up to 50%. These results are directly related to the degree of disorder within the assemblies, as well as with larger inter-particle contact area for smaller nanoparticles. The relatively high disorder of the Ag 50 substrate accompanied by the presence of organics which could prevent the effective binding of the analyte are likely to be responsible for the high signal fluctuations on the Ag substrate. Ag particles are additionally sensitive to oxidation, so the formation of a thin oxide layer can affect the SERS performance. To probe homogeneity over large areas, SERS maps were recorded from at least three different areas distributed over the substrate. The intra-sample average signal variation did not exceed 5% for AuNRs, but amounted 7%, 10% and 13% for Au 30, 50 and 100, respectively. In small, middle, and big AuNSs the SERS signal fluctuated less than 15%. Reproducibility of the SERS response was studied by repeating sample preparation with different nanoparticle batches, finding average batch-to-batch intensity fluctuations lower than 5% for AuNRs and 15% for AuNPs. When 4-MBA SERS spectra were recorded using 532 and 633 nm excitations, different results were obtained, as at 532 nm the most intense signals were obtained from Ag 50, reaching intensities two orders of magnitude higher than those from AuNP substrates (**Figure 3.16e**). In line with the SERS electromagnetic mechanism, recorded intensities were lower from Ag 50 at 633 nm but higher from AuNPs (**Figure 3.16f**). AuNS substrates did not show SERS activity when excited with both high energy laser lines.

As additional advantages of this system, we show that detection can be performed directly from solution and using a portable Raman spectrometer. Thus, we measured SERS from substrates immersed in 10 µM 4-MBA solutions. Exemplarily, the spectrum and map for the AuNR sample are shown in **Figure 3.17**. The average SERS intensity (at 785 nm) only varies by 2.5%. For other nanoparticle assemblies we recorded in solution the same average intensity deviations and point-to point fluctuations as measured in air.

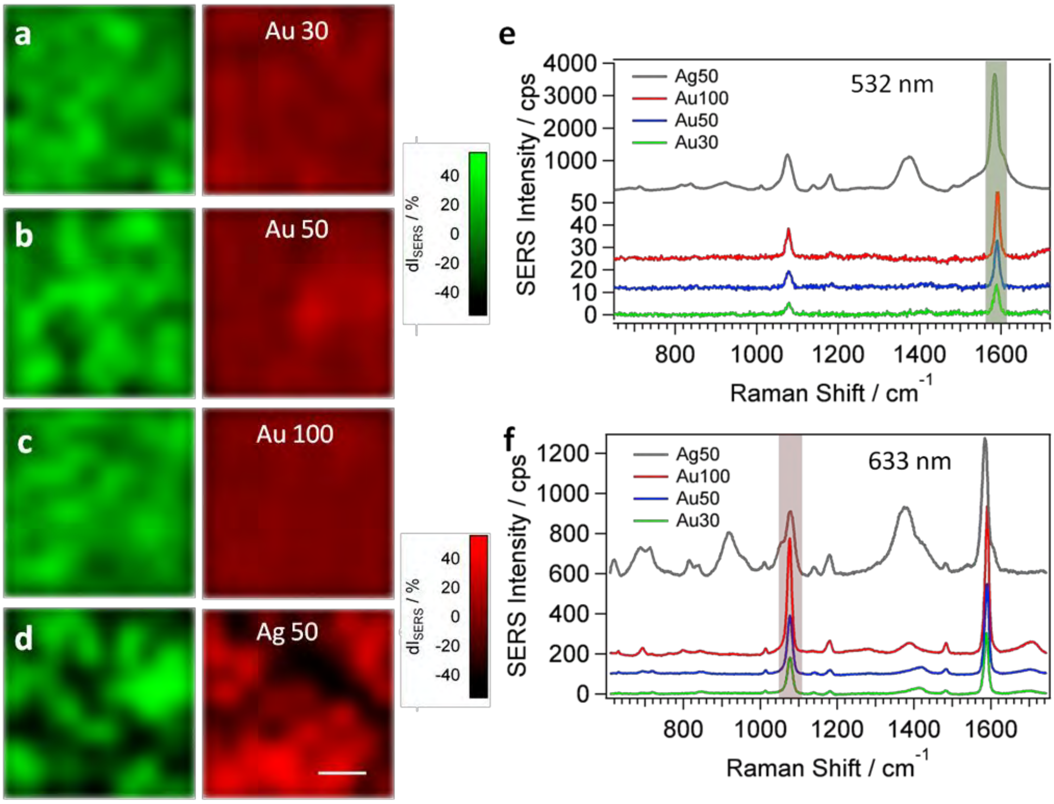

Figure 3.16 Averaged 4-MBA SERS spectra (10 µM) on Au 30 (**a**), Au 50 (**b**), Au 100 (**c**) and Ag 50 (**d**) substrates with excitation at 532 and 633 nm, and corresponding SERS mappings at 1585 cm^{-1} (green scale, green-shaded peaks in **e**) for 532 nm and 1078 cm^{-1} (red scale, red-shaded peaks in (f) for 633nm, as a function of the average intensity deviation dI (in %). Corresponding averaged SERS spectra at 532 nm and 633 nm were plotted in (**e**) and (**f**), respectively. The scale bar is 4 µm.

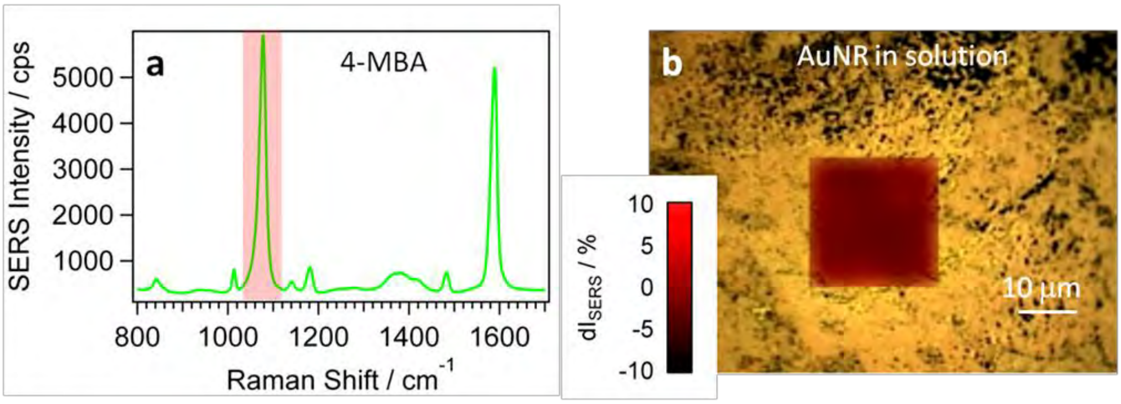

Figure 3.17 Averaged SERS spectrum of 4-MBA (10 µM) on a AuNR substrate immersed in water (**a**) at 785 nm, and corresponding SERS mapping at 1078 cm^{-1} (red scale, red-shaded peaks in a, as function of the average intensity deviation dI in % (**b**).

Applicability outside the laboratory will also require using easy to handle standard analytical equipment for rapid detection, instead of sophisticated scientific set-ups. We measured 4-MBA on the AuNR substrate using a portable Raman spectrometer (BWTEK, i-Raman-785S) working at a fixed 785 nm excitation wavelength. P_{laser} and t_{int} were adjusted so that the 4-MBA SERS intensities in both set-ups were of the same order of magnitude without damaging the substrate, e.g. through high power exposition. To reach these conditions, $P_{laser} = 19\,mW$ measured at sample and $t_{int} = 1\,s$ were needed (laser spot size of about 80 µm). We thus measured at 3 randomly chosen points distributed over the whole surface and the average is shown in **Figure 3.13a**, with a standard deviation of 7%.

SERS enhancement factors (EF) were calculated by means of the frequently used equation,[227]

$$EF = \frac{I_{SERS}}{N_{SERS}} \cdot \frac{N_{bulk}}{I_{Raman}} \qquad \textit{Equation 3.1}$$

where I_{SERS} and I_{Raman} represent the 4-MBA signal intensities recorded from the probed number of molecules absorbed on the substrate (N_{SERS}) and from the number of molecules within the scattering volume (N_{bulk}) of a solid powder, respectively. For determination of the scattering volume from the bulk material the depth of field approach presented by Khan et al.[228] was used, resulting in $N_{bulk}(785\ \text{nm}) \approx 1013 \cdot$ $N_{SERS}(785\ \text{nm})$ was estimated to be 108 assuming formation of a 4-MBA monolayer. I_{Raman} and I_{SERS} were measured with 95 and 3517 cps, respectively, leading to an EF (785 nm) of approx. $3.7 \cdot 10^6$ in the case of the AuNR substrate. This value is of the same order of magnitude as previously reported values.[228]

We finally show that the obtained nanoparticle organosols can also be used for secondary coating with an amphiphilic polymer that has been previously reported as suitable for biological applications.[68,192] After removal of excess DDT by centrifugation of the dispersion in chloroform, the reported polymer coating procedure was applied using dodecylamine modified polyisobutylene-alt-maleic anhydride (PMA). The hydrophopic nanoparticles were thus wrapped with the polymer *via* hydrophobic interactions between the side chains of the polymer (dodecylamine) and the NP ligands. The particles could then be transferred into water, where the charged polymer shell provides sufficient stability in biofluids. Representative Vis-NIR spectra and TEM images (**Figure 3.18**) of PMA coated AuNSs confirm the colloidal stability of the particles upon polymer coating. TEM images of negatively stained, polymer coated Au NSs confirm the presence of an organic layer wrapping the particles in water. A white shell surrounding the NPs can be clearly appreciated for PMA-coated particles (**Figure 3.18b**, **c**).

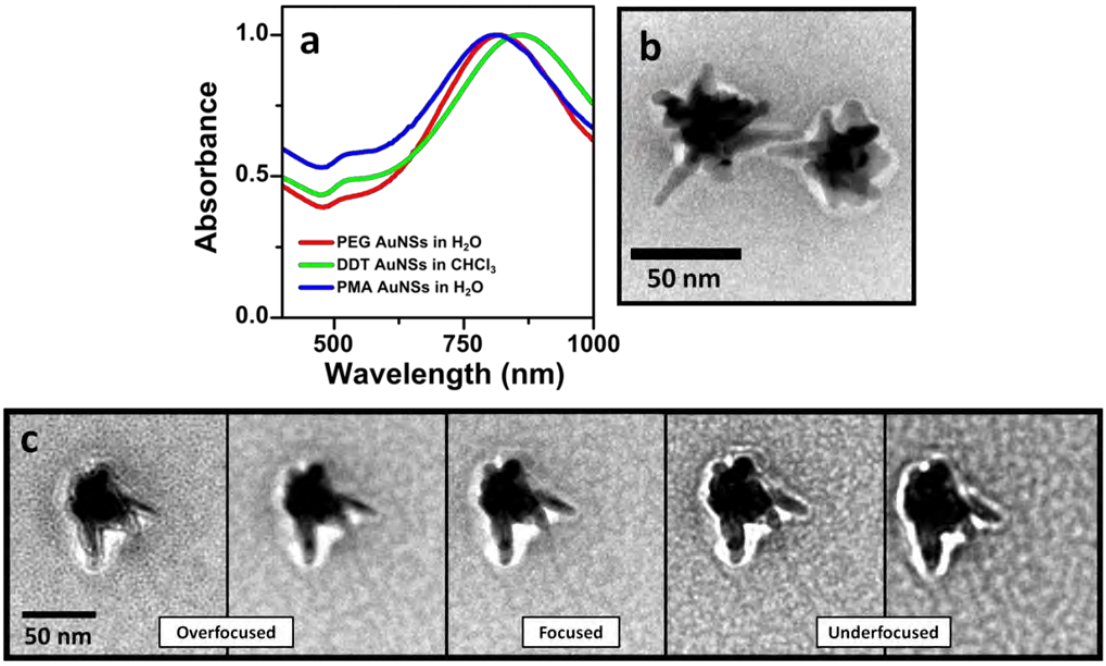

Figure 3.18. (**a**) UV-Vis spectra of PEG-SH stabilized Au NSs in water (red), after transfer into $CHCl_3$ with PEG/DDT (green), and again in water after PMA coating (blue). TEM image (**b**) and TEM focus series (**c**) of negatively stained polymer coated Au NSs.

3.4 Conclusions

A general route for transferring AuNSs from aqueous dispersions into chloroform and other organic solvents has been developed. The method can be also applied to Ag and Au nanoparticles of arbitrary sizes and shapes, such as spheres or nanorods. The transferred particles are stable in chloroform for months and can be readily dried, purified, and redispersed in various organic solvents. This efficient phase transfer procedure is based on functionalization of the nanoparticles' surface with a mixture of PEG-SH and DDT. Whilst DDT provides the required hydrophobicity for the nanoparticles to reach the organic phase, PEG-SH provides enough stability to avoid aggregation during phase transfer. Using ethanol:hexane 1:4 mixtures as spreading solvent, homogeneous extended self-assembled nanoparticle monolayers were obtained on the centimeter scale. Whereas the self-assembly of plasmonic nanoparticles at liquid interfaces has been traditionally restricted due to limited size of nanoparticles available in organic solvents, limited stability, and complicated experimental procedures, the method proposed here allows us to obtain plasmonic nanoparticles in organic solvents with no restriction in size, shape or surface chemical composition, readily forming nanoparticle assemblies. The close packing of the plasmonic nanoparticles favors plasmon coupling, thus providing enhanced plasmonic features. We compared the SERS activity between the different plasmonic substrates fabricated by detection of 4-MBA, finding that AuNP and AuNR self-assembled monolayers displayed optimum SERS performance in air and in solution for 785 and 633 nm excitation lasers, with high signal reproducibility, robustness and relatively low point-to-point fluctuations. We also showed that high-end experimental set-ups are not necessary to obtain intense and reproducible SERS signals from our assemblies. Additionally, the obtained hydrophobic nanoparticles proved suitable for additional polymer coating, thereby broadening potential applications due to the obtained high stability under biological conditions.

CHAPTER 4

Encoded-Gold Nanostars for Multiplexed SERS Cell Differentiation

ABSTRACT

Surface enhanced Raman scattering nanotags are appealing contrast agents that offer important advantages over classical (bio)labeling methods. They present high photostability, sensitivity and superior multiplexed capacity due to the small line width of vibrational Raman bands. In addition, the enhanced optical contrast and tissue penetration achieved by using NIR light render them excellent candidates for *in vivo* Raman imaging. The synthesis of new SERS-codes suitable for biological applications requires the use of metal nanoparticles with high plasmonic enhancing efficiency. In this regard, anisotropic nanostructures such as Au nanostars, which present optical responses in the tissue optical transparency window, are attractive platforms for the design of SERS-encoded nanoparticles. We report in this chapter a general method to prepare highly stable SERS-encoded Au nanostars, based on the procedure described in Chapter 3. Using a combination of thiolated polyethylene glycol and a Raman-active molecule, SERS nanotags were obtained in organic solvents and subsequently polymer wrapped and transferred into water with high colloidal stability and biocompatibility. These SERS nanoplatform are ideal candidates for use with live cells, as we demonstrate through multiplex bioimaging of different cell lines.

4.1 Introduction

Surface enhanced Raman scattering encoded nanoparticles are presented as alternative contrast agents that offer multiple possibilities toward a variety of biological applications.[135,136,229] As the intrinsic Raman cross section of most biomolecules, such as proteins and lipids, is extremely low, often compounds (*i.e.*, codes) with comparatively high cross sections are commonly used as Raman reporters (RaRs) to monitor specific events at the molecular level. Thus, a typical SERS label (also called SERS nanotag) is composed of a noble metal nanoparticle (NP) as Raman signal amplifier, covered with a monolayer of RaR molecules as fingerprint marker and an external coating.[124] Flexibility in size and shape, high photostability,[230] low cytotoxicity due to the use of gold NPs (AuNPs),[15] and the narrow spectral width (~ 1 nm)[231] compared *e.g.* with quantum dots (~ 30-50 nm) and conventional dyes (~ 50 nm),[232] offer great advantages over common fluorescence-active probes, rendering them particularly attractive for in vitro and in vivo multiplexing and bioimaging.[138,233–236]

In the design of biocompatible SERS labels the coating layer plays an important role as it acts as a protective shell, preventing the possible leaching of RaR molecules, NP contamination from interfering molecules in the medium, and plasmon coupling induced by NP-NP interactions. Therefore, the resulting surfaces are suitable for chemical functionalization and provide high colloidal NP stability. In addition, the external shell can also support specific sites for biological recognition.[237] Among the different encapsulation strategies, the most employed ones include the use of bovine serum albumin,[129,238–242] liposomes,[243–245] silica[130,132,230,246–249] or polymers.[68,127,128,192,250–254] Although silica as a cheap and well-known coating has been successfully applied to different *in vitro*[132,233,247] and *in vivo* targets,[138,235] its stability is known to be strongly dependent on the specific synthesis and morphology. For instance, amorphous silica particles were shown to agglomerate fast within standard buffer and cell medium such as phosphate buffer saline (PBS) and Dulbecco's modified Eagle's medium (DMEM) when concentrations of 10^{13} mL^{-1} were used.[255] As silica growth is kinetically controlled, the exclusive encapsulation of individual NPs (and not of dimers or trimers by uncontrolled aggregation) and the formation of a defect-free uniform shell, require slow and precisely selected growth conditions.[130,230,249] The stability of mesoporous silica is dependent on different factors such as temperature, medium and surface modification,[256–258] and the material is also degradable within body fluids as well as in cytoplasm and lysosomes[259,260] On the other hand, thiolated polyethylene glycol (PEG) has been used to prepare AuNP tags for *in vivo* tumor targeting.[252,253] Dye-encoded gold octahedrons were encapsulated with poly(N-isopropylacrylamide) and used as SERS tags for the detection and imaging of tumor biomarkers.[128] SERS-labeled AuNPs were also coated with mixed amphiphilic polymer brushes, assembled into vesicles and conjugated to target cancer cells.[254] Moreover, amphiphilic polymers, such as dodecylamine modified polyisobutylene-alt-maleic anhydride (PMA), have been extensively employed for the encapsulation of different kinds of NPs providing high colloidal stability and making them suitable for use under biological conditions.[68,127,192]

Another crucial factor when designing a SERS nanotag is the choice of plasmonic NP-RaR combination. For *in vitro* and *in vivo* SERS applications, excitation with wavelengths ranging from the red to the near infrared (NIR), the so-called “biological transparency window”, provides optimal transmission through tissues due to both low scattering and low absorption, thereby minimizing tissue auto-fluorescence[261,262] and maximizing penetration of the radiation.[150,263] Thus, during the past decade large progress has been done concerning the synthesis and design of SERS-labeled nanostructures that absorb in the NIR range.[99,124] Development of ultrasensitive NIR RaRs[241] as well as the fine-tuning of localized surface plasmon resonances (LSPRs) are the most common strategies to improve the sensitivity of the SERS label. It has been shown that LSPRs of branched AuNPs such as Au nanostars (AuNSs) can be easily tuned over a wide wavelength range down to the NIR by simply changing the aspect ratio.[46] Furthermore, AuNSs are superior Raman-enhancing materials compared to isolated spherical AuNPs due to the high electromagnetic field enhancements at their sharp tips.[103,264]

In the previous chapter we showed that AuNPs of different sizes and shapes can be functionalized with a mixture of dodecanethiol (DDT) and PEG, transferred into organic solvents and subsequently coated with an additional layer of the hydrophilic polymer PMA.[265,266] Following a similar strategy, we describe here the synthesis of a new class of SERS tags based on PMA encapsulated AuNSs. This novel approach combines the use of aromatic hydrophobic thiols which, on one hand strongly bind to the gold surface generating a strong Raman signal and on the other hand act as a capping agent that fully covers PEG pre-stabilized AuNSs. Once Raman labeled AuNSs are obtained, further PMA coating leads to SERS tags that are highly stable in water and therefore suited for multiplexed SERS cellular imaging.[128,236,253] In this way, breast cancer cells could be identified with simple and multiplex SERS labels either by different SERS signal intensities due to variation of the targeting efficiency, the deconvolution of the superimposed multiplexed signal or the detection of separated signals due to highly specific targeting.[267–269] We first characterized these new NIR-sensitive SERS tags in aqueous solution, using highly phagocytic macrophages as test cells. We then applied them for bio-imaging of different types of cancer and endothelial cells. Finally, in a proof of concept experiment, single breast cancer cells of five different lines were distinguished by SERS imaging from a unique ***quintuple*** cell co-culture, thereby highlighting the stability and strong signal that can be detected from these PMA-coated labels.

4.2 Experimental Section

Materials

Milli-Q water (resistivity 18.2 MΩ·cm) was used in all experiments. Hydrogen tetrachloroaurate trihydrate ($HAuCl_4 \cdot 3H_2O$, ≥99.9%), sodium citrate tribasic dihydrate (≥98%), silver nitrate ($AgNO_3$, ≥99%), L-ascorbic acid (AA, ≥99%), O-[2-(3-mercaptopropionylamino) ethyl]-O’-methylpolyethylene glycol (PEG, MW 5,000 g/mol), Benzenethiol (BT, ≥98%), 1-Naphthalenethiol (1-NaT, 99%), 2-Naphthalenethiol (2-NaT, 99%), 4-Methylbenzenethiol (4-MBT, 98%), Biphenyl-4-thiol (4-BPT, 97%), 4-Mercaptopyridine (4-MP, 95%), 9-Mercaptofluorene (MF, ≥96.5%), poly(isobutylene-alt-maleic anhydride), (average Mw ~6,000 g/mol), dodecylamine (98%) and chloroform ($CHCl_3$, ≥99.8%) were purchased from Sigma-Aldrich. Tetramethylrhodamine cadaverine (TAMRA, $\lambda_{ex} = 544$ nm, $\lambda_{em} = 571$ nm, #A1318) was purchased from Life Technologies (Invitrogen). Hydrochloric acid solution (37%) was purchased from Panreac. All glassware was washed with aqua regia, rinsed 3-fold with Milli-Q water and dried before use.

Synthesis of Gold Nanostars

AuNSs were prepared by a seed-mediated growth method.[39] The seed solution was prepared by adding 5 mL of 1% citrate solution to 95 mL of boiling 0.5 mM $HAuCl_4$ solution under vigorous stirring. After 15 min of boiling, the solution was left to cool and then kept at 4 °C for long-term storage. For the synthesis of AuNSs of approximately 50 nm diameter and with an LSPR maximum located around 750 nm, 2.5 mL of the above citrate-stabilized seed solution was added to 50 mL of 0.25 mM $HAuCl_4$ solution (with 50 µL of 1M HCl) in a 20 mL glass vial at room temperature under moderate stirring. Quickly, 500 µL of silver nitrate ($AgNO_3$) 3 mM and 250 µL of ascorbic acid (AA) 100 mM were added simultaneously. The solution rapidly turned from light red to greenish, indicating the formation of AuNSs. Immediately after growth, the solution was stirred with 410 µL of PEG-SH 0.1 mM for 15 min, washed by centrifugation at 1190 g, 25 min, 10 ºC and redispersed in water.

Polymer preparation

The synthetic procedure followed to prepare the amphiphilic polymer, PMA, was adapted from previous publications.[69,270] During preparation, 75% of the anhydride rings from the polyisobutylene-alt-maleic anhydride hydrophilic backbone were reacted with dodecylamine ligand, leaving 25% free. For fluorescence imaging of cells with AuNSs, 2% of these anhydride rings were modified with TAMRA dye.

Gold nanostar codification

AuNSs were fully coated with the corresponding Raman-reporter (RaR) molecule (4-MP, 1-NaT, BT, 4-MBT, 2-NaT, 4-BPT, TAMRA and MF) via organic phase transfer, following a modification of a previously reported method.[265] Raman-active molecules were incorporated as capping ligands. 2.5 mL of PEG pre-stabilized AuNSs 1.5 mM (Au^0 concentration) was stirred with a $CHCl_3$ solution of the Raman-active molecule. The amount of Raman-active molecules present on the AuNSs surface was calculated to be 155 molecules per nm^2, assuming that the AuNS diameter is 50 nm. Phase transfer occurred after vigorous stirring for periods between 15 min and 1 hour. Only the transfer with 4-MP was assisted by addition of 250 µL NaOH 1M and required overnight stirring. Upon transfer to $CHCl_3$, the organosols were purified by centrifugation (1320 g; 25 min; 10 ºC) and washing to remove excess of free thiols.

Precipitation was facilitated by adding ethanol to the chloroform solution (1:5). For further use, the samples were stored at 4 ºC.

Polymer encapsulation

For secondary coating of the SERS encoded NPs with PMA, 2.5 mL of the AuNS solutions ([NP] ~ 1.5 x 10^{-10} M) in $CHCl_3$ were mixed with the prepared amphiphilic polymer dissolved in $CHCl_3$ (V_P = 10 µL, c_P = 0.05 M, $R_{p/area}$ = 150 nm^{-2}) in a 25 mL round bottom flask. The mixtures were stirred and the solvent was slowly evaporated. The resulting solid films containing the NPs were dissolved in 28 mM sodium borate buffer at pH 12.[265] After polymer coating the particles were purified and the Au^0 concentration was adjusted to 0.5 mM.

Cell cultures

SK-BR3 and HCC1395 were purchased from ATCC (LGC Standards, Barcelona). MDA.MB.435S cells were kindly provided by Prof. Wolfgang Parak’s group. SK-BR3 cells were grown in McCoys media, HCC1395 and CAMA-1 cells were grown in Dulbecco´s Modified Eagle´s Medium (DMEM) media supplemented with 1% sodium pyruvate, MDA.MB.435S, A549 and J774 cells were grown in DMEM media, and MCF-7 cells were grown in DMEM supplemented with insulin (0.01 mg/mL). HUVEC cells were grown in F12-K media supplemented with endothelial cell growth factor (ECGF, 30 µg/mL and heparin (0.1 mg/mL). All cell media were supplemented with 10% FBS and 1% PS. All cells were passaged using Trypsin-EDTA and were grown in a humidified atmosphere at 37 °C with 5% CO_2. All media and supplements were purchased from Invitrogen.

Cell preparation for SERS imaging

Cell uptake of PMA_{TAMRA}-coated NPs was imaged using fluorescence (confocal or normal), and dark field microscopy. In some cases cells were counterstained with DAPI and wheat germ agglutinin (WGA)-Alexa Fluor 647 (WGA-AF647) (both from Invitrogen). For dark field imaging, cells were grown in glass-bottomed dishes with an etched grid (Ibidi, Germany) so that the same cells could be identified using fluorescence and dark field microscopy. As an oil condenser was used for dark field imaging, the cells had to be fixed and mounted with a glass coverslip, and the whole sample inverted. Cells were detached from growth flasks, counted and plated in 96-well cell culture plates at $1 \cdot 10^5$ cells/mL, 100 µL/well. HUVEC cells were plated at approximately a 10-fold lower concentration. In the case of J774 or MCF-7 cells, cells were plated directly at the same concentration in a specially made cell slide formed of a 2 cm diameter ring glued onto a quartz microscope 75×25 mm^2 slide (Electron Microcopy Sciences). Dentist glue (Twinsil, Germany) was used as it is non-toxic and can easily be removed. The total volume was approximately 200 µL. Cells were allowed to adhere for a few hours before addition of SERS tags. Prior to this experiment various trials using TAMRA-labelled SERS tags at the same concentration and with equivalent properties were used to determine levels of uptake (**Figure 4.9**). The results suggested that a final NP concentration of 0.1 mM resulted in a high level of NP uptake. Whilst some cells showed higher levels of uptake than others, these could not be altered by increasing the NP concentration. Cells were incubated with SERS tags for approximately 18 h, followed by extensive washing with PBS to remove non-endocytosed NPs. HCC, SK-BR3, MDA.MB.435S and CAMA-1 cells were removed from the 96-well plate using trypsin-EDTA and split into two batches. One batch, equivalent to 1 well of a 96-well plate (initial cell number 10,000 cells), was plated in a specialised well made using a cut 1.5 mL Eppendorf tube, with lid removed and a ring cut measuring a few mm, glued onto a quartz microscope slide (Electron Microcopy Sciences or Helma), using the above mentioned dentist glue. The second batch of cells was combined, centrifuged and resuspended in a total volume of 200 µL complete DMEM media. These cells were added to the single MCF-7 culture (2 cm diameter dish) to obtain a quintuple culture, each cell line containing NPs with a specific Raman tag. Wells were covered lightly with Parafilm to prevent evaporation.

SERS measurements

SERS was measured with a confocal Raman microscope (Renishaw inVia) equipped with 1024×512 CCD detectors using a 785 nm laser excitation source (maximum output of 270 mW) and a 1200 l/mm diffraction grating. For reference and performance test SERS experiments, 500 µL of encoded AuNSs in aqueous solution ($[Au^0] = 0.5$ mM) was pored in 1 mL glass vials (ThermoFisher) and spectra were collected using a 10× objective (numerical aperture NA=0.35) in expanded scan mode with an integration time of 10 s and a laser power of 18.3 mW. SERS measurements in cells were carried out in static mode (center of scattered wavenumber 1200 cm^{-1}) with an integration time of 1 s and a laser power of 15.6 mW. For SERS imaging of cells the spectra were measured on a selected grid with a point distance of 2 µm in x- and y direction. The maps were then created by plotting the intensity of a component-specific SERS signal as a function of grid position. The average laser powers were experimentally determined by means of a thermal laser sensor and a power meter (both from Ophir) in air.

Characterization

TEM images were collected with a JEOL JEM-1400PLUS transmission electron microscope operating at 120 kV, using carbon coated 400 square mesh copper grids. UV-Vis optical extinction spectra were recorded using an Agilent 8453 UV-Vis diode-array spectrophotometer. The fluorescence of the NPs was measured with a Horiba Jovin-Ivon Fluorolog fluorimeter upon excitation at $\lambda_{ex} = 530$ nm. Imaging was performed with a confocal laser scanning microscope (LSM510, Zeiss), equipped with lasers allowing excitation at 544 nm (TAMRA) and 405 nm (DAPI), and an Axio Cell observer (Zeiss) with LED excitation at 365 nm and 570 nm for DAPI and TAMRA, respectively. Details regarding imaging are given in the descriptions of the corresponding assays.

4.3 Results and Discussion

4.3.1 Preparation of SERS-encoded nanostars

A schematic illustration of the preparation of the SERS-encoded AuNSs is presented in **Figure 4.1**. The procedure can be divided in various steps. First AuNSs are synthesized and stabilized via PEG functionalization. Afterwards, phase transfer from water into $CHCl_3$ is induced during which the AuNS solution is vigorously stirred with a $CHCl_3$ solution of the corresponding Raman reporter (RaR). Finally, these particles were overcoated with the amphiphilic polymer PMA.

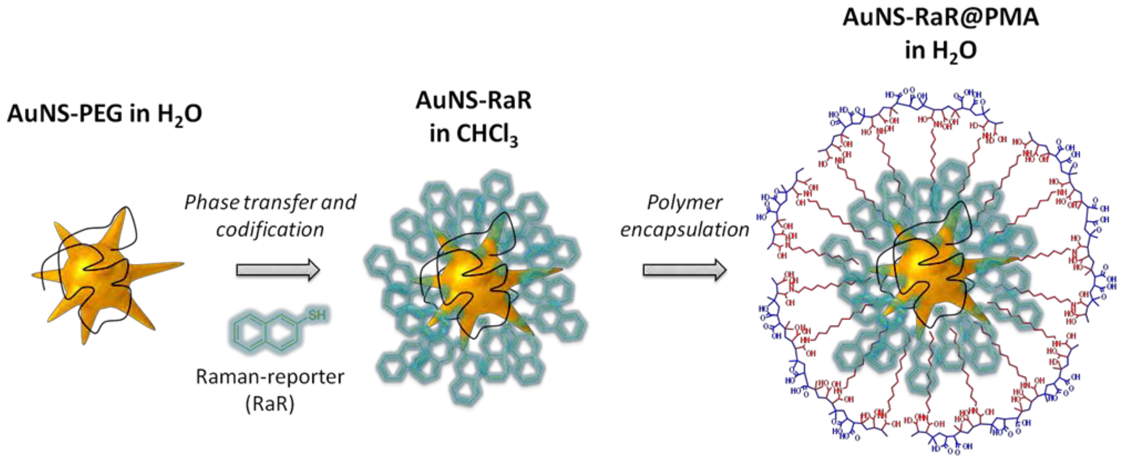

Figure 4. 1 Representation of the Raman encoded-AuNSs preparation. AuNSs pre-stabilized with PEG are coated with the Raman-tag during phase transfer from water into $CHCl_3$. The formed hydrophobic AuNSs are then wrapped with PMA, leading to stable and water soluble encoded AuNSs.

Two main conditions are essential to ensure successful phase transfer and codification of AuNSs: (i) the Raman active molecules must be highly soluble in $CHCl_3$, otherwise complete transfer is hard to achieve as the RaR molecules also act as stabilizing agents; (ii) the use of thiol or amine-terminated molecules that can strongly bind to gold facilities the fast phase transfer and avoids leaching of the SERS molecule form the Au surface during the application. The codification strategy presented here favors all these conditions while allowing us to optimize the SERS signal by providing maximum accessibility of the molecule to the NP surface. BT, 1-NaT, 2-NaT, 4-MBT and 4-BPT, are all SERS-active thiols with high solubility in $CHCl_3$. 4-MP presents poorer solubility, so complete phase transfer requires longer incubation times, as well as the addition of a base to deprotonate the pyridine ring and decrease its aqueous solubility. TAMRA can also promote phase transfer since it is soluble in $CHCl_3$ and its free amino group can also bind the gold surface. The method can be applied to any other Raman-active molecules that are sufficiently soluble in $CHCl_3$ and display affinity toward gold. To avoid any undesirable nanoparticle aggregation, pre-stabilization of AuNSs with PEG appears to be a critical step, as previously reported.[192,265] The addition of the RaR molecule without previous PEG stabilization was found to lead to irreversible aggregation. However, when AuNSs are functionalized with PEG, the RaR molecule surface coverage can be adjusted and high values achieved, thereby ensuring maximum SERS efficiency of the codes. Saturation of the RaR molecules on the AuNS surface can be achieved by decreasing the PEG concentration, however colloidal stability is then compromised. Upon transfer into $CHCl_3$, a red shift of the LSPR maximum can be observed for all the AuNS codes, due to an increase in the local refractive index. The absence of plasmon band broadening (**Figs. 2a-f**, **4.3** and **4.6**) reflects the high colloidal stability of the AuNS codes favored by steric repulsion between the hydrophobic ligands. Besides, in agreement with previous reports,[62,265] the strong aging process that takes place after synthesis of surfactant free AuNS can be prevented by surface capping with thiolated compounds. Therefore, codification also guarantees surface passivation.

Because biological applications demand the use of water soluble nanoparticles with high stability, after SERS codification the particles were encapsulated with PMA, which provides aqueous solubility due to its hydrophilic backbone. The hydrophobic AuNS codes were thus wrapped with the polymer *via* hydrophobic interactions between the multiple aliphatic chains of the polymer (dodecylamines) and the AuNS capping ligands. After coating and dispersion in water, a slight blueshift of the LSPR maximum was observed (**Figs. 4.2a-f, 4.4** and **4.5**). **Figure 2g-l** shows representative TEM images of PMA coated RaR-AuNSs (AuNS-RaR@PMA). Well dispersed particles that preserve sharp tips were obtained. Negative staining confirmed the presence of the organic layer wrapping the particles, since a light halo surrounding the star-shaped particles can be clearly observed in TEM (**Figure 2g-l** inset).

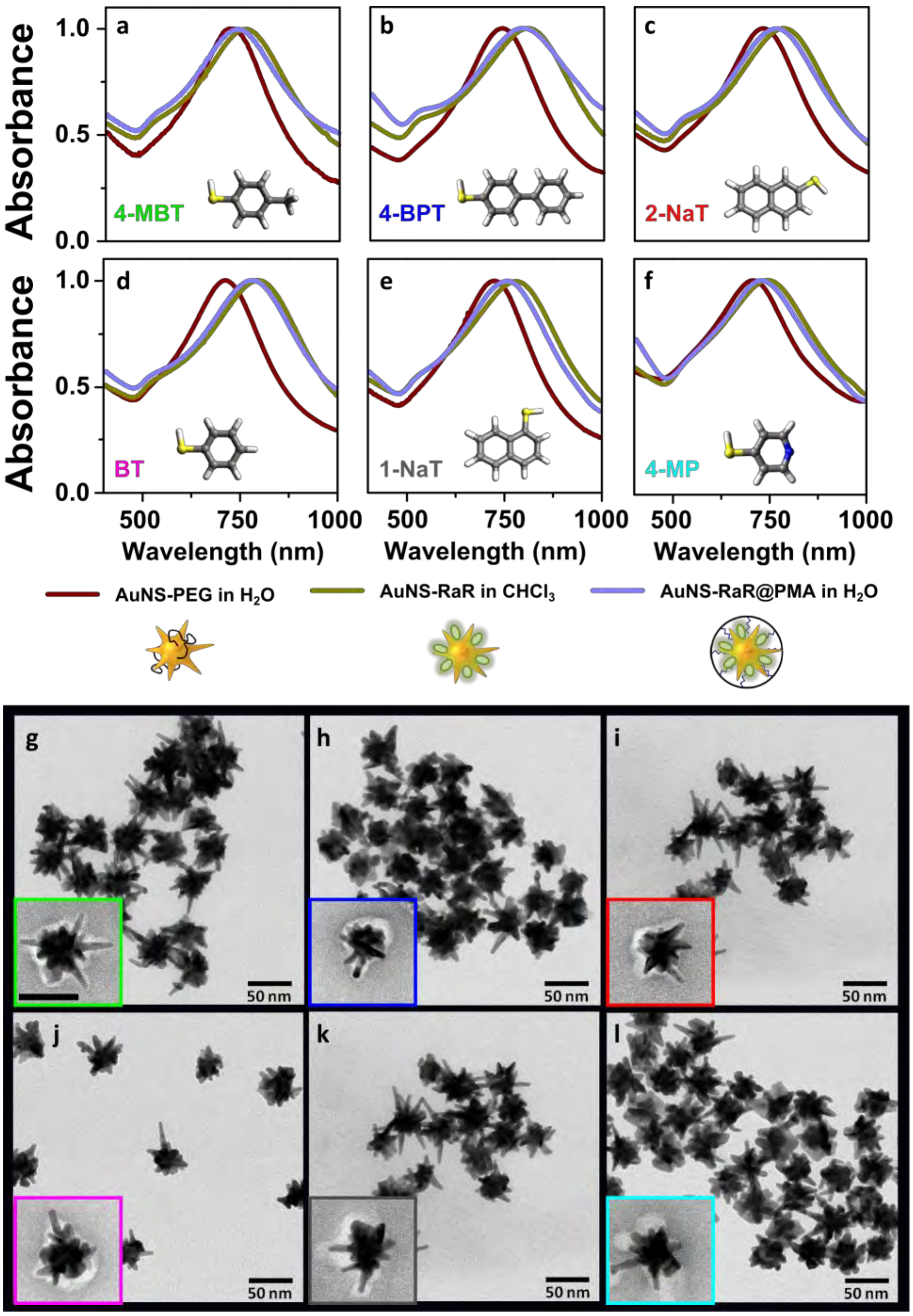

Figure 4.2. (a-f) Normalized Vis-NIR spectra of PEG-AuNSs before codification (red), and after coating with the corresponding Raman-active molecules (RaR-AuNSs; green) and after PMA encapsulation (AuNS-RaR@PMA; blue) using the following Raman reporters: from left to right, 4-methylbenzenethiol (4-MBT), biphenyl-4-thiol (4-BPT), 2-naphthalenethiol (2-NaT), benzenethiol (BT), 1-naphthalenethiol (1-NaT) and 4-Mercaptopyridine (4-MP). Molecular structures are included as insets. **(g-l)** TEM images of AuNS-RaR@PMA for 4-MBT, 4-BPT, 2-NaT, BT, 1-NaT, and 4-MP, respectively. Inset, TEM images of negatively stained particles (scale bars: 50 nm).

The charged coating shell addiotionally provides the AuNS codes with long-term colloidal stability. **Figure 4.3a**,**b** shows the evolution of Vis-NIR spectra for bare AuNSs and RaR-AuNS@PMA, respectively. As expected, a significant LSPR blueshift is observed for as-synthesized AuNSs, resulting in particle reshaping where the tips become rounded, as previously reported (**Figure 4.3c**). Importantly, for PMA coated AuNSs the plasmon band remains essentially unaltered for long periods of time due to the anti-aging effect of the thiolated capping ligands, as described in Chapter 2. Meanwhile, the charged polymer shell provides sufficient stability in water that no LSPR shift nor particle reshaping are observed (**Figure 4.3 d**).

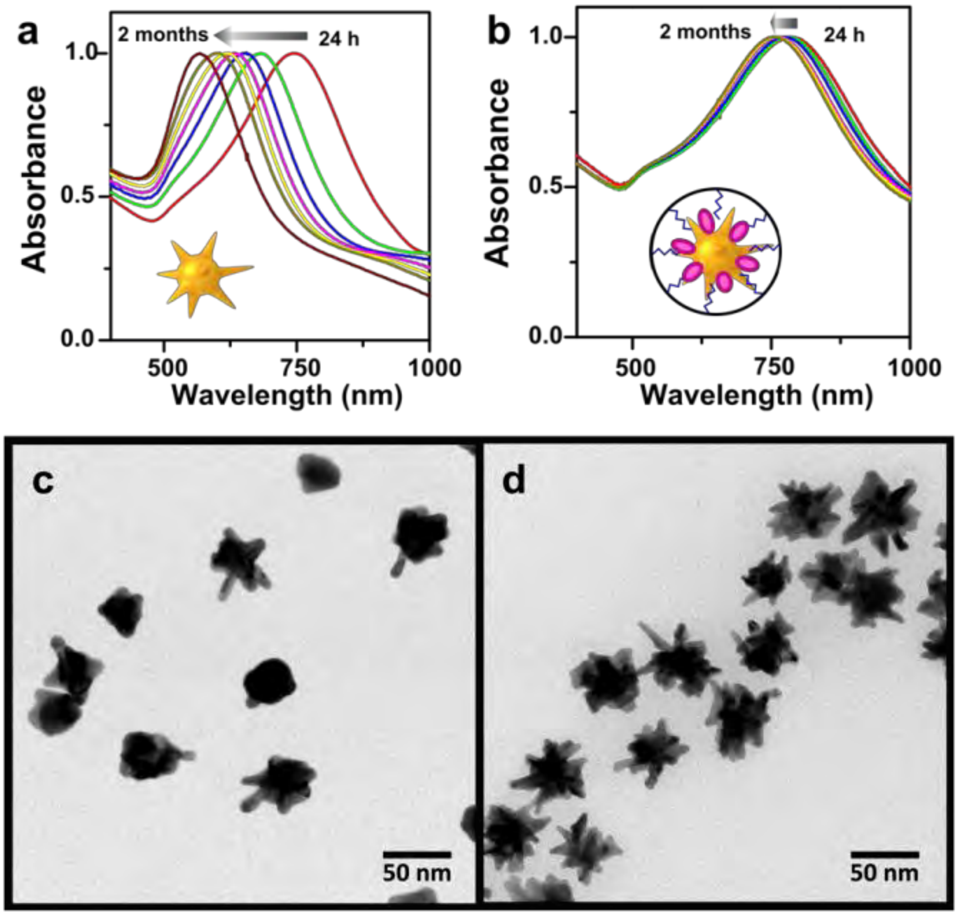

Figure 4.3. (**a**, **b**) Evolution of (normalized) Vis-NIR spectra for of bare (**a**) and AuNS-RaR@PMA (**b**). (**c**, **d**) Corresponding TEM images after two month of particle synthesis (**c**) and coating (**d**).

4.3.2 Surface Enhanced Raman Scattering

SERS efficiency of AuNP codes *vs.* AuNS codes

It is worth noting that preserving the spiky structure of the SERS encoded particles is extremely important. As NIR light is required for biological applications,[150] plasmonic nanoparticles with tip plasmon modes at such frequencies are highly efficient Raman enhancers. Although the formation of aggregates could be a strategy to increase the SERS intensity of spherical AuNPs due to hot spot formation, control over the aggregation process is usually hard to achieve. To prove the SERS efficiency of star-shaped as compared to spherical nanoparticles, AuNSs of two different sizes and 100 nm AuNPs were prepared and encoded with 1-NaT as RaR. The SERS spectra of 1-NaT (**Figure 4.4**) clearly shows that star-shaped particles with LSPR band peaking at 750 nm are necessary to obtain a meaningful SERS signal from polymer-coated nanoparticles using an excitation wavelength of 785 nm. Meanwhile, no SERS was obtained from spherical AuNPs, from which strong SERS at 785 nm can be only observed when the NPs were strongly aggregated, e.g. upon drop-casting onto a solid support (not shown) or at least partially aggregated.[271,272] Such partial aggregation is sometimes difficult to determine by standard UV-vis measurements because the far-field behavior does not necessarily reflect the SERS related near-field response.[273] In our case, the absence of SERS signal indicates that the PMA polymer coating efficiently suppresses NP aggregation in solution and therefore confirms that the intrinsic field enhancement of isolated AuNPs is too weak to result in a detectable SERS signal.[272] As expected, the PMA polymer coating protects the nanoparticle against aggregation in solution and therefore the intrinsic SERS effect of AuNPs with LSPR maximum around 550 nm is too low to result in a detectable signal. Therefore, AuNSs with NIR LSPRs[46] and strong field enhancement at their tips[35,36,43] appear to be excellent candidates for the fabrication of SERS tags.

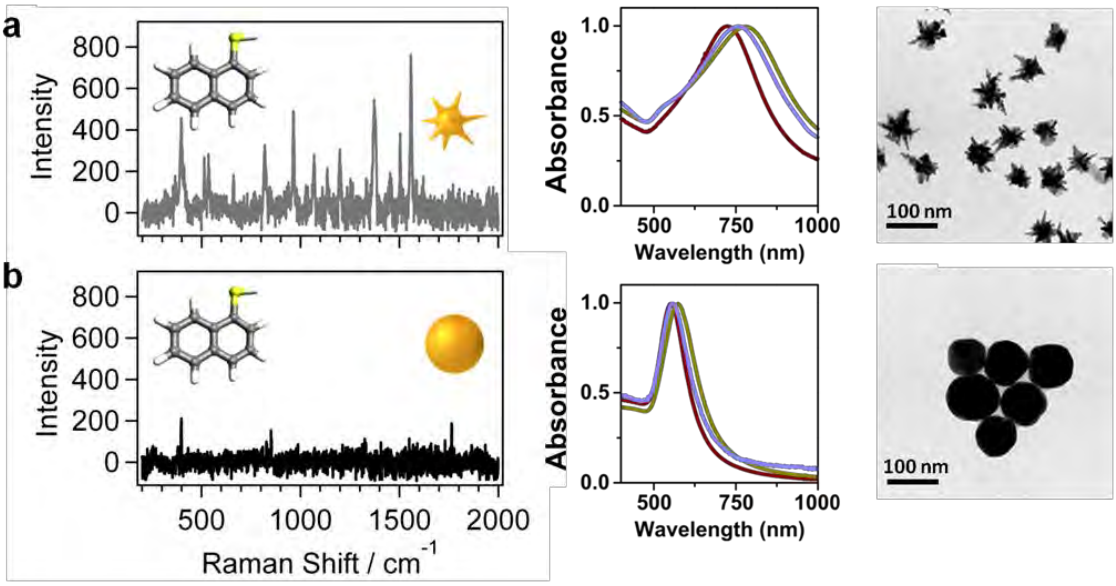

Figure 4.4. SERS spectra of 1-NaT encoded 50 nm AuNS@PMA (**a**) and 100 nm AuNP@PMA nanopheres (**b**) at 785 nm excitation. Also shown are the Vis-NIR spectra of the bare particles (blue), after 1-NaT functionalization in CH_3Cl (green) and after PMA coating (magenta) and the corresponding TEM images of the NPs codes.

In order to optimize the plasmonic nanoparticles, larger AuNSs of ~100 nm diameter and AuNSs synthesized by the PVP method[46] (**Figure 4.5**) were also studied. However, the intensity of the 1-NaT SERS spectrum was not significantly improved and therefore these different AuNSs were not used and all SERS experiments were performed using the original (~ 50 nm in diameter) AuNSs.

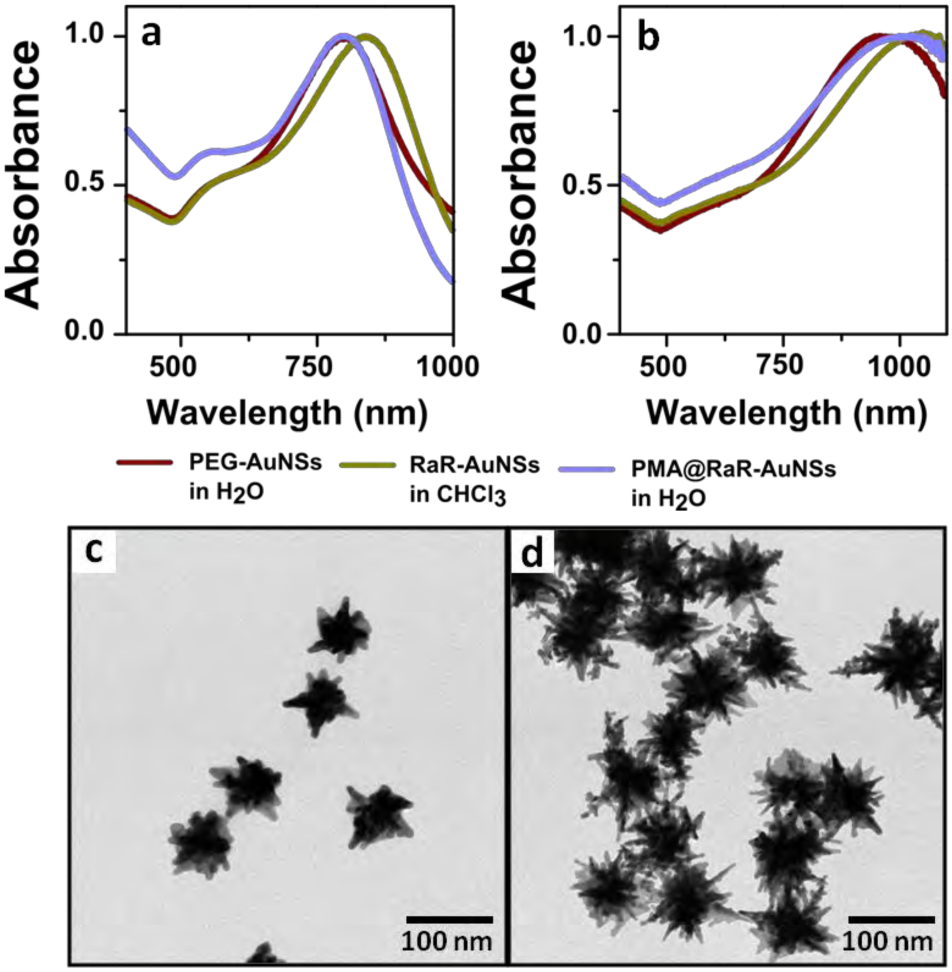

Figure 4.5. Normalized Vis-NIR spectra of AuNSs synthesized by the PVP method (**a**) and 100 nm surfactant free AuNSs (**b**) before codification and PEG stabilization (red), after coating with 1-NaT in $CHCl_3$ (green) and after PMA encapsulation in H_2O (blue). (**c**, **d**) Respective TEM images of AuNS@PMA.

SERS imaging of individual cell lines

Six AuNS@PMA samples were prepared, each encoded with a different thiolated dye as RaR (all concentrations were adjusted to $[Au^0] = 0.5$ mM). Shown in **Figure 4.6** are the SERS spectra of the AuNS-RaR@PMA labels represented by a corresponding color.

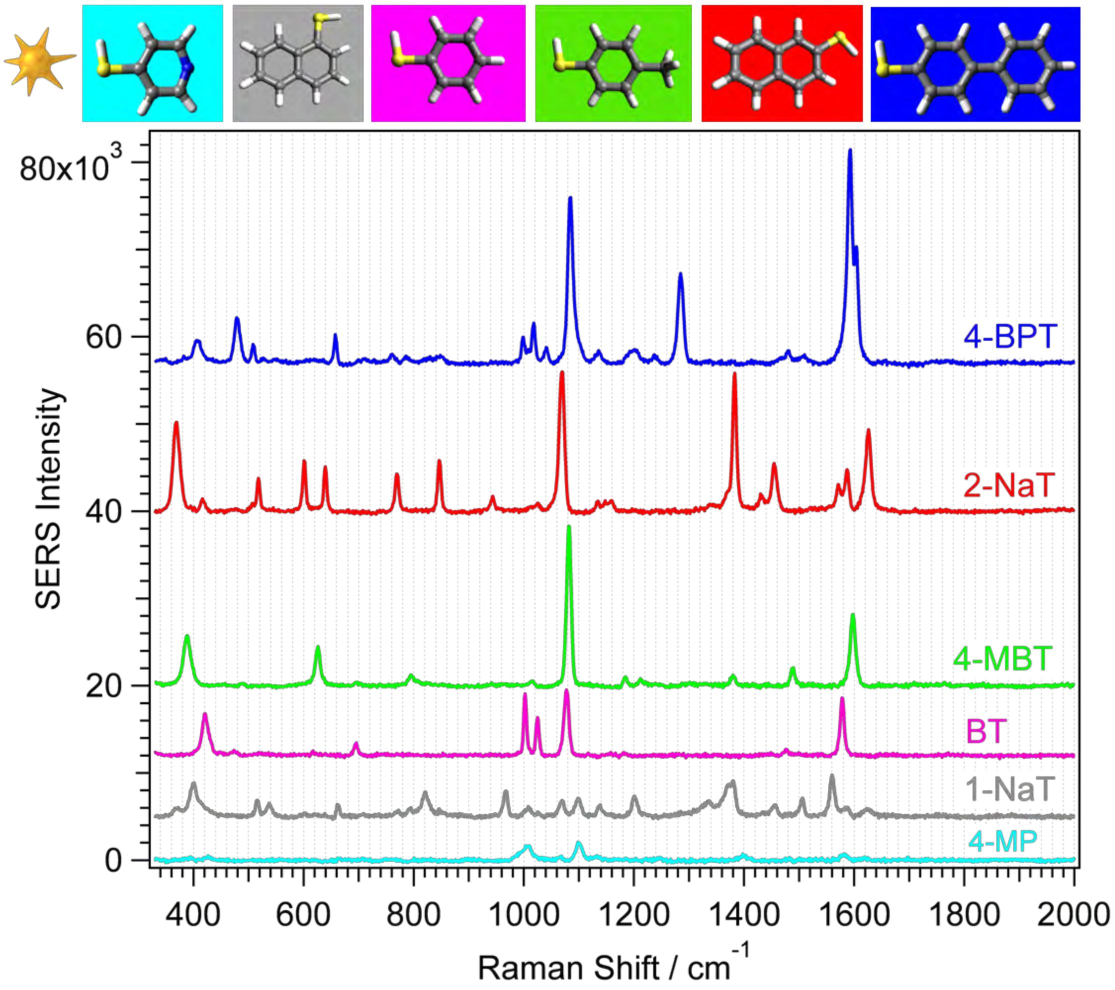

Figure 4.6. SERS spectra of six differently encoded SERS tags AuNS-RaR@PMA measured in solution under the following conditions: $[Au^0] = 0.5$ mM, $P_{laser} = 18.4$ mW for $\lambda_{ex} = 785$ nm and $t_{int} = 10$s with a 10× objective (NA = 0.35). Five scans were accumulated and averaged and an off-set applied for more convenient data representation. RaR 3D molecular structures created using the Avogadro Software package are presented on top of the figure and highlighted with the corresponding color.

SERS measurements of the AuNS-RaR@PMA tags reveal the complete fingerprint of the corresponding encoded RaR. It is important to note that no additional signals originating from the polymer were detected. A set of the most dominant vibrations together with the assignment for each RaR is despicted in **Table 4.1**. We observed in general that the highest SERS signal was generated by AuNS-4-BPT@PMA, followed by 2-NaT and 4-MBT codes, whereas one order of magnitude lower intensities were recorded from BT, 1-NaT and 4-MP. These differences are probably not only related to different molecular Raman cross sections, but also to variations of the density of molecules bound to the AuNS surface because of different RaR binding affinities to Au metal and to the different stability in the apolar organic medium.

RaR code	$\widetilde{\nu}_{vib}$ **/ cm^{-1} (in solution)**	$\widetilde{\nu}_{vib}$ **/ cm^{-1} (in cell)**	**mode assignment**
4-MP	1005	1015	Ring breathing
	1099		Trigonal ring breathing with C=S
		1131	C-H deformation
		1227	C-H in plane deformation
		1279	C-H in plane deformation
		1311	Not assigned
	1581		Ring stretch with nitrogen
1-NaT	820	822	Ring breathing
	967	965	C-H twist
	1070	1072	C-H bending
	1200	1200	C-H bending
	1367/1380	1365/1382	Ring stretching
	1505	1505	Ring stretching
	1560	1560	Ring stretching
BT	1002	1002	Ring out-of-plane deformation
	1025	1025	C–C symmetric stretching
	1077	1079	Ring in plane deformation
	1578	1578	C-C assimetric stretching
4-MBT	1083	1084	Ring breathing and C-H in plane bending combination
	1488	1487	Not assigned
	1597	1598	Ring stretching
2-NaT	640	641	Ring deformation
	769	770	Ring deformation
	846	850	C-H twist
	1070	1070	C-H bending
	1383	1382	Ring stretching
	1453	1454	Ring stretching
	1586	1587	Ring stretching
	1626	1625	Ring stretching
4-BPT	1084	1083	C-H bending
	1285	1284	Ring stretching
	1593/1604	1593/1603	Ring stretching

Table 4.1. Characteristic vibrations of 4-MP, 1-NaT, BT, 4-MBT, 2-NaT and 4-BPT measured from the SERS label in aqueous solution and after cell incubation and its assignment.

As a proof of concept for the applicability of our SERS tags for cell detection and differentiation, we studied the SERS performance of the AuNS-RaR@PMA labels in cells, namely in a macrophage continuous cell line with known phagocytotic abilities. J774 macrophages were individually treated with all six AuNS-RaR@PMA labels, keeping the NP concentration and incubation time constant for each system. After several washing steps the SERS spectra in the J774 cultures were analyzed, thereby providing an estimate of the uptake efficiency of AuNS-RaR@PMA. The observation of black dots within J744 in the transmission light images in **Figure 4.7** suggest the successful uptake of all SERS tags.

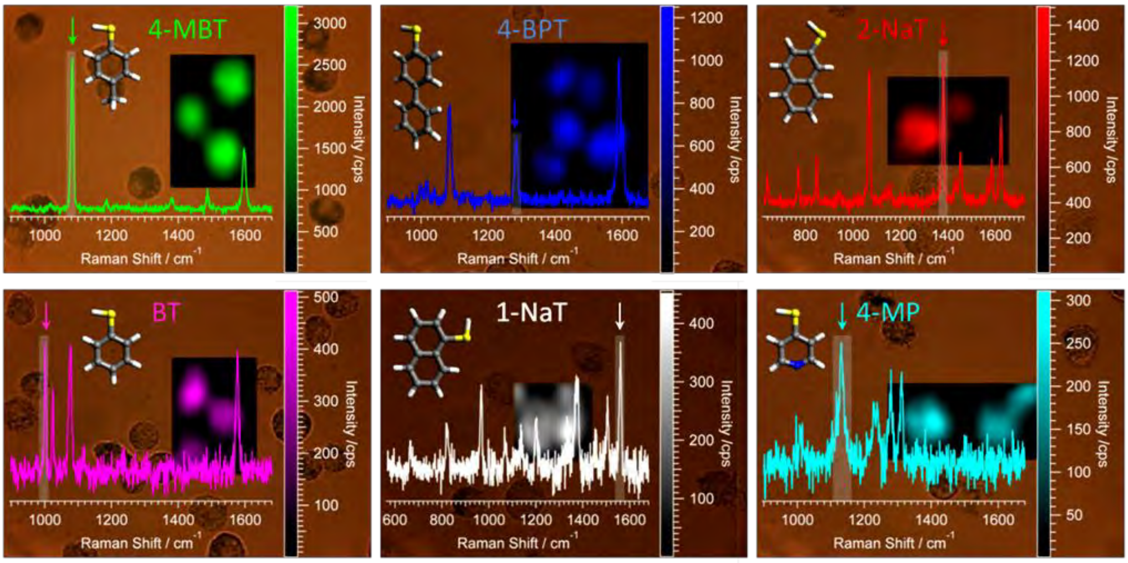

Figure 4.7. Optical and SERS images combined with the corresponding vibrational fingerprint spectra, for six different SERS tags incubated with J774 macrophages. The arrows indicate the specific signal used for the 2D SERS map generation: 1080 cm^{-1} (4-MBT), 1280 cm^{-1} (4-BPT), 1380 cm^{-1} (2-NaT), 1004 cm^{-1} (BT), 1580 cm^{-1} (1-NaT), and 1120 cm^{-1} (4-MP).

The images shown in **Figure 4.7** were obtained from samples individually incubated with each AuNS-RaR@PMA tag, and overlapped with RaR SERS images (colored map) of the same area and the corresponding vibrational fingerprint spectrum (curve of the same color). SERS maps were created by plotting the intensity of a specific vibration for each RaR, which is typically the most intense one (except for 4-BPT), namely 1080 cm^{-1} (4-MBT), 1280 cm^{-1} (4-BPT), 1380 cm^{-1} (2-NaT), 1004 cm^{-1} (BT) 1580 cm^{-1} (1-NaT), and 1120 cm^{-1} (4-MP). The same molecule-specific vibrations were applied for all subsequent SERS maps within this chapter, always using the same color for each code. From the SERS images we conclude that: i) the SERS signal is only detected from those areas where cells are present and no signal is found from free tags in solution or attached to the glass support; ii) although the intensity can strongly vary due to the distribution of accumulated tags, SERS signal can be detected from all the measured cells indicating efficient uptake; iii) the SERS spectra of the RaRs are not affected by attachment to the cell surface or by endocytosis (except 4-MP); iv) the variation of RaR intensity measured from J744 follows the same trend as that detected from free NPs in solution, with one exception (4-MBT exhibits the strongest signal from J744); and v) the SERS tag signal is stable over a time span of at least 3 h after addition to cells. The application of AuNS-RaR@PMA labels is not only restricted to J774 cells but can also be used with other cell lines. RaR signals were successfully detected in cells of different tissue origin, for example, A549, MCF-7 and HUVEC combined with BT, 2-NaT and 4-BPT, respectively (**Figure 4.8)**

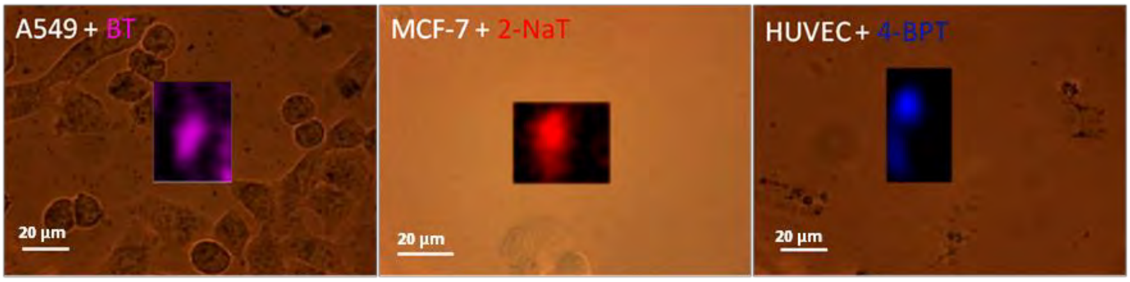

Figure 4.8. SERS imaging of cancer cells by mapping one characteristic vibrational frequency: A549, MCF-7 and HUVEC using AuNS@PMA loaded with BT, 2-NaT and 4-BPT, respectively.

Differentiation of breast cancer cells

The final goal of this work is to differentiate various types of breast cancer cells by SERS bio-imaging. As the successful detection of the cell is strongly dependent on the nanotag loading, we first studied the uptake of SERS tags by means of (confocal) fluorescence imaging using PMA fluorescently labeled with TAMRA (PMA_{TAMRA}), during AuNS-code preparation. Breast cancer cells from the lines HCC1395, SK-BR3, MDA.MB.435S, CAMA-1 and MCF-7 were incubated overnight with BT-$AuNS@PMA_{TAMRA}$, at a final Au^0 concentration of 0.1 mM. All cells showed strong levels of uptake and z-stacks confirmed intracellular presence, with limited membrane bound AuNSs after intensive washing of non-endocytosed material (**Figure 4.9**).

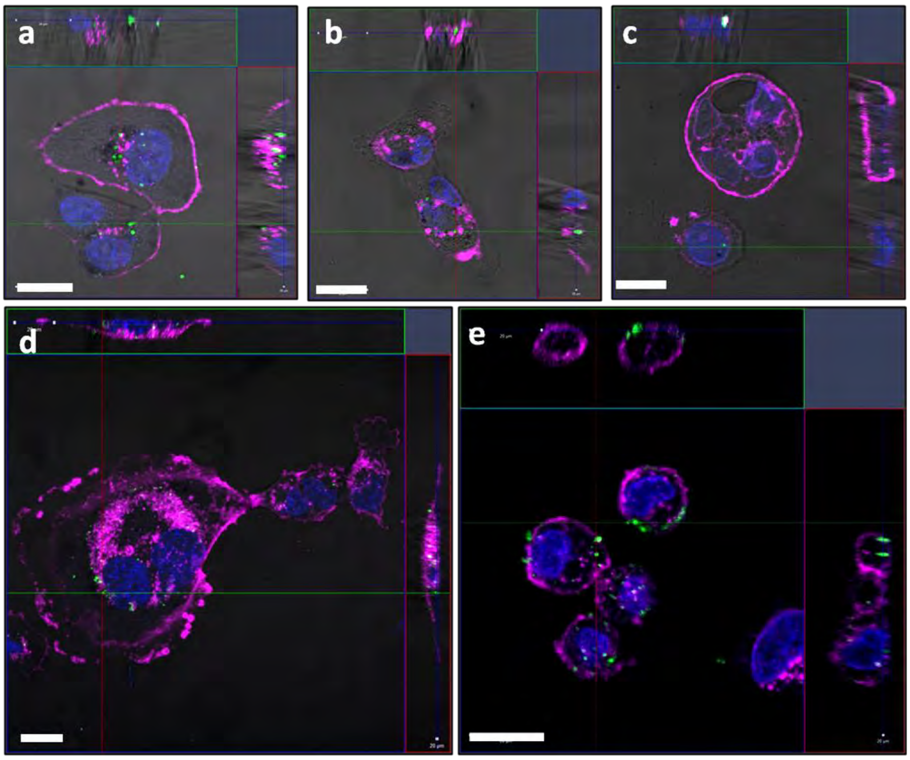

Figure 4.9. Z-stack images taken using a Zeiss confocal to show nanoparticle uptake in MCF-7 (**a**), MDA.MB.435S (**b**), CAMA-1 (**c**), HCC1395 (**d**) and SK-BR3 (**e**). Cells are stained with DAPI (blue; nucleus) and WGA647 (pink; membrane). AuNS-BT@PMA$_{\text{TAMRA}}$ particles were false-colored green to show contrast. Scale bars 20µm.

As some cells appeared to show higher levels of uptake, these were paired post-analysis with SERS tags expressing weaker Raman signals, and *vice versa*. At this time, breast cancer cells were incubated with non-fluorescent AuNS-RaR@PMA tags under the same conditions and after thorough washing of non-endocytosed particles, cells were transferred to quartz glass slides for both single and quintuple SERS measurements, meaning single-call and five-cell co-cultures respectively. To demonstrate the all-purpose application of these SERS nanotags, we used two different sets of cell-RaR combinations (herein called C1 and C2) for bioimaging and for cell differentiation experiments (see **Table 4.2**).

	Cell type				
Set	**SK-BR3**	**HCC1395**	**MCF-7**	**CAMA1**	**MDA.MB.435S**
C1	1-NaT	BT	4-BPT	4-MBT	2-NaT
C2	4-BPT	4-MBT	2-NaT	BT	1-NaT

Table 4.2. Sets C1 and C2 for the combination of breast cancer cells with AuNS-RaR@PMA.

Figure 4.10 shows the 2D SERS maps for C1. We clearly see that the RaR SERS is present for the five cell types but the intensity can strongly vary for each cell and each RaR molecule. In a few cases unbalanced nanotag uptake can lead to some cells being (almost) undetectable by SERS (see SK-BR3 with the low-intensity 1-NaT and CAMA-1 with the high-intensity 4-MBT in **Figure 4.10**). To evaluate the detection probability of specific cell lines, statistical SERS measurements (one spectrum per cell = single-point maps) of at least 30 individual cells per line were performed. The blue-colored dots shown in the bottom-right image of **Figure 4.10** indicate that 4-BPT was detected from 98% of measured MCF-7 cells, with SERS intensities ranging from 0 (black) to 200 cps (bright blue).

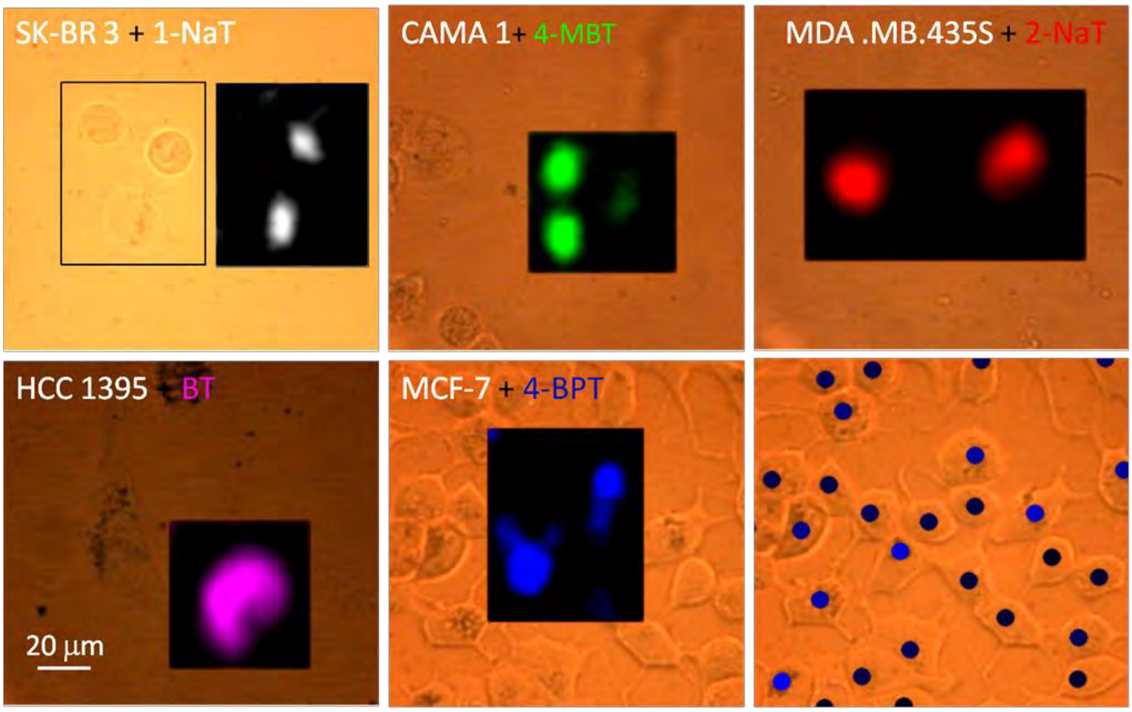

Figure 4.10 Correlated transmited light and SERS images of breast cancer cells corresponding to the cell-RaR combination C1. Statistical SERS measurements by single-point SERS mapping (last image) allow a fast analysis of cell detection efficiency (here: 4-BPT is found in 98% of measured MCF-7 cells).

SERS imaging of the single-cell C2 cultures is found to be qualitatively similar to that for S1 (**Figs. 4.11a**, **4.12a** and **4.13a**). Single point SERS mappings with more than 30 cells per culture analyzed for the complete set C2 revealed that, 48% of SK-BR3, 94% of CAMA1, 97% of HCC1395, and 78% of both MCF-7 and MDA.MB.435S, could be identified by the characteristic label vibrations previously selected from J744 test samples in **Figure 4.7** (selected images in **Figs. 4.11b**, **4.12b** and **4.13b**). The corresponding reference spectra were taken from the single cell measurements of C2 (**Figure 4.13c**). Subsequently, the cells were observed to survive for at least 48 h under optimal conditions (medium, 37 ºC, 2% CO_2), indicating the low toxicity of the tags. Interestingly, no RaR signal was detected outside of the cells even after 24 h, suggesting high AuNS-RaR@PMA and RaR stability, as well as a low rate of digestion or exocytosis of AuNS-RaR@PMA.

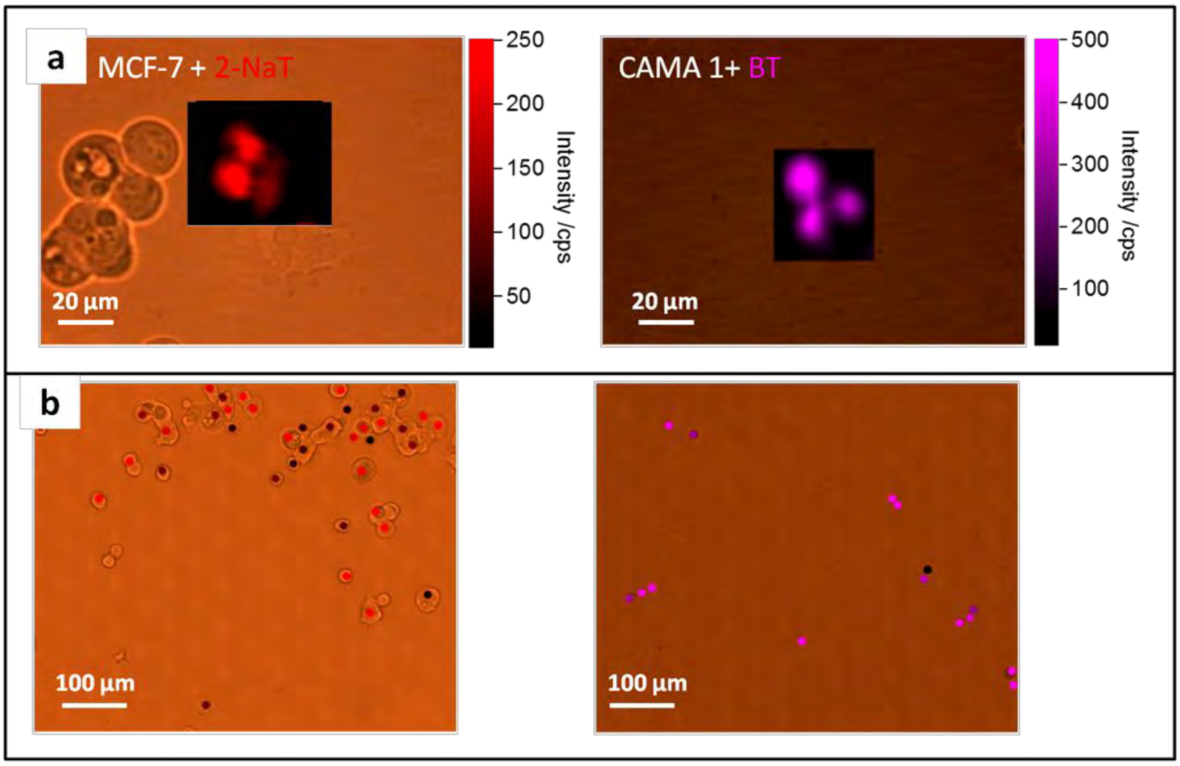

Figure 4.11. (**a**) SERS imaging of individual MCF-7 and CAMA1 using 2-NaT and BT encoded AuNS@PMA tags, respectively. (**b**) Corresponding large area point mappings. Note that the black dot in the CAMA1 sample in (**b**) is not measured outside of the cell area.

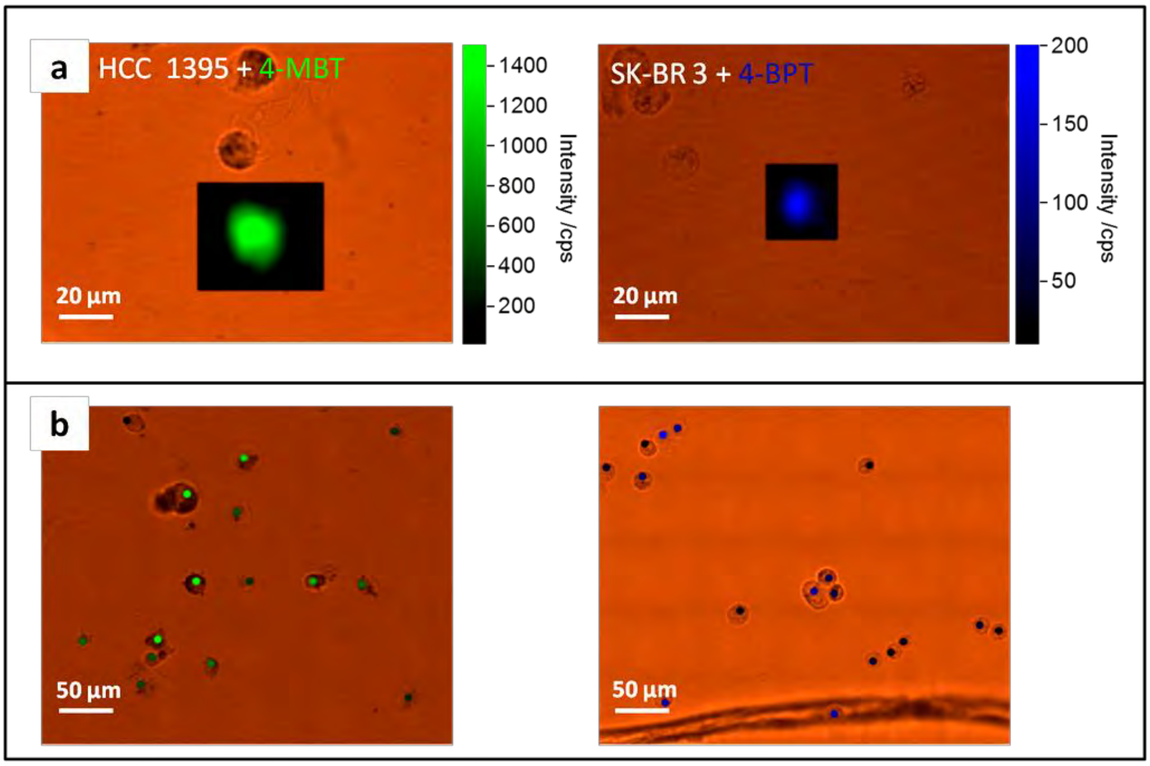

Figure 4.12. (**a**) SERS imaging of individual HCC1395 and SK-BR3 cells using 4-MBT and 4-BPT encoded AuNS@PMA tags, respectively. (**b**) Corresponding large area point mappings.

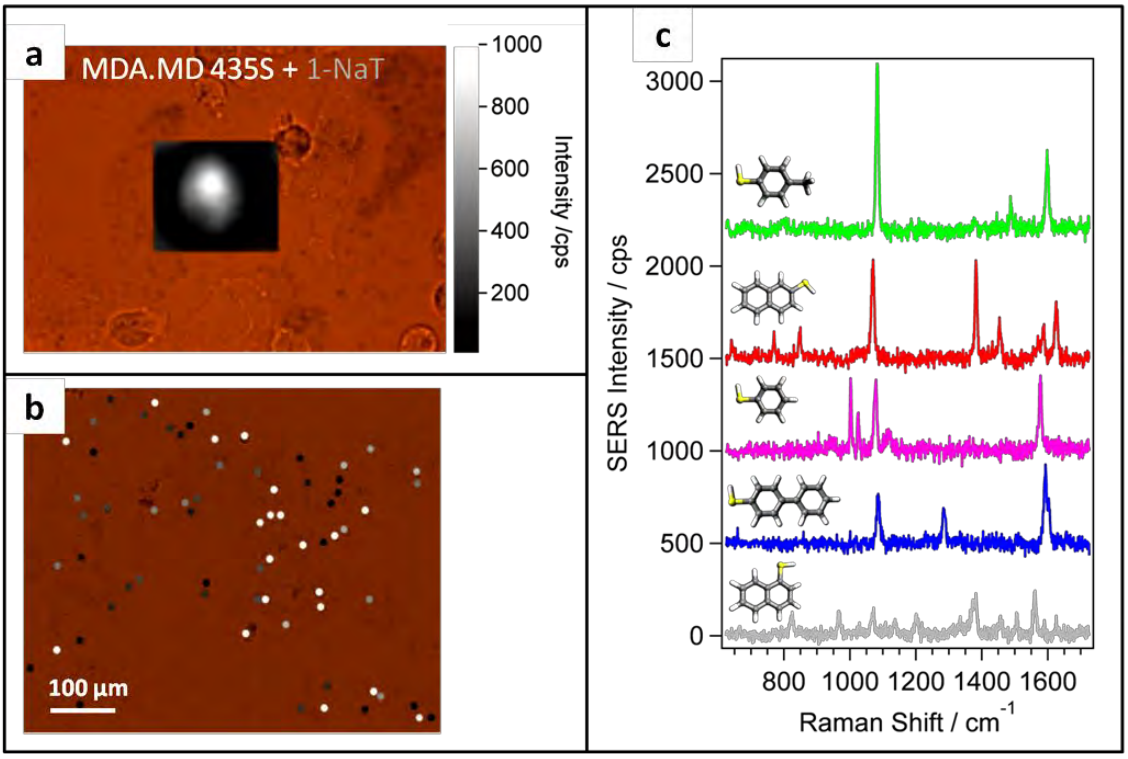

Figure 4.13. SERS imaging of an individual MDA.MD.435S cell using 1-NaT encoded AuNS@PMA tags. (**b**) Corresponding large area point mapping. (**c**) Typical single SERS spectrum of each RaR obtained from samples in **Figs. 4.11 - 4.13**.

The ultimate challenge in this work was imaging of a ***quintuple*** breast cancer cell co-culture, aiming at differentiation of all different cells on the basis on their AuNS-RaR@PMA uptake. A large-scale SERS map of a sample containing *ca.* equal parts of the five cell types, preincubated with their relevant encoded AuNS-RaR@PMA tags, was recorded and the spectra were analyzed using the Wire 3.4 software provided by Renishaw. In contrast to the single cell images, each spectrum was compared with the whole fingerprint spectrum obtained from the single cell samples as references (**Figure 4.14c**), assigned to the relevant RaR compound and plotted with the previously defined RaR color code. In **Figure 4.14a**, the so-created SERS image shows then the composition of the scanned area. We can clearly differentiate five RaRs corresponding to the presence of the different breast cancer cells within the scanned area. As observed from the single-cell cultures, the SERS signal was detected exclusively in the areas occupied by cells.

To evaluate the reliability of the differentiation method and to quantify larger areas of the cell mixture, we analyzed three different positions of the sample measuring individual cells by single-point SERS mapping. The result of the SERS composition image of the largest area (0.12 mm^2) containing 250 cells is shown in **Figure 4.14b**. The detailed conclusion of quantitative composition is given in **Table 4.3**, which shows that 87% of the total amount of measured cells could be unambiguously differentiated, whereas 2% show a SERS signature corresponding to a superposition of two different RaR codes (see white- and red-encircled blue dots in **Figure 4.14b**) This could happen when two cells are not well separated or one cell sits on top of another. The exocytosis of nanotags by one cell and the endocytosis by another cell type is another possible but less likely scenario because a critical tag accumulation is required for SERS signal generation. Finally, 11% of the cells do not show assignable SERS signal due to ineffective nanoparticle loading.

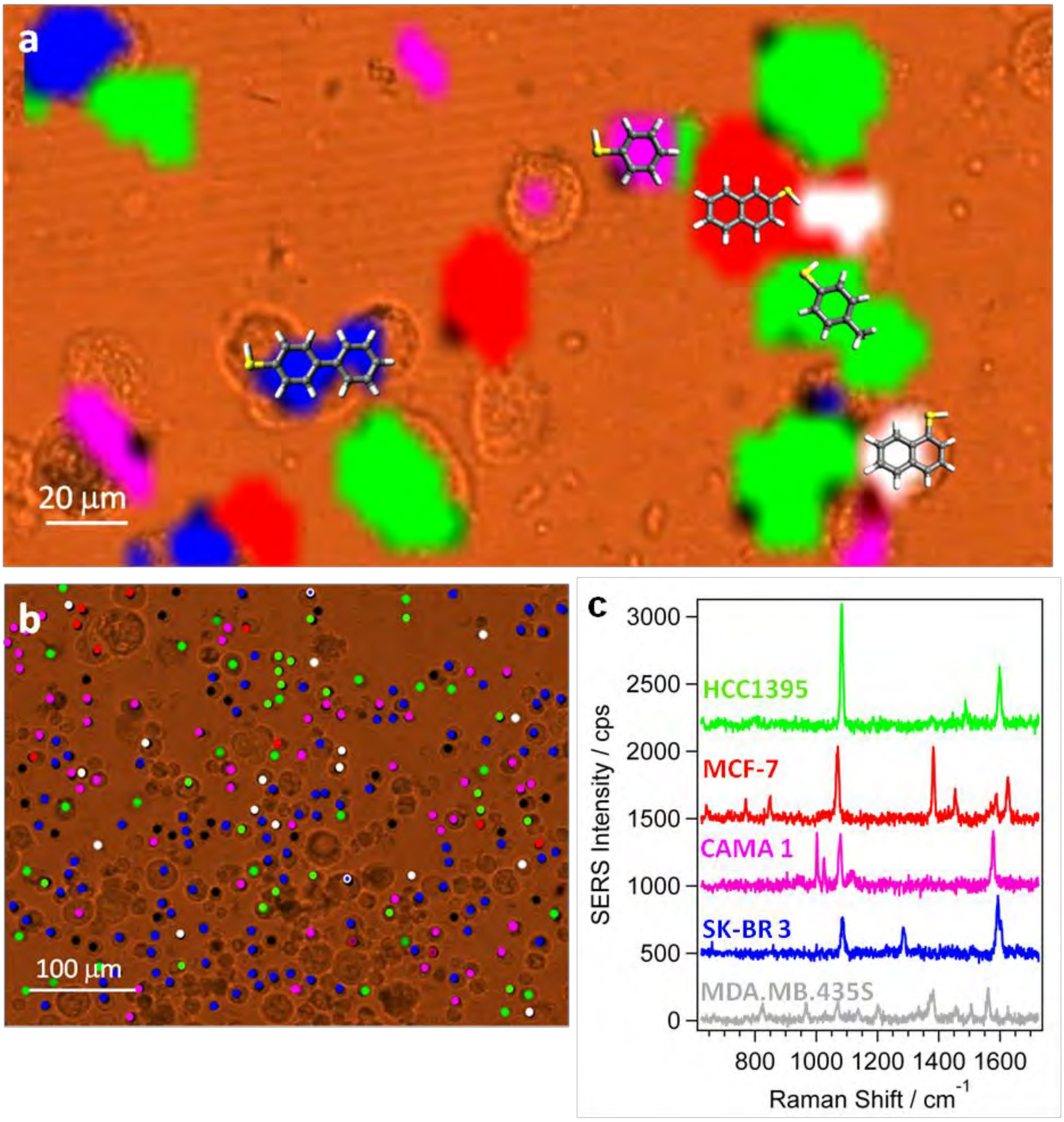

Figure 4.14 Compositional assignment of a quintuple cell mixture using RaR labelled SERS nanotags. Bioimaging of the cell mixture (**a**), large-scale SERS point mapping to quantify the composition of 250 cells within an area of 0.12 mm^2 (**b**) using the reference RaR fingerprints obtained from single cell cultures (**c**).

Assigned cell type (87%)					**Not assigned cell type (13%)**	
SK-BR3	**HCC1395**	**MCF-7**	**CAMA 1**	**MDA.MB.435S**	**Ambiogous**	**No Signal**
37%	19%	4%	20%	6%	2%	11%

Table 4.3 Quantitative SERS analysis of the percentage of cells containing RaR-AuNS@PMA, using the combination C2 detailed in **Table 4.1**.

4.4 Conclusions

We report a straightforward protocol for the preparation of highly stable and biocompatible SERS-encoded AuNSs. The codification method is based on the general solvent-exchange procedure explained in the previous chapter of this thesis. Therefore, it can be extended to nanoparticles of different sizes, shapes and composition, and to the use of different Raman active molecules. PMA is employed to confer particle solubility and stability under biological conditions, whereas the spiky AuNS structure is preserved upon passivation of the gold surface *via* thilated RaR binding. NIR absorbing AuNS codes appear to be ideal SERS-labels in bioapplications, as we demonstrated by performing SERS bioimaging of different cells lines incubated with different encoded AuNS@PMA. Furthermore, we successfully distinguished between five types of breast cancer cells that were mixed after internatization of the highly efficient SERS tags. The results confirm the reliability and multiplexing capability of the SERS-encoded AuNSs. This rapid and feasible SERS-based method could be applied to specifically target different cancer cells, thereby allowing and improving disease dectection at early stages.

CHAPTER 5

Gold Nanostar-coated Polystyrene Beads as Bifunctional Nanoprobes for *in vivo* Cell Multimodal Imaging

ABSTRACT

Hybrid colloidal nanocomposites comprising fluorescent polystyrene beads and gold nanostars are reported as bifunctional nanoprobes for bioimaging. These assembled nanostructures are excellent Raman enhancers due to plasmon features in the near infrared biological transparency window region. Using 4-mercaptobenzoic acid as a Raman-active molecule, we compared the SERS response of polystyrene beads loaded with different Au nanostar densities and showed that intermediate nanostar loadings lead to superior SERS performance, which could be readily detected *in vitro* in cell cultures. In addition, the efficient combination of both fluorescence and SERS activity in the same nanostructured particle opens up possibilities for application in multimodal bioimaging.

5.1 Introduction

Surface enhanced Raman scattering (SERS) imaging is a novel modality of Raman microscopy that is gaining increasing attention due to its numerous advantages, as described in the previous chapter of this PhD. thesis. This technique merges well known concepts from both fluorescence and conventional Raman imaging, but overcomes the limitations (e.g. photobleaching, narrow excitation with broad emission profiles and peak overlap) of using conventional dyes or quantum dots (QDs).[99,136] Therefore, the design of new and multifunctional SERS nanoprobes that combine metal nanoparticles and specific Raman labels/reporter molecules is an important research area that is gaining popularity in the biological field.[124,274] Besides the many studies reported to date, the fabrication of multifunctional nanoprobes that integrate two of more functionalities still remains challenging. For instance, fluorescence is often quenched when a dye is adsorbed very close to the metal surface, often giving rise to surface enhanced resonance Raman scattering (SERRS).[275] Plasmon enhanced fluorescence can also occur, but it is affected by multiple parameters such as metal nanoparticle size, and shape as well as the distance between the fluorophore and the plasmonic surface.[276,277] The incorporation of fluorescence and SERS activity in the same nanostructure entity constitutes an elegant approach that allows independent tracking and imaging of objects using these two different optical tools. Depending on the application, important issues such as the slow SERS imaging speed could be successfully resolved.[278] Fluorescent-SERS tags can be generated in various ways. For example, Cho and co-workers developed specific fluorescent-SERS dots composed of silica spheres containing silver nanoparticles, fluorescent dyes and specific Raman labels. Silica encapsulated SERS nanoparticles were labeled with organic dyes and by adjusting the silica shell thickness so that fluorescence quenching was prevented.[279] Au NP aggregates tagged with Raman reporters were also coated with silica and water-soluble CdTe QDs, and then used as fluorescent-SERS switchable probes for imaging of living cells.[280] Interestingly, *in vivo* imaging was first demonstrated using Au nanorods (AuNRs) functionalized with NIR fluorescent dyes.[281] In general, these bimodal imaging methods have significant advantages such as real-time, high contrast imaging and deep detection ability in tissues.

We developed a simple method to fabricate fluorescent-SERS nanoprobes that can be employed to image living cells. Such bifunctional probes are colloidal nanocomposites made of a fluorescent polystyrene (PS) particle as matrix, onto which star-shaped gold nanoparticles (Au nanostars, AuNSs) were assembled. Similar hybrid nanomaterials have been used in the past to achieve enhanced optical, magnetic and catalytic properties.[282–285] PS-based are known as plasmonic supports with high robustness, easy manipulation, resistance to particle aggregation and they can additionally display high SERS activity.[286] PS is additionally one of the most commonly used polymeric materials due to its low toxicity, high stability in water and easy synthesis and surface functionalization.[287] The synthetic procedure for the preparation of PS spheres coated with metal nanoparticles usually involves two different approaches. Metal particles can be grown *in situ* onto the PS microsphere surface, yielding gold nanoparticles of different sizes by simply adjusting the amount and type of reducing agent, or the concentration of PS microspheres.[288] A similar strategy employs aniline-modified PS beads where not only the size but also the morphology of the AuNPs can be tuned, by modifying the gold salt concentration.[289] Silver nanoparticle-PS composites can also be prepared by the reduction of $[Ag(NH_3)_2]^+$ complex ions onto poly-dopamine modified PS surfaces.[290] Differently charged PS beads have been used to deposit AgNPs by reduction with ascorbic acid,[291] whereas poly(styrene-co-acrylic acid) (PSA) microspheres were covered with AgNPs using polyvinylpyrrolidone (PVP) as a reducing agent, which additionally facilitated further encapsulation with silica shells.[292] Various structures of semishell, nano-crescent or nanoshells can be obtained with the direct overgrowth of gold on hybrid colloidal dimers consisting of Au and PS nanoparticles.[293]

The second approach for the preparation of metal NPs-PS composites requires to synthesize first the NPs and then assemble them onto a modified PS surface, which typically allows better control over the desired size and shape of the NPs. Thus, to specifically attach AuNPs with sizes ranging from 1 to 20 nm, PS beads have been functionalized with thiol-terminated groups.[294] Amino-functionalized PS spheres have also be coated with different PVP-stabilized metal nanoparticles (Pd, Pt and FePt NPs) under acidic conditions.[295] The same approach was applied to assemble AuNRs capped with PVP and sodium dodecyl sulfate (SDS), with a fine control over the obtained surface coverage.[296] Therefore, taking advantage of the enormous possibilities of this approach, complex anisotropic gold nanostructures, such as AuNSs have been successfully adsorbed onto fluorescent PS bead surfaces. The Raman reporter molecule 4-mercaptobenzoic acid (4-MBA) was used to compare the relative SERS response for nanocolloids presenting different AuNS loading densities. As an example of application, multimodal imaging of live human lung cancer cells was performed using SERS, fluorescence and dark field optical microscopy. Furthermore we observed that the SERS signal inside the cells could be further increased by incorporating a particular type of small AuNP carrying two different capping ligands, known as rippled AuNP (rAuNP), which have been reported to increase cell uptake due to their high cell membrane affinity.[297] We present these novel nanostructures as non-toxic and biocompatible imaging contrast agents with interesting properties regarding SERS applications that notably improve the capabilities of isolated AuNSs for *in vitro* cell imaging.

5.2 Experimental Section

Materials

Milli-Q water (resistivity 18.2 MΩ·cm) was used in all experiments. Hydrogen tetrachloroaurate trihydrate ($HAuCl_4 \cdot 3H_2O$, ≥99.9%), sodium citrate tribasic dihydrate (≥98%), silver nitrate ($AgNO_3$, ≥99%), L-ascorbic acid (AA, ≥99%), O-[2-(3-mercaptopropionylamino)ethyl]-O'methylpolyethylene glycol (PEG-SH, Mw 5,000 g/mol), 4-mercaptobenzoic acid (4-MBA, 90%), were purchased from Sigma-Aldrich. Hydrochloric acid solution (HCl, 37%) was purchased from Panreac. Fluorescently labeled amino-functionalized PS beads ($\lambda_{ex}/\lambda_{em}$= 477nm/519nm; NP size 483±3 nm) were purchased from IKERLAT polymers. Non-labeled carboxylic acid-functionalized PS beads were a gift from the same company. All glassware was washed with aqua regia, rinsed 3-fold with milli-Q water and dried before use. A549 cells were kindly provided by Dr. Sergio Moya (CIC biomaGUNE, Donostia-San Sebastian). Dulbecco´s Modified Eagle´s Medium (DMEM), Fetal Bovine Serum (FBS), 1% Penicillin-Streptomycin (PStrep), Trypsin-EDTA, Wheat Germ Agglutinin-AF647 (WGA647) and 4′,6-Diamidine-2′-phenylindole dihydrochloride (DAPI) were purchased from Invitrogen. MTT cell proliferation kit was purchased from Roche.

Sample characterization

Transmission electron microscopy (TEM) images were collected with a JEOL JEM-1400PLUS microscope operating at 120 kV, using carbon coated 400 square mesh copper grids. HAADF-STEM images and electron tomography tilt series were acquired at the University of Antwerp by the group of Prof. Sara Bals, using a double aberration corrected cubed FEI Titan 50-80 electron microscope operated at 300 kV. For the reconstruction of the series we used the SIRT algorithm, as implemented in the ASTRA toolbox.[298] Vis-NIR optical extinction spectra were recorded using an Agilent 8453 UV-Vis diode-array spectrophotometer.

Synthesis and assembly of gold nanostars

AuNSs were prepared by a modified seed-mediated growth method.[50] Briefly, the seed solution was prepared by adding 5 mL of a 1 % citrate solution to 95 mL of boiling 0.5 mM $HAuCl_4$ solution under vigorous stirring. After 15 min of boiling, the solution was cooled down to room temperature and then kept at 4 °C for long-term storage. The as-synthesized Au nanoparticle seeds had an LSPR maximum at 519 nm. For Au NS synthesis, 500 µL of the citrate-stabilized seed solution were added to 10 mL of $HAuCl_4$ (0.25 mM) solution containing 10 µL of HCl (1.0 M) in a 20 mL glass vial at room temperature under moderate stirring. Quickly, 100 µL of $AgNO_3$ (3 mM) and 50 µL of AA (100 mM) were added simultaneously to the above solution, which rapidly turned from light red to greenish indicating the formation of AuNSs. Immediately after synthesis, the solution was stirred with PEG-SH (final concentration $7 \cdot 10^{-7}$ M) for 15 min, washed by centrifugation (1190 g, 25 min, 10 °C) and redispersed in water. The Au^0 concentration of the AuNS solution was adjusted to 0.5 mM. To form AuNS-PS assemblies, 1mL of PEG-stabilized AuNS solution 0.5 mM was added dropwise onto 100 µL of PS colloid in an eppendorf tube under sonication and the particle mixture was incubated overnight. Three different initial PS concentrations (0.15, 0.3 and 1.0 % in solids) were used to obtain *high*, *medium* and *low* AuNS loading, respectively. The unbound AuNSs were removed by two centrifugation steps (1770 g, 3 min, 20 °C) and the samples were redispersed in Milli-Q water adjusting the concentrations to $1.5 \cdot 10^{-2}$ (PS, % in solids).

Synthesis and assembly of rAuNP

Amphiphilic small gold nanoparticles co-functionalized with hydrophobic and hydrophilic thiolated alkanes, known as rippled AuNPs (rAuNP), were synthesized using a slightly modified version of the Brust-Schriffin method.[299] 0.9 mmol of $HAuCl_4$ was dissolved in 150 mL of ethanol and then 0.9 mmol of a mixture of mercaptoundecane sulfonate and 1-octanethiol (2:1) was added while stirring the reaction mixture, then a saturated ethanol solution of $NaBH_4$ was added dropwise for 2 h. The solution was stirred for 3 h and the reaction vessel was then placed in a refrigerator overnight. Precipitated particles were collected via vacuum filtration with quantitative filter paper. NPs were washed with ethanol, methanol and acetone and dried under vacuum. To completely remove unbound ligands, particles were dialyzed using 59 segments of cellulose ester dialysis membrane (Pierce, SnakeSkin, MWCO 3500) that were placed in 1 L beakers of Milli-Q water and stirred slowly. The beakers were recharged with fresh water *ca.* every 8 h over the course of 72 h. The NP solutions were collected from the dialysis tubes, and the solvent was removed under vacuum at <45 °C. For AuNS-rAuNP-PS assembly, 1 mL of the as-assembled AuNS-PS beads was incubated overnight with 0.25 mL of rAuNP 0.8 mM. The particles were centrifuged twice (1770 g, 5 min, 20 °C) to remove free rAuNP and the concentration of PS was adjusted to be $1.5 \cdot 10^{-2}$ (% in solids).

Synthesis and assembly of citrate gold nanoparticles (AuNP). Growth of gold tips on AuNP-PS particles

Small citrate gold nanoparticles (AuNPs) displaying LSPR maximum at 519 nm and average size around 14 nm were prepared by adding 5 mL of 1% citrate solution to 95 mL of boiling 0.5 mM $HAuCl_4$ solution under vigorous stirring. After 15 min of boiling, the solution was cooled down to room temperature and then kept at 4 °C for long-term storage.[300] 1mL of the as-synthesized AuNPs was added onto 0.1mL of PS beads (2.5% in solids). Unbound AuNPs were removed by two centrifugation steps (1770 g, 5 min, 20 °C) and the precipitate was redispersed in 1 mL of milli-Q water. 100 μL of these AuNP-coated PS beads was used in a typical 10 mL nanostar synthesis as seeds to growth Au tips.[50]

Synthesis and assembly of PVP-coated gold nanostars and silver nanoparticles (AgNPs)

PVP-coated AuNSs were synthesized as previously reported.[46] In a typical synthesis 82 μL of an aqueous solution of 50 mM $HAuCl_4$ was mixed with 15 mL of 10 mM PVP solution in DMF. After 20 minutes, 43 μL of a preformed dispersion of 15 nm PVP-coated Au seeds in ethanol ($[Au^0]$ = 4.2 mM) was added and within five minutes the solution color changed from pink to blue, indicating the formation of gold nanostars. The particles were purified by centrifugation (4 times, 1770 g, 60 min, 20 °C) and redispersed in water. The concentration of Au^0 was adjusted to 0.5 mM and the assembly onto the PS surface was carried out as explained above. AgNPs with LSPR at 420 nm were synthesized following a published method.[209] A 100 mL volume of an aqueous solution containing sodium citrate (5 mM) and tannic acid (TA) 2 mM was prepared and heated with a heating mantle in a three-neck round bottomed flask for 15 min under vigorous stirring. A condenser was used to prevent evaporation of the solvent. After boiling had commenced, 1 mL of $AgNO_3$ (25 mM) was injected into this solution. The solution became bright yellow immediately. The particles were washed by centrifugation (2 times, 6000 rpm, 30 min, 20 °C) to remove excess TA and then redispersed in sodium citrate 1.1 mM. 1 mL of as-purified AgNPs was added dropwise onto 100 µL of PS beads (0.15 % in solids) under sonication and the samples were incubated overnight. Unbound AgNPs were removed by two centrifugation steps (1770 g, 5min, 20 °C).

Cell culture

Human lung epithelial cancer cells (A549) were grown in DMEM supplemented with 10% FBS and 1% PSstrep (known as cDMEM). Cells were passaged using Trypsin-EDTA. For SERS, confocal and dark field microscopy, between $5\cdot10^4$ to $2\cdot10^5$ cells were plated in glass bottomed dishes with marked grids (“Grid-50”, Ibidi) and allowed to adhere overnight. Fluorescently labeled AuNS-PS particles were added to cells at a final concentration of PS (% in solids) from $7.5\cdot10^{-4}$ to $3.75\cdot10^{-4}$, depending on the experiment setup, and left for various timepoints at 37 °C to allow particle uptake.

Confocal and dark field microscopy

Particle uptake in A549 cells was imaged using a Zeiss LSM Confocal microscope with 477 nm excitation and a 500-550 nm BP filter. Either 40x (numerical aperture, NA=1.3) or 63x (NA=1.4) objectives were used. Multichannel (transmission and fluorescence) Z-stacks were taken using ZEN software. For darkfield images, cells were fixed using 4% formaldehyde (20 min, room temperature) and mounted using a #1.5 coverslip and mounting fluid (Dako). Once dry, the dish was inverted and viewed using a Nikon Eclipse Ti-U microscope equipped with a 60x (NA=0.7) objective and oil condenser. A neutral density (ND) and neutral colour balance (NCB) filter were inserted. Photos were taken using 0.1 s exposure and light intensity levels and other variables were unchanged for the different samples.

Cell viability

Nanoparticle induced cytotoxicity was measured using the MTT assay. A549 cells were plated in 96 well plates at $1 \cdot 10^4$ cells/well and allowed to adhere before adding NPs at final PS concentrations ranging from $1.5 \cdot 10^{-3}$ to $9.4 \cdot 10^{-5}$ % in solids Cells were incubated for 66 h before removal of the cell media and addition of MTT reagent (1/20 dilution in cDMEM). Cells were incubated for 1.5 h at 37 ºC followed by removal of the supernatant and addition of DMSO to lyse cells. Absorbance was read at 550 nm and cell viability calculated as a percentage of the control.

SERS measurements

SERS was measured with a confocal Raman microscope (Renishaw inVia) equipped with 1024×512 CCD detectors using a 785 nm laser excitation source (maximum output of 250 mW) and a 1200 l/mm diffraction grating. For reference and test SERS experiments, 1 mL of 4-MBA labeled AuNS-PS beads (*low*, *medium* and *high* AuNS loading, final 4-MBA concentration 1 mM) was placed in a 1 mL glass vial (ThermoFisher) and spectra were collected using a 10× objective (NA=0.35) in expanded scan mode with an integration time of 10 s and a laser power of 11 mW. SERS measurements in cells were carried out in static mode (center of scattered wavenumber 1200 cm^{-1}) with an integration time of 1s and a laser power of 15 mW using a water immersion 40x objective (NA=0.85). For SERS imaging of cells the spectra were measured on a grid with a point distance of 2 μm in x- and y directions. The maps were generated by plotting the intensity of the 4-MBA ring stretch vibration at 1080 or 1580 cm^{-1} as a function of grid position. The average laser powers were measured in air after passing the laser beam through the objectives used in the corresponding experiments by means of a photodiode sensor (PD300-3W) and a power meter (Nova, both from Ophir).

5.3 Results and Discussion

Monodispersed PS beads coated with AuNSs were prepared using a two-step procedure: first, PEG-coated AuNS were synthesized through a well-known seed-mediated growth method and were subsequently assembled onto the PS beads surface. This strategy leads to particularly stable nanostructures and allows suitable control over the final plasmonic performace. It is important to mention that, when Au nanosphere-coated PS beads were use as seeds to directly growth gold tips, aggregated and non-uniform particles were obtained whereby branched structures of different sizes and shapes protrude from the polymer surface (**Figure 5.1a**). Therefore, production of a homogeneous assembly with a high degree of monodispersity required the attachment of pre-synthesized AuNSs onto the amine-functionalized PS bead surface (**Figure 5.2**). As previously reported, when carboxylic acid-functionalized PS spheres were used, AuNSs did not interact with the polymer surface (**Figure 5.1b**).[296]

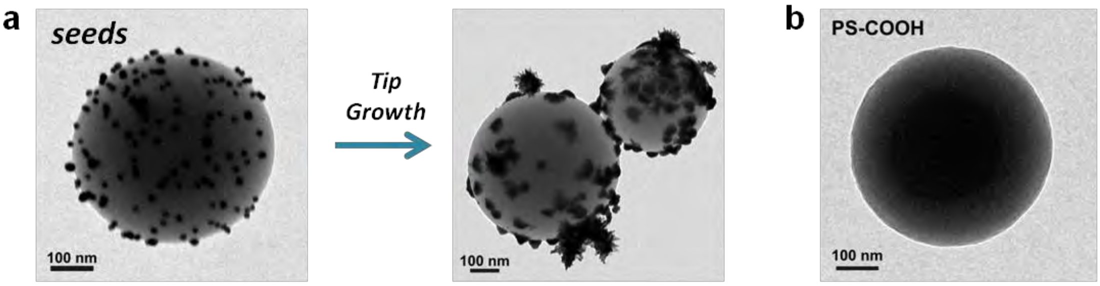

Figure 5. 1 TEM images of gold nanoparticle-coated PS bead used as seeds and non-uniform "spiky" particles obtained after *in situ* tip growth (**a**). (**b**) TEM image of COOH-functionalized PS beads showing lack of attachment of AuNSs.

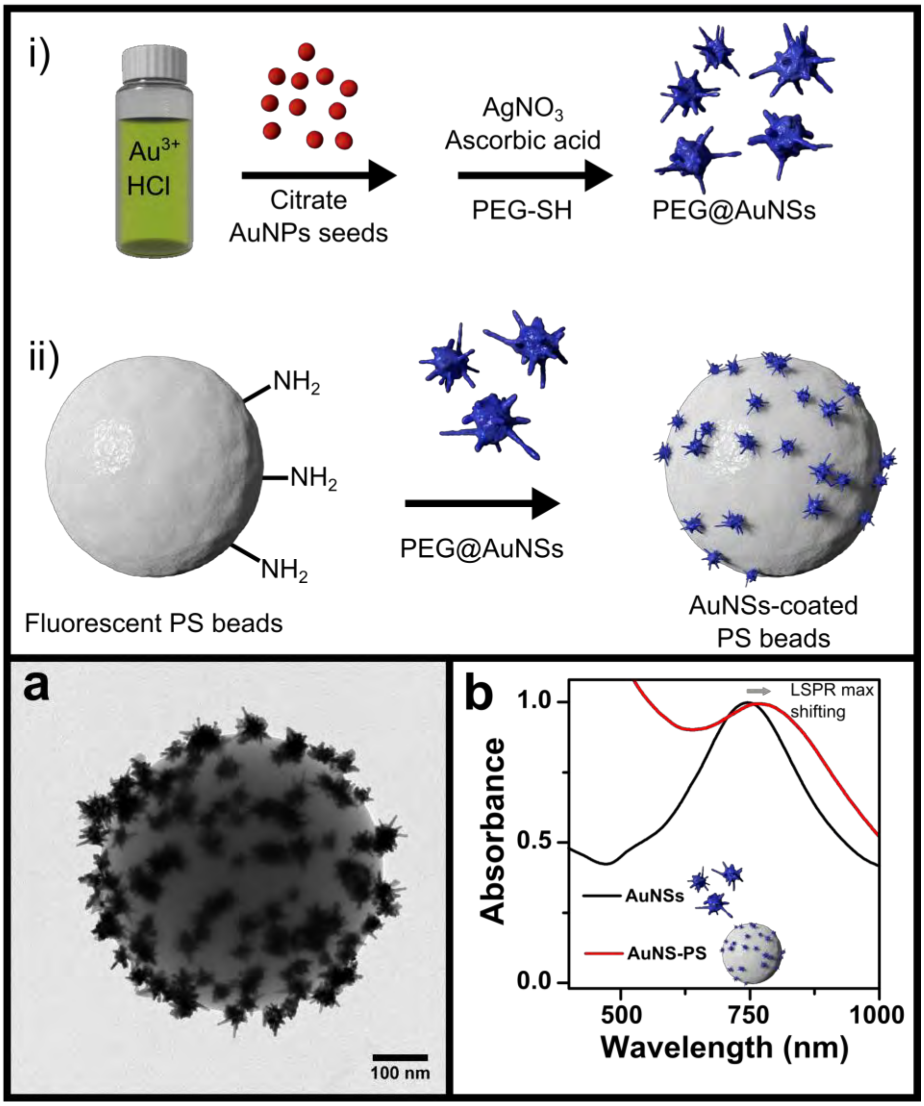

Figure 5. 2 Top panel: Schematic illustration of the gold nanostar synthesis (**i**) and assembly process (**ii**). **Bottom panel:** TEM image of an AuNS-PS bead (**a**) and Vis-NIR spectra (**b**) of AuNS (black) and AuNS-PS (red) particles.

Due to the strong affinity of amino groups with the gold surface, polymer beads were fully covered with AuNSs, as confirmed by TEM (**Figure 5.2a**). In addition, annular dark-field scanning TEM (ADF-STEM) analysis was carried out for detailed analysis of individual assembled particles. As shown in **Figure 5.3a** the central polymer particle was found to be homogeneously surrounded by smaller and brighter objects that correspond to AuNSs. Electron tomography and three dimensional (3D) reconstruction of the same sample provided additional information about the AuNS distribution 3D. The 3D reconstruction image (**Figure 5.3b**) shows that AuNSs (in yellow) are found around the whole polystyrene surface (in blue).

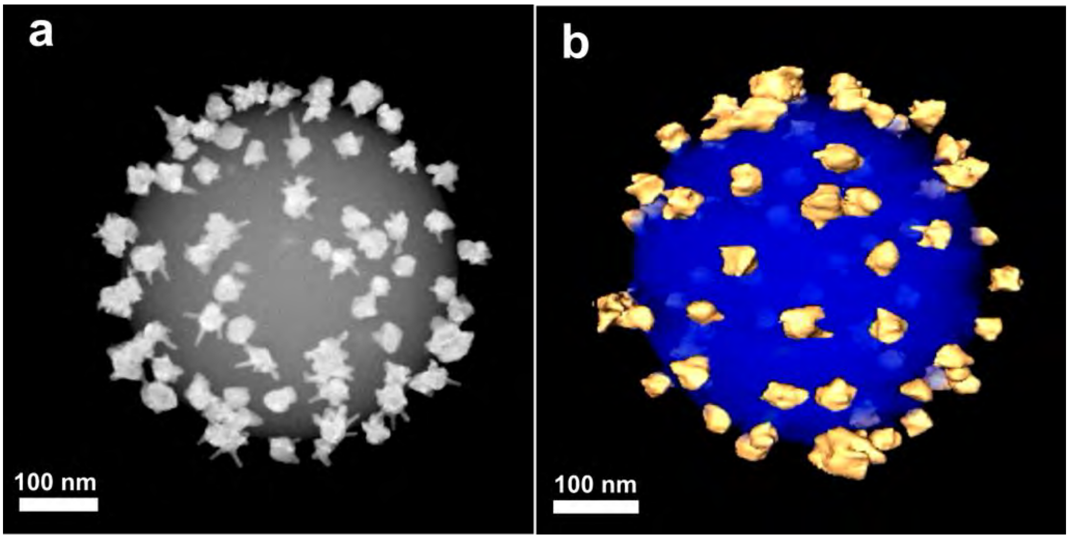

Figure 5. 3 ADF-STEM (**a**) and 3D reconstruction (**b**) images of an individual AuNS-PS bead.

Interestingly, we carried out a similar strategy for the assembly of other metallic nanoparticles such as PVP-stabilized AuNSs[46] or AgNPs[209] and found that these NPs can also be assembled onto the colloidal polymer substrates (**Figure 5.4**). Extensive washing was required for PVP-coated AuNSs prior to assembly on beads, to remove much of the polymer from the gold surface, allowing a better interaction between Au and the amino groups at the PS surface. Cleaning of AgNPs was also necessary followed by redispersion in citrate solution after synthesis to remove excess of reactants from the synthesis and thereby ensure suitable interaction with the PS surface.

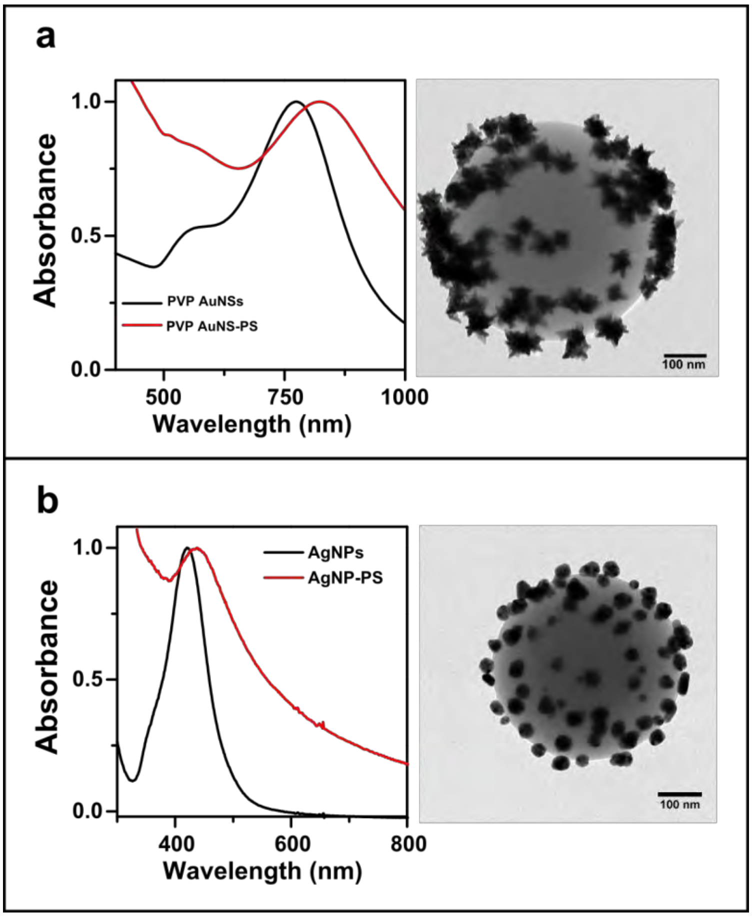

Figure 5.4 Vis-NIR spectra (left) and TEM images (right) of PS assembled with PVP-coated AuNSs (**a**) and AgNPs (**b**). The Vis-NIR spectra in black correspond to the dispersed plasmonic particles.

Another advantage of this process is that the amount of AuNS per PS bead could be readily controlled by changing the concentration of PS and keeping constant the AuNS concentration. Thus, PS spheres can be loaded with *low* (**Figure 5.5a**), *medium* (**Figure 5.5b**) or *high* AuNS densities (**Figure 5.5c**). However, we observed that excessive increase of AuNS concentration induced AuNS aggregation and uniform coatings could not be obtained.

As initially targeted, the plasmonic coating provides interesting optical properties to the PS cores. The spiky shape of the AuNSs alone gives rise to a localized surface plasmon resonance (LSPR) band corresponds to localized modes at the tips, as well as a less intense shoulder that corresponds to the core plasmon mode.[47] A similar optical response was found for the AuNS-coated PS spheres, however with a clear LSPR redshift which is likely due to a combination of plasmon coupling due to close proximity between some AuNSs on the PS surface, and the local increase of refractive index near the AuNSs because of binding to PS (**Figures 5.2b** and **5.4**).[168] Whilst

AuNSs and PVP coated AuNSs dispersed in H_2O present maximum plasmon bands located at 747 and 775 nm, respectively, after assembly onto the PS surface, corresponding redshifts of 26 and 49 nm. For AgNPs, the LSPR maximum shifts from 420 to 438 nm when the particles are covering the PS surface (**Figure 5.4b**). When the AuNS density was increased, the intensity of the AuNSs LSPR band was correspondingly increased, as reflected in the Vis-NIR spectra of the different AuNS-coated PS beads (**Figure 5.5d**).

When targeting applications in SERS, high electromagnetic fields are required, which may arise either from tip plasmons in sharp NPs[264,301] or from the generation of nm-sized gaps between neighboring NPs,[302–304] forming so-called hot-spots. In this respect our system can be considered as particulary interesting since AuNSs with a large number of sharp tips are located close to one another when assembled onto the PS surface. Therefore, we studied the SERS response from these hybrid plasmonic assemblies using 4-MBA as a Raman probe molecule. **Figure 5.5e** depicts representative SERS spectra of 4-MBA when PS beads are loaded with *high*, *medium* and *low* AuNS densities. The most prominent peaks appear at 1580 and 1078 cm^{-1}, corresponding to ν(C−C) ring stretch and ring breathing modes of the molecule, respectively.[221,305] Interestingly, the sample with the highest density of AuNS (*high* AuNS) did not result in the highest SERS intensity. This unexpected result can be explained by the possibility of plasmon deactivation due to the overlap of the particle branches. Previous studies have demonstrated that contrarily to what happens with particles of other shapes (i.e. spheres), the interaction between tips with different orientations and geometries leads to distroying rather than generating active hot spots.[306] In fact, it has also been observed in **Chapter 3** of this thesis that a monolayer of densely packed spherical NPs generates a much higher SERS signal than a dense monolayer of AuNSs. Recent theoretical studies[307] demonstrated that increasing the AuNS concentration on flat supports until the formation of a high density monolayer does not significantly increase the intensity of the expected SERS signal.

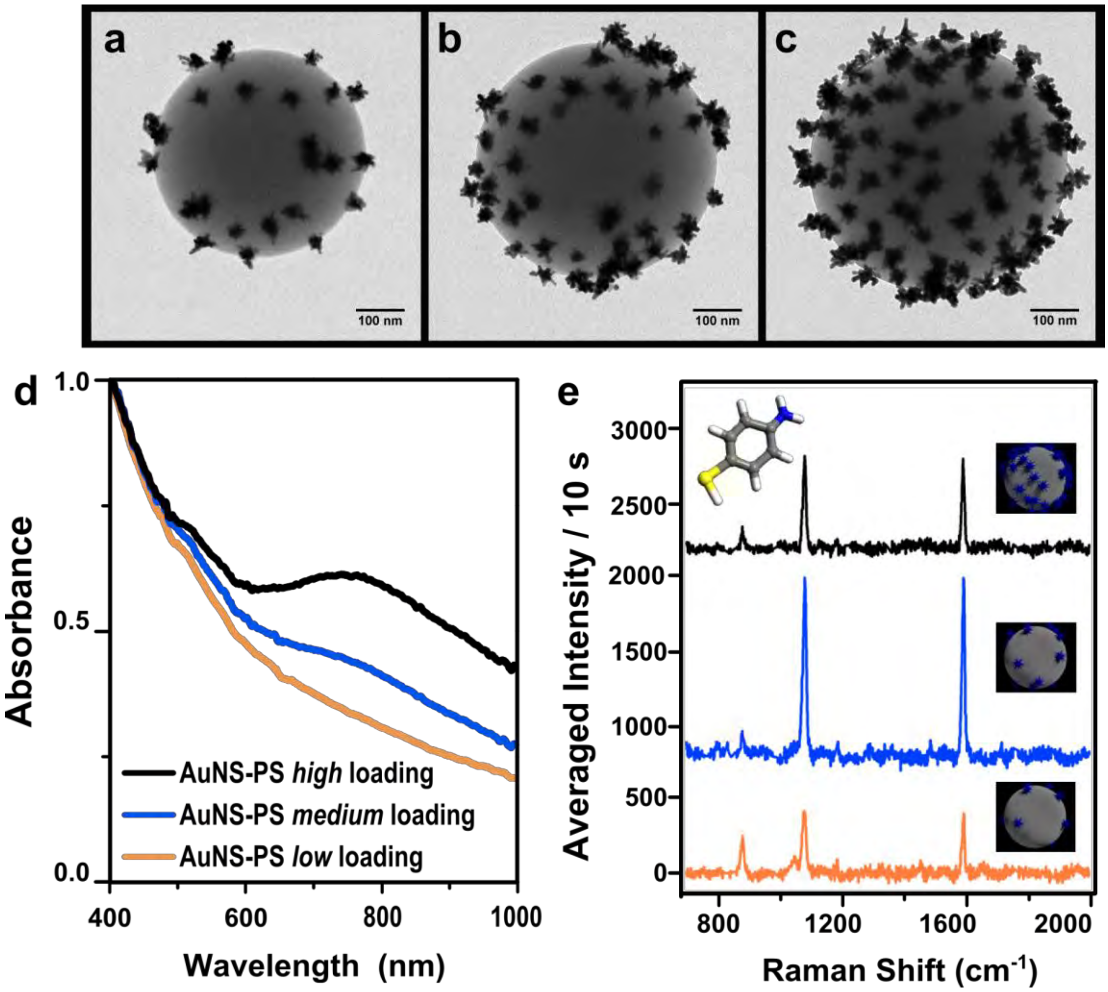

Figure 5.5 TEM images (**a**-**c**), Vis-NIR spectra (**d**) and SERS spectra (**e**) of PS beads loaded with different AuNS densities (orange=*low*, blue= *medium* and black=*high*) and subsequently labeled with 4-MBA. The SERS spectra were background corrected and plotted after applying an offset for more convenient data presentation.

Since application to biological imaging requires highly efficient SERS probes, we selected the most efficient assembly configuration (*medium* AuNS density) together with living A549 cells. In an attempt to further increase the SERS signal intensity from the nanostructured colloids we additionally incorporated small Au nanoparticles (ca. 5 nm) that are capped with a mixture of hydrophobic and hydrophilic thiolated alkanes (known as rippled AuNP, rAuNP), and which have been reported to display high affinity toward binding onto cell membranes.[297] We therefore hypothesized that the adsorption of such rAuNPs on AuNS-PS beads would aid in bead-cell membrane association and also potentially in the SERS response due to the presence of a higher density of AuNPs. *Medium* loaded nanocomposites were thus decorated with rAuNPs using the same self-assembly strategy as that for adsorption of AuNS onto PS beads

(**Figure 5.6a**). Interestingly, the new rAuNP coating was found to increase the stability of the composite nanostructures, as confirmed by zeta potential measurements (**Figure 5.6b**). Prior to incubation with cells, we tested the stability of AuNS-rAuNP-PS particles in cDMEM media. Composites were dispersed in cDMEM and incubated for 24 hours. **Figure 5.6c** displays the Vis-NIR spectra of the particles before and after incubation in cDMEM. It can be clearly observed that the LSPR band was not altered after dispersion in cell medium and TEM analysis confirmed the absence the aggregation. It is worth noting that even under biological conditions we found no sign of nanoparticle detachment from the PS surface and the sharp tips of AuNSs were also preserved (**Figure 5.6c**, inset).

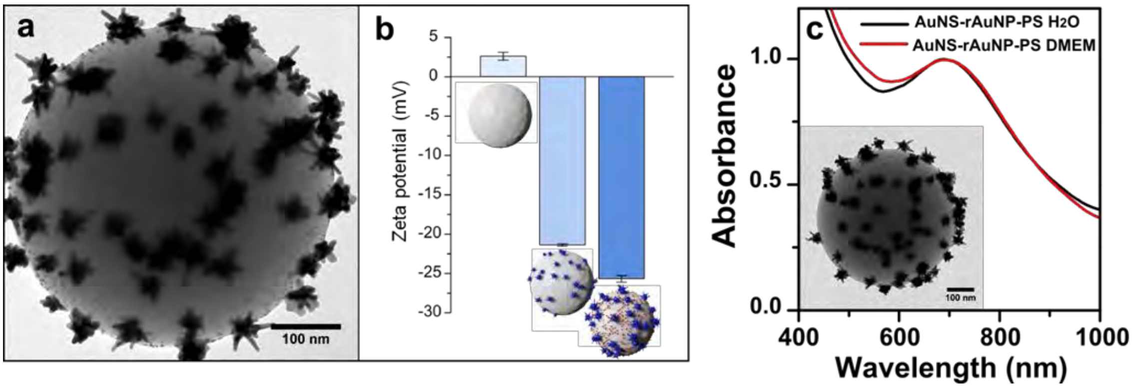

Figure 5. 6 (**a**) TEM image of a PS bead decorated with AuNS and rAuNP. (**b**) Zeta potential of PS beads and PS beads coated with AuNSs and AuNS-rAuNP. (**c**) Vis-NIR spectra of AuNS-rAuNP-PS particles before (black) and after (red) incubation for 24h in cDMEM. Inset: TEM image of AuNS-rAuNPs-PS beads after 24h incubation in cDMEM.

For SERS experiments in cells, 4-MBA was again used as a reporter, since it provides a strong SERS signal under 785 nm excitation (biological transparency window), it strongly adsorbs onto the Au surface, prevents AuNS reshaping, and the negative charges of carboxylic groups notably increase nanoparticle stability. **Figure 5.7** illustrates the SERS spectra of 4-MBA-encoded free AuNSs, AuNS-PS and AuNS-rAuNP-PS beads internalized by A549 living cells. The obtained SERS spectra perfectly reflect the fingerprint of the probe molecule and no interference peaks were observed from the cells or the buffer solution under the present experimental conditions. For both types of self-assembled structures, AuNS-rAuNP-PS and AuNS-PS, a remarkably higher SERS intensity was observed as compared to isolated AuNSs. Remarkably, an additional 2-fold improvement in SERS signal intensity could be obtained by including rAuNPs on AuNS-PS bead assemblies (**Figure 5.7b**,**c**). This behavior was found to be highly reproducible for various cells and also different particle batches. These results suggest a higher level of uptake of AuNS- rAuNP-PS beads as compared to their non-rAuNP containing counterparts.

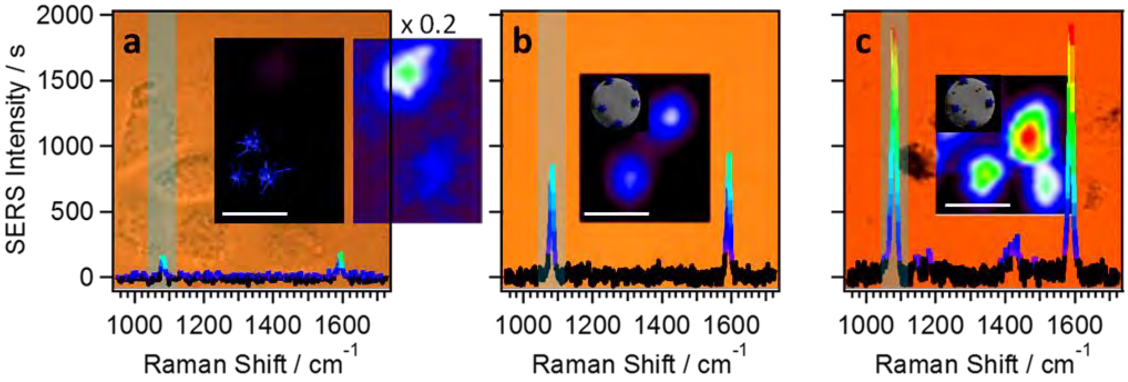

Figure 5. 7 2D-SERS map for the color-shaded vibration at 1078 cm^{-1} and corresponding single-point SERS spectrum (typically selected from the highest intensity) of A549 cells incubated with 4-MBA labeled free AuNS (**a**), AuNS-PS beads (**b**) and AuNS-rAuNP-PS beads (**c**). The concentration of incubated AuNS was constant in all samples; the SERS spectra presented were baseline corrected. The same intensity color scale was used for single-point SERS spectra and 2D maps. The white scale bars correspond to 20 μm.

To verify this hypothesis, we incubated both types of assemblies with two additional cells lines. Whilst we noted that the improvement in the SERS signal was not the same in absolute numbers as compared toA549 cell uptake, we observed the same trend when incubating the particles with human MCF-7 breast cancer cells and murine J774 macrophages (**Figure 5.8**). Therefore, interpretation of this observation requires taking into consideration different factors that affect cell-particle interactions. For instance, cellular uptake strongly depends on the size, shape and surface chemistry of the particles.[308,309] It has also been reported that nanoparticle clustering can facilitate cell uptake.[310] In this respect, we propose that our system notably improves the use of AuNSs for SERS bio-imaging, since higher SERS efficiency in living cells is observed when the nanoparticles are assembled onto a colloidal support, as compared to the corresponding free encoded plasmonic particles.

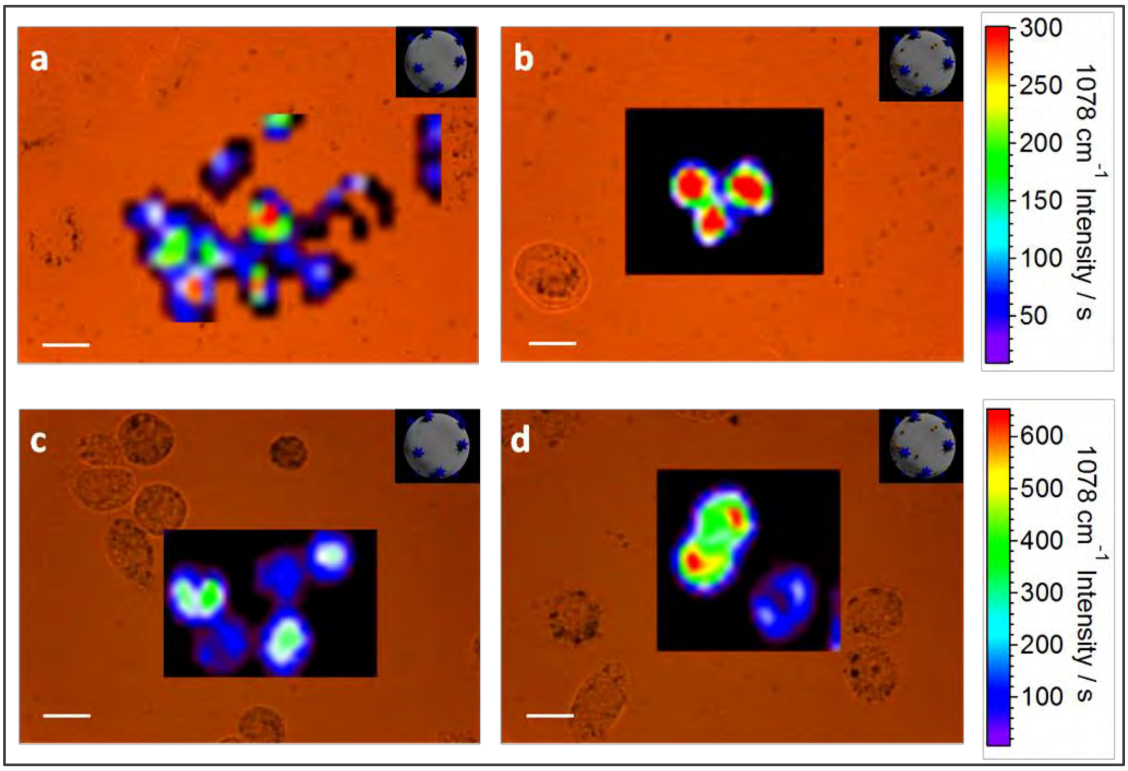

Figure 5. 8 Bright-field optical micrographs overlaid with SERS mapping images of the 1078 cm^{-1} vibration for the 4-MBA tag, using *medium*-loaded AuNS-PS incubated with MCF-7 (**a**) and J774 (**c**) in comparison with *medium*-loaded AuNS-rAuNP-PS also incubated with MCF-7 (**b**) and J774 (**d**). The intensity scales were normalized (see cell-dependent color scale). For both cell lines, AuNS-rAuNP-PS lead to more intense SERS signals. In the case of MCF-7 the intensity difference is lower than for J774, but it is remarkable that a high signal was obtained from a larger and more homogeneous cell area. Scale bars 20μm.

In order to understand better the relationship between cellular uptake of composite nanotags and the measured SERS signal, we incubated cells with fluorescently labeled PS beads, also containing AuNPs, and monitored their uptake by correlated confocal fluorescence and SERS microscopy. Importantly, the green fluorescent dye was selected to avoid overlap of its emission wavelength with the excitation wavelength for the SERS reporter molecule. Using a numbered grid, the emission of the PS beads (in the 500-550 nm window) and the SERS intensity map of the 1078 cm^{-1} signal of 4-MBA-encoded AuNS-rAuNP-PS assemblies could be visualized for the very same A549 cells (**Figure 5.9**). Bright green fluorescence from individual beads located inside cells (**Figure 5.9a, z-stack**) as well as intense SERS (**Figure 5.9b**) was clearly observed using this simple setup. While SERS imaging is relatively time consuming, fluorescence imaging appears to be more intuitive and acquisition was faster. Thus, the integration of both functionalities in the same composite particle allows us to perform complementary imaging, thereby compensating the main deficiencies of both techniques.

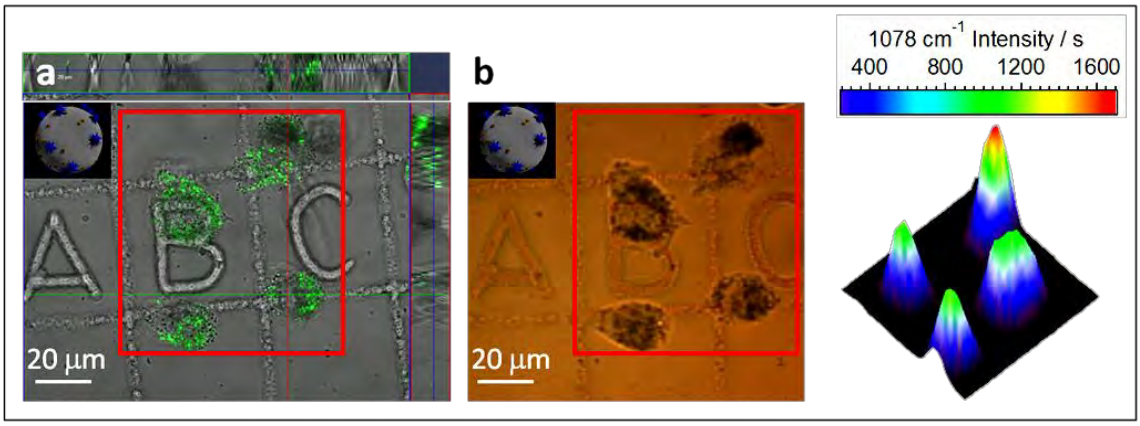

Figure 5.9 Confocal fluorescence correlated with SERS microscopy for living A549 cells using *medium*-AuNS-rAuNP-PS beads. (**a**) Map of the emission between 500-550 nm of the fluorescent dye in PS beads; (**b**) bright-field optical image (left) and 3D-intensity map of the 1078 cm^{-1} vibration of 4-MBA tag excited at 785 nm (right). The red border in **a** and **b** indicates the area used for SERS imaging. The color represents the background-corrected and fitted intensity at 1078 cm^{-1}. Conditions for SERS spectra: laser power 16 mW, integration time 1s, 40 x immersion objective.

Regardless of the fluorescence of the PS particle support and the SERS of the tag, the scattering properties of the used nanoparticles allow for additional cell imaging modalities using conventional dark-field (DF) optical microscopy. Depending on the size, shape and material, nanoparticles can strongly scatter light, which can be detected under DF illumination conditions.[311] Shown in **Figure 5.10** are correlated fluorescence and DF images for AuNS-rAuNP-PS particles internalized by A549 cells. Bright objects and green dots match for both DF and fluorescence images. We therefore demonstrate the high versatility of our composite particle system to separately track nanoobjects within living cells by means of different and complementary imaging tools.

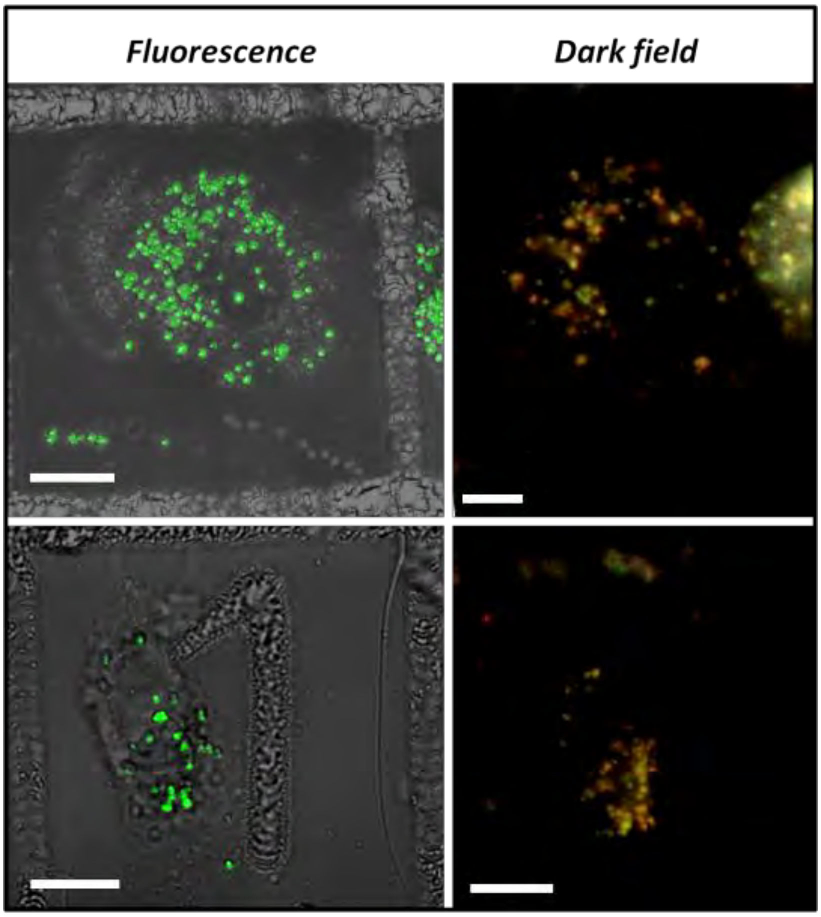

Figure 5.10 Correlated fluorescence (left) and dark-field images (right) of AuNS-rAuNP-PS beads internalized by A549 cells (scale bars are 10 µm).

We finally conducted cell viability assays whereby A549 cells were incubated with different concentration of AuNSs, AuNS-PS and PS particles for 66 h (**Figure 5.11**). Very low levels of toxicity were appreciated, mainly at the highest particle concentrations. Bearing in mind the long incubation time this may be due to a reduction in cell proliferation and not due to toxic effects of the corresponding nanoparticle system, which is also supported by visual observation of the cells.

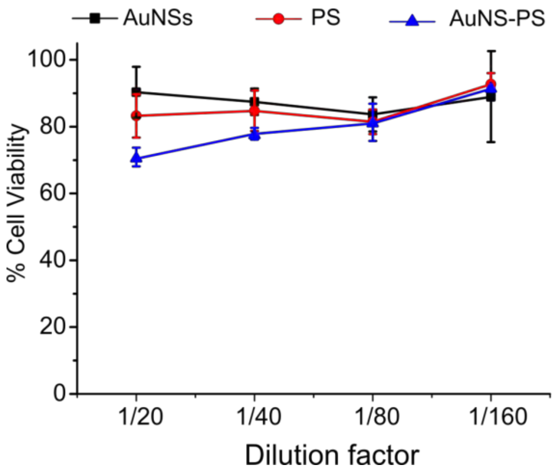

Figure 5.11 MTT assay results for A459 cells incubated during 66 hours with different concentrations of AuNSs (black), PS (red) and AuNS-PS (blue) particles. The initial particle solutions (AuNSs 0.5mM and PS and AuNS-PS 1.5·10-2 % PS in solids) were diluted from 20 to 160 times (i.e. concentration increases from right to left).

5.3 Conclusions

We have prepared SERS-encoded AuNS-decorated PS beads that can be used as nanoprobes for multimodal bioimaging. AuNS are excellent Raman-enhancing materials displaying LSPRs peaking in the biological transparency window. When AuNs are assembled onto fluorescent PS beads high cell permeability was observed and the integration of multiple functionalities in the same nanostructure allows imaging of living cells using different microscopy tools such as (confocal) fluorescence, SERS and DF microscopy. We additionally showed that PS beads with intermediate AuNS loadings show the highest SERS response. Using 4-MBA as reporter molecule we successfully imaged A459, MCF-7 and J774 cells by SERS mapping. Through additional rAuNP co-adsorption the SERS performance of the composite PS beads was further improved. Our assembled nanostructures combining fluorescent and SERS activity can be considered as promising nanoprobes for future biological applications.

General Conclusions

Altogheter this thesis represents a significant advancement in the preparation, functionalization and stabilization of gold nanostars for application as SERS tags. Different approaches have been developed to prepare highly stable and biocompatible gold nanostars and gold nanostar-based hybrid materials, which display plasmon resonances within the "biological transparency window", as well as great Raman enhancing activity. We also demonstrated the excellent ability of these engineered nanostructures for *in vitro* SERS bioimaging. We expect that these novel optical nanoprobes will represent an important contribution in the biomedical field, not only for *in vitro* applications also for the progress of new *in vivo* diagnostic and therapeutic tools. Even though specific conclusions have been included at the end of each chapter, the most relevant, overall conclusions of the research described in this thesis are presented herein.

1. Gold nanostars have been successfully functionalized with a mixture of two ligands that act as stabilizers and can direct the growth of an outer gold shell leading to exotic nanostructures presenting intrinsic hot spots.

   a. A mixture of BDT and CTAC has been used to stabilize AuNSs, avoiding aggregation and particle reshaping. Other common capping ligands, such as CTAC, 4-MBA, PEG-SH, ATP or BSPP have been tested, resulting in strong LSPR blueshift and broadening due to nanoparticle oxidation and aggregation.

   - **b.** BDT modified AuNSs of different sizes were used as seeds to futher direct encapsulation with a gold shell. Unusual nanostructures were obtained for different [Au^{3+}]/[Au^0] ratios employed in shell growth. TEM images showed that high R values lead to fully encapsulated AuNSs, while Janus-like particles were obtained when decreasing R. These morphological changes are in agreement with the recorded changes in the Vis-NIR spectra. HAADF-STEM tomography analysis further confirmed the presence of internal nanometric gaps where BDT molecules are trapped.

   - **c.** Since BDT has a high Raman cross section and is located in the internal gaps where enhanced EM fields are expected, we compared the efficiency of the intrinc hot spots. The results showed that semishell-coated AuNSs displayed the highest SERS intensity.

   - **d.** These SERS-encoded particles are considered promising nanoprobes that can be used for futures applications such as sensing and imaging.

2. Gold nanostars and other plasmonic nanoparticles, such as silver, gold nanoparticles and gold nanorods, were stabilized in hydrophobic solvents and assembled into SERS-active monolayers.

   - **a.** Using PEG-SH as pre-stabilizer and DDT as hydrophobic capping ligand, all the plasmonic nanoparticles were succesfully transferred into organic media (such as chloroform). TEM and Vis-NIR spectroscopy confirmed the absence of aggregation and the long-term stability (months) of the obtained particles. In particular for AuNSs, thiol coating prevents particle reshaping, preserving the sharpness of the gold tips.

   b. The obtained organic colloids can be dispersed in several organic solvents. Using mixtures of ethanol and hexane the nanoparticles were assembled into extensive monolayers, so that short interparticle distances lead to significant plasmon coupling, as reflected in the Vis-NIR spectra of the plasmonic substrates obtained. Using 4-MBA as probe molecule, the SERS performance of the different plasmonic substrates was also compared. AuNR and AuNP films showed the highest SERS signal, which can be explained considering that they support LSPR bands in resonance with the excitation wavelength.

   c. The phase transfer of plasmonic nanoparticles represents an important strategy for many applications in nanotechnology. The obtained hydrophobic nanoparticles were also suitable for further polymer coating. Therefore, water solubility and stabilization in biological conditions, which is imperative for bioapplications, was achieved.

3. SERS-encoded gold nanostars have been prepared and successfully used to image and differenciate breast cancer cells.

   a. PEG-stabized AuNSs were functionalized with a variety of SERS-active thiolated molecules. These Raman reporters (RaR) are soluble in organic solvents and can readily induce the phase transfer of AuNSs. Additional polymer coating allows obtaining SERS-encoded AuNSs, which are highly stable in biological conditions.

   b. The SERS efficiency of encoded-AuNPs and AuNSs was compared. Interestingly, we observed no SERS signal for spherical particles under NIR illumination, which confirmed that isolated AuNPs are not SERS-active so that spiky nanoparticles with LSPRs in the NIR and high EM fields at their tips should be used as SERS-tags.

   c. The prepared SERS-tags were internalized by different cell lines. An effective SERS bioimaging system was demonstrated by succesfully distinguishing between breast cancer cells within a complex culture.

   d. We have proved the reliability and multiplexing capability of SERS-encoded AuNSs, which could be applied for specific targeting of cancer cells as well as for *in vivo* SERS imaging.

4. Bifunctional probes made of fluorescent PS beads and Au nanostars were fabricated and demonstrated their huge potential as tags for multimodal bioimaging.

   a. PEG-SH stabilized AuNSs were assembled onto amino-functionalized PS beads *via* complexation with $-NH_2$ groups. Adjusting the AuNSs/PS ratio it was possible to tune the AuNS loading onto the PS surface.

   b. Using 4-MBA as probe molecule, the SERS response of the different assembled structures was studied as a function of AuNS loading, showing that intermediate AuNS concentrations lead to higher SERS intensities.

   c. Fluorescent and SERS-active nanoprobes were internalized by A459 cells, so that using confocal fluorescence-SERS microscopy correlative imaging of living cells could be performed. Additionally, the scattering properties of these particles allow for additional cell imaging using dark-field microscopy, confirming the high versatility of our system towards biological multimodal imaging.

RESUMEN

Nanoestrellas de Oro: Síntesis, Estabilización y Aplicaciones como Nanomarcadores SERS

Objetivos

El trabajo presentado en esta tesis está centrado en la síntesis y estabilización de nanopartículas de oro con forma de estrella (*nanoestrellas de oro*), así como en sus aplicaciones relacionadas con la espectroscopía por *dispersión Raman aumentada en superficie*, (SERS). Esta tesis ha sido desarrollada en el Grupo de BioNanoPlasmónica del Centro de Investigación Cooperativa en Biomateriales (CIC biomaGUNE, Donostia-San Sebastián). Las principales líneas de investigación en el *BioNanoPlasmonic Lab* están relacionadas con la síntesis y ensamblaje de nanopartículas plasmónicas de composición, tamaño y forma controlada, donde la gran cantidad de estudios fundamentales realizados ha permitido desarrollar multitud de aplicaciones prácticas, destancando especialmente aquellas relacionadas con la biodetección mediante SERS. En relación con su etapa anterior ligada al grupo de investigación de Química Coloidal en el Departamento de Química Física de la Universidad de Vigo, el grupo de BioNanoPlasmónica posee gran experiencia sobre el estudio de nanopartículas de oro de geometría anisotrópica. En concreto, se han desarrollado estudios pioneros sobre nanostrellas de oro. Siguiendo esta dirección, esta tesis se ha enfocado en la preparación de marcadores SERS basados en nanoestrellas de oro. El contenido de cada capítulo se describe brevemente a continuación:

En el **Capítulo 1** se presenta una introducción general, donde conceptos básicos como la síntesis de nanopartículas de oro, propiedades ópicas y funcionalización de nanopartículas metálicas, aplicaciones prácticas o el origen del fenómeno SERS, son tratados.

En el **Capítulo 2** se describe la estabilización de nanoestrellas de oro usando una mezcla de ligandos compuesta por un ditiol y un surfactante. Estas nanoestrellas a su vez son empleadas como semillas para dirigir el crecimiento de una concha de oro externa. De esta forma se obtienen partículas de diversas y exóticas morfologías que presentan huecos internos nanométricos donde se generan altos campos eléctromagnéticos y la molécula de ditiol está atrapada.

Las nanoestrellas de oro también pueden ser estabilizadas usando una mezcla de polietilenglicol tiolado y moléculas tioladas más pequeñas, como dodecanotiol (DDT) o compuestos aromáticos activos en SERS. Así, en el **Capítulo 3** se presenta un método general para transferir de fase nanoestrellas de oro y otras partículas plasmónicas, como nanoesferas de oro y plata, y nanorods de oro. Usando DDT como ligando hidrofóbico capaz de inducir la transferencia a fase orgánica, se obtienen nanocoloides hidrofóbicos que son ensamblados en monocapas activas en SERS. En el **Capítulo 4** se describe la preparación de nanoestrellas de oro codificadas usando la misma estrategia pero empleando tioles SERS-activos. A su vez, mediante recubrimientos poliméricos, estos nanomarcadores pueden ser solubilizados en agua y empleados para aplicaciones biológicas, tal como se demuestra al analizar diferentes líneas celulares mediante bio-imagen SERS.

Por último, el **Capítulo 5** trata sobre el ensamblaje de nanoestrellas de oro sobre substratos coloidales. En concreto, microesferas de poliestireno fluorescente han sido cargadas de nanoestrellas de oro y empleadas como nanomarcadores SERS bifuncionales.

En resumen, se espera que esta tesis contribuya de forma significativa al diseño y la preparación de nanomateriales plasmónicos funcionalizados a medida, altamente estables, biocompatibles y con gran potencial para SERS. En concreto, estudios biomédicos realizados con nanomarcadores SERS muestran resultados prometedores. Por tanto, el trabajo presentado en esta tesis podría contribuir de forma muy importante a la fabricación de nuevas y más sofisticadas nanoplataformas SERS.

6.1 Introducción

A pesar de que el concepto es relativamente reciente, el uso de los nanomateriales se remonta a tiempos remotos. Un buen ejemplo de ello es la famosa *Copa de Licurgo*, fabricada en la época de los romanos (siglo IV a.C.) y que se exhibe en el Museo Británico de Londres.[16] La presencia de nanopartículas de oro y plata en dicha copa es responsables de su tonalidad verde, cuando refleja la luz incidente, pero roja cuando la luz es transmitida a través del vidrio que la forma. Hoy sabemos que los colores brillantes característicos de nanopartículas de metales como la plata, el oro o el cobre, se deben a las *resonancias plasmónicas* que estos presentan y que se corresponden con los modos de oscilación de los electrones de conducción en resonancia con radiaciones electromagnéticas incidentes.[2] Cuando dichos modos están confinados en la interfase metal-dieléctrico y la luz interacciona con partículas mucho menores que su longitud de onda (nanopartículas), se produce lo que se conoce como *resonancia de plasmón superficial localizada* (LSPR, del nombre en inglés).[1,3] Debido a este fenómeno, las nanopartículas metálicas presentan propiedades únicas que han permitido numerosos e increíbles avances científicos en diversas áreas tales como la biomedicina y la biotecnología,[4] la biodetección,[5] la energía solar[6] o las ciencias de la computación,[8] entre otras.

Las propiedades ópticas de las nanopartículas plasmónicas pueden ser ajustadas a lo largo del espectro visible (Vis) e infrarrojo (IR) en función de su tamaño, forma, estado de agregación y de las propiedades dieléctricas del medio que las rodea.[89] En este sentido, el desarrollo de la Química Coloidal ha permitido diseñar y obtener materiales con la respuesta óptica adecuada para cada aplicación práctica. Aunque la preparación de nanopartículas esféricas y monodispersas de oro se conoce desde mediados de siglo XX,[18] durante las últimas décadas la comunidad científica se ha interesado especialmente en el estudio de nanopartículas que presentan morfologías anisótropas.[19–]

[21] Esto se debe fundamentalmente a que sus propiedades ópticas, electrónicas, magnéticas o catalíticas son diferentes, y muchos casos superiores, a las que presentan nanopartículas con geometría esférica. Por ejemplo, se pueden generar campos electromagnéticos de alta intensidad en las aristas y vértices agudos de nanopartículas anisótropas con geometría triangular, cilíndrica o estrellada, siendo por tanto estas partículas particularmente atractivas para la *espectroscopía por dispersión Raman aumentada en superficie* (SERS).[101,104] En concreto, las nanoestrellas de oro (AuNSs) resultan de enorme interés, ya que presentan LSPRs en la región del infrarrojo cercano (NIR) del espectro electromagnético así como múltiples *puntos calientes* (campos electromagnéticos de muy alta intensidad) en los extremos de sus afiladas puntas.[103,105] Esta tesis está centrada en el estudio de las nanoestrellas de oro como partículas plasmónicas funcionales que poseen un gran potencial para aplicaciones en SERS.

Se han desarrollado diversos protocolos para preparar nanopartículas de oro con forma de estrella, la mayoría de ellos basados en el conocido método de crecimiento de nanopartículas a partir de semillas metálicas previamente preparadas. Esta estrategia permite obtener un mejor control sobre los procesos de nucleación y crecimiento y por lo tanto mejorar la dispersión de tamaños en las partículas obtenidas. Así, uno de los métodos desarrollados para la obtención de AuNSs con alto rendimiento y monodispersidad combina el poder reductor del polímero polivinipirrolidona (PVP) y el disolvente dimetilformamida (DMF).[46] Se obtienen así nanoestrellas de oro que presentan múltiples puntas cuando se reducen iones Au^{3+} en presencia de semillas de oro previamente recubiertas con PVP. Además, el tamaño de las nanoestrellas se puede ajustar fácilmente modificando la concentración de semillas. El mismo método se ha empleado también para crecer puntas sobre “semillas” que presentan otras geometrías tales como nanocables[48] o nanobastones.[49] Especialmente interesante resulta la síntesis “sin surfactante” publicada por Vo-Dinh y colaboradores, ya que al no utilizar polímeros o surfactantes como estabilizantes, se facilita la funcionalización de las nanopartículas para aplicaciones posteriores.[50] Para la reducción de $HAuCl_4$ se emplea ácido ascórbico (AA) en presencia de nitrato de plata ($AgNO_3$) y AuNPs (13 nm de diámetro) estabilizadas con citrato como semillas. Para evitar la oxidación de las semillas y obtener alta monodispersidad en la síntesis, es necesario trabajar bajo condiciones ácidas empleando ácido chlorídrico. Los iones Ag^+ y Cl^- parecen desempeñar un papel clave en la formación de las puntas y por tanto en la obtención de

AuNSs. Nanoestructuras híbridas, tales como nanoesferas tipo Janus de Au,[54] y AuNPs, NTs y NRs rodeados de sílice mesoporosa,[55] se han empleado también como semillas para crecer puntas de oro obteniendo nanopartículas con propiedades plasmónicas muy particulares.

En cuanto a las propiedades ópticas de las AuNSs, tal como se aprecia en la **Figura 6.1a**, la geometría estrellada da lugar a una ancha banda plasmónica principal y un hombro de menor intensidad que se corresponden con los modos plasmónicos de las puntas y el nucleo, respectivamente.[47] De hecho, las puntas actúan como una especie de "nanoantena" intensificando de forma extraordinaria el campo electromagnético en sus extremos. Mediante espectroscopía por pérdida de energía de electrones (EELS) en un microscopio de transmisión y barrido (STEM) se ha podido demostrar la presencia de dichos campos electromagnéticos localizados justamente en los extremos de las puntas de las nanoestrellas, lo cual además está de acuerdo con predicciones teóricas realizadas para el mismo sistema (**Figura 6.1b-d**).[103] Es por ello que las nanoestrellas de oro se consideran particularmente interesantes para SERS, ya que no se requiere inducir su agregación para la formación de *puntos calientes.*

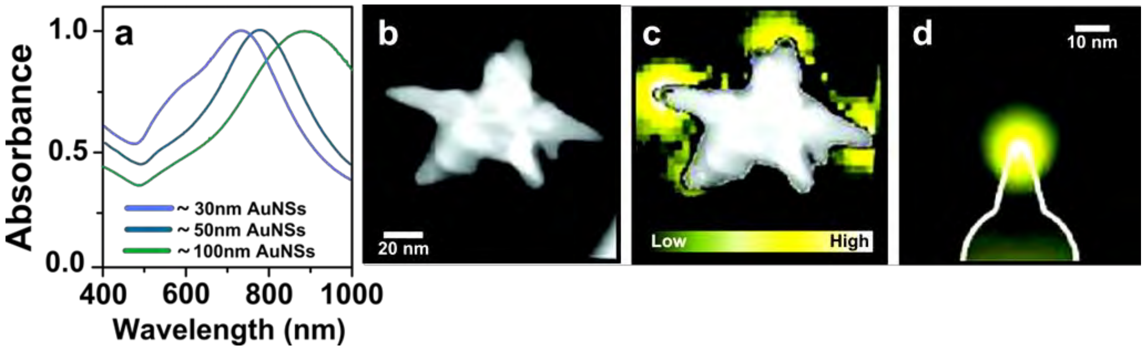

Figura 6.1. (**a**) Espectros Vis-NIR de AuNSs de diferentes tamaños. (**b**) Imagen de alta resolución STEM en campo oscuro de una nanoestrella de oro individual. (**c**) Mapa de intensidad de EELS de la misma partícula. (**d**) Mapa de intensidad de EELS calculado de la resonancia plasmónica en el extremo de una punta de nanopartícula.

Las nanopartículas plasmónicas pueden emplearse para SERS bajo configuraciones muy diversas. En cualquier caso, el sustrato ideal para SERS debe cumplir varios requisitos, como son reproducibilidad en su preparación, estabilidad química y alto *factor de aumento de la señal Raman* (enhancement factor, *EF*). Este último, que puede llegar a alcanzar magnitudes del orden 10^{14}, viene dado por el cociente entre la intensidad SERS y la intensidad Raman convencional y por tanto ofrece una estimación de cúanto se amplifica la señal Raman en SERS.[312] Para implementar la detección por SERS, se pueden distinguir dos estrategias principales según se usen o no nanopartículas plasmónicas marcadas con moléculas activas en SERS. Por ejemplo, se han dectectado concentraciones zeptomolares de diferentes analitos empleando substratos basados en AuNSs que no están marcadas.[103,171] Por otra parte, nanopartículas plasmónicas modificadas con moléculas que presentan una alta sección eficaz de SERS (también conocidos como nanocódigos SERS), pueden emplearse para la detección indirecta de diferentes moléculas diana. En este sentido, la microscopía SERS es considerada como una nueva herramienta analítica muy apta para bioanálisis y que presenta numerosas ventajas comparada con otras técnicas ópticas como la microscopía de fluorescencia, la cual emplea puntos cuánticos y fluoróforos orgánicos.[99] Entre estas ventajas destacan la alta sensitividad, la presencia de bandas espectrales muy estrechas que permiten simultanear varios análisis y la alta fotoestabilidad que presentan los marcadores Raman.[124] Normalmente, aparte de la nanopartícula plasmónica y la molécula activa en SERS, se requiere la encapsulación del marcador SERS usando una capa externa que puede estar formada por un polímero u otro material como la sílice o un material proteico, por ejemplo. De esta forma se confiere a la partícula codificada una mayor robustez física, estabilidad de la señal Raman y se evita la contaminación química y biológica procedente del medio. La microscopía SERS se ha empleado ampliamente para la detectar biomarcadores en células cancerígenas,[133] microorganimos como virus o bacterias[135] y también para obtener imágenes *in vivo* de células, tejidos y órganos.[99]

6.2 Estabilización y Encapsulación de Nanoestrellas de Oro mediante Ditioles

En el **Capítulo 2** se describe la utilización de una mezcla de ligandos orgánicos (1,4 dimercaptobenceno, BDT, y cloruro de cetiltrimetilamonio, CTAC) para estabilizar de forma eficiente nanoestrellas de oro que han sido sintetizadas sin otro surfactante, de forma que los ligandos evitan la agregación coloidal y la oxidación de las partículas. A su vez, estas nanoestrellas recubiertas con BDT han sido utilizadas como “semillas” para dirigir el crecimiento de una capa de oro a su alrededor, dando lugar a geometrías muy particulares que presentan huecos internos donde se generan campos electromagnéticos son muy intensos (puntos calientes) y las moléculas de BDT se encuentran atrapadas.

En primer lugar, se estudió la estabilidad de AuNSs de 25 nm (diámetro aproximado del núcleo) inmediatamente después de su síntesis. Se emplearon como estabilizates CTAC (1 mM), BDT (10 µM) y una mezcla CTAC-BDT (10 mM - 10 µM). Para AuNSs no recubiertas (desnudas) y para CTAC-AuNSs se observa un desplazamiento significativo de la banda plasmónica hacia longitudes de onda más bajas, lo cual indica que la superficie de la nanoestrella no está pasivada y por lo tanto se oxida rápidamente. Cuando se usa BDT sin embargo, no se observa dicha oxidación aunque la banda plasmónica aparece más ancha debido a que el ligando induce agregación. Solamente con la mezcla CTAC-BDT la banda plasmónica permanece inalterada y conserva su forma original (**Figura 6.2a**). Esto se refleja en las correspondientes imágenes de microscopía electrónica de transmisión (TEM). Mientras que las AuNSs desnudas adquieren formas redondeadas debido a su oxidación, las nanoestrellas estabilizadas con CTAC-BDT conservan su estructura puntiaguda inicial (**Figure 6.2b**).

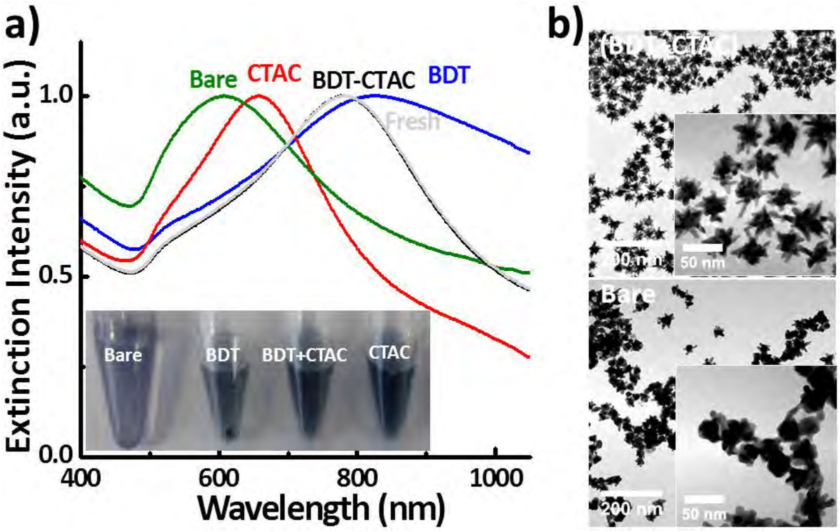

Figura 6.2. (a) Espectros UV-Vis de AuNSs inmediatamente después de la síntesis ("fresh"), después de ser estabilizadas con diferentes ligandos (CTAC, BDT y mezcla CTAC-BDT) y sin estabilizar ("bare"). Se incluye una fotografía de los diferentes coloides después de 3 horas. **(b)** Imágenes TEM a distintos aumentos de las AuNSs en presencia y en ausencia de la mezcla CTAC-BDT.

AuNSs estabilizadas con CTAC-BDT fueron empleadas a su vez como "semillas" para su encapsulación con una capa de oro. Curiosamente, cuando se modifica la relación entre [Au^{3+}] y [Au^{0}] (R), se obtienen nanopartículas con morfologías diversas e intrigantes. Al aumentar R, se observa una disminución gradual la banda correspondiente a los modos plasmónicos de las puntas (**Figura 6.3a**). Efectivamente, según las imágenes de TEM analizadas, al aumentar R aumenta la encapsulación de las nanoestrellas, de forma que se obtienen partículas Janus nanoestrella-nanoesfera (R=4.8), nanoestrellas parcialmente encapsuladas en las cuales solo algunas puntas sobresalen (R=9.6) y nanoestrellas completamente encapsuladas (R=19.1) (**Figura 6.3b**). La **Figura 6.3c** muestra la estructura tridimensional de una de las partículas encapsuladas formada a partir de imágenes de microscopía electrónica de barrido por transmisión acoplado a un detector de campo oscuro anular de alto ángulo (HAADF-STEM). En la imagen, los huecos internos presentes en la estructura aparecen como una especie de “burbujas” (indicadas mediante una flecha). En una sección transversal de la reconstrucción 3D, dichos huecos se aprecian como zonas oscuras entre la nanoestrella (semilla) y la semiconcha de oro formada (**Figura 6.3d**, círculo blanco).

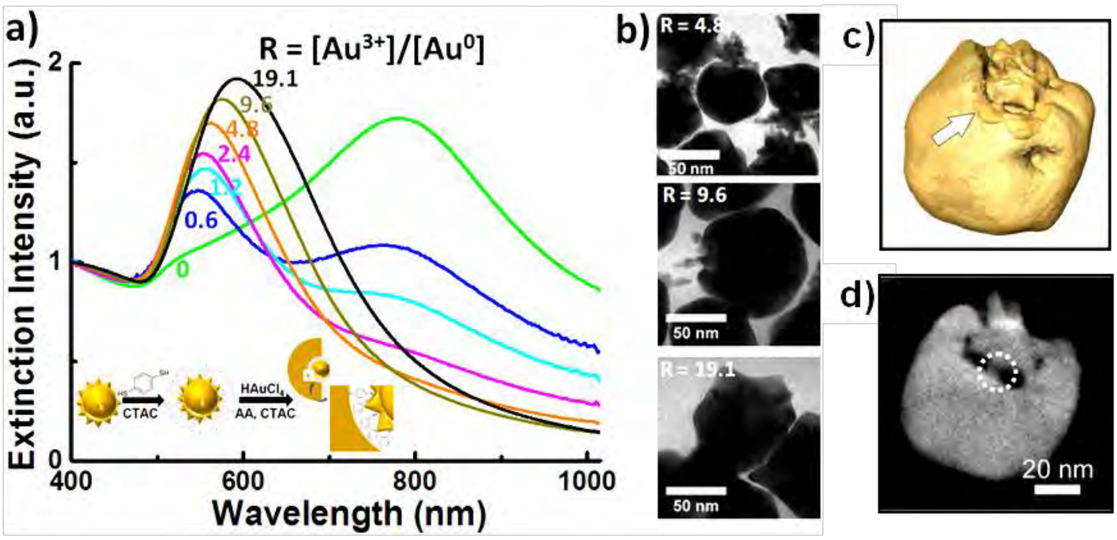

Figura 6.3. **(a)** Espectros UV-Vis de las nanoestructuras formadas usando diferentes valores de R y AuNSs estabilizadas con BDT como semillas. En el interior, esquema representativo del crecimiento. **(b)** Imágenes TEM de las nanoestructuras formadas a R = 4.8, 9.6 y 19.1. **(c)** Reconstrucción tridimensional de una nanoestrella parcialmente encapsulada (R = 9.6) a partir de imágenes de HAADF-STEM. La flecha blanca señala los huecos formados entre la AuNS original (semilla) y la semiconcha de Au formada. **(d)** Sección transversal de la reconstrucción 3D que muestra la conexión entre semilla y semiconcha (círculo blanco), así como los huecos internos formados.

Precisamente, una de las propiedades más interesantes que presentan estas nanoestrucuturas está relacionada con la presencia de estos huecos nanométricos en su interior (~4.5 nm de tamaño medio), los cuales contienen BDT (molécula Raman activa) y además se espera que localizen campos electromagnéticos de muy alta intensidad. Así, mediante SERS se comparó la eficiencia de los puntos calientes intrínsecos de las diferentes nanoestructuras formadas. En la **Figura 6.4** se aprecia como al aumentar el valor de R la intensidad SERS para la vibración a 1072 cm^{-1} del BDT también aumenta hasta alcanzar un valor máximo para R = 9.8, correspondiente a AuNSs parcialmente encapsuladas. Los resultados obtenidos sugieren que estas nanoestructuras podrían emplarese en multitud de aplicaciones como marcadores SERS muy eficientes.

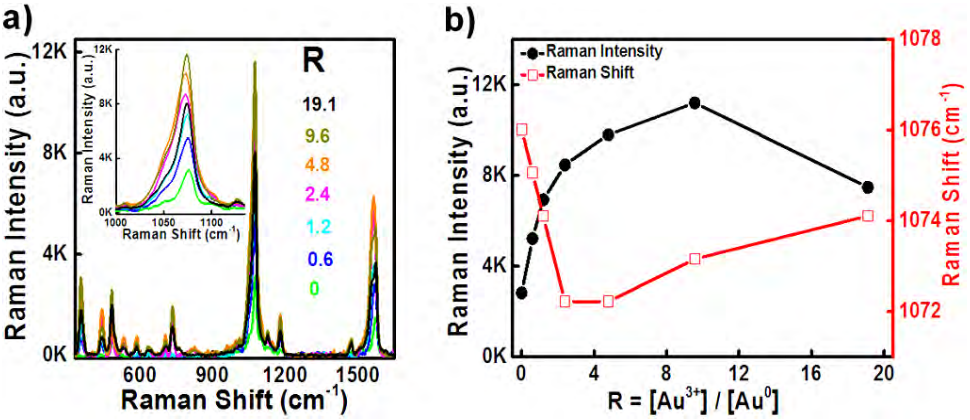

Figura 6.4. **(a)** Espectros SERS del BDT atrapado en el interior de las nanoestructuras formadas a diferentes valores de R. Todas las muestras presentan la misma concentración original de BDT usada para estabilizar las AuNSs. **(b)** Intensidad SERS y posición del modo de vibración "CH bending" del BDT para diferentes valores de R.

6.3 Nanopartículas Plasmónicas Hidrófobas: Estabilidad y Auto-ensamblaje de Monocapas Activas en SERS

En el **Capítulo 3** se desarrolla un método general para la transferencia de nanopartículas plásmonicas desde una fase acuosa a un medio orgánico. Para ello se emplea una mezcla de los ligandos polietilenglicol (PEG) y 1-dodecanotiol (DDT), en la cual PEG actúa como preestabilizante y DDT como agente hidrófobo capaz de inducir la transferencia de agua a cloroformo. Además de nanoestrellas de oro, este método se ha empleado también para estabilizar y transferir párticulas esféricas (AuNPs), nanobastones (AuNRs) y nanopartículas de plata (AgNPs) sintetizadas en medio acuoso. Los espectros UV-Vis y las imágenes TEM analizadas confirman la ausencia de agregación (**Figura 6.5**).

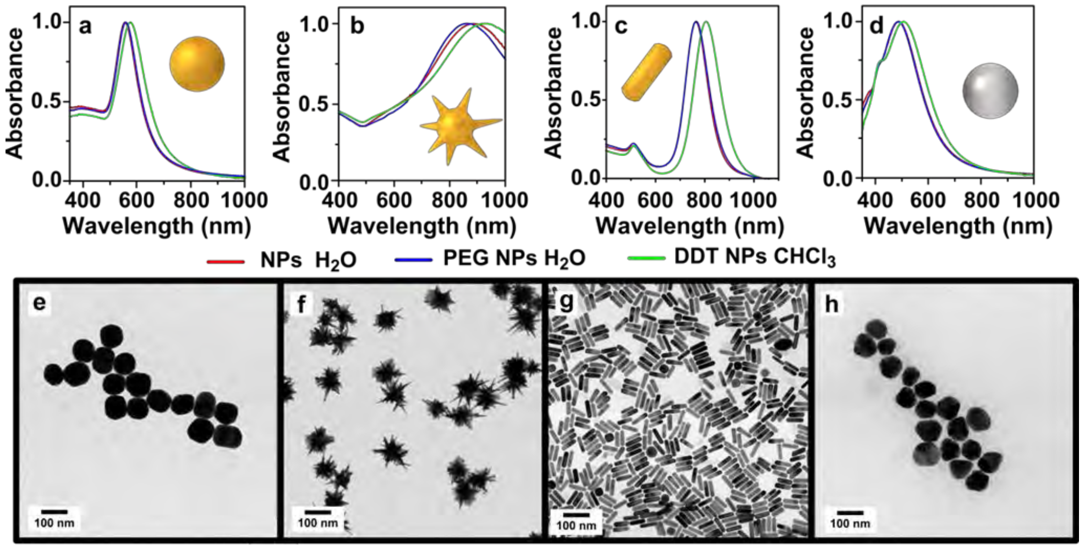

Figura 6.5. Espectros Vis-NIR en agua (líneas rojas), tras la funcionalización con PEG (líneas azules) y después de la transferencia a $CHCl_3$ con DDT (líneas verdes), e imágenes TEM de AuNPs (**a**, **e**), AuNSs (**b**, **f**), AuNRs (**c**, **g**) y AgNPs (**d**, **h**).

Los coloides hidrófobos obtenidos resultan estables durante meses y además pueden ser redispersados en diferentes disolventes orgánicos. Usando una mezcla etanol-hexano (1:4) se obtuvieron asimismo extensas monocapas de nanopartículas, que una vez transferidas a soportes sólidos fueron analizadas por TEM, SEM, Vis-NIR y empleadas como substratos para SERS.

La eficiencia SERS de los diferentes substratos se comparó usando ácido 4-mercaptobenzoico (4-MBA) como analito a una concentración de 10 µM. En la **Figura 6.6a** se muestran los espectros SERS obtenidos para los diferentes substratos plasmónicos. Las intensidades más altas corresponden a monocapas de AuNPs y AuNRs, mostrando los substratos de AuNSs y AgNPs intensidades significativamente más bajas. Este comportamiento puede explicarse teniendo en cuenta que, tal como predice el mecanismo electromagnético (EM), los mayores factores de aumento SERS se obtienen al excitar la correspondiente resonancia plasmónica. Debido al acoplamiento plásmonico entre nanopartículas muy próximas, se produce un desplazamiento al rojo de la banda plasmónica cuando las nanopartículas están ensambladas. Precisamente para los subtratos de AuNPs y AuNRs el máximo de la banda plasmónica se encuentra alrededor de 785 nm, que coincide con longitud de onda del láser usado para excitar la muestra. El máximo acoplamiento plasmónico ocurre para los substratos de nanoestrellas, que presentan bandas plasmónicas muy anchas en la zona del IR. Por otro lado, cuando la muestra se ilumina usando otras longitudes de onda los resultados obtenidos son diferentes. De acuerdo otra vez con el mecanismo electromagnético, a 532 y 633 nm las intensidades más altas registradas corresponden a los subtratos AgNPs y AuNPs, respectivamente, no observándose ninguna señal para la muestra de AuNSs.

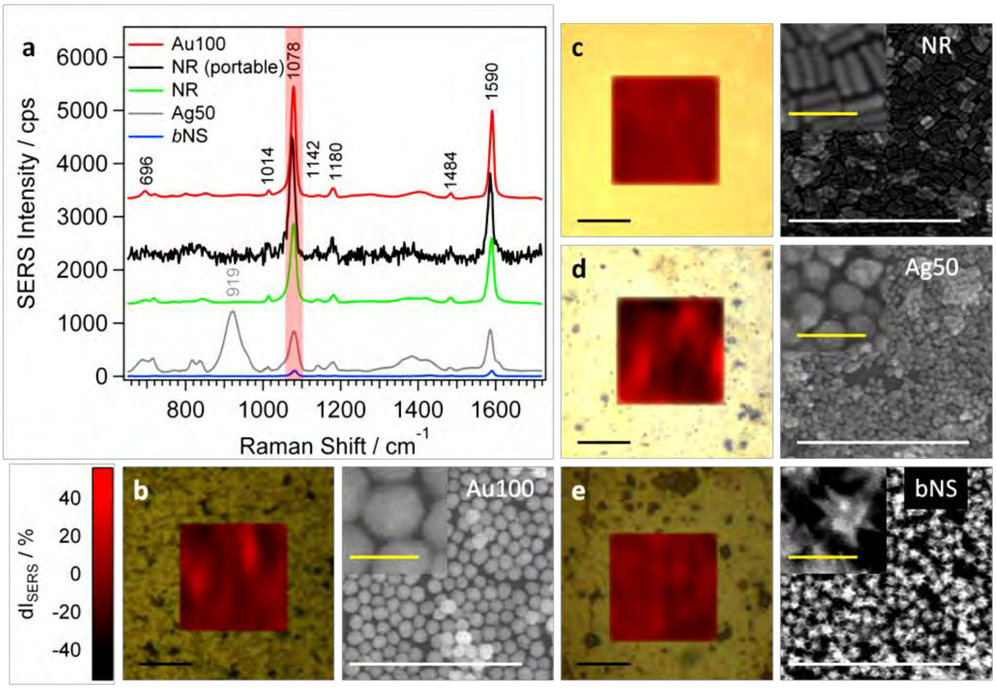

Figure 6.6. (**a**) Espectros SERS de 4-MBA obtenidos usando los distintos sustratos. (**b**-**e**) Mapas SERS de la vibración a 1078 cm^{-1} (banda sombreada en rojo en **a**) e imágenes SEM representativas de cada ensamblaje antes de la incubación con el analito, para AuNPs 100 nm (**b**), AuNRs (**c**), AgNPs 50 nm (**d**) y AuNSs (*big diameter,* **e**). El espectro en negro en **a** fue obtenido sobre la muestra de AuNRs usando un equipo Raman portátil. Escalas en negro, blanco y amarillo: 10 µm, 1µm y 100 nm, respectivamente.

Asimismo, las nanopartículas hidrófobas obtenidas se pueden solubilizar de nuevo en agua mediante recubrimiento con polímeros anfífilos. PMA (anhídrido maleico de poliisobutileno modificado con dodecilamina) es un polímero ampliamente utilizado para estabilizar nanopartículas hidrófobas en medios biológicos. Por lo tanto, AuNSs estabilizadas con dodecanotiol y disueltas en cloroformo fueron recubiertas con PMA y redispersadas en agua gracias a las interacciones hidrófobas entre las cadenas laterales alifáticas del polímero y las moléculas de dodecanotiol que estabilizan la nanoestrella. En la **Figura 6.7** se muestra el espectro Vis-NIR de las nanoestrellas de oro antes y después de la encapsulación polimérica. Se muestra además una imagen de TEM de una muestra con tinción negativa, en la que se puede observar la capa de PMA rodeando a la nanopartícula. Se ha demostrado que este tipo de recubrimientos aporta alta estabilidad coloidal en medios celulares e impide la agregación de las nanopartículas incluso en condiciones extremas de pH y fuerza iónica.

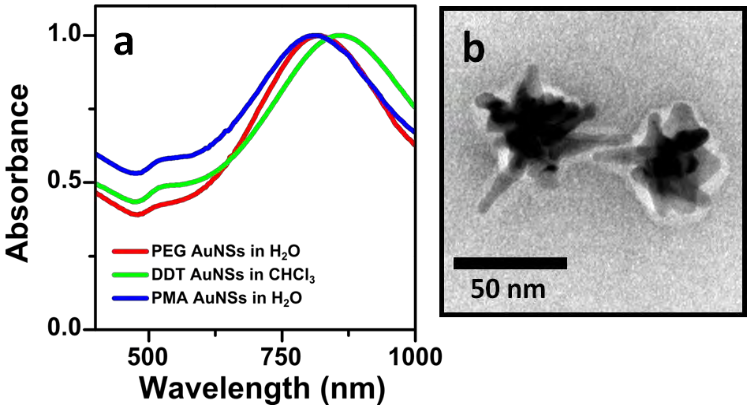

Figura 6.7. (**a**) Espectros Vis-NIR de AuNSs estabilizadas con PEG (rojo), después de ser tranferidas a cloroformo con DDT (verde) y tras ser encapsuladas con el polímero PMA (azul). (**b**) Imagen TEM de AuNSs encapsuladas con PMA tras tinción negativa.

6.4 Nanoestrellas de Oro Codificadas para Multianálisis y Diferenciación de Células Tumorales mediante SERS

En el **Capítulo 4** se describe la preparación de nanomarcadores SERS basados en nanoestrellas de oro y su aplicación para la deteción y diferenciación de células tumorales. Para ello, se emplea una estrategia análoga a la desarrollada en el Capítulo 3. AuNSs estabilizadas con PEG fueron tranferidas a cloroformo empleando en este caso ligandos tiolados que son activos en Raman. Se obtuvieron así partículas hidrófobas y codificadas en SERS, que a su vez pueden ser recubiertas con PMA y solubilizadas en agua. Estos nanocódigos SERS se consideran especialmente interesantes para aplicaciones biológicas[99] en las que es necesario iluminar dentro de la llamada "ventana de transparencia biológica".[263] De este modo, utilizando seis moléculas diferentes activas en Raman (4-MBT, 4-Metilbencenotiol; 4-BPT, 4-fenilbencenotiol; 2-NaT, 2-Naftalenotiol; BT, Bencenotiol; 1-NaT, 1-Naftalenotiol y 4-MP, 4-Mercaptopiridina) se han preparado seis nanomarcadores diferentes que pueden ser claramente diferenciados mediante SERS. Dichos nanomarcadores se utilizaron a continuación para identificar diferentes líneas celulares. En la **Figura 6.8** puede observarse una imagen SERS de macrófagos J774 tras ser incubados individualmente con los diferentes nanocódigos SERS. De la misma forma, usando un co-cultivo más complejo como el formado por 5 lineas diferentes de células tumorales mamarias (HCC1395, MCF-7, CAMA-1, SKBR3 y MDA.MB435S), se ha comprobado el alto potencial de estos nanomarcadores para diferenciar células de forma rápida y eficaz mediante bio-imagen SERS (**Figura 6.9**).

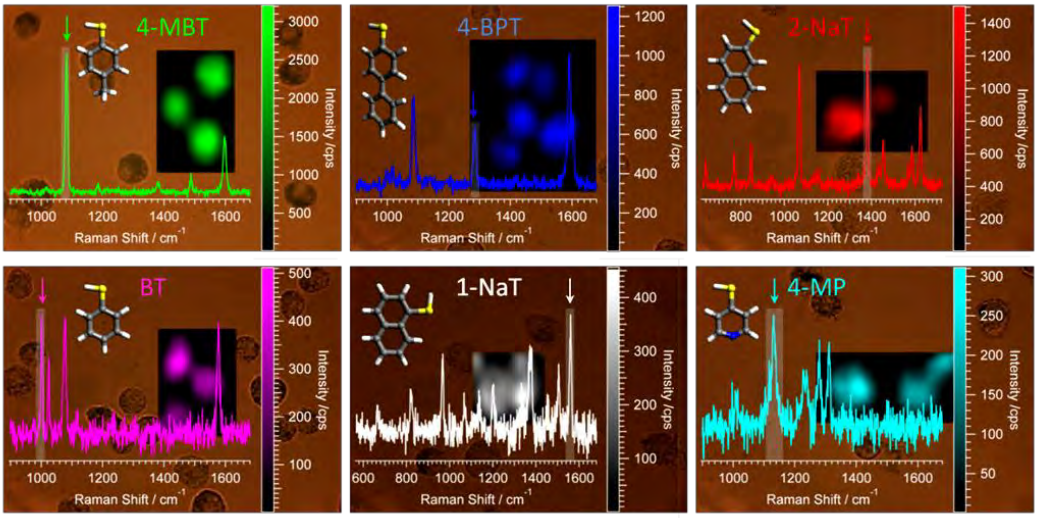

Figura 6.8. Imágenes SERS superpuestas sobre imágenes ópticas de campo claro y combinadas con el espectro SERS de los diferentes nanomarcadores incubados con macrófagos J774. Las flechas indican la vibración específica empleada para generar los correspondientes mapas SERS.

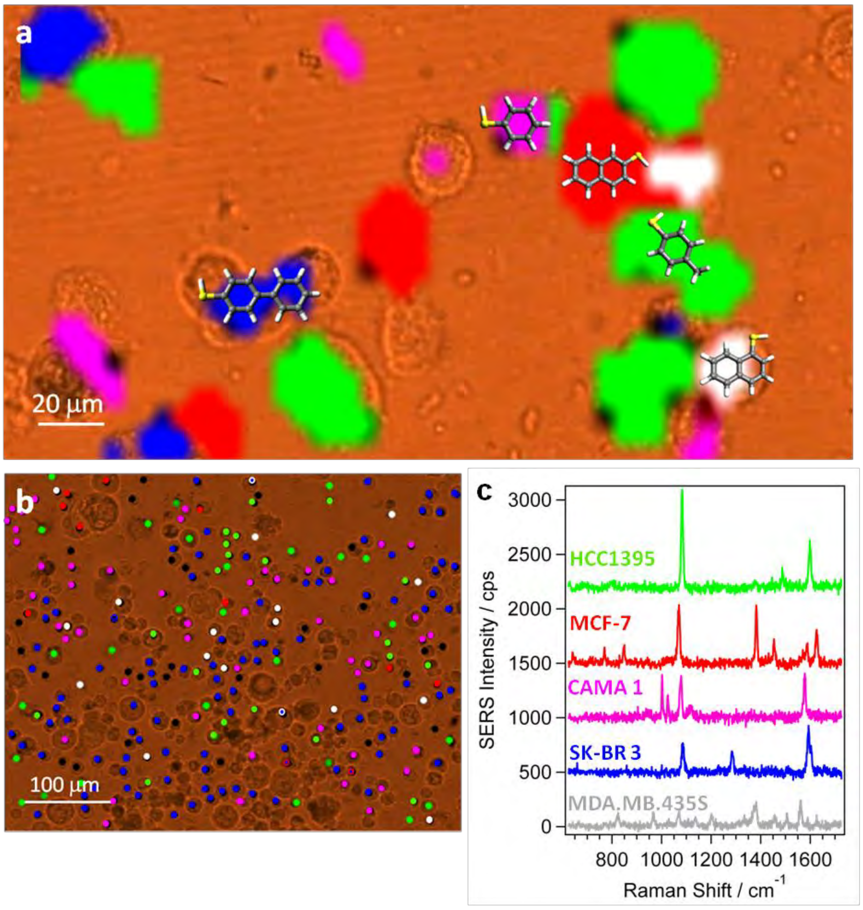

Figura 6.9. (**a**) Imagen SERS de una mezcla quíntuple de células tumorales mamarias. (**b**) Imagen a gran escala (0.12 mm^2) mostrando la diferenciación de 250 células tras medir en cada punto el espectro de referencia de cada nanomarcador, mostrados en (**c**).

6.5 Sistemas de Bio-Imagen Multimodal basados en Microsesferas de Poliestireno Recubiertas con Nanoestrellas de Oro

En el **Capítulo 5** se describe la preparación de partículas plasmónicas híbridas compuestas de una partícula central de poliestireno (PS) fluorescente rodeada de nanoestrellas de oro, las cuales se han aplicado como sistemas de bio-imagen multimodal. Microesferas de poliestireno (diámetro ~475 nm) funcionalizadas con grupos amino han sido empleadas como soportes coloidales para ensamblar AuNSs estabilizadas con PEG. Modificando la relación PS/AuNS se ha conseguido controlar la densidad de AuNSs sobre la superficie polimérica. El recubrimiento plasmónico confiere nuevas propiedades ópticas al núcleo polimérico y se ha demostrado que este tipo de ensamblajes son particularmente interesantes para aplicaciones de SERS. Usando 4-MBA como molécula activa en Raman, se ha comparado la respuesta SERS de diferentes partículas compuestas cuando la densidad de AuNSs es baja, media y alta (**Figura 6.10**). Se ha observado que la muestra con densidad media de estrellas presenta la mayor actividad SERS. Esto podría explicarse teniendo en cuenta que procesos de desactivación de puntos calientes pueden tener lugar cuando hay interacciones punta-punta entre estrellas de distinta geometría y orientación.[306] Además, tal como se explica en el Capítulo 3, monocapas densas de AuNSs generan menor intensidad SERS que aquellas formadas por otras partículas plasmónicas (por ejemplo, nanoesferas o nanobastones de oro).[265]

AuNSs y partículas ensambladas codificadas con 4-MBA han sido internalizadas en células A459. Además, con objeto de aumentar la interación con la membrana celular, se han coadsorbido sobre la superficie polimérica partículas de oro pequeñas funcionalizadas con una mezcla de alcanos (conocidas como *rippled* AuNP, rAuNP).[297] Los resultados muestran intensidades SERS más altas cuando las AuNSs se encuentran ensambladas y también cuando se emplean los nanohíbridos AuNS-rAuNP-PS, lo cual sugiere una mayor internalización celular de estas partículas.

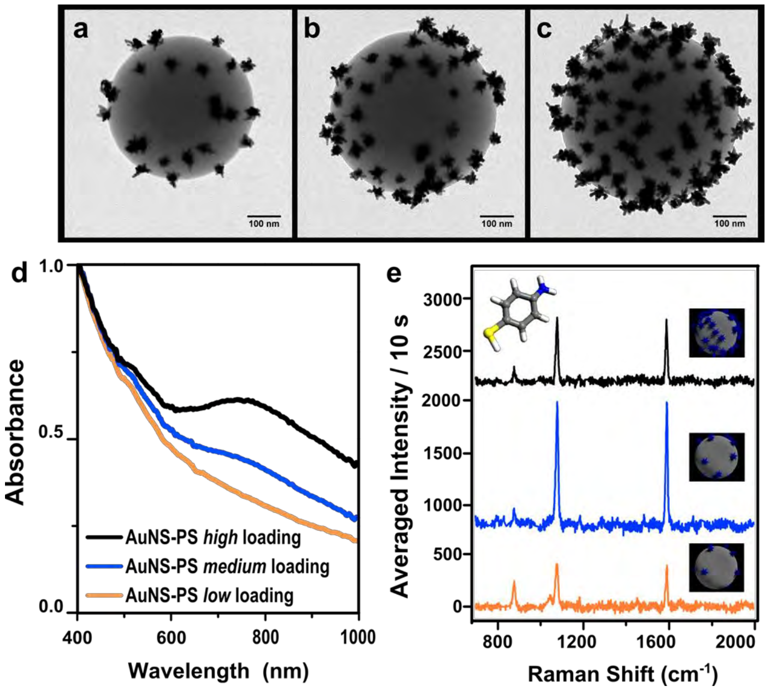

Figura 6.10 Imágenes TEM (**a**-**c**), espectros Vis-NIR (**d**) y SERS de esferas de PS cargadas con diferentes densidades de AuNSs (naranja=densidad de AuNSs baja, azul=media y negra=alta) y marcadas con 4-MBA.

Por otra parte, se han tomado imágenes celulares correlativas usando microscopía confocal-SERS y de campo oscuro (**Figura 6.11**).

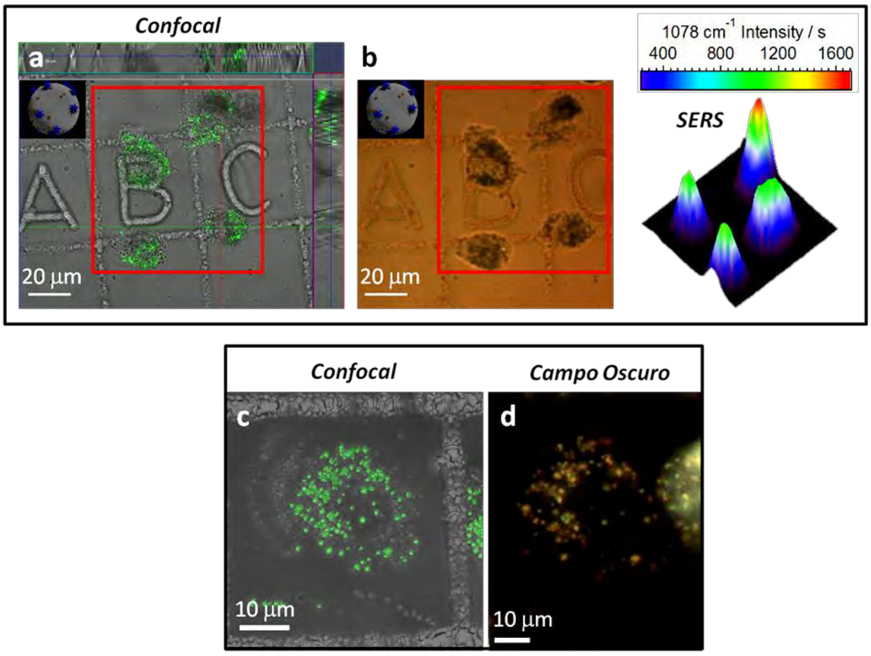

Figura 6. 11 Imágenes correlativas de microscopía confocal-SERS y confocal-campo oscuro de células A459 tras la internalización de partículas AuNS-rAuNP-PS. La imagen (**a**) muestra la emisión entre 500-550 nm del marcador fluorescente incorporado en el PS y (**b**) la transmisión y el mapa 3D de intensidades SERS de la vibración a 1078 cm^{-1} del marcador 4-MBA a 785 nm. (**c**) y (**d**) muestran imágenes correlativas de la misma muestra obtenidas mediante microscopía confocal y de campo oscuro, respectivamente.

En definitiva, la integración de diferentes funcionalidades en una misma partícula ha permitido obtener imágenes de cultivos celulares usando técnicas microscópicas diferentes, pero complementarias entre sí. Los resultados obtenidos confirman la versatilidad de estas partículas como sistemas de bio-imagen multimodal.

6.6 Conclusiones

El desarrollo de esta tesis supone un importante avance en la preparación, funcionalización y estabilización de nanoestrellas de oro, así como en su aplicación como nanomarcadores SERS. Diferentes estrategias han sido desarrolladas para obtener nanoestrellas de oro altamente eficientes en SERS, coloidalmente estables, biocompatibles y con resonancias plasmónicas situadas en la llamada “ventana de transparencia biológica”. Se ha demostrado el alto potencial de estos nanomateriales para realizar bio-imagen SERS *in vitro*. De igual forma, futuras aplicaciones biomédicas dirigidas al diagnóstico y tratamiento de enfermedades podrían desarrollarse también *in* *vivo*. Las conclusiones más relevantes que se pueden extraer de la investigación llevada a cabo durante esta tesis se detallan a continuación.

1. Nanoestrellas de oro han sido funcionalizadas usando una mezcla de ligandos, los cuales estabilizan y además dirigen el crecimiento de una capa de oro externa, formándose así nanoestructuras de geometría muy particular y que presentan puntos calientes internos.
   - **a.** BDT y CTAC se han empleado para estabilizar de forma eficiente AuNSs, evitando la agregación de las partículas así como la oxidación de la superficie de oro.
   - **b.** BDT-AuNSs de diferentes tamaños han sido empleadas como semillas y encapsuladas bajo una cubierta de oro. Se han obtenido diferentes geometrías al variar la relación [Au^{3+}]/ [Au^{0}], R, utilizada. Así, valores altos de R dan lugar a AuNSs totalmente encapsuladas, mientras que se obtienen semiconchas y estructuras tipo Janus al disminuir R. Estos cambios morfológicos se reflejan en los espectros Vis-NIR de las correspondientes nanoestructuras. Además, imágenes de tomografía mediante HAADF-STEM muestran la presencia de huecos nanométricos internos.
   - **c.** Se ha comparado la eficiencia en SERS de las diferentes nanoestructuras. BDT presenta una alta sección eficaz de SERS y además se encuentra atrapada en huecos nanométricos donde se generan campos electromagnéticos de alta intensidad. Los resultados muestran una mayor eficiencia SERS para las nanoestructuras obtenidas con forma de semiconcha.
   - **d.** Estas partículas codificadas podrían utilizarse como nanomarcadores eficientes en futuras aplicaciones de bio-imagen y detección por SERS.
2. Nanoestrellas de oro así como otras partículas plasmónicas (nanobastones de oro y nanoesferas de oro y plata) han sido estabilizadas en medio orgánico y ensambladas en monocapas activas en SERS.

a. Usando PEG-SH como pre-estabilizante y DDT como ligando hidrófobo se ha conseguido transferir con éxito a medio orgánico las diferentes partículas plasmónicas. De acuerdo con las imágenes TEM y los espectros Vis-NIR de los organosoles obtenidos, las nanopartículas permanecen estables y bien dispersas después de la transferencia de fase. En el caso de las AuNSs, gracias al recubrimiento tiolado, se consigue evitar la oxidación de las puntas de oro y mantener así la geometría estrellada.

b. Estas partículas hidrófobas pueden dispersarse en diferentes solventes orgánicos y ser ensambladas en extensas monocapas cuando se emplean mezclas de etanol-hexano. De esta forma, se han podido fabricar diferentes substratos plasmónicos para SERS. Usando como analito la molécula de 4-MBA, se ha comprobado que películas formadas por nanoesferas y nanobastones de oro dan lugar a intensidades SERS más altas. Esto puede explicarse considerando el fuerte acoplamiento plasmónico que se produce cuando las partículas se encuentran muy próximas entre sí, lo cual provoca en ciertas estructuras (nanoestrellas principalmente) un notable desplazamiento de la banda plasmónica hacia el IR, de forma que deja de estar en resonancia con la longitud de onda de excitación.

c. Por otra parte, estas partículas hidrófobas pueden recubrirse también con polímiros anfifílicos. PMA ha sido empleado para obtener AuNSs solubles en agua y estables en condidiones biológicas.

3. Se han preparado nanoestrellas de oro codificadas, las cuales se han utilizado como nanomarcadores para diferenciar células tumorales mediante SERS.

a. AuNSs estabilizadas con PEG-SH han sido funcionalizadas con diferentes ligandos tiolados activos en SERS. Estos marcadores Raman, todos ellos solubles en medio orgánico, pueden inducir la tranferencia de fase de las AuNSs. El recubrimiento adicional con PMA permite obtener AuNSs codificadas, las cuales son nanomarcadores-SERS ideales para aplicaciones biológicas.

   b. Se ha comparado la eficiencia SERS de nanomarcadores basados en AuNPs y AuNSs. Se ha confirmado que partículas esféricas aisladas no son activas en SERS cuando se emplea radiación NIR. Por tanto, AuNSs cuyas respuestas ópticas se encuentran en el NIR y que presentan altos campos EM localizados en sus puntas, pueden ser utilizadas para aplicaciones de SERS en biología.

   c. Se han empleado siferentes AuNSs codificadas para obtener bio-imágenes SERS de diferentes líneas celulares, demostrándose además la eficacia de este sistema para diferenciar cultivos celulares complejos, como el formado por una mezcla quíntuple de células tumorales mamarias.

4. Se han fabricado marcadores bifuncionales compuestos de microesferas fluorescentes de poliestireno y nanoestrellas de oro, los cuales poseen un alto potencial para aplicaciones en bio-imagen multimodal.

   a. AuNSs estabilizadas con PEG-SH han sido ensambladas sobre microesferas de PS fluorescente funcionalizadas con grupos amino. Debido a la interacción favorable entre el oro y los grupos $–NH_2$, se ha conseguido decorar totalmente la superficie de PS con partículas estrelladas. Además, ajustando la relación AuNS/PS se ha podido controlar la densidad de AuNSs sobre la superfice polimérica.

   b. La eficiencia en SERS de los diferentes ensamblajes se ha comparado usando 4-MBA. Los resultados muestran que densidades intermedias de AuNSs son más favorables para SERS.

   c. Estos nanomarcadores fluorescentes y SERS-activos han sido internalizados en células A459. Utilizando microscopía confocal y SERS se han podido obtener bio-imágenes correlativas de células vivas. Además, debido a que estas partículas dispersan fuertemente la luz, también se han podido obtener imágenes de células usando microscopía de campo oscuro, lo cual confirma la alta versatilidad de estos nanomarcadores como sistemas de bio-imagen multimodal.

References

1. Liz-Marzán, L. M., Murphy, C. J. & Wang, J. Nanoplasmonics. *Chem. Soc. Rev.* **43,** 3820–3822 (2014).
2. *Surface Plasmons on Smooth and Rough Surfaces and on Gratings*. **111,** (Springer Berlin Heidelberg, 1988).
3. Craig F. Bohren, D. R. H. *Absorption and Scattering of Light by Small Particles*. (Wiley-VCH Verlag GmbH, 1998).
4. Webb, J. A. & Bardhan, R. Emerging advances in nanomedicine with engineered gold nanostructures. *Nanoscale* **6,** 2502–2530 (2014).
5. Anker, J. N. *et al.* Biosensing with plasmonic nanosensors. *Nat. Mater.* **7,** 442–453 (2008).
6. Atwater, H. A. & Polman, A. Plasmonics for improved photovoltaic devices. *Nat. Mater.* **9,** 205–213 (2010).
7. Mukherjee, S. *et al.* Hot Electrons Do the Impossible: Plasmon-Induced Dissociation of H2 on Au. *Nano Lett.* **13,** 240–247 (2013).
8. Zijlstra, P., Chon, J. W. M. & Gu, M. Five-dimensional optical recording mediated by surface plasmons in gold nanorods. *Nature* **459,** 410–413 (2009).
9. Pastoriza-Santos, I., Sánchez-Iglesias, A., Rodríguez-González, B. & Liz-Marzán, L. M. Aerobic Synthesis of Cu Nanoplates with Intense Plasmon Resonances. *Small* **5,** 440–443 (2009).
10. Knight, M. W. *et al.* Aluminum for Plasmonics. *ACS Nano* **8,** 834–840 (2014).

11. Liu, X. & T. Swihart, M. Heavily-doped colloidal semiconductor and metal oxide nanocrystals: an emerging new class of plasmonic nanomaterials. *Chem. Soc. Rev.* **43,** 3908–3920 (2014).
12. Comin, A. & Manna, L. New materials for tunable plasmonic colloidal nanocrystals. *Chem. Soc. Rev.* **43,** 3957–3975 (2014).
13. García de Abajo, F. J. Graphene Plasmonics: Challenges and Opportunities. *ACS Photonics* **1,** 135–152 (2014).
14. Eustis, S. & El-Sayed, M. A. Why gold nanoparticles are more precious than pretty gold: Noble metal surface plasmon resonance and its enhancement of the radiative and nonradiative properties of nanocrystals of different shapes. *Chem. Soc. Rev.* **35,** 209 (2006).
15. Dreaden, E. C., Alkilany, A. M., Huang, X., Murphy, C. J. & El-Sayed, M. A. The golden age: gold nanoparticles for biomedicine. *Chem. Soc. Rev.* **41,** 2740–2779 (2012).
16. Freestone, I., Meeks, N., Sax, M. & Higgitt, C. The Lycurgus Cup — A Roman nanotechnology. *Gold Bull.* **40,** 270–277 (2007).
17. Faraday, M. The Bakerian Lecture: Experimental Relations of Gold (and Other Metals) to Light. *Philos. Trans. R. Soc. Lond.* **147,** 145–181 (1857).
18. Turkevich, J., Stevenson, P. C. & Hillier, J. A study of the nucleation and growth processes in the synthesis of colloidal gold. *Discuss. Faraday Soc.* **11,** 55–75 (1951).
19. Gong, J., Li, G. & Tang, Z. Self-assembly of noble metal nanocrystals: Fabrication, optical property, and application. *Nano Today* **7,** 564–585 (2012).

20. Li, N., Zhao, P. & Astruc, D. Anisotropic Gold Nanoparticles: Synthesis, Properties, Applications, and Toxicity. *Angew. Chem. Int. Ed.* **53,** 1756–1789 (2014).

21. Grzelczak, M., Pérez-Juste, J., Mulvaney, P. & Liz-Marzán, L. M. Shape control in gold nanoparticle synthesis. *Chem. Soc. Rev.* **37,** 1783–1791 (2008).

22. Yuan, H., Fales, A. M., Khoury, C. G., Liu, J. & Vo-Dinh, T. Spectral characterization and intracellular detection of Surface-Enhanced Raman Scattering (SERS)-encoded plasmonic gold nanostars. *J. Raman Spectrosc.* **44,** 234–239 (2013).

23. Carbert, J. Gold-based enamel colours. *Gold Bull.* **13,** 144–150 (1980).

24. Murphy, C. J. *et al.* Anisotropic Metal Nanoparticles: Synthesis, Assembly, and Optical Applications. *J. Phys. Chem. B* **109,** 13857–13870 (2005).

25. Jana, N. R., Gearheart, L. & Murphy, C. J. Seed-Mediated Growth Approach for Shape-Controlled Synthesis of Spheroidal and Rod-like Gold Nanoparticles Using a Surfactant Template. *Adv. Mater.* **13,** 1389–1393 (2001).

26. Nikoobakht, B. & El-Sayed, M. A. Preparation and Growth Mechanism of Gold Nanorods (NRs) Using Seed-Mediated Growth Method. *Chem. Mater.* **15,** 1957–1962 (2003).

27. Gole, A. & Murphy, C. J. Seed-Mediated Synthesis of Gold Nanorods: Role of the Size and Nature of the Seed. *Chem. Mater.* **16,** 3633–3640 (2004).

28. Carbó-Argibay, E. *et al.* Chemical Sharpening of Gold Nanorods: The Rod-to-Octahedron Transition. *Angew. Chem.* **119,** 9141–9145 (2007).

29. Millstone, J. E., Wei, W., Jones, M. R., Yoo, H. & Mirkin, C. A. Iodide Ions Control Seed-Mediated Growth of Anisotropic Gold Nanoparticles. *Nano Lett.* **8,** 2526–2529 (2008).

30. Huang, X., Neretina, S. & El-Sayed, M. A. Gold Nanorods: From Synthesis and Properties to Biological and Biomedical Applications. *Adv. Mater.* **21,** 4880–4910 (2009).

31. Scarabelli, L., Grzelczak, M. & Liz-Marzán, L. M. Tuning Gold Nanorod Synthesis through Prereduction with Salicylic Acid. *Chem. Mater.* **25,** 4232–4238 (2013).

32. Carbó-Argibay, E. *et al.* The Crystalline Structure of Gold Nanorods Revisited: Evidence for Higher-Index Lateral Facets. *Angew. Chem. Int. Ed.* **49,** 9397–9400 (2010).

33. Goris, B. *et al.* Atomic-scale determination of surface facets in gold nanorods. *Nat. Mater.* **11,** 930–935 (2012).

34. Johnson, C. J., Dujardin, E., Davis, S. A., Murphy, C. J. & Mann, S. Growth and form of gold nanorods prepared by seed-mediated, surfactant-directed synthesis. *J. Mater. Chem.* **12,** 1765–1770 (2002).

35. Liu, M. & Guyot-Sionnest, P. Mechanism of silver(I)-assisted growth of gold nanorods and bipyramids. *J. Phys. Chem. B* **109,** 22192–22200 (2005).

36. Ming, T. *et al.* Growth of Tetrahexahedral Gold Nanocrystals with High-Index Facets. *J. Am. Chem. Soc.* **131,** 16350–16351 (2009).

37. Li, J. *et al.* Synthesis of tetrahexahedral Au nanocrystals with exposed high-index surfaces. *Chem. Commun.* **46,** 5109–5111 (2010).

38. Katz-Boon, H. *et al.* Three-Dimensional Morphology and Crystallography of Gold Nanorods. *Nano Lett.* **11,** 273–278 (2011).

39. Guerrero-Martínez, A., Barbosa, S., Pastoriza-Santos, I. & Liz-Marzán, L. M. Nanostars shine bright for you: Colloidal synthesis, properties and applications of

branched metallic nanoparticles. *Curr. Opin. Colloid Interface Sci.* **16,** 118–127 (2011).

40. Chen, S., Wang, Z. L., Ballato, J., Foulger, S. H. & Carroll, D. L. Monopod, Bipod, Tripod, and Tetrapod Gold Nanocrystals. *J. Am. Chem. Soc.* **125,** 16186–16187 (2003).

41. Sau, T. K. & Murphy, C. J. Room Temperature, High-Yield Synthesis of Multiple Shapes of Gold Nanoparticles in Aqueous Solution. *J. Am. Chem. Soc.* **126,** 8648–8649 (2004).

42. Nehl, C. L., Liao, H. & Hafner, J. H. Optical Properties of Star-Shaped Gold Nanoparticles. *Nano Lett.* **6,** 683–688 (2006).

43. Wu, H.-L., Chen, C.-H. & Huang, M. H. Seed-Mediated Synthesis of Branched Gold Nanocrystals Derived from the Side Growth of Pentagonal Bipyramids and the Formation of Gold Nanostars. *Chem. Mater.* **21,** 110–114 (2009).

44. Yuan, H. *et al.* Shape and SPR Evolution of Thorny Gold Nanoparticles Promoted by Silver Ions. *Chem. Mater.* **19,** 1592–1600 (2007).

45. Pastoriza-Santos, I. & Liz-Marzán, L. M. N,N-Dimethylformamide as a Reaction Medium for Metal Nanoparticle Synthesis. *Adv. Funct. Mater.* **19,** 679–688 (2009).

46. Senthil Kumar, P., Pastoriza-Santos, I., Rodríguez-González, B., Javier García de Abajo, F. & Liz-Marzán, L. M. High-yield synthesis and optical response of gold nanostars. *Nanotechnology* **19,** 015606 (2008).

47. Barbosa, S. *et al.* Tuning Size and Sensing Properties in Colloidal Gold Nanostars. *Langmuir* **26,** 14943–14950 (2010).

48. Pazos-Pérez, N. *et al.* Growth of Sharp Tips on Gold Nanowires Leads to Increased Surface-Enhanced Raman Scattering Activity. *J. Phys. Chem. Lett.* **1,** 24–27 (2010).
49. Novikov, S. M. *et al.* Gold Spiky Nanodumbbells: Anisotropy in Gold Nanostars. *Part. Part. Syst. Charact.* **31,** 77–80 (2014).
50. Yuan, H. *et al.* Gold nanostars: surfactant-free synthesis, 3D modelling, and two-photon photoluminescence imaging. *Nanotechnology* **23,** 075102 (2012).
51. Nalbant Esenturk, E. & Hight Walker, A. R. Surface-enhanced Raman scattering spectroscopy via gold nanostars. *J. Raman Spectrosc.* **40,** 86–91 (2009).
52. Grzelczak, M., Pérez-Juste, J., Mulvaney, P. & Liz-Marzán, L. M. Shape control in gold nanoparticle synthesis. *Chem. Soc. Rev.* **37,** 1783 (2008).
53. Grzelczak, M. *et al.* Influence of Iodide Ions on the Growth of Gold Nanorods: Tuning Tip Curvature and Surface Plasmon Resonance. *Adv. Funct. Mater.* **18,** 3780–3786 (2008).
54. Rodríguez-Fernández, D., Altantzis, T., Heidari, H., Bals, S. & M. Liz-Marzán, L. A protecting group approach toward synthesis of Au–silica Janus nanostars. *Chem. Commun.* **50,** 79–81 (2014).
55. Sanz-Ortiz, M. N., Sentosun, K., Bals, S. & Liz-Marzán, L. M. Templated Growth of Surface Enhanced Raman Scattering-Active Branched Gold Nanoparticles within Radial Mesoporous Silica Shells. *ACS Nano* (2015). doi:10.1021/acsnano.5b04744
56. Kim, F., Connor, S., Song, H., Kuykendall, T. & Yang, P. Platonic Gold Nanocrystals. *Angew. Chem. Int. Ed.* **43,** 3673–3677 (2004).
57. Sánchez-Iglesias, A. *et al.* Synthesis and Optical Properties of Gold Nanodecahedra with Size Control. *Adv. Mater.* **18,** 2529–2534 (2006).

58. Lofton, C. & Sigmund, W. Mechanisms Controlling Crystal Habits of Gold and Silver Colloids. *Adv. Funct. Mater.* **15,** 1197–1208 (2005).

59. Scarabelli, L., Coronado-Puchau, M., Giner-Casares, J. J., Langer, J. & Liz-Marzán, L. M. Monodisperse Gold Nanotriangles: Size Control, Large-Scale Self-Assembly, and Performance in Surface-Enhanced Raman Scattering. *ACS Nano* **8,** 5833–5842 (2014).

60. Paul, A. *et al.* Identification of Higher Order Long-Propagation-Length Surface Plasmon Polariton Modes in Chemically Prepared Gold Nanowires. *ACS Nano* **6,** 8105–8113 (2012).

61. SKRABALAK, S. E. *et al.* Gold Nanocages: Synthesis, Properties, and Applications. *Acc. Chem. Res.* **41,** 1587–1595 (2008).

62. Vega, M. M. *et al.* Long-term stability of surfactant-free gold nanostars. *J. Nanoparticle Res.* **16,** 1–6 (2014).

63. Sperling, R. A. & Parak, W. J. Surface modification, functionalization and bioconjugation of colloidal inorganic nanoparticles. *Philos. Transact. A Math. Phys. Eng. Sci.* **368,** 1333–1383 (2010).

64. Love, J. C., Estroff, L. A., Kriebel, J. K., Nuzzo, R. G. & Whitesides, G. M. Self-assembled monolayers of thiolates on metals as a form of nanotechnology. *Chem. Rev.* **105,** 1103–1169 (2005).

65. Lin, S.-Y., Tsai, Y.-T., Chen, C.-C., Lin, C.-M. & Chen, C. Two-Step Functionalization of Neutral and Positively Charged Thiols onto Citrate-Stabilized Au Nanoparticles. *J. Phys. Chem. B* **108,** 2134–2139 (2004).

66. Alkilany, A. M. *et al.* Cellular Uptake and Cytotoxicity of Gold Nanorods: Molecular Origin of Cytotoxicity and Surface Effects. *Small* **5,** 701–708 (2009).

67. Yang, J., Lee, J. Y. & Ying, J. Y. Phase transfer and its applications in nanotechnology. *Chem. Soc. Rev.* **40,** 1672 (2011).

68. Zhang, F. *et al.* Polymer-coated nanoparticles: a universal tool for biolabelling experiments. *Small* **7,** 3113–3127 (2011).

69. Pellegrino, T. *et al.* Hydrophobic Nanocrystals Coated with an Amphiphilic Polymer Shell: A General Route to Water Soluble Nanocrystals. *Nano Lett.* **4,** 703–707 (2004).

70. Jiang, S. *et al.* Surface-functionalized nanoparticles for biosensing and imaging-guided therapeutics. *Nanoscale* **5,** 3127–3148 (2013).

71. Liz-Marzán, L. M., Giersig, M. & Mulvaney, P. Synthesis of Nanosized Gold−Silica Core−Shell Particles. *Langmuir* **12,** 4329–4335 (1996).

72. Kim, J. Y., Yoon, S. B. & Yu, J.-S. Fabrication of nanocapsules with Au particles trapped inside carbon and silica nanoporous shells. *Chem. Commun.* 790–791 (2003). doi:10.1039/B211714B

73. Guerrero-Martínez, A., Pérez-Juste, J. & Liz-Marzán, L. M. Recent Progress on Silica Coating of Nanoparticles and Related Nanomaterials. *Adv. Mater.* **22,** 1182–1195 (2010).

74. Cho, E. C., Au, L., Zhang, Q. & Xia, Y. The Effects of Size, Shape, and Surface Functional Group of Gold Nanostructures on Their Adsorption and Internalization by Cells. *Small* **6,** 517–522 (2010).

75. Cobley, C. M., Chen, J., Cho, E. C., Wang, L. V. & Xia, Y. Gold nanostructures: a class of multifunctional materials for biomedical applications. *Chem. Soc. Rev.* **40,** 44 (2011).

76. Wiley: Absorption and Scattering of Light by Small Particles - Craig F. Bohren, Donald R. Huffman. at <http://eu.wiley.com/WileyCDA/WileyTitle/productCd-0471293407.html>

77. Willets, K. A. & Van Duyne, R. P. Localized Surface Plasmon Resonance Spectroscopy and Sensing. *Annu. Rev. Phys. Chem.* **58,** 267–297 (2007).

78. Mie, G. Beiträge zur Optik trüber Medien, speziell kolloidaler Metallösungen. *Ann. Phys.* **330,** 377–445 (1908).

79. Light scattering by small particles. By H. C. van de Hulst. New York (John Wiley and Sons), London (Chapman and Hall), 1957. Pp. xiii, 470; 103 Figs.; 46 Tables. 96s. *Q. J. R. Meteorol. Soc.* **84,** 198–199 (1958).

80. Gans, R. Über die Form ultramikroskopischer Goldteilchen. *Ann. Phys.* **342,** 881–900 (1912).

81. Kreibig, U. & Vollmer, M. *Optical Properties of Metal Clusters*. **25,** (Springer Berlin Heidelberg, 1995).

82. Jain, P. K., Lee, K. S., El-Sayed, I. H. & El-Sayed, M. A. Calculated Absorption and Scattering Properties of Gold Nanoparticles of Different Size, Shape, and Composition: Applications in Biological Imaging and Biomedicine. *J. Phys. Chem. B* **110,** 7238–7248 (2006).

83. García de Abajo, F. J. & Howie, A. Relativistic Electron Energy Loss and Electron-Induced Photon Emission in Inhomogeneous Dielectrics. *Phys. Rev. Lett.* **80,** 5180–5183 (1998).

84. Draine, B. T. & Flatau, P. J. Discrete-Dipole Approximation For Scattering Calculations. *JOSA A* **11,** 1491–1499 (1994).

85. Myroshnychenko, V. *et al.* Modeling the Optical Response of Highly Faceted Metal Nanoparticles with a Fully 3D Boundary Element Method. *Adv. Mater.* **20,** 4288–4293 (2008).
86. Hao, F., Nehl, C. L., Hafner, J. H. & Nordlander, P. Plasmon Resonances of a Gold Nanostar. *Nano Lett.* **7,** 729–732 (2007).
87. Liz-Marzán, L. M. Tailoring Surface Plasmons through the Morphology and Assembly of Metal Nanoparticles. *Langmuir* **22,** 32–41 (2006).
88. Sosa, I. O., Noguez, C. & Barrera, R. G. Optical Properties of Metal Nanoparticles with Arbitrary Shapes. *J. Phys. Chem. B* **107,** 6269–6275 (2003).
89. Kelly, K. L., Coronado, E., Zhao, L. L. & Schatz, G. C. The Optical Properties of Metal Nanoparticles: The Influence of Size, Shape, and Dielectric Environment. *J. Phys. Chem. B* **107,** 668–677 (2003).
90. de Aberasturi, D. J., Serrano-Montes, A. B. & Liz-Marzán, L. M. Modern Applications of Plasmonic Nanoparticles: From Energy to Health. *Adv. Opt. Mater.* **3,** 602–617 (2015).
91. *Surface-Enhanced Raman Scattering*. **103,** (Springer Berlin Heidelberg, 2006).
92. Stiles, P. L., Dieringer, J. A., Shah, N. C. & Van Duyne, R. P. Surface-Enhanced Raman Spectroscopy. *Annu. Rev. Anal. Chem.* **1,** 601–626 (2008).
93. Kneipp, K., Kneipp, H., Itzkan, I., Dasari, R. R. & Feld, M. S. Ultrasensitive chemical analysis by Raman spectroscopy. *Chem. Rev.* **99,** 2957–2976 (1999).
94. Jeanmaire, D. L. & Van Duyne, R. P. Surface raman spectroelectrochemistry: Part I. Heterocyclic, aromatic, and aliphatic amines adsorbed on the anodized silver electrode. *J. Electroanal. Chem. Interfacial Electrochem.* **84,** 1–20 (1977).

95. Kambhampati, P., Child, C. M., Foster, M. C. & Campion, A. On the chemical mechanism of surface enhanced Raman scattering: Experiment and theory. *J. Chem. Phys.* **108,** 5013–5026 (1998).

96. Michaels, A. M., Jiang & Brus, L. Ag Nanocrystal Junctions as the Site for Surface-Enhanced Raman Scattering of Single Rhodamine 6G Molecules. *J. Phys. Chem. B* **104,** 11965–11971 (2000).

97. Schlücker, S. Surface-Enhanced Raman Spectroscopy: Concepts and Chemical Applications. *Angew. Chem. Int. Ed.* **53,** 4756–4795 (2014).

98. Sharma, B., Frontiera, R. R., Henry, A.-I., Ringe, E. & Van Duyne, R. P. SERS: Materials, applications, and the future. *Mater. Today* **15,** 16–25 (2012).

99. Wang, Y., Yan, B. & Chen, L. SERS Tags: Novel Optical Nanoprobes for Bioanalysis. *Chem. Rev.* **113,** 1391–1428 (2013).

100. Kleinman, S. L., Frontiera, R. R., Henry, A.-I., Dieringer, J. A. & Duyne, R. P. V. Creating, characterizing, and controlling chemistry with SERS hot spots. *Phys. Chem. Chem. Phys.* **15,** 21–36 (2012).

101. Bryant, G. W., García de Abajo, F. J. & Aizpurua, J. Mapping the Plasmon Resonances of Metallic Nanoantennas. *Nano Lett.* **8,** 631–636 (2008).

102. Nelayah, J. *et al.* Mapping surface plasmons on a single metallic nanoparticle. *Nat. Phys.* **3,** 348–353 (2007).

103. Rodríguez-Lorenzo, L. *et al.* Zeptomol Detection Through Controlled Ultrasensitive Surface-Enhanced Raman Scattering. *J. Am. Chem. Soc.* **131,** 4616–4618 (2009).

104. Shiohara, A., Wang, Y. & Liz-Marzán, L. M. Recent approaches toward creation of hot spots for SERS detection. *J. Photochem. Photobiol. C Photochem. Rev.* **21,** 2–25 (2014).

105. Hrelescu, C., Sau, T. K., Rogach, A. L., Jäckel, F. & Feldmann, J. Single gold nanostars enhance Raman scattering. *Appl. Phys. Lett.* **94,** 153113 (2009).

106. Hrelescu, C. *et al.* Selective Excitation of Individual Plasmonic Hotspots at the Tips of Single Gold Nanostars. *Nano Lett.* **11,** 402–407 (2011).

107. Allgeyer, E. S., Pongan, A., Browne, M. & Mason, M. D. Optical Signal Comparison of Single Fluorescent Molecules and Raman Active Gold Nanostars. *Nano Lett.* **9,** 3816–3819 (2009).

108. Aslan, K., Wu, M., Lakowicz, J. R. & Geddes, C. D. Metal Enhanced Fluorescence Solution-based Sensing Platform 2: Fluorescent Core-Shell Ag@SiO2 Nanoballs. *J. Fluoresc.* **17,** 127–131 (2007).

109. Sepúlveda, B., Angelomé, P. C., Lechuga, L. M. & Liz-Marzán, L. M. LSPR-based nanobiosensors. *Nano Today* **4,** 244–251 (2009).

110. Huang, X., Jain, P. K., El-Sayed, I. H. & El-Sayed, M. A. Plasmonic photothermal therapy (PPTT) using gold nanoparticles. *Lasers Med. Sci.* **23,** 217–228 (2007).

111. Carregal-Romero, S. *et al.* NIR-light triggered delivery of macromolecules into the cytosol. *J. Control. Release Off. J. Control. Release Soc.* **159,** 120–127 (2012).

112. Obare, S. O., Hollowell, R. E. & Murphy, C. J. Sensing Strategy for Lithium Ion Based on Gold Nanoparticles. *Langmuir* **18,** 10407–10410 (2002).

113. Lee, J.-S., Han, M. S. & Mirkin, C. A. Colorimetric detection of mercuric ion (Hg2+) in aqueous media using DNA-functionalized gold nanoparticles. *Angew. Chem. Int. Ed Engl.* **46,** 4093–4096 (2007).

114. Saha, K., Agasti, S. S., Kim, C., Li, X. & Rotello, V. M. Gold Nanoparticles in Chemical and Biological Sensing. *Chem. Rev.* **112,** 2739–2779 (2012).

115. Elghanian, R., Storhoff, J. J., Mucic, R. C., Letsinger, R. L. & Mirkin, C. A. Selective Colorimetric Detection of Polynucleotides Based on the Distance-

Dependent Optical Properties of Gold Nanoparticles. *Science* **277,** 1078–1081 (1997).

116. Li & Rothberg, L. J. Label-Free Colorimetric Detection of Specific Sequences in Genomic DNA Amplified by the Polymerase Chain Reaction. *J. Am. Chem. Soc.* **126,** 10958–10961 (2004).
117. Pan, B. *et al.* End-to-end self-assembly and colorimetric characterization of gold nanorods and nanospheres via oligonucleotide hybridization. *Nanotechnology* **16,** 1776 (2005).
118. Hone, D. C., Haines, A. H. & Russell, D. A. Rapid, Quantitative Colorimetric Detection of a Lectin Using Mannose-Stabilized Gold Nanoparticles. *Langmuir* **19,** 7141–7144 (2003).
119. Lee, K.-S. & El-Sayed, M. A. Gold and Silver Nanoparticles in Sensing and Imaging: Sensitivity of Plasmon Response to Size, Shape, and Metal Composition. *J. Phys. Chem. B* **110,** 19220–19225 (2006).
120. Marinakos, S. M., Chen, S. & Chilkoti, A. Plasmonic Detection of a Model Analyte in Serum by a Gold Nanorod Sensor. *Anal. Chem.* **79,** 5278–5283 (2007).
121. Haes, A. J., Hall, W. P., Chang, L., Klein, W. L. & Van Duyne, R. P. A Localized Surface Plasmon Resonance Biosensor: First Steps toward an Assay for Alzheimer's Disease. *Nano Lett.* **4,** 1029–1034 (2004).
122. Dasary, S. S. R., Singh, A. K., Senapati, D., Yu, H. & Ray, P. C. Gold Nanoparticle Based Label-Free SERS Probe for Ultrasensitive and Selective Detection of Trinitrotoluene. *J. Am. Chem. Soc.* **131,** 13806–13812 (2009).
123. Huang, X., El-Sayed, I. H., Qian, W. & El-Sayed, M. A. Cancer Cells Assemble and Align Gold Nanorods Conjugated to Antibodies to Produce Highly Enhanced,

Sharp, and Polarized Surface Raman Spectra: A Potential Cancer Diagnostic Marker. *Nano Lett.* **7,** 1591–1597 (2007).

124. Wang, Y. & Schlücker, S. Rational design and synthesis of SERS labels. *Analyst* **138,** 2224–2238 (2013).
125. Cao, Y. C., Jin, R. & Mirkin, C. A. Nanoparticles with Raman spectroscopic fingerprints for DNA and RNA detection. *Science* **297,** 1536–1540 (2002).
126. Qian, X. *et al.* In vivo tumor targeting and spectroscopic detection with surface-enhanced Raman nanoparticle tags. *Nat. Biotechnol.* **26,** 83–90 (2008).
127. Yang, M. *et al.* Development of Polymer-Encapsulated Metal Nanoparticles as Surface-Enhanced Raman Scattering Probes. *Small* **5,** 198–202 (2009).
128. Bodelón, G. *et al.* Au@pNIPAM SERRS Tags for Multiplex Immunophenotyping Cellular Receptors and Imaging Tumor Cells. *Small* n/a–n/a (2015). doi:10.1002/smll.201500269
129. Yuan, H. *et al.* Quantitative SERRS Multiplexing of Biocompatible Gold Nanostars for in vitro and ex vivo detection. *Anal. Chem.* **85,** 208–212 (2013).
130. Mulvaney, S. P., Musick, M. D., Keating, C. D. & Natan, M. J. Glass-Coated, Analyte-Tagged Nanoparticles: A New Tagging System Based on Detection with Surface-Enhanced Raman Scattering. *Langmuir* **19,** 4784–4790 (2003).
131. Küstner, B. *et al.* SERS Labels for Red Laser Excitation: Silica-Encapsulated SAMs on Tunable Gold/Silver Nanoshells. *Angew. Chem. Int. Ed.* **48,** 1950–1953 (2009).
132. Rodríguez-Lorenzo, L. *et al.* Intracellular mapping with SERS-encoded gold nanostars. *Integr. Biol.* **3,** 922–926 (2011).

133. Wang, G. *et al.* Detection of the Potential Pancreatic Cancer Marker MUC4 in Serum Using Surface-Enhanced Raman Scattering. *Anal. Chem.* **83,** 2554–2561 (2011).

134. Ryu, K. *et al.* Use of peptide for selective and sensitive detection of an Anthrax biomarker via peptide recognition and surface-enhanced Raman scattering. *J. Raman Spectrosc.* **41,** 121–124 (2010).

135. Porter, M. D., Lipert, R. J., Siperko, L. M., Wang, G. & Narayanan, R. SERS as a bioassay platform: fundamentals, design, and applications. *Chem. Soc. Rev.* **37,** 1001–1011 (2008).

136. Schlücker, S. SERS Microscopy: Nanoparticle Probes and Biomedical Applications. *ChemPhysChem* **10,** 1344–1354 (2009).

137. Schlücker, S. *et al.* Immuno-Raman microspectroscopy: In situ detection of antigens in tissue specimens by surface-enhanced Raman scattering. *J. Raman Spectrosc.* **37,** 719–721 (2006).

138. Zavaleta, C. L. *et al.* Multiplexed imaging of surface enhanced Raman scattering nanotags in living mice using noninvasive Raman spectroscopy. *Proc. Natl. Acad. Sci.* **106,** 13511–13516 (2009).

139. Maiti, K. K. *et al.* Multiplex targeted in vivo cancer detection using sensitive near-infrared SERS nanotags. *Nano Today* **7,** 85–93 (2012).

140. Weissleder, R. A clearer vision for in vivo imaging. *Nat. Biotechnol.* **19,** 316–317 (2001).

141. Durr, N. J. *et al.* Two-Photon Luminescence Imaging of Cancer Cells Using Molecularly Targeted Gold Nanorods. *Nano Lett.* **7,** 941–945 (2007).

142. Wang, Y. *et al.* SV119-gold nanocage conjugates: a new platform for targeting cancer cellsvia sigma-2 receptors. *Nanoscale* **4,** 421–424 (2012).

143. Gao, L., Vadakkan, T. J. & Nammalvar, V. Nanoshells for in vivo imaging using two-photon excitation microscopy. *Nanotechnology* **22,** 365102 (2011).

144. Menon, J. U. *et al.* Nanomaterials for photo-based diagnostic and therapeutic applications. *Theranostics* **3,** 152–166 (2013).

145. Yu, M. K., Park, J. & Jon, S. Targeting Strategies for Multifunctional Nanoparticles in Cancer Imaging and Therapy. *Theranostics* **2,** 3–44 (2012).

146. Dreaden, E. C., Mwakwari, S. C., Sodji, Q. H., Oyelere, A. K. & El-Sayed, M. A. Tamoxifen-poly(ethylene glycol)-thiol gold nanoparticle conjugates: enhanced potency and selective delivery for breast cancer treatment. *Bioconjug. Chem.* **20,** 2247–2253 (2009).

147. Scialabba, C. *et al.* Inulin-based polymer coated SPIONs as potential drug delivery systems for targeted cancer therapy. *Eur. J. Pharm. Biopharm. Off. J. Arbeitsgemeinschaft Für Pharm. Verfahrenstechnik EV* **88,** 695–705 (2014).

148. Tonga, G. Y., Saha, K. & Rotello, V. M. Interfacing Nanoparticles and Biology: New Strategies for Biomedicine. *Adv. Mater. Deerfield Beach Fla* **26,** 359–370 (2014).

149. Baffou, G., Quidant, R. & Girard, C. Heat generation in plasmonic nanostructures: Influence of morphology. *Appl. Phys. Lett.* **94,** 153109 (2009).

150. Smith, A. M., Mancini, M. C. & Nie, S. Bioimaging: Second window for in vivo imaging. *Nat. Nanotechnol.* **4,** 710–711 (2009).

151. Tsai, M.-F. *et al.* Au Nanorod Design as Light-Absorber in the First and Second Biological Near-Infrared Windows for in Vivo Photothermal Therapy. *ACS Nano* **7,** 5330–5342 (2013).

152. Oldenburg, S. J., Averitt, R. D., Westcott, S. L. & Halas, N. J. Nanoengineering of optical resonances. *Chem. Phys. Lett.* **288,** 243–247 (1998).

153. Loo, C., Lowery, A., Halas, N., West, J. & Drezek, R. Immunotargeted Nanoshells for Integrated Cancer Imaging and Therapy. *Nano Lett.* **5,** 709–711 (2005).

154. in (eds. Grobmyer, S. R. & Moudgil, B. M.) (Humana Press, 2010). at <http://link.springer.com/protocol/10.1007/978-1-60761-609-2_7>

155. Chen, W. *et al.* Targeting pancreatic cancer with magneto-fluorescent theranostic gold nanoshells. *Nanomed.* **9,** 1209–1222 (2014).

156. Nanospectra Biosciences, Inc. at <http://www.nanospectra.com/technology/aurolasetherapy.html>

157. Sun, Y., Mayers, B. T. & Xia, Y. Template-Engaged Replacement Reaction: A One-Step Approach to the Large-Scale Synthesis of Metal Nanostructures with Hollow Interiors. *Nano Lett.* **2,** 481–485 (2002).

158. Huang, X., El-Sayed, I. H., Qian, W. & El-Sayed, M. A. Cancer Cell Imaging and Photothermal Therapy in the Near-Infrared Region by Using Gold Nanorods. *J. Am. Chem. Soc.* **128,** 2115–2120 (2006).

159. Jo, H., Youn, H., Lee, S. & Ban, C. Ultra-effective photothermal therapy for prostate cancer cells using dual aptamer-modified gold nanostars. *J. Mater. Chem. B* **2,** 4862–4867 (2014).

160. Wang, Y. *et al.* Comparison Study of Gold Nanohexapods, Nanorods, and Nanocages for Photothermal Cancer Treatment. *ACS Nano* **7,** 2068–2077 (2013).

161. Maestro, L. M. *et al.* Quantum Dot Thermometry Evaluation of Geometry Dependent Heating Efficiency in Gold Nanoparticles. *Langmuir* **30,** 1650–1658 (2014).

162. Pissuwan, D., Niidome, T. & Cortie, M. B. The forthcoming applications of gold nanoparticles in drug and gene delivery systems. *J. Controlled Release* **149,** 65–71 (2011).

163. Huschka, R., Neumann, O., Barhoumi, A. & Halas, N. J. Visualizing Light-Triggered Release of Molecules Inside Living Cells. *Nano Lett.* **10,** 4117–4122 (2010).

164. Topete, A. *et al.* Polymeric-Gold Nanohybrids for Combined Imaging and Cancer Therapy. *Adv. Healthc. Mater.* **3,** 1309–1325 (2014).

165. Yavuz, M. S. *et al.* Gold nanocages covered by smart polymers for controlled release with near-infrared light. *Nat. Mater.* **8,** 935–939 (2009).

166. De Cock, L. J. *et al.* Polymeric Multilayer Capsules in Drug Delivery. *Angew. Chem. Int. Ed.* **49,** 6954–6973 (2010).

167. Paasonen, L. *et al.* Gold nanoparticles enable selective light-induced contents release from liposomes. *J. Control. Release Off. J. Control. Release Soc.* **122,** 86–93 (2007).

168. Alvarez-Puebla, R., Liz-Marzán, L. M. & García de Abajo, F. J. Light Concentration at the Nanometer Scale. *J. Phys. Chem. Lett.* **1,** 2428–2434 (2010).

169. Guerrero-Martínez, A., Barbosa, S., Pastoriza-Santos, I. & Liz-Marzán, L. M. Nanostars shine bright for you. *Curr. Opin. Colloid Interface Sci.* **16,** 118–127 (2011).

170. Rodríguez-Lorenzo, L., Álvarez-Puebla, R. A., de Abajo, F. J. G. & Liz-Marzán, L. M. Surface Enhanced Raman Scattering Using Star-Shaped Gold Colloidal Nanoparticles †. *J. Phys. Chem. C* **114,** 7336–7340 (2010).

171. Fabris, L. *et al.* Gold Nanostar Substrates for SERS-based Chemical Sensing in the Femtomolar Regime. *Nanoscale* (2014). doi:10.1039/c4nr02513j

172. Vo-Dinh, T. *et al.* Plasmonic nanoprobes: from chemical sensing to medical diagnostics and therapy. *Nanoscale* **5,** 10127–10140 (2013).

173. Rodríguez-Lorenzo, L., Romo-Herrera, J. M., Pérez-Juste, J., Alvarez-Puebla, R. A. & Liz-Marzán, L. M. Reshaping and LSPR tuning of Au nanostars in the presence of CTAB. *J. Mater. Chem.* **21,** 11544 (2011).

174. Zeng, J., Roberts, S. & Xia, Y. Nanocrystal-Based Time–Temperature Indicators. *Chem. – Eur. J.* **16,** 12559–12563 (2010).

175. Alvarez-Puebla, R. A. & Liz-Marzán, L. M. Traps and cages for universal SERS detection. *Chem. Soc. Rev.* **41,** 43–51 (2012).

176. Fales, A. M., Yuan, H. & Vo-Dinh, T. Development of Hybrid Silver-Coated Gold Nanostars for Nonaggregated Surface-Enhanced Raman Scattering. *J. Phys. Chem. C* **118,** 3708–3715 (2014).

177. Fales, A. M., Yuan, H. & Vo-Dinh, T. Silica-Coated Gold Nanostars for Combined Surface-Enhanced Raman Scattering (SERS) Detection and Singlet-Oxygen Generation: A Potential Nanoplatform for Theranostics. *Langmuir* **27,** 12186–12190 (2011).

178. Wang, Y., Polavarapu, L. & Liz-Marzán, L. M. Reduced Graphene Oxide-Supported Gold Nanostars for Improved SERS Sensing and Drug Delivery. *ACS Appl. Mater. Interfaces* **6,** 21798–21805 (2014).

179. Lim, D.-K. *et al.* Highly uniform and reproducible surface-enhanced Raman scattering from DNA-tailorable nanoparticles with 1-nm interior gap. *Nat. Nanotechnol.* **6,** 452–460 (2011).

180. Song, J. *et al.* SERS-Encoded Nanogapped Plasmonic Nanoparticles: Growth of Metallic Nanoshell by Templating Redox-Active Polymer Brushes. *J. Am. Chem. Soc.* **136,** 6838–6841 (2014).

181. Gandra, N. & Singamaneni, S. Bilayered Raman-Intense Gold Nanostructures with Hidden Tags (BRIGHTs) for High-Resolution Bioimaging. *Adv. Mater.* **25,** 1022–1027 (2013).

182. Wang, Y. *et al.* Specific functionalization of CTAB stabilized anisotropic gold nanoparticles with polypeptides for folding-mediated self-assembly. *J. Mater. Chem.* **22,** 20368–20373 (2012).

183. Hamon, C., Novikov, S., Scarabelli, L., Basabe-Desmonts, L. & Liz-Marzán, L. M. Hierarchical Self-Assembly of Gold Nanoparticles into Patterned Plasmonic Nanostructures. *ACS Nano* **8,** 10694–10703 (2014).

184. Oh, J.-W., Lim, D.-K., Kim, G.-H., Suh, Y. D. & Nam, J.-M. Thiolated DNA-Based Chemistry and Control in the Structure and Optical Properties of Plasmonic Nanoparticles with Ultrasmall Interior Nanogap. *J. Am. Chem. Soc.* **136,** 14052–14059 (2014).

185. Zhao, B. *et al.* Gold nanostructures encoded by non-fluorescent small molecules in polyA-mediated nanogaps as universal SERS nanotags for recognizing various bioactive molecules. *Chem. Sci.* **5,** 4460–4466 (2014).

186. Feng, Y. *et al.* An Unconventional Role of Ligand in Continuously Tuning of Metal–Metal Interfacial Strain. *J. Am. Chem. Soc.* **134,** 2004–2007 (2012).

187. Alvarez-Puebla, R. A. *et al.* Gold nanorods 3D-supercrystals as surface enhanced Raman scattering spectroscopy substrates for the rapid detection of scrambled prions. *Proc. Natl. Acad. Sci.* **108,** 8157–8161 (2011).

188. Alvarez-Puebla, R. A., Zubarev, E. R., Kotov, N. A. & Liz-Marzán, L. M. Self-assembled nanorod supercrystals for ultrasensitive SERS diagnostics. *Nano Today* **7,** 6–9 (2012).

189. Joo, S. W., Han, S. W. & Kim, K. Adsorption of 1,4-Benzenedithiol on Gold and Silver Surfaces: Surface-Enhanced Raman Scattering Study. *J. Colloid Interface Sci.* **240,** 391–399 (2001).

190. Yoshida, A., Imazu, K., Li, X., Okamoto, K. & Tamada, K. Spectroscopic properties of multilayered gold nanoparticle 2D sheets. *Langmuir* **28,** 17153–17158 (2012).

191. Zhou, J. *et al.* Adjusting the inter-particle spacing of a nanoparticle array at the sub-nanometre scale by thermal annealing. *Chem. Commun.* **50,** 14547–14549 (2014).

192. Soliman, M. G., Pelaz, B., Parak, W. J. & del Pino, P. Phase Transfer and Polymer Coating Methods toward Improving the Stability of Metallic Nanoparticles for Biological Applications. *Chem. Mater.* **27,** 990–997 (2015).

193. Underwood, S. & Mulvaney, P. Effect of the Solution Refractive Index on the Color of Gold Colloids. *Langmuir* **10,** 3427–3430 (1994).

194. Vijaya Sarathy, K., Kulkarni, G. U. & Rao, C. N. R. A novel method of preparing thiol-derivatised nanoparticles ofgold, platinum and silver forming superstructures. *Chem. Commun.* 537–538 (1997).

195. Li, L., Leopold, K. & Schuster, M. Comparative study of alkylthiols and alkylamines for the phase transfer of gold nanoparticles from an aqueous phase to n-hexane. *J. Colloid Interface Sci.* **397,** 199–205 (2013).

196. Wang, X., Xu, S., Zhou, J. & Xu, W. A rapid phase transfer method for nanoparticles using alkylamine stabilizers. *J. Colloid Interface Sci.* **348,** 24–28 (2010).

197. Lista, M., Liu, D. Z. & Mulvaney, P. Phase Transfer of Noble Metal Nanoparticles to Organic Solvents. *Langmuir* **30,** 1932–1938 (2014).

198. Goulet, P. J. G., Bourret, G. R. & Lennox, R. B. Facile Phase Transfer of Large, Water-Soluble Metal Nanoparticles to Nonpolar Solvents. *Langmuir* **28,** 2909–2913 (2012).

199. Alkilany, A. M., Yaseen, A. I. B., Park, J., Eller, J. R. & Murphy, C. J. Facile phase transfer of gold nanoparticles from aqueous solution to organic solvents with thiolated poly(ethylene glycol). *RSC Adv* **4,** 52676–52679 (2014).

200. Liu, M. *et al.* Exploring the amphiphilicity of PEGylated gold nanorods: mechanical phase transfer and self-assembly. *Chem. Commun.* **49,** 9350 (2013).

201. Yuan, H., Fales, A. M. & Vo-Dinh, T. TAT Peptide-Functionalized Gold Nanostars: Enhanced Intracellular Delivery and Efficient NIR Photothermal Therapy Using Ultralow Irradiance. *J. Am. Chem. Soc.* **134,** 11358–11361 (2012).

202. Qian, K., Yang, L., Li, Z. & Liu, J. A new-type dynamic SERS method for ultrasensitive detection. *J. Raman Spectrosc.* **44,** 21–28 (2013).

203. Wu, Z., Liu, Y., Zhou, X., Shen, A. & Hu, J. A 'turn-off' SERS-based detection platform for ultrasensitive detection of thrombin based on enzymatic assays. *Biosens. Bioelectron.* **44,** 10–15 (2013).

204. Domenici, F., Bizzarri, A. R. & Cannistraro, S. SERS-based nanobiosensing for ultrasensitive detection of the p53 tumor suppressor. *Int. J. Nanomedicine* **6,** 2033–2042 (2011).

205. Dong, J. *et al.* Ultrasensitive surface-enhanced Raman scattering detection of alkaline phosphatase. *Anal. Methods* **6,** 9168–9172 (2014).

206. Zheng, J. *et al.* Universal Surface-Enhanced Raman Scattering Amplification Detector for Ultrasensitive Detection of Multiple Target Analytes. *Anal. Chem.* **86,** 2205–2212 (2014).

207. Bastús, N. G., Comenge, J. & Puntes, V. Kinetically Controlled Seeded Growth Synthesis of Citrate-Stabilized Gold Nanoparticles of up to 200 nm: Size Focusing versus Ostwald Ripening. *Langmuir* **27,** 11098–11105 (2011).

208. Ye, X. *et al.* Improved Size-Tunable Synthesis of Monodisperse Gold Nanorods through the Use of Aromatic Additives. *ACS Nano* **6,** 2804–2817 (2012).

209. Bastús, N. G., Merkoçi, F., Piella, J. & Puntes, V. Synthesis of Highly Monodisperse Citrate-Stabilized Silver Nanoparticles of up to 200 nm: Kinetic Control and Catalytic Properties. *Chem. Mater.* **26,** 2836–2846 (2014).

210. Hostetler, M. J. *et al.* Alkanethiolate Gold Cluster Molecules with Core Diameters from 1.5 to 5.2 nm: Core and Monolayer Properties as a Function of Core Size. *Langmuir* **14,** 17–30 (1998).

211. Zelakiewicz, B. S., de Dios, A. C. & Tong. 13C NMR Spectroscopy of 13C1-Labeled Octanethiol-Protected Au Nanoparticles: Shifts, Relaxations, and Particle-Size Effect. *J. Am. Chem. Soc.* **125,** 18–19 (2003).

212. Zhao, S.-Y., Chen, S.-H., Wang, S.-Y., Li, D.-G. & Ma, H.-Y. Preparation, Phase Transfer, and Self-Assembled Monolayers of Cubic Pt Nanoparticles. *Langmuir* **18,** 3315–3318 (2002).

213. Dong, A., Chen, J., Vora, P. M., Kikkawa, J. M. & Murray, C. B. Binary nanocrystal superlattice membranes self-assembled at the liquid-air interface. *Nature* **466,** 474–477 (2010).

214. Giner-Casares, J. J., Brezesinski, G. & Möhwald, H. Langmuir monolayers as unique physical models. *Curr. Opin. Colloid Interface Sci.* **19,** 176–182 (2014).

215. Giner-Casares, J. J. & Liz-Marzán, L. M. Plasmonic nanoparticles in 2D for biological applications: Toward active multipurpose platforms. *Nano Today* **9,** 365–377 (2014).

216. Shiohara, A., Langer, J., Polavarapu, L. & Liz-Marzán, L. M. Solution processed polydimethylsiloxane/gold nanostar flexible substrates for plasmonic sensing. *Nanoscale* **6,** 9817–9823 (2014).

217. Michota, A. & Bukowska, J. Surface-enhanced Raman scattering (SERS) of 4-mercaptobenzoic acid on silver and gold substrates. *J. Raman Spectrosc.* **34,** 21–25 (2003).

218. Talley, C. E., Jusinski, L., Hollars, C. W., Lane, S. M. & Huser, T. Intracellular pH Sensors Based on Surface-Enhanced Raman Scattering. *Anal. Chem.* **76,** 7064–7068 (2004).

219. Bishnoi, S. W. *et al.* All-Optical Nanoscale pH Meter. *Nano Lett.* **6,** 1687–1692 (2006).

220. Pallaoro, A., Braun, G. B., Reich, N. O. & Moskovits, M. Mapping Local pH in Live Cells Using Encapsulated Fluorescent SERS Nanotags. *Small* **6,** 618–622 (2010).

221. Varsányi, G. *Assignments for vibrational spectra of seven hundred benzene derivatives,*. (1974).

222. Kwon, Y. J., Son, D. H., Ahn, S. J., Kim, M. S. & Kim, K. Vibrational Spectroscopic Investigation of Benzoic Acid Adsorbed on Silver. *J. Phys. Chem.* **98,** 8481–8487 (1994).

223. Suh, J. S. & Kim, J. Three distinct geometries of surface-adsorbed carboxylate groups. *J. Raman Spectrosc.* **29,** 143–148 (1998).

224. McFarland, A. D., Young, M. A., Dieringer, J. A. & Van Duyne, R. P. Wavelength-Scanned Surface-Enhanced Raman Excitation Spectroscopy. *J. Phys. Chem. B* **109,** 11279–11285 (2005).

225. Tebbe, M., Maennel, M., Fery, A., Pazos-Perez, N. & Alvarez-Puebla, R. A. Organized Solid Thin Films of Gold Nanorods with Different Sizes for Surface-Enhanced Raman Scattering Applications. *J. Phys. Chem. C* **118,** 28095–28100 (2014).

226. Litorja, M., Haynes, C. L., Haes, A. J., Jensen, T. R. & Van Duyne, R. P. Surface-Enhanced Raman Scattering Detected Temperature Programmed Desorption: Optical Properties, Nanostructure, and Stability of Silver Film over SiO2 Nanosphere Surfaces. *J. Phys. Chem. B* **105,** 6907–6915 (2001).

227. Cai, W. B. *et al.* Investigation of surface-enhanced Raman scattering from platinum electrodes using a confocal Raman microscope: dependence of surface roughening pretreatment. *Surf. Sci.* **406,** 9–22 (1998).

228. Khan, M. A., Hogan, T. P. & Shanker, B. Surface-enhanced Raman scattering from gold-coated germanium oxide nanowires. *J. Raman Spectrosc.* **39,** 893–900 (2008).

229. Dougan, J. A. & Faulds, K. Surface enhanced Raman scattering for multiplexed detection. *Analyst* **137,** 545–554 (2012).

230. Doering, W. E. & Nie, S. Spectroscopic Tags Using Dye-Embedded Nanoparticles and Surface-Enhanced Raman Scattering. *Anal. Chem.* **75,** 6171–6176 (2003).

231. McCreery, R. L. *Raman Spectroscopy for Chemical Analysis: McCreery/Raman Spectroscopy.* (John Wiley & Sons, Inc., 2000). at <http://doi.wiley.com/10.1002/0471721646>

232. *Principles of Fluorescence Spectroscopy.* (Springer US, 2006). at <http://link.springer.com/10.1007/978-0-387-46312-4>

233. Wang, H.-N. & Vo-Dinh, T. Multiplex detection of breast cancer biomarkers using plasmonic molecular sentinel nanoprobes. *Nanotechnology* **20,** 065101 (2009).

234. Matschulat, A., Drescher, D. & Kneipp, J. Surface-Enhanced Raman Scattering Hybrid Nanoprobe Multiplexing and Imaging in Biological Systems. *ACS Nano* **4,** 3259–3269 (2010).

235. Keren, S. *et al.* Noninvasive molecular imaging of small living subjects using Raman spectroscopy. *Proc. Natl. Acad. Sci.* **105,** 5844–5849 (2008).

236. Samanta, A., Das, R. K., Park, S. J., Maiti, K. K. & Chang, Y. T. Multiplexing SERS nanotags for the imaging of differentiated mouse embryonic stem cells (mESC) and detection of teratoma in vivo. *Am. J. Nucl. Med. Mol. Imaging* **4,** 114–124 (2014).

237. Abramczyk, H. & Brozek-Pluska, B. Raman Imaging in Biochemical and Biomedical Applications. Diagnosis and Treatment of Breast Cancer. *Chem. Rev.* **113,** 5766–5781 (2013).

238. Su, X. *et al.* Composite Organic−Inorganic Nanoparticles (COINs) with Chemically Encoded Optical Signatures. *Nano Lett.* **5,** 49–54 (2005).

239. Sun, L. *et al.* Composite Organic−Inorganic Nanoparticles as Raman Labels for Tissue Analysis. *Nano Lett.* **7,** 351–356 (2007).

240. McCabe, A. F. *et al.* SERRS labelled beads for multiplex detection. *Faraday Discuss.* **132,** 303–308 (2006).

241. Samanta, A. *et al.* Ultrasensitive Near-Infrared Raman Reporters for SERS-Based In Vivo Cancer Detection. *Angew. Chem. Int. Ed.* **50,** 6089–6092 (2011).

242. Driskell, J. D. *et al.* Low-Level Detection of Viral Pathogens by a Surface-Enhanced Raman Scattering Based Immunoassay. *Anal. Chem.* **77,** 6147–6154 (2005).

243. Tam, N. C. M., Scott, B. M. T., Voicu, D., Wilson, B. C. & Zheng, G. Facile Synthesis of Raman Active Phospholipid Gold Nanoparticles. *Bioconjug. Chem.* **21,** 2178–2182 (2010).

244. Ip, S., MacLaughlin, C. M., Gunari, N. & Walker, G. C. Phospholipid membrane encapsulation of nanoparticles for surface-enhanced Raman scattering. *Langmuir ACS J. Surf. Colloids* **27,** 7024–7033 (2011).

245. Tam, N. C. M. *et al.* Porphyrin–Lipid Stabilized Gold Nanoparticles for Surface Enhanced Raman Scattering Based Imaging. *Bioconjug. Chem.* **23,** 1726–1730 (2012).

246. Fernández-López, C. *et al.* Highly Controlled Silica Coating of PEG-Capped Metal Nanoparticles and Preparation of SERS-Encoded Particles. *Langmuir* **25,** 13894–13899 (2009).

247. Rodríguez-Fernández, D., Langer, J., Henriksen-Lacey, M. & Liz-Marzán, L. M. Hybrid Au–SiO2 Core–Satellite Colloids as Switchable SERS Tags. *Chem. Mater.* **27,** 2540–2545 (2015).

248. Mir-Simon, B., Reche-Perez, I., Guerrini, L., Pazos-Perez, N. & Alvarez-Puebla, R. A. Universal One-Pot and Scalable Synthesis of SERS Encoded Nanoparticles. *Chem. Mater.* **27,** 950–958 (2015).

249. Freeman, R. G. *et al.* Detection of biomolecules using nanoparticle surface enhanced Raman scattering tags. in **5705,** 114–122 (2005).

250. Stokes, R. J. *et al.* SERRS-active nanoparticle-polymer beads for ultra-sensitive biodiagnostic applications. *Micro Ampamp Nano Lett.* **1,** 57–61 (2006).

251. McLintock, A., Hunt, N. & Wark, A. W. Controlled side-by-side assembly of gold nanorods and dye molecules into polymer-wrapped SERRS-active clusters. *Chem. Commun.* **47,** 3757–3759 (2011).

252. Qian, X. *et al.* In vivo tumor targeting and spectroscopic detection with surface-enhanced Raman nanoparticle tags. *Nat. Biotechnol.* **26,** 83–90 (2008).

253. Dinish, U. S., Balasundaram, G., Chang, Y.-T. & Olivo, M. Actively targeted in vivo multiplex detection of intrinsic cancer biomarkers using biocompatible SERS nanotags. *Sci. Rep.* **4,** 4075 (2014).

254. Song, J., Zhou, J. & Duan, H. Self-Assembled Plasmonic Vesicles of SERS-Encoded Amphiphilic Gold Nanoparticles for Cancer Cell Targeting and Traceable Intracellular Drug Delivery. *J. Am. Chem. Soc.* **134,** 13458–13469 (2012).

255. Izak-Nau, E., Voetz, M., Eiden, S., Duschl, A. & Puntes, V. F. Altered characteristics of silica nanoparticles in bovine and human serum: the importance of nanomaterial characterization prior to its toxicological evaluation. *Part. Fibre Toxicol.* **10,** 56 (2013).

256. Teng, Z. *et al.* Mesoporous Silica Hollow Spheres with Ordered Radial Mesochannels by a Spontaneous Self-Transformation Approach. *Chem. Mater.* **25,** 98–105 (2013).

257. Lin, Y.-S. & Haynes, C. L. Impacts of Mesoporous Silica Nanoparticle Size, Pore Ordering, and Pore Integrity on Hemolytic Activity. *J. Am. Chem. Soc.* **132,** 4834–4842 (2010).

258. Fontecave, T., Sanchez, C., Azaïs, T. & Boissière, C. Chemical Modification As a Versatile Tool for Tuning Stability of Silica Based Mesoporous Carriers in Biologically Relevant Conditions. *Chem. Mater.* **24,** 4326–4336 (2012).

259. Chen, G., Teng, Z., Su, X., Liu, Y. & Lu, G. Unique Biological Degradation Behavior of Stöber Mesoporous Silica Nanoparticles from Their Interiors to Their Exteriors. *J. Biomed. Nanotechnol.* **11,** 722–729 (2015).

260. Zhai, W. *et al.* Degradation of hollow mesoporous silica nanoparticles in human umbilical vein endothelial cells. *J. Biomed. Mater. Res. B Appl. Biomater.* **100B,** 1397–1403 (2012).

261. Lee, S. *et al.* Biological Imaging of HEK293 Cells Expressing PLCγ1 Using Surface-Enhanced Raman Microscopy. *Anal. Chem.* **79,** 916–922 (2007).

262. Faulds, K., Barbagallo, R. P., Keer, J. T., Smith, W. E. & Graham, D. SERRS as a more sensitive technique for the detection of labelled oligonucleotides compared to fluorescence. *Analyst* **129,** 567–568 (2004).

263. Weissleder, R. A clearer vision for in vivo imaging. *Nat. Biotechnol.* **19,** 316–317 (2001).

264. Nalbant Esenturk, E. & Hight Walker, A. R. Surface-enhanced Raman scattering spectroscopy via gold nanostars. *J. Raman Spectrosc.* **40,** 86–91 (2009).

265. Serrano-Montes, A. B. *et al.* A General Method for Solvent Exchange of Plasmonic Nanoparticles and Self-Assembly into SERS-Active Monolayers. *Langmuir* **31,** 9205–9213 (2015).

266. Soliman, M. G. M., Pelaz, B., Parak, W. J. & del Pino, P. Phase Transfer and Polymer Coating Methods towards Improving Stability of Metallic Nanoparticles for Biological Applications. *Chem. Mater.* 150120182325004 (2015). doi:10.1021/cm5043167

267. Yang, J. *et al.* Distinguishing breast cancer cells using surface-enhanced Raman scattering. *Anal. Bioanal. Chem.* **402,** 1093–1100 (2011).

268. Lee, S. *et al.* Rapid and sensitive phenotypic marker detection on breast cancer cells using surface-enhanced Raman scattering (SERS) imaging. *Biosens. Bioelectron.* **51,** 238–243 (2014).

269. Nima, Z. A. *et al.* Circulating tumor cell identification by functionalized silver-gold nanorods with multicolor, super-enhanced SERS and photothermal resonances. *Sci. Rep.* **4,** (2014).

270. Lin, C.-A. J. *et al.* Design of an Amphiphilic Polymer for Nanoparticle Coating and Functionalization. *Small* **4,** 334–341 (2008).

271. Pierre, M. C. S. & Haes, A. J. Purification Implications on SERS Activity of Silica Coated Gold Nanospheres. *Anal. Chem.* **84,** 7906–7911 (2012).

272. Zhang, Y., Walkenfort, B., Yoon, J. H., Schlücker, S. & Xie, W. Gold and silver nanoparticle monomers are non-SERS-active: a negative experimental study with silica-encapsulated Raman-reporter-coated metal colloids. *Phys. Chem. Chem. Phys.* **17,** 21120–21126 (2015).

273. Doherty, M. D., Murphy, A., Pollard, R. J. & Dawson, P. Surface-Enhanced Raman Scattering from Metallic Nanostructures: Bridging the Gap between the Near-Field and Far-Field Responses. *Phys. Rev. X* **3,** 011001 (2013).

274. Xie, W. & Schlücker, S. Rationally designed multifunctional plasmonic nanostructures for surface-enhanced Raman spectroscopy: a review. *Rep. Prog. Phys.* **77,** 116502 (2014).

275. Wang, H. & Zou, S. A generalized electrodynamics model for surface enhanced Raman scattering and enhanced/quenched fluorescence calculations. *RSC Adv.* **3,** 21489–21493 (2013).

276. Ming, T., Chen, H., Jiang, R., Li, Q. & Wang, J. Plasmon-Controlled Fluorescence: Beyond the Intensity Enhancement. *J. Phys. Chem. Lett.* **3,** 191–202 (2012).

277. Nepal, D., Drummy, L. F., Biswas, S., Park, K. & Vaia, R. A. Large Scale Solution Assembly of Quantum Dot–Gold Nanorod Architectures with Plasmon Enhanced Fluorescence. *ACS Nano* **7,** 9064–9074 (2013).

278. Hsieh, H.-Y. *et al.* Fabrication and modification of dual-faced nano-mushrooms for tri-functional cell theranostics: SERS/fluorescence signaling, protein targeting, and drug delivery. *J. Mater. Chem.* **22,** 20918–20928 (2012).

279. Yu, K. N. *et al.* Multiplex Targeting, Tracking, and Imaging of Apoptosis by Fluorescent Surface Enhanced Raman Spectroscopic Dots. *Bioconjug. Chem.* **18,** 1155–1162 (2007).

280. Wang, Z., Wu, H., Wang, C., Xu, S. & Cui, Y. Gold aggregates- and quantum dots- embedded nanospheres: Switchable dual-mode image probes for living cells. *J. Mater. Chem.* **21,** 4307–4313 (2011).

281. Qian, J., Jiang, L., Cai, F., Wang, D. & He, S. Fluorescence-surface enhanced Raman scattering co-functionalized gold nanorods as near-infrared probes for purely optical in vivo imaging. *Biomaterials* **32,** 1601–1610 (2011).

282. Huang, Z., Tang, F. & Zhang, L. Morphology control and texture of Fe3O4 nanoparticle-coated polystyrene microspheres by ethylene glycol in forced hydrolysis reaction. *Thin Solid Films* **471,** 105–112 (2005).

283. Levin, C. S. *et al.* Magnetic−Plasmonic Core−Shell Nanoparticles. *ACS Nano* **3,** 1379–1388 (2009).

284. Lee, J.-H., Mahmoud, M. A., Sitterle, V., Sitterle, J. & Meredith, J. C. Facile preparation of highly-scattering metal nanoparticle-coated polymer microbeads and their surface plasmon resonance. *J. Am. Chem. Soc.* **131,** 5048–5049 (2009).

285. Han, J., Liu, Y. & Guo, R. Reactive Template Method to Synthesize Gold Nanoparticles with Controllable Size and Morphology Supported on Shells of

Polymer Hollow Microspheres and Their Application for Aerobic Alcohol Oxidation in Water. *Adv. Funct. Mater.* **19,** 1112–1117 (2009).

286. Mir-Simon, B. *et al.* SERS efficiencies of micrometric polystyrene beads coated with gold and silver nanoparticles: the effect of nanoparticle size. *J. Opt.* **17,** 114012 (2015).

287. Piskin, E., Tuncel, A., Denizli, A. & Ayhan, H. Monosize microbeads based on polystyrene and their modified forms for some selected medical and biological applications. *J. Biomater. Sci. Polym. Ed.* **5,** 451–471 (1994).

288. Li, Y. *et al.* Facile and Controlled Fabrication of Functional Gold Nanoparticle-coated Polystyrene Composite Particle. *Macromol. Rapid Commun.* **32,** 1741–1747 (2011).

289. Gong, J., Zu, X., Mu, W. & Deng, Y. In situ self-assembly synthesis of gold nanoparticle arrays on polystyrene microspheres and their surface plasmon resonance. *Colloid Polym. Sci.* **291,** 239–244 (2012).

290. Zhu, W. *et al.* Facile Synthesis of Mono-Dispersed Polystyrene (PS)/Ag Composite Microspheres via Modified Chemical Reduction. *Materials* **6,** 5625–5638 (2013).

291. Zhang, N., Yu, X., Hu, J., Xue, F. & Ding, E. Synthesis of silver nanoparticle-coated poly(styrene-co-sulfonic acid) hybrid materials and their application in surface-enhanced Raman scattering (SERS) tags. *RSC Adv.* **3,** 13740–13747 (2013).

292. Li, J.-M. *et al.* Poly(styrene-co-acrylic acid) core and silver nanoparticle/silica shell composite microspheres as high performance surface-enhanced Raman spectroscopy (SERS) substrate and molecular barcode label. *J. Mater. Chem.* **21,** 5992–5998 (2011).

293. Jeong, E. *et al.* Three-Dimensional Reduced-Symmetry of Colloidal Plasmonic Nanoparticles. *Nano Lett.* **12,** 2436–2440 (2012).

294. Shi, W., Sahoo, Y., Swihart, M. T. & Prasad, P. N. Gold Nanoshells on Polystyrene Cores for Control of Surface Plasmon Resonance. *Langmuir* **21,** 1610–1617 (2005).

295. Pilapil, B. K., Wang, M. C. P., Paul, M. T. Y., Nazemi, A. & Gates, B. D. Self-assembly of nanoparticles onto the surfaces of polystyrene spheres with a tunable composition and loading. *Nanotechnology* **26,** 055601 (2015).

296. Guo, I. W., Pekcevik, I. C., Wang, M. C. P., Pilapil, B. K. & Gates, B. D. Colloidal core–shell materials with 'spiky' surfaces assembled from gold nanorods. *Chem. Commun.* **50,** 8157–8160 (2014).

297. Verma, A. *et al.* Surface-structure-regulated cell-membrane penetration by monolayer-protected nanoparticles. *Nat. Mater.* **7,** 588–595 (2008).

298. Palenstijn, W. J., Batenburg, K. J. & Sijbers, J. Performance improvements for iterative electron tomography reconstruction using graphics processing units (GPUs). *J. Struct. Biol.* **176,** 250–253 (2011).

299. Brust, M., Walker, M., Bethell, D., Schiffrin, D. J. & Whyman, R. Synthesis of thiol-derivatised gold nanoparticles in a two-phase Liquid–Liquid system. *J. Chem. Soc. Chem. Commun.* 801–802 (1994). doi:10.1039/C39940000801

300. Kimling, J. *et al.* Turkevich Method for Gold Nanoparticle Synthesis Revisited. *J. Phys. Chem. B* **110,** 15700–15707 (2006).

301. McLellan, J. M., Siekkinen, A., Chen, J. & Xia, Y. Comparison of the surface-enhanced Raman scattering on sharp and truncated silver nanocubes. *Chem. Phys. Lett.* **427,** 122–126 (2006).

302. Nie, S. & Emory, S. R. Probing Single Molecules and Single Nanoparticles by Surface-Enhanced Raman Scattering. *Science* **275,** 1102–1106 (1997).

303. Jiang, Bosnick, K., Maillard, M. & Brus, L. Single Molecule Raman Spectroscopy at the Junctions of Large Ag Nanocrystals. *J. Phys. Chem. B* **107,** 9964–9972 (2003).

304. Ma, W. *et al.* A SERS active gold nanostar dimer for mercury ion detection. *Chem. Commun.* (2013). doi:10.1039/c3cc39087j

305. Lee, S. B., Kim, K. & Kim, M. S. Surface-enhanced Raman scattering of o-mercaptobenzoic acid in silver sol. *J. Raman Spectrosc.* **22,** 811–817 (1991).

306. Aldeanueva-Potel, P. *et al.* Spiked Gold Beads as Substrates for Single-Particle SERS. *ChemPhysChem* **13,** 2561–2565 (2012).

307. D.M. Solís, J. M. Taboada, L.M. Liz-Marzán, F. Obelleiro & F.J. García de Abajo. Personal communication.

308. Chithrani, B. D., Ghazani, A. A. & Chan, W. C. W. Determining the Size and Shape Dependence of Gold Nanoparticle Uptake into Mammalian Cells. *Nano Lett.* **6,** 662–668 (2006).

309. Gratton, S. E. A. *et al.* The effect of particle design on cellular internalization pathways. *Proc. Natl. Acad. Sci.* **105,** 11613–11618 (2008).

310. Jia, H.-Z. *et al.* Virus-Surface-Mimicking Surface Clustering of AuNPs onto DNA-Entrapped Polymeric Nanoparticle for Enhanced Cellular Internalization and Nanocluster-Induced NIR Photothermal Therapy. *Adv. Sci.* n/a–n/a (2015). doi:10.1002/advs.201500108

311. Jain, P. K., Lee, K. S., El-Sayed, I. H. & El-Sayed, M. A. Calculated absorption and scattering properties of gold nanoparticles of different size, shape, and

composition: applications in biological imaging and biomedicine. *J. Phys. Chem. B* **110,** 7238–7248 (2006).

312. Le Ru, E. C. & Etchegoin, P. G. Quantifying SERS enhancements. *MRS Bull.* **38,** 631–640 (2013).

List of Publications

D. Jiménez de Aberásturi, **A.B. Serrano-Montes**, L. M. Liz-Marzán. *Modern Applications of Plasmonic Nanoparticles: from Energy to Health* Advance Optical Materials **2015**, *3*, 602-617.

Y. Wang, **A.B. Serrano-Montes**, K. Sentosun, S. Bals, L. M. Liz-Marzán. *Stabilization and Encapsulation of Gold Nanostars Mediated by Dithiols*, Small **2015**, *11*, 4314-4320.

A.B. Serrano-Montes, D. Jiménez de Aberásturi, J. Langer, J.J. Giner-Casares, L. Scarabelli, A. Herrero, L.M. Liz-Marzán. *A General Method for Solvent-Exchange of Plasmonic Nanoparticles and Self-Assembly into SERS-active Monolayers*, Langmuir **2015**, *31*, 9205-9213.

A. B. Serrano-Montes, J. Langer, M. Henriksen-Lacey, D. Jiménez de Aberásturi, K. Sentosun, A. Bekdemir, S. Bals, L.M. Liz-Marzán. *Gold Nanostar-coated Fluorescent Polystyrene Beads as Bifunctional Nanoprobes for in vitro Multimodal Imaging of Live Cells*, Manuscript in preparation.

D. Jiménez de Aberásturi, J. Langer, **A.B. Serrano-Montes**, M. Henriksen-Lacey, W. Parak, L.M. Liz-Marzán. *Encoded-Gold Nanostars for Multiplexed SERS Cell Diferentiation*, Manuscript in preparation.

C. Hamon, M. Henriksen-Lacey, A. La Porta, J. Langer, L. Scarabelli, **A.B. Serrano-Montes**, G. González-Rubio, L. Basabe-Desmonts, L. M. Liz-Marzán. *Tunable nanoparticle and cell assembly using combined self-powered microfluidics and micro-contact printing*, Manuscript in preparation.

Agradecimientos

Quizás esta sea la parte más difícil de escribir. Son tantas las personas que me han acompañado en este recorrido…

Empezar agradeciendo a todo el increíble grupo de *BioNanoPlasmonics*. En primer lugar a mi director de tesis Luis, por haberme dado la oportunidad de hacer esta tesis en biomaGUNE, por su dedicación y su paciencia. El poder trabajar en su grupo sin duda me ha aportado muchísimo no solo a nivel profesional, también a nivel personal. Ha sido una experiencia única. Gracias por todo Luis.

BioNanoPlasmonics es una familia… ¡y todos coincidimos en que Ada cuida bien de ella! ¡Gracias por estar siempre ahí, y por organizar los *groups meetings* y los *gin tonics*! A MartaSan y Pablo… por todos los viajes juntos, por las escapadas y caminatas al monte, ¡y por esa inolvidable tarde en vuestro jardín! Gracias a Denis, que se nos doctoró y lo perdimos un poco… ¡pero siempre serás *mi pañero*! A Juanjo, por nuestros inicios en el Kiskurra, ¡y las cenas en la sociedad! A Leo, ¡por todas las canciones que hemos bailado moviendo nuestra melena y por la sidra que hemos compartido! A Judith, por sacar siempre los mejores *specs* ¡y por todas las birras que nos hemos tomado por SAVVY! Dorleta y Susana… las conocimos en el Rici, ¡y sabíamos que eran un buen fichaje! ¡Gracias a Dorleta por su gran ayuda en el *lab* y Susana por actitud deportista y motivadora! A Malte, por enseñarme nociones básicas de escalada ¡y acompañarme con el *Jagermeister*! A Malou, por cuidar tan bien de las células. A Joseba, ¡por nuestra gran noche de karaoke! A Guille, por ese buen jamón extremeño. A María, por su buena compañía tanto en la oficina como en el *gym*. A Yusong, por ayudarme con gran parte del trabajo de esta tesis. En general gracias a todos los que me habéis acompañado durante este tiempo: Isa, Perce, Cyrille, Lakshmi, Ibisate…A los recién llegados: ¡*seguid manteniendo el ambiente tan especial de este grupo*! Por último a Andrea, ¡tú has sido el mejor resultado de mi tesis! Gracias por acompañarme en los buenos y en los malos momentos, y por enseñarme a ser mejor persona a tu lado.

Durante estos tres años me ha faltado algo… Mi gente del sur. Os he echado de menos Casti, Inma, Sarita, Anais, Ro, Mjou, Tere, Mari Carmen, Loli, *Shh, amoh...* ¡Gracias por vuestras visitas al norte (doble en el caso de Sara)! ¡Y por las buenas *junteritas*! ¡Sois únicas! A “mi prima” Auri, gracias por todos los años que compartimos juntas en la carrera, a Cantero por venir a Vigo con su esposa, y a Juanlu ¡por esa visita a Karlsruhe!

Las últimas palabras se las quiero dedicar a mi familia. A mis hermanos Santi, Jesús y Jose, por los infinitos viajes al aeropuerto, por vuestra ayuda y sobre todo por toda la fuerza en los malos momentos. A mi abuela, que fue tan especial para mí… Y a mi padre y a mi madre, por apoyarme siempre en todas mis decisiones, por vuestro cariño, vuestro amor y vuestra comprensión. Especialmente a mi madre, por sobrellevar más que nadie la distancia.